

**UCSF**

**UC San Francisco Electronic Theses and Dissertations**

**Title**

The role of TGF $\beta$  Mediated Osteocytic Perilacunar/canalicular Remodeling in Age-related Bone Fragility

**Permalink**

<https://escholarship.org/uc/item/018319q0>

**Author**

Schurman, Charles August

**Publication Date**

2022

Peer reviewed|Thesis/dissertation

The role of TGFβ Mediated Osteocytic Perilacunar/canalicular Remodeling in Age-related Bone Fragility

by  
Charles Schurman

DISSERTATION

Submitted in partial satisfaction of the requirements for degree of  
DOCTOR OF PHILOSOPHY

in

Bioengineering

in the

GRADUATE DIVISION

of the

UNIVERSITY OF CALIFORNIA, SAN FRANCISCO

AND

UNIVERSITY OF CALIFORNIA, BERKELEY

Approved:

DocuSigned by:

*Tamara Alliston*

Tamara Alliston

E233CABEF261499...

Chair

DocuSigned by:

*Ralph Marcucio*

Ralph Marcucio

DocuSigned by:

*Phillip Messersmith*

Phillip Messersmith

7A2D9A0DDA2449D...

Committee Members

**Copyright 2021  
by  
Charles A Schurman**

## Acknowledgements

The irony is not lost on me that this is the last portion I am attempting to write but will likely be the first part read by many of you who find this document. Penning, or rather typing, out these final words I do not without a small portion of apprehension and procrastination as it means the final closing of my time as a student. As part of my graduate school journey, and my academic journey as a whole, I have been very grateful and blessed to have met and been supported by so many individuals that have enriched my time and made this journey worth the effort. Science is too hard to do alone and times to thank those who journey with are few and far between. I will, with my best effort, include all I can in my thanks but there are doubtlessly those out there who have impacted me and my time here that I do not know or will miss in my recounting here, so first to those unnamed here, thank you.

To Dr. Tamara Alliston, my mentor, advisor, boss, colleague, and friend, I owe the greatest due. Thank you for allowing me to join your lab when I had nowhere else to go - who knew all those years ago that I couldn't have found a more perfect home for my graduate education that fog-covered Parnassus on the 11<sup>th</sup> floor of Medical Sciences. Through your example I have become not only a better scientist but a better person. Your scientific diplomacy and grace are traits to be esteemed and I try to emulate them whenever I can. Your trust in me to try new things allowed me to follow my own curiosities but you were always on hand to steer me back on course if I was ever too "creative" in my thinking. Your excitement for science always inspired me to work harder to find the answers to the questions we both had. Your championing of a healthy work-life balance, and protecting one's personal well-being, I believe, lets all of us in the lab live as better more well-rounded scientists and this quality is unfortunately not as common in science and academia as it should be. I once asked what your mentoring style was for me and you sort of casually mentioned that you didn't really have one for me because I didn't need much direct mentoring, but I believe you just living your authentic self was mentoring style I needed that you provided and allowed me to flourish scientifically and personally. I am so lucky to count you among

one of the people I will have a life-long connection with and am grateful everyday to have been one of your students.

To all the members of the Alliston lab, past and present, thank you for creating a family where coming to lab and work was never dull, dreary, or something I dreaded. Lab trivia, taco night, coffee runs, cocktails by Golden Gate park, lunch at Taboun, making dioramas out of spare office and lab supplies, dressing up our little AbCam plush dinosaurs from vendor fairs, true crime podcasts during dissections, all these and more are times I will treasure. To my senior students who laid excellent examples of how to be a graduate student and to work in our shared space, Courtney and Dave, thank you for being direct mentors and model individuals. Dave and Courtney were the power duo of the lab and left large shoes to fill. To the post docs Neha, Serra, Gabby, and Claire, thank you for the guidance and patience and friendship. Claire, you set up the opportunity for me to bring my material science skills into the lab and without your work my project wouldn't be half of what it is. Gabby you left us too soon (don't worry she's fine she just got a new job very fast) but I know you're only a snapchat away. You're a personal hero of mine and I wish you the absolute best whether it's in industry or academia but I know I'll get to be along for that ride. Neha, you helped me become a molecular biologist, something I never truly expected would happen, and your comradery in lab was always needed. Serra, someone who's eyes wouldn't glaze over when I discussed math, thank you for your incredible example and work ethic, all that three-point bending weeks away from giving birth to your second child, you are truly the definition of persistent and reliable. To our many team members who managed the mice and were always there with an extra hand JJ, Jenny, Minali, and Clarissa, thank you for being of support and helping with the many many many mice in my study and willingness to jump into a dissection on moment's notice. To Cristal, our in lab captain, I can't count the number of times I rounded your bay with questions or concerns or for you to show me how to turn on the microscope again or if you had the next protocol I was looking for, your cheer and patience with me to help me figure out my next steps were invaluable. To Jihee, I am grateful to have spent time with you in lab and

I am excited to see you succeed in your future in whatever way you choose, you are truly bright and skilled and your work ethic inspired me to work harder and longer myself. Luke, for putting up with me talking out loud across the bench from you and good humor when I would rant about bone density or the newest pet peeve of mine on any given day meant more than simple conversation to me so thank you for being my drafted sounding board. Thank you to my rotation and summer students Jay and Caleb, for letting me explore different mentorship styles and following my stream of conscious directions and yet still being up for any next thing I asked from you. And last but certainly not least, my sister in arms, my comrade in a lab coat, the good doctor Karsyn Bailey. Despite our maybe rocky start, you became one of my closest friends and my biggest ally in lab. Thank you for patience and cheer. I miss our communal vent sessions and those sidewise nonverbal glances that meant “lets go get ‘coffee’ ”.

Beyond just the Alliston lab, I have to thank all of the ortholabs for being part of our larger lab family. In particular I have to thank all our admin support, Jessica, Maryam, Dylan, Pui-Yee, and all the others for answering my many emails. To Spencer, my east-bay train buddy, thank you for all the insightful conversations during our journey home about your time as a post doc, it helped inform my future decision to remain in science if just a little longer. To Dr. Aaron Fields, Dr. Wenhan Chang, Dr. Jeff Lotz, and Dr. Richard Schnieder, thank you for your additional mentorship and willingness to discuss different aspects of my project.

To all my additional mentors and supporters, including my thesis committee Dr. Ralph Marcucio and Dr. Phil Messersmith, my project benefitted from your guidance and insights. To all the other PIs, researchers, and collaborators I had the pleasure of working with across the country (and beyond!) thank you for lending me spots on your papers and adding to my own project, including Dr.s Chelsea, Ginger, Amy, Teresita, Sarah, Simon, Ryan, and Steffaan, I owe you thanks. Special thanks to Simon Melov and Jessica Garrison at the Buck Institute for the gift of the truly oldest mice on the planet that got my project started and off to a fantastic start, I look forward to working with you and the Buck again someday.

To Ryan Orendorff, my best friend and roommate for four long years, thanks for taking me in as a bright eyed, hopefully first year graduate student. I get it now, this was hard. All our steak dinners, video gaming, late night talks, dim sum, moving apartments three times, your several times almost passing away from strep, you were a wonderful presence to come home to and I miss you and wish you the best in Colorado. Thank you for thanklessly debugging my code when I couldn't get it to work, and letting me store mice bones occasionally in our fridge!

To all the BioEs and especially my cohort, I am very proud to be an alumnus with all of you. Stephen, Claudia, Kaz, Bryan, Andy, Kristin, and the rest, you made getting through this time together fun and entertaining.

The McGee house! Chris, Charlie, Al, Caveman, and Kristen, you gave me a home during the pandemic and for that I will be forever grateful. I surely would not have survived 2020 and 2021 alone in my apartment without the option to run down the block and commiserate the end of the world with our quarantine bubble. Being a part of this found family has saved my life in more ways than one and without your energy and ability to recharge me there was no way I would have finished my last few years of my doctorate. Thank you and I love you guys.

And finally, my family, Tim, Heidi, Alex, uncle Bob and Ivanna, you are my rock and greatest source of strength. We are small but mighty and I know no matter the situation I have your support and love. To my parents specifically, thank you for trusting in me and allowing me to follow my passions and pursue research. Your values and work ethic I take with me everywhere and you both continue to be inspirations for me in how to craft my life and live in this crazy world. Alex, I don't know how you did it, but despite it all you became a decent role model. You work so hard that its difficult for me to stand out anymore, so I'll just have to keep getting better! I look forward to that dinner not too far away where we can sit around, all the Doctor Schurmans, and celebrate all we've accomplished.

And to you reader, if you're still here, thank you, and enjoy.

## Contributions

I would like to acknowledge all of my co-authors on previously published manuscripts and book chapters that are contained in this dissertation. Portions of Chapter 3 are based on work in the peer-reviewed article “Investigating Osteocytic Perilacunar/Canalicular Remodeling” by Cristal S. Yee, **Charles A Schurman**, Carter R. White, and Tamara N. Alliston published in *Current Osteoporosis Reports* and the book chapter “Assessment of Osteocytes: Techniques for Studying Morphological and Molecular Changes Associated with Perilacunar/Canalicular Remodeling of the Bone Matrix” by Neha S. Dole, Cristal S. Yee, **Charles A. Schurman**, Sarah L. Dallas, and Tamara N. Alliston in *Methods in Molecular Biology (2021)*. Chapter 4 is based on the peer-reviewed article “Disrupted Osteocyte Connectivity and Pericellular Fluid Flow in Bone with Aging and Defective TGF $\beta$  Signaling” by **Charles A Schurman**, Stefaan W. Verbruggen, and Tamara N. Alliston in *The Proceedings of the National Academy of Sciences of the United States of America*.



## **Abstract**

The role of TGF $\beta$  Mediated Osteocytic Perilacunar/canalicular Remodeling in Age-related Bone Fragility

By

Charles A Schurman

Age-related bone fragility results from the decline of both bone mass and quality over a lifetime. While therapies exist that focus on bolstering bone mass, little is known about the cellular and molecular mechanisms controlling bone quality (BQ). Osteocytes comprise 90-95% of all bone cells and regulate local quality through perilacunar/canalicular remodeling (PLR). However, little is known about their role in the age-related bone fragility. Aging in bone leads to several bone quality defects including uncoupling of bone deposition and resorption, alterations to bone material properties, and degeneration of the underlying osteocyte Lacuno/canalicular Network (LCN). While the coordinated decline of these behaviors remains unexplained the role of osteocytes in each of these processes implicate osteocytes in bone aging.

Several hallmarks of aged bone also appear in bone from mice with limited transforming growth factor beta (TGF $\beta$ ) signaling in osteocytes, including poor fracture resistance and degeneration of the osteocyte LCN. Loss of TGF $\beta$  signaling in osteocytes also results in decreased expression of PLR enzymes responsible for maintaining bone material properties. Thus, a similar phenotype arises with aging and with the losses to TGF $\beta$  signaling in osteocytes. However, the extent to which these similarities are mechanistically related remains unclear.

This work outlines the study of PLR and tracks TGF $\beta$  signaling and PLR in osteocytes over a lifetime to uncover molecular and mechanical mechanisms partially responsible for age-related bone fragility. Identification of specific mechanical weaknesses, the molecular and chemical players behind them, and the cellular processes responsible for their emergence provide new therapeutic targets for improving bone quality and fracture resistance with age.

## Table of Contents

<b>Chapter 1: Introduction</b> .....	1
References.....	17
<b>Chapter 2: Materials and Methods</b> .....	22
References.....	39
<b>Chapter 3: Considerations for Studying Perilacunar/Canalicular Remodeling</b> .....	43
<b>&amp; Assorted Protocols</b> .....	43
Protocol - Molecular Assessment of Osteocytic PLR via qRT-PCR .....	58
Protocol - Molecular Assessment of Osteocytic PLR via Immunohistochemistry .....	63
Protocol - Molecular Assessment of Osteocytic PLR via Tartrate Resistant Acid Phosphatase Staining .....	65
Protocol - Morphological Assessment of Osteocytic PLR via Silver Nitrate Stain (2D) .....	70
Protocol - Morphological Assessment of Osteocytic PLR via Dil/Phalloidin Stain (3D) .....	73
Protocol - Canalicular Length (2D).....	78
Protocol - LCN Area / Bone Area (2D).....	79
Protocol - Lacunar Number Density from 2D Fluorescent Tile Scans or Large Bone Sections .....	80
Protocol - Whole Mount Image Processing to generate RGBs, 8-Bit, and Binary Images (3D) .....	82
Protocol - LCN Volume Fraction (3D) .....	85
Protocol - Canalicular Spacing (3D).....	86
Protocol - Canalicular Tortuosity (3D).....	87
Protocol - Canaliculi per Osteocyte (3D).....	89
References:.....	97

<b>Chapter 4: Disrupted Osteocyte Connectivity and Pericellular Fluid Flow in</b>	
<b>Bone with Aging and Defective TGF<math>\beta</math> Signaling .....</b>	<b>108</b>
References.....	129
<b>Chapter 5: The Role of TGF<math>\beta</math>-regulated Osteocytic Perilacunar/canalicular</b>	
<b>Remodeling in Age-related Bone Fragility.....</b>	<b>134</b>
References.....	171
<b>Chapter 6: Summary, Conclusions, and Future Directions .....</b>	<b>179</b>
References.....	192

## List of Figures

<b>Figure 1.1:</b> Brittle versus ductile fracture in materials and bone.....	4
<b>Figure 1.2:</b> Hierarchical order of bone.....	6
<b>Figure 1.3:</b> T $\beta$ RII <sup>ocy-/-</sup> and aged bone demonstrate hallmarks of PLR suppression .....	15
<b>Figure 2.1:</b> Sample preparation for tensile testing .....	31
<b>Figure 3.1:</b> Homeostatic control of bone mass and quality by osteoblasts, osteoclasts, and osteocytes .....	45
<b>Figure 3.2:</b> Diversity in the histological appearance of the lacunocanalicular network (LCN) across species and bones.....	47
<b>Figure 3.3:</b> Housekeeping gene selection and stability for aged osteocytes .....	52
<b>Figure 3.4:</b> Molecular assessment of PLR.....	53
<b>Figure 3.5:</b> Stains highlighting morphological changes in osteocytes associated with PLR.....	63
<b>Figure 3.6:</b> Canalicular Dendrite Segmentation and Quantification at the Sprouting Point via IMARIS.....	87
<b>Figure 4.1:</b> Aged and T $\beta$ RII <sup>ocy-/-</sup> bone share molecular and canalicular morphologic changes.....	106
<b>Figure 4.2:</b> Nodal analysis shows maintenance of network architecture but loss of total network interactions with age and TGF $\beta$ signaling disruption in osteocytes.....	108
<b>Figure 4.3:</b> Aged and T $\beta$ RII <sup>ocy-/-</sup> osteocyte networks have limited pathway availability and lower transport capabilities in in silico connectomic models .....	111
<b>Figure 4.4:</b> Finite Element models of individual osteocytes .....	113
<b>Figure 4.5:</b> Fluid dynamics modeling demonstrates lower fluid velocity and shear stress as a function of pericellular space volume and not canalicular morphology .....	116
<b>Figure 5.1:</b> Similar transcriptional regulation in aged bone and bone with osteocytic interruptions to TGF $\beta$ signaling .....	130

<b>Figure 5.2:</b> Age-related degeneration of the osteocyte network in males occurs in a TGF $\beta$ - dependent method but may occur through other mechanisms in females.....	133
<b>Figure 5.3:</b> T $\beta$ RII <sup>ocy-/-</sup> bone demonstrates tissue level fragility similar to aged bone stiffening.....	138
<b>Figure 5.4:</b> Accelerated bone growth and aging in T $\beta$ RII <sup>ocy-/-</sup> cortical bone.....	140
<b>Figure 5.5:</b> Synchrotron SAXS/WAXD shows altered collagen behavior in T $\beta$ RII <sup>ocy-/-</sup> bone during in situ tensile testing.....	145
<b>Figure 5.6:</b> Collagen quality is impacted by both age and osteocytic TGF $\beta$ signaling.....	149
<b>Supplemental Figure 5.1:</b> Evaluation of load-displacement curves revealed changes to mechanical behavior during bending tests despite no change to energy dissipated during fracture.....	161
<b>Supplemental Figure 5.2:</b> Within genotype comparison of collagen strain with age shows increased collagen strain in male and female T $\beta$ RII <sup>ocy-/-</sup> bone. ....	162

## List of Tables

<b>Table 3.1:</b> Reverse transcription master mix.....	60
<b>Table 3.2:</b> Thermocycler reverse transcription temperature gradient guide.....	61
<b>Table 3.3:</b> PLR gene primers for RT-qPCR.....	61
<b>Table 3.4:</b> iQ-SYBR Green mastermix for qPCR.....	62
<b>Table 3.5:</b> Thermocycler RT-qPCR temperature cycle guide.....	62
<b>Table 5.1:</b> Univariable and Multilevel linear mixed models describe age as the primary Driver of lost TGF $\beta$ ligand abundance .....	135
<b>Table 5.2:</b> $\mu$ CT Trabecular parameters for aged T $\beta$ RII <sup>ocy-/-</sup> bone. ....	142

## List of Abbreviations

AFM	Atomic Force Microscopy
AGEs	Advanced Glycation End-products
BC	Betweenness Centrality
BMD	Bone Mineral Density
BQ	Bone Quality
BSA	Bovine Serum Albumin
cc	Clustering Coefficient
CD	Connective density
CED	Camurati Engelman disease
CML	Carboxymethyl lysine
Ctrl	Control
DAPI	4'-6-Diamidino-2-phenylindole
DHLNL	Dihydroxylysinoxorleucine
Dil	1,1'-Dioctadecyl-3,3,3',3'-Tetramethylindocarbocyanine Perchlorate
DMSO	Dimethyl sulfoxide
DPD	Deoxy pyridinoline
ECM	Extracellular matrix
EDTA	Ethylenediaminetetraacetic Acid
EtOH	Ethanol
FE	Finite Element
FFPE	Formalin-fixed, paraffin-embedded
FTIR	Fourier Transform Infrared Spectroscopy
HA	Hydroxyapatite
HLNL	Hydroxylysinoxorleucine
HPLC	High-performance Liquid Chromatography
LCN	Lacuno/canalicular Network
LOX	Lysyl Oxidase
LOXL	Lysyl Oxidase Like
MMPs	Matrix Metalloproteinases
NBF	Neutral buffered formalin
NDS	Normal Donkey Serum
OCT	Optimum cutting temperature

OI	Osteogenesis Imperfecta
P2	Second Legendre Coefficient
PBS	Phosphate Buffered Saline
PCS	Pericellular fluid space
PFA	Paraformaldehyde
PLR	Perilacunar/canalicular Remodeling
PTH	parathyroid hormone
PTHrP	parathyroid hormone-related peptide
PYD	Pyridinoline
RNA	Ribonucleic Acid
RT	Room Temperature
SAXS	Small-angle X-ray scattering
SEM	Scanning Electron Microscope/Microscopy
SNT	Simple Neurite Tracer
SOST	Sclerostin
SRmT	Synchrotron radiation Micro-Tomography
TDE	2,2'-Thiodiethanol
TGF $\beta$	Transforming growth factor beta
TMD	Tissue Mineral Density
T $\beta$ RII	TGF $\beta$ type II receptor
WAXD	wide-angle X-ray diffraction



# Chapter 1: Introduction

Skeletal fragility is as much a biologic and clinical concern as it is a mechanical, material, and engineering affair. Any study of the skeletal strength and fracture should be concerned with its cellular and biologic origin as well as its nature as a hierarchically ordered structural material. Noting on the later, as a structural system the skeleton can be thought of in engineering terms and theories to classify and qualify its behavior in varying situations of mechanical demand. Using these schools of thought, one can understand the physics behind the forces exerted upon the skeleton as a structure and how it may 'fail' under differing applied loads and strains to assay the maximum extents to which the skeleton can function within this role. However, the skeleton's nature as a biologic material elevates it above general static engineered materials as it has the capability to grow, to adapt, and even to renew. This remarkable capability to reverse damage through cellular and molecular means places the skeleton among the echelon of materials current engineers and designers can only dream about, self-renewing stability. Again however, as all biologic systems are bound to do, the skeleton and its cellular components age and the

mechanisms responsible for its material upkeep go awry and thus its structural stability suffers. Biologic mechanisms and life itself are then centered in the narrative of skeletal health and the defense against skeletal fragility. In this work, we will consider the aging skeleton, and more poignantly skeletal material, from both sides as a living and dynamic biologic system and as an engineered structural material generated and managed by its biologic components.

### **Strength or Toughness?**

The conflict between strength and toughness is at the heart of most structurally designed materials, and even as a biologic material designed over millennia and crafted by evolution, the skeleton does not escape this conflict of duality. Almost all structural materials, designed by humans at least, must meet the requirements that they are both strong, able to hold or resist amounts of required weight or applied load, while also being tough, or damage resistant. The skeleton is no different as it must support the weight of the body, articulate against itself, and enable locomotion with as little damage as possible all while avoiding catastrophic failure. Perhaps in a twist of metaphysical irony, the properties of strength and toughness can be mutually exclusive.<sup>1</sup> Where “strength” in engineering terms describes the ability for a material to resist unrecoverable deformation, “toughness” is the ability to absorb energy without failure, generally directly through limited deformation after yielding, known as plastic deformation. Thus, where in the common vernacular these terms are often taken to mean the same thing, materials science and engineering focuses on the interplay between the mechanisms contributing individually to both strength and toughness. In fact, a material's toughness is traditionally thought of as a combination its strength, initial resistance to movement, and its ductility, it's plastic deformation capacity post initial movement. By definition, these two properties are considered mutually exclusive. Thus, it is the both the ability to “carry” weight and the ability to experience a change in structure without losing much integrity that confers toughness to a material. As such, it is lower strength and higher toughness materials that often win out in situations where avoidance of abject

failure or fracture is the primary goal. Across the animal kingdom the effects of evolutionary preference for high toughness and lower hardness or stiffness in load bearing bones is seen through the differences in modulus, mineral content, and work to fracture when comparing the bovine femur and the bulla from a toothed whale.<sup>2</sup> The femoral bovine bone has a higher bending strength and work of fracture than the bulla - a portion of the whale's highly developed sonar and hearing apparatus that does not support body weight - but lower mineral content and elastic modulus. These mechanical differences account for the differences in roles that these two specific bones play in the body where the flexibility and toughness of the femur enables mechanical support and locomotion and the bulla's rigidity enables the precise sensing of minute vibrations in the ocean. The skeleton's mechanical properties are then specifically optimized for their context and function and so the appendicular skeleton focuses on maximizing toughness.

If then toughness is to be prioritized for the longevity of a loading bearing material and the criteria for its evaluation as a structure as a whole, knowledge of the origin of toughness within the skeleton must be considered. Bone itself consists mainly of type I collagen, arranged in lamella or sheets of fibers, and inorganic calcium phosphate mineral (hydroxyapatite - HA) in the form of small crystals along and within the collagen fibers.<sup>3,4</sup> Alive, bone contains between 10% and 20% water and of its dry mass approximately 60-70% is the bone mineral. The rest is known as the organic matrix which is primarily collagen type I but also contains a collection of other bone-associated proteins critical for mineralization and assembly<sup>5</sup>. Because bone is dominated in composition by its mineral constituents, it is generally classified and behaves as a brittle material<sup>6</sup>. Brittle materials are usually inelastic, or do not deform much before fracture or failure, think of a ceramic pot (**Fig. 1.1A**). Brittle ceramic materials and bone material (**Fig. 1.1B**) are also high in strength and hardness (the ability to withstand indentation), because the rigid crystals that compose these minerals are small and irregularly placed creating numerous dislocations or continuity errors within the material<sup>7,8</sup>. In deformation terms, their inflexible crystal structures and irregular arrangements make it more difficult for neighboring granular pieces, or grains, of mineral

within ceramics to slide past themselves and allow the whole material to engage in plastic deformation. In addition, the brittle nature of ceramics can be connected in part to grain boundary/interfacial effects where within an individual crystal/grain, plastic deformation is impeded by the inability of charged atoms to be displaced from their equilibrium positions. This contrasts with traditionally tough materials, such as most metals (**Fig. 1.1C**), where plastic deformation is allowed by movement of atoms from one equivalent lattice position to another allowing crystals and/or grains to individually stretch before finally being pulled out of the bulk material. This is the physical root of brittleness in ceramics, they resist motion but once moved the discontinuous pieces are no longer held together and the system fractures. Because bone is a brittle material, dominated by strength but desiring toughness, other aspects than its mineral must lend toughness to bone.

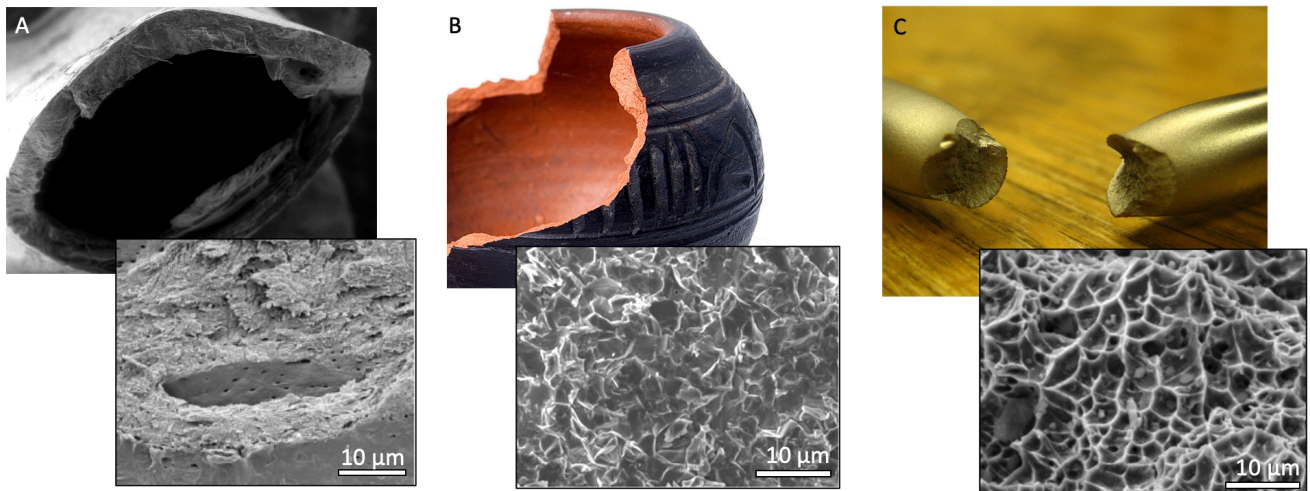


**Figure 1.1: Brittle versus ductile fracture in materials and bone.** Materials of different types experience fracture in different ways. Most minerals and hard ceramics (A,B) are unable to engage in plastic deformation and experience brittle fracture on the nanoscale where rigid crystals that cannot deform are either cleaved through or split at crystal and grain boundaries leaving an uneven, sharp surface as seen through SEM (B, inset). Bone mineral (A) is mainly ceramic in nature and fractures primarily in a brittle fashion with little stretching of the mineral crystals as seen by the rough surface in the SEM (A, inset) surrounding the more polished surface of an inner osteocyte lacuna. Ductile materials, like metals (C) that have intrinsically high toughness, are able to plastically deform after yielding before failure resulting in necking, or stretching, of the material on the macroscale and an accompanying dimpling/cupping pattern on the nanoscale (C, inset) as the result of individual metal crystals stretching prior to separation from the bulk material.

## **Bone as a Hierarchically Ordered Material**

Bone belongs to another specialized class of materials that are hierarchically ordered, meaning the bone material has transcending levels of organization on multiple length scales from the smallest most principal nanoscale components up to whole-tissue levels<sup>3,9</sup> (**Fig.1.2**). Each level attains specific properties at its principle length scale that add to bone's toughness, but also acquires emergent behaviors from each successive layer underneath it. The specific number eof levels of hierarchy in bone from the nano, micro, to macro length scales can depend upon species and overall body size.

As discussed, bone is primarily composed of a mineral known as hydroxyapatite ( $\text{Ca}_5(\text{PO}_4)_3(\text{OH})$ ). This mineral is arranged in hexagonal crystals composed of two individual base molecules and so its chemical structure is usually represented as  $\text{Ca}_{10}(\text{PO}_4)_6(\text{OH})_2$  to indicate the two-sided nature of the crystal unit cell<sup>5</sup>. Other trace minerals, fluoride, chloride, and carbonates may substitute the terminal hydroxides to generate additional specialized minerals, although this is more likely to occur in tooth enamel than within bone. The chemical bonds holding the crystal together are on the order of Angstroms, or tenths of nanometers, and crystallize into long slender crystals nanometers in length<sup>10</sup>. These crystals form the smallest level of order within bone and represent 60-70% of bone by mass and are what grant bone its brittleness and strength.

Bone's toughness on the other hand, is generated primarily through its organic components. On the organic, or carbon-based, side bone on the nanoscale is a collection of amino acid chains each individual piece blueprinted in DNA of the collagen I genes. Collagen I itself is a protein encoded by two separate genes: alpha-one and alpha-two. These alpha-one and alpha-two 'sub-chain' proteins combine in a 2:1 ratio, wind together, and become the next level of order known as the tropocollagen triple-helix. Chemical bonds among the sub-chains bind the individual pro-collagen molecules together generating a new structure around 300 nanometers in length. The new tropocollagen molecule, a twisted and kinked structure, has more rigidity than the individual alpha chains and its wound structure grants a certain amount of 'spring-like' stretching

capability, the first emergent tensile capability found in bone that will go on to generate tissue scale toughness for the whole tissue.

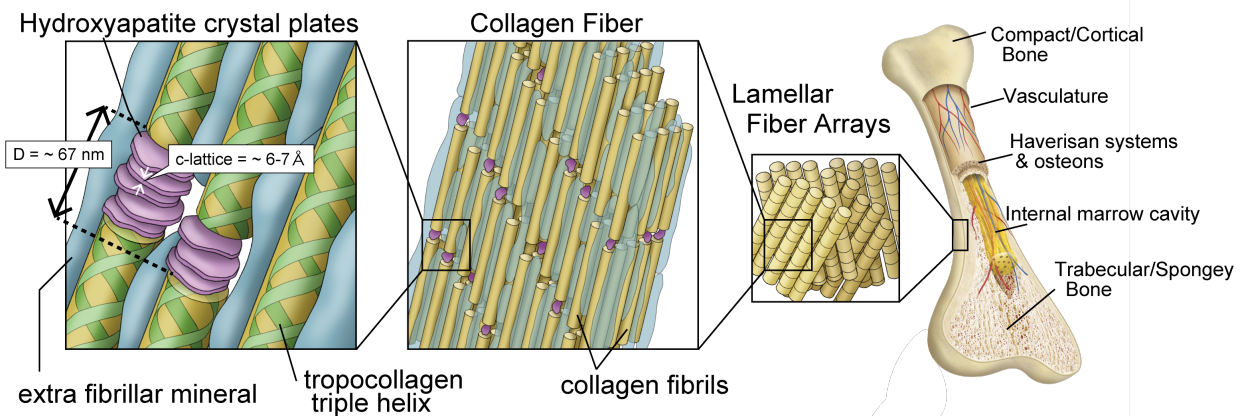


**Figure 1.2: Hierarchical order of bone.** Bone has transcending levels of organization from the nanoscale up to the whole tissue level. The primary scale where bone becomes a composite material exists at its most basic level of organization where mineral crystals and collagen protein assemble to form periodic structures. Patterning of this composite material in successively higher levels grants bone toughness and tensile properties absent from bone mineral alone.

Stepping up another level, the organic and inorganic portions of bone, collagen and mineral, come together to create the composite mineralized collagen fibril. On this level, individual tropocollagen helices are arranged in regular intervals both longitudinally and latitudinally with HA crystals orderly inserted with the gaps between the terminal ends of tropocollagen, or less ordered along the lengths of the fibrils<sup>11,12</sup>. The individual tropocollagen helices are connected to one another through a series of interfibrillar chemical crosslink events tightly controlled through an enzymatic maturation process<sup>13</sup>. These crosslinking events generate another level of tensile strength for bone, connecting hundreds of individual collagen helices into millimeter length collagen fibrils with regular spacing about 67 nanometers apart known as the collagen “d-spacing”. Individual helices within this superstructure are able to unbind and slide against one another when highly stretched where mechanical energy is consumed to unbind individual helices from their fibrils<sup>9</sup>. Further still, these collagen fibrils are collected into yet another larger structure as fibril arrays or long fibers tens of millimeters in length. Superficial interaction of collagen with

other non-collagenous bone proteins, (bone sialoprotein, dentin matrix phosphatase-1, osteocalcin, etc...), may interact with one another and loosely bound positive ions such as calcium and magnesium through electrostatic and other weak bond interactions to generate “sacrificial bonds”<sup>14</sup>. These sacrificial bonds may be separated and reformed during minimal stretching and add another layer of tensile strength and toughness to bone.

Collagen fibers and fiber arrays are laid out in layers known as lamella in the next level of bone hierarchy. Within a single lamella, many collagen fibers run parallel next to one another while multiple lamella can be stacked upon one another in vary orientations, depending on bone type, to generate fiber patterns 3–7  $\mu\text{m}$  thick.<sup>4</sup> Common orientations for layering these fiber patterns include a “woven” or less ordered orientations common in immature not-yet-remodeled bone, and as “twisted plywood” structures as found in mature cortical, or lamellar long bone. In cortical, compact bone of the diaphysis, lamella encircle central points and form concentric circles to create bone columns called osteons around either the central marrow cavity, as seen in smaller mammals like mice, or around blood vessels and canals to generate what are known as haversian systems in larger mammals. For smaller mammals, like mice commonly used in scientific research, this is the final layer of order before lamella are shaped and molded into the final bone, as the central marrow cavity and outer periosteal cellular layers are sufficient to provide long bones with appropriate vascular and oxygen supply. However, for humans and other larger mammals that require additional vascular supply to cortical bone compartments, circular osteons and their internal haversian systems make up the next to last layer of order in bone.

For us and other larger animals, impacting edges of osteons meet each other at more highly mineralized boarders called cement lines. Cement lines are important in larger bones as they create inhomogeneities within the bulk material that can help redirect and absorb energy during cracking. Collections of osteons come together to form the largest portions of cortical bone, while spongy or trabecular bone is composed of thinner lamellar sheets surrounded by marrow towards the metaphysis and epiphysis of long bones. The delineation between compact, cortical

bone, and spongy, trabecular bone is one of the largest levels of delineation in bone hierarchy and depends on the orientation and arrangement of its underlying lamella. As a part of this final layer of bone order is the overall shape of the bone. While the molecular control mechanisms that determine the sophisticated geometry of bones remains under study, their final shapes are tightly related to function as is seen in the diversity of bone shape, size, and function.<sup>2</sup>

### **Mechanisms of Toughening**

At each level toughness and strength are drawn from the specific composition and arrangement of the material at that length scale and those underneath. Bone can increase its toughness and fracture resistance in two primary ways, through intrinsic or extrinsic toughening mechanisms. First, in intrinsic toughness, bone can increase the energy required to initiate a crack by deforming plastically before a crack begins. Second, it can increase its use of extrinsic toughening mechanisms or behaviors that act behind a progressing crack to shield remaining material from the crack tip<sup>8,9</sup>. Unfortunately, bone mineral has little intrinsic toughness because it is primarily a brittle ceramic. Unlike metals and other non-brittle materials, bone mineral does not engage in much plastic deformation after yielding. Instead, after yielding, the stressed mineral rapidly fractures allowing crack progression. What little plastic deformation bone does have is derived from its nature as a composite material with organic components and multiple levels of structure. Thus, the few abilities collagen has to stretch and slide grant bone its limited plasticity. These include fibrillar uncoiling and sliding and sacrificial bonding, mechanisms on the scale of tens to hundreds of nanometers on the lower levels of hierarchy. Past this, bone can engage in extrinsic toughening mechanisms, or behaviors that can reduce the energy of a growing crack behind the advancing edge of the defect to increase its toughness post-yield. These behaviors essentially extend the life of the material even in the presence of a defect/crack. They include 1) constrained microcracking that can relieve built up strain in the material generated by the compressive edge of an advancing crack, 2) unbroken ligament bridging parallel to the direction of the advancing



crack that provides small amounts of structure within the crack, 3) collagen-fibril bridging perpendicular to the crack that holds material together longer in the crack wake, and 4) crack deflection that can redirect the crack along longer paths before ultimate fracture. Each of these mechanisms relies on the composite nature of bone and the specific ways that its hierarchical structure allows for motion to relieve or reduce internal strains.

As a complex material bone has many ways to resist and reduce mechanical stresses and strains but many of these rely on motion or damage of underlying structures. In an instance of sudden impact or deformation, if bone sufficiently halts the progression of a crack and prevents complete failure, there is still the presence of a large defect within the material. Even everyday wear and tear can generate microcracks or fibrillar motion known in the long term as fatigue damage<sup>15,16</sup>. In living bone, cellular mechanisms of remodeling, to be discussed in more detail in later chapters, can actively repair and reestablish structural integrity<sup>17</sup>. While not considered a specific method of “toughening”, these cellular behaviors greatly enhance the overall lifetime of bone and can even repair full fractures should they occur, thus damage that may spell the end for other engineered materials is able to be compensated for by biologic action within bone.

### **Losing Bone Toughness**

Besides the generation of diffuse microdamage there are several additional possible alterations to the bone material that can negatively impact the toughness of bone. First and most obvious are deficits to bone mineral content. Prolonged lack of dietary calcium or vitamin D deficiency may negatively affect bone mass and can develop into disease conditions such as Rickets and osteomalacia where bone softens and becomes more fracture prone. Osteopenia and osteoporosis, clinical conditions of low bone mass, are also linked to genetic abnormalities that prevent the normal accrual of bone mass during growth and adolescence as well as drug affects and other lifestyle conditions (smoking, heavy alcohol use, lack of exercise, etc...). Previously healthy elderly individuals are also at risk for osteoporosis as bone resorption can outpace bone

deposition in aged individuals<sup>18</sup>. While it can occur through several ways, the direct loss of bone mineral in the skeleton reduces its strength and resistance to fracture directly impacting toughness.

Less well understood are the changes to the organic matrix of bone upon which toughness is more directly related. The collagen matrix of bone requires chemical crosslinking to establish its levels of order that allow for fibril motion and stretching. In some genetic disorders, mutations within the collagen I genes, for example Osteogenesis Imperfecta (OI), prevent the normal formation of the collagenous matrix needed for bone growth and results in under-mineralized but also misshaped bones with insufficient mechanical properties<sup>19</sup>. Some forms of OI are linked to the inability for mutated collagen to serve as a reservoir for molecular regulators of bone, such as Transforming Growth Factor Beta (TGF $\beta$ ), and over activity of these molecules on the cellular level can lead to imbalanced bone cell activity disrupting bone homeostasis and strength. These direct modifications or mutations within the collagen producing genes can produce collagen unable to provide its mechanical and biologic functions.

Even if the collagen genes are unaffected, other genetic disorders may impact the final collagen matrix. As part of the collagen maturation process, procollagen molecules undergo several steps of enzymatic post-translational modification. In some genetic disorders, such as Ehlers-Danlos syndrome that results in Lysyl Hydroxylase insufficiency or malfunction, collagen does not progress through these maturation stages properly because the enzymes required are defective<sup>20,21</sup>. This prevents proper collagen cross-linking that is necessary for the matrix stabilization. Several other enzymes are involved in the many steps of this process and alterations to their activity may impact collagen, and thus bone, stability.

Collagen is additionally prone to excessive crosslinking in non-enzymatic manners that can impair the flexibility of bone. These cross-links, also known as advanced glycation end-products (AGEs), occur through the Maillard reaction where extracellular sugars spontaneously react with amino groups along collagen to form new molecular connections along and between

collagen fibrils<sup>13,22</sup>. Because of their spontaneous nature and reliance on free-floating sugars, AGEs are particularly influential with age and diseases like Diabetes where they can accumulate up to as much as ten times with age than their original concentrations<sup>23</sup>. Such excessive levels of crosslinking have been shown to tighten collagen molecules and prevent intrinsic toughening mechanisms in bone such as fibrillar sliding.

An additional, and often overlooked, alteration to bone collagen that may affect mechanical properties is racemization and isomerization of the collagen molecule. Racemization is the spontaneous conversion of the native form of amino acids or sugars to the rare D form, the mirror-imaged version of the same molecule. These events are spontaneous and can cause kinks in the peptide backbone of collagen impacting mechanical behavior. Accumulation of D-isomers is common in tissues with low turnover such as dentin, the lower skin dermis, cartilage, and aged bone. In bone, racemization and isomerization have shown to involve the aspartic acid residue within the end-regions of type I collagen in the so called CTX sequence. Because of high bone remodeling in children, isomerized collagen is continuously cleared during bone remodeling and growth and high levels of this altered collagen do not accumulate. In adults, where bone remodeling is slower than the rate of isomerization, the equilibrium is achieved, resulting in a fairly constant  $\alpha/\beta$ -CTX ratio from the age of 20 years and above where about only 20% of CTX peptide remains in its original  $\alpha$  form and 80% is isomerized<sup>24,25</sup>. While the direct mechanical consequences are currently unknown, elderly individuals with high (within the top quartile) urinary  $\alpha/\beta$ -CTX ratios had elevated risk of fracture independent of hip bone mass and bone turnover rate<sup>13,22</sup>. Though the direct mechanisms by which racemization and isomerization may interfere with bone toughness remain unknown, the association with age-related fracture and slower bone remodeling is of concern. Alterations to the chemical nature of collagen fibrils and their interactions with neighboring fibrils, either by interrupting natural maturation processes or

additional alterations beyond these, can negatively affect the ability for collagen to properly engage in toughening mechanisms.

Comprising anywhere from 10 to 20% of bone volume in a living system, water is a determinant of bone's mechanical stability. Within bone water can be classified to one of two specific compartments: bound water and pore water<sup>26</sup>. Bound water is water that is structurally and chemically incorporated to the chemical constituents of bone or hydrostatically held near the hydrophilic residues of the collagen molecule (e.g., lysine, arginine, and hydroxyproline). Bound water contributes directly to bone toughness by conferring ductility or plasticity to bone and decreases with age along with fracture resistance. In rodents, the degree of mineralization within cortical bone increases throughout life, while bound water fraction decreases, suggesting that increased mineralization may displace water within the bone matrix over time. Atomic force microscopy (AFM) studies have shown that a small decrease in water content (from 12% by weight to 9% by weight of water) drastically increased the stiffness of bundles of mineralized fibrils and increased molecular packing of the collagen relative to the mineral phase.<sup>27,28</sup> Notched bending tests on dehydrated bone samples displayed a loss of extrinsic toughening mechanisms specifically the inability to form fibrous bridges in the wake of the crack<sup>29</sup>. Thus dehydration of bone leading to a loss of bound water is detrimental in many ways to proper bone mechanics. Pore water is water that resides within the channels of the Haversian system as well as within the smaller lacunar/canalicular network in which osteocytes reside. Pore water largely doesn't contribute to bone mechanics but can be involved in viscoelastic effects such as hydraulic stiffening where, at high strain rates, bone with high porosity and increased pore water may benefit from some mechanical stiffening<sup>30,31</sup>. To see large effects through hydraulic stiffening, however, pore volumes must be increased to 30-40% of bone volume, and this predisposes bone to several other structural weaknesses. Water provides many functions chemically and structurally, and dehydration of the bone, particularly with age, is determinantal to toughness by decreasing collagen flexibility and increasing overall brittleness.

## **Cellular and Molecular Regulation of Bone Material Properties**

The skeleton is susceptible to many physical and chemical changes that may alter its material properties, toughness, and mechanical stability. While the nature of these changes and how their presence directly impacts bone material properties and fracture resistance are understood from an engineering and physical perspective, the sophistication of our understanding of these physical mechanisms dwarfs our understanding of the biological mechanisms that are responsible for achieving them. Because these chemical and physical alterations primarily occur on the lowest length scales, it is appropriate to observe the direct enactors of these events and the regulatory systems that manage these changes on the same length scales. Primarily, when considering bone matrix material properties, the focus lands on bone embedded osteocytes - the dominant cell type within bone<sup>32</sup>. Osteocytes reside directly within the bone matrix, represent 90 to 95 percent of all cells in the adult skeleton, and directly regulate bone matrix material properties, and thus bone quality, in a number of ways. Osteocytes act to coordinate and balance the activity of osteoblasts and osteoclasts, the bone surface-residing cells that deposit and resorb bone respectively<sup>33</sup>. Osteocytes also engage with their own local bone material through a process known as perilacunar/canalicular remodeling (PLR) that allows them to control local bone matrix properties<sup>33,34</sup>. By orchestrating the activity of the other major bone cell types and by directly interacting with the bone matrix themselves, osteocytes have recently become known as the “master regulators” of bone health and homeostasis. In PLR, osteocytes excrete several factors that directly engage their local bone matrix including matrix metalloproteinases (MMPs) and other proteolytic enzymes as well as change their local pH to resorb and reform surrounding mineral. PLR may be active at low levels constantly to recycle damaged or worn-out bone material or called upon to create dramatic change within the skeleton, such as occurs during lactation to release calcium from the skeleton for milk production within mammals. By interacting with bone material at the cellular scale and below, osteocytes play a major role in the molecular regulation of bone material properties.

Of the many molecular and biologic regulators of bone cell behavior, Transforming Growth Factor Beta has multifaceted effects on the three bone cell types to regulate both bone mass and bone quality<sup>35,36</sup>. Osteoblasts produce and store inactive TGF $\beta$  within the mineralized bone extracellular matrix (ECM) in a latent form<sup>37</sup>. TGF $\beta$  activation can be achieved through integrins and mechanical stimulation, or by acid catalyzed by bone resorbing osteoclasts<sup>38</sup>. TGF $\beta$  regulates bone mass by promoting osteoblast differentiation and migration, and promoting bone resorbing osteoclast survival, helping to couple formation and resorption<sup>39</sup>. In osteocytes, TGF $\beta$  plays important roles in the regulation of both bone mass and bone quality by coordinating mechanoregulated bone formation through control of sclerostin and by mediating perilacunar/canalicular remodeling<sup>34,40,41</sup>. Through osteocytic PLR, TGF $\beta$  regulates bone quality, and more specifically the material properties of bone, independently of bone mass. Loss of TGF $\beta$  signaling in osteocytes of mice resulted in suppressed gene expression of enzymes characteristic of PLR that directly engage the bone material. Bones from these mice displayed cellular defects through lost integrity of the osteocyte network and exhibited poor material properties and reduced fracture toughness<sup>34</sup>. Limiting TGF $\beta$  signaling in osteocytes disrupted PLR, an important homeostatic mechanism that supports material properties and toughening mechanisms, and resulted in losses to bone quality and bone toughness.

### **Osteocytes, Age, and TGF $\beta$**

As one of the direct regulators of the bone extracellular matrix and bone material properties, osteocyte PLR is a critical homeostatic mechanism used to renew bone quality throughout life. However, bone quality declines with age through numerous ways including chemical alterations to bone matrix that modify material properties, changes to bone shape and microstructure, and through accumulation of fatigue damage and microcracking. The toughening mechanisms that increase fracture resistance in bone rest on the function of mineralized collagen which is susceptible to chemical and enzymatic factors. Throughout a lifetime bone remodeling decreases

through incompletely understood mechanisms and bone accumulates modifications through changes to collagen crosslinking, water content, and others.<sup>42-44</sup> Previous studies on aged mouse bone demonstrate that excessive crosslinking limits the ability of collagen to deform under stress preventing crack bridging and lowering bone toughness<sup>43</sup>. In addition, the cessation of bone remodeling with age allows for the accumulation of micro-cracks in bone and lowers overall toughness<sup>16</sup>. The changes that occur to the bone matrix with age are related to osteocyte function and identify osteocytes as a possible cellular agent responsible for bone aging. The molecular mechanisms behind the declines in osteocyte function however remain unexplained.

I found that the low bone quality phenotype of aged bone resembled that of bone with interruptions to osteocyte TGF $\beta$  signaling in which osteocyte PLR is suppressed (T $\beta$ RII<sup>ocy-/-</sup>). These similarities hint at a common mechanism responsible for low bone remodeling and bone weakness with age. Biochemical studies on old human bone show declining levels of TGF $\beta$  ligand with age<sup>45</sup>, and my recent preliminary data from RNA sequencing on aged mice bone shows lower expression of TGF $\beta$  and PLR related genes across a lifetime (**Fig. 1.3**). These changes coincides with a decrease in overall bone material quality and an increase in clinical fracture<sup>46</sup>. While the nanoscale material qualities and collagen modifications of T $\beta$ RII<sup>ocy-/-</sup> mice have yet to be characterized, our previous studies demonstrate notable bone quality defects and diminished PLR in these mice. Given that aged bone and bones from T $\beta$ RII<sup>ocy-/-</sup> mice share several hallmarks of poor bone quality, this work will test the hypothesis that declining TGF $\beta$  signaling in osteocytes with age leads to an arrest of osteocyte behavior and bone remodeling altering bone homeostasis and allowing for the

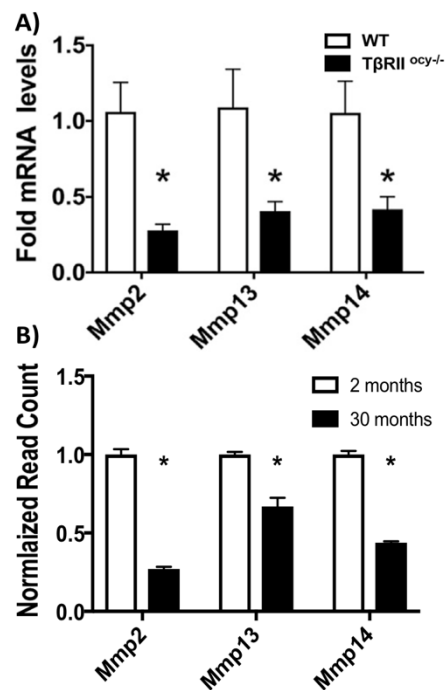


**Figure 1.3** T $\beta$ RII<sup>ocy-/-</sup> and aged bone demonstrate hallmarks of PLR suppression A) RT-qPCR from T $\beta$ RII<sup>ocy-/-</sup> and B) RNAseq of aged bones show significant repression of enzymes critical for PLR. \* P<0.05, n=4-6

accumulation of modifications to the bone matrix which results in worsening bone quality over a lifetime.

This work utilizes a combination of engineering and molecular biology approaches to demonstrate the effects of age on bone material properties and trace the molecular roots of these changes over time. Using a novel mouse line of disrupted TGF $\beta$  signaling in osteocytes, aged bone tissue and its cellular components are rigorously evaluated using a suite of sophisticated techniques including high resolution fluorescent confocal microscopy, robust computer modeling, synchrotron aided X-ray examination of bone tissue, and RNA sequencing. Combination of these advanced techniques allow for the assessment of the effects of aging on bone on a resolution and breadth not yet attempted and builds a comprehensive understanding of the cellular, molecular, and material roots of age-related bone fragility.



## References

1. Currey, J. D. The design of mineralised hard tissues for their mechanical functions. *J Exp Biology* 202, 3285–94 (1999).
2. Currey, J. D. Mechanical properties of bone tissues with greatly differing functions. *J Biomech* 12, 313–319 (1979).
3. Reznikov, N., Shahar, R. & Weiner, S. Bone hierarchical structure in three dimensions. *Acta Biomaterialia* 10, 3815–3826 (2014).
4. Reznikov, N., Shahar, R. & Weiner, S. Three-dimensional structure of human lamellar bone: The presence of two different materials and new insights into the hierarchical organization. *Bone* 59, 93–104 (2014).
5. Boskey, A. L. Bone composition: relationship to bone fragility and antiosteoporotic drug effects. *Bonekey Reports* 2, 447 (2013).
6. Koester, K. J., Ager, J. W. & Ritchie, R. O. The true toughness of human cortical bone measured with realistically short cracks. *Nat Mater* 7, 672–677 (2008).
7. Bieniawski, Z. T. Mechanism of brittle fracture of rock Part I—theory of the fracture process. *Int J Rock Mech Min* 4, 395–406 (1967).
8. Nalla, R. K., Kinney, J. H. & Ritchie, R. O. Mechanistic fracture criteria for the failure of human cortical bone. *Nat Mater* 2, 164–168 (2003).
9. Ritchie, R. O. The conflicts between strength and toughness. *Nat Mater* 10, 817–822 (2011).
10. Turunen, M. J. *et al.* Bone mineral crystal size and organization vary across mature rat bone cortex. *J Struct Biol* 195, 337–344 (2016).
11. Gupta, H. S. *et al.* Cooperative deformation of mineral and collagen in bone at the nanoscale. *Proceedings of the National Academy of Sciences* 103, 17741–17746 (2006).

12. Pabisch, S., Wagermaier, W., Zander, T., Li, C. & Fratzl, P. Imaging the Nanostructure of Bone and Dentin Through Small- and Wide-Angle X-Ray Scattering. *Methods in Enzymology* 532, 391–413 (2013).
13. Garnero, P. The contribution of collagen crosslinks to bone strength. *BoneKEy Reports* 1, 182 (2012).
14. Fantner, G. E. *et al.* Sacrificial bonds and hidden length dissipate energy as mineralized fibrils separate during bone fracture. *Nat Mater* 4, 612–616 (2005).
15. Lee, T. C., O'Brien, F. J. & Taylor, D. The nature of fatigue damage in bone. *Int J Fatigue* 22, 847–853 (2000).
16. Seref-Ferlengez, Z., Kennedy, O. D. & Schaffler, M. B. Bone microdamage, remodeling and bone fragility: how much damage is too much damage? *BoneKEy Reports* 4, 644 (2015).
17. Robling, A. G. & Turner, C. H. Mechanical Signaling for Bone Modeling and Remodeling. *Crit Rev Eukar Gene* 19, 319–338 (2009).
18. Almeida, M. Aging mechanisms in bone. *Bonekey Reports* 1, (2012).
19. Alessandra, C. *et al.* How Tough Is Brittle Bone? Investigating Osteogenesis Imperfecta in Mouse Bone. *Journal of Bone and Mineral Research* 29, 1392–1401 (2014).
20. Unnanuntana, A., Rebolledo, B. J., Khair, M. M., DiCarlo, E. F. & Lane, J. M. Diseases Affecting Bone Quality: Beyond Osteoporosis. *Clinical Orthopaedics and Related Research*® 469, 2194–2206 (2010).
21. Callewaert, B., Malfait, F., Loeys, B. & Paepe, A. D. Ehlers-Danlos syndromes and Marfan syndrome. *Best Pract Res Clin Rheumatology* 22, 165–189 (2008).
22. Saito, M. & Marumo, K. Collagen cross-links as a determinant of bone quality: a possible explanation for bone fragility in aging, osteoporosis, and diabetes mellitus. *Osteoporosis International* 21, 195–214 (2009).

23. Acevedo, C. *et al.* Contributions of Material Properties and Structure to Increased Bone Fragility for a Given Bone Mass in the UCD-T2DM Rat Model of Type 2 Diabetes. *J. Bone Miner. Res.* 27, 219–1075 (2018).
24. Cloos, P. A. & Fledelius, C. Collagen fragments in urine derived from bone resorption are highly racemized and isomerized: a biological clock of protein aging with clinical potential. *Biochem J* 345 Pt 3, 473–80 (2000).
25. Fledelius, C., Johnsen, A. H., Cloos, P. A. C., Bonde, M. & Qvist, P. Characterization of Urinary Degradation Products Derived from Type I Collagen IDENTIFICATION OF A  $\beta$ -ISOMERIZED ASP-GLY SEQUENCE WITHIN THE C-TERMINAL TELOPEPTIDE ( $\alpha$ 1) REGION\*. *J Biol Chem* 272, 9755–9763 (1997).
26. Nyman, J. S. *et al.* Manipulating the Amount and Structure of the Organic Matrix Affects the Water Compartments of Human Cortical Bone. *Jbmr Plus* 3, e10135 (2019).
27. Wenger, M. P. E., Bozec, L., Horton, M. A. & Mesquida, P. Mechanical Properties of Collagen Fibrils. *Biophys J* 93, 1255–1263 (2007).
28. Faingold, A. *et al.* The effect of hydration on mechanical anisotropy, topography and fibril organization of the osteonal lamellae. *J Biomech* 47, 367–372 (2014).
29. Yan, J., Daga, A., Kumar, R. & Mecholsky, J. J. Fracture toughness and work of fracture of hydrated, dehydrated, and ashed bovine bone. *J Biomech* 41, 1929–1936 (2008).
30. Ural, A., Zioupos, P., Buchanan, D. & Vashishth, D. The effect of strain rate on fracture toughness of human cortical bone: A finite element study. *J Mech Behav Biomed* 4, 1021–1032 (2011).
31. Liebschner, M. A. K. & Keller, T. S. Hydraulic Strengthening Affects the Stiffness and Strength of Cortical Bone. *Ann Biomed Eng* 33, 26–38 (2005).
32. Buenzli, P. R. & Sims, N. A. Quantifying the osteocyte network in the human skeleton. *Bone* 75, 144–150 (2015).

33. Schaffler, M. B., Cheung, W.-Y., Majeska, R. & Kennedy, O. Osteocytes: Master Orchestrators of Bone. *Calcified Tissue Int* 94, 5–24 (2014).
34. Dole, N. S. *et al.* Osteocyte-Intrinsic TGF- $\beta$  Signaling Regulates Bone Quality through Perilacunar/Canalicular Remodeling. *Cell Rep* 21, 2585–2596 (2017).
35. Edwards, J. R. *et al.* Inhibition of TGF- $\beta$  signaling by 1D11 antibody treatment increases bone mass and quality in vivo. *J. Bone Miner. Res.* 25, 2419–2426 (2010).
36. Balooch, G. *et al.* TGF-beta regulates the mechanical properties and composition of bone matrix. *Proc. Natl. Acad. Sci. U.S.A.* 102, 18813–18818 (2005).
37. Erlebacher, A., Filvaroff, E. H., Ye, J.-Q. & Derynck, R. Osteoblastic Responses to TGF- $\beta$  during Bone Remodeling. *Mol Biol Cell* 9, 1903–1918 (1998).
38. Oursler, M. J. Osteoclast synthesis and secretion and activation of latent transforming growth factor  $\beta$ . *J Bone Miner Res* 9, 443–452 (1994).
39. Weivoda, M. M. *et al.* Osteoclast TGF- $\beta$  Receptor Signaling Induces Wnt1 Secretion and Couples Bone Resorption to Bone Formation. *J Bone Miner Res* 31, 76–85 (2016).
40. Nguyen, J., Massoumi, R. & Alliston, T. CYLD, a mechanosensitive deubiquitinase, regulates TGF $\beta$  signaling in load-induced bone formation. *Bone* 131, 115148 (2019).
41. Nguyen, J., Tang, S. Y., Nguyen, D. & Alliston, T. Load Regulates Bone Formation and Sclerostin Expression through a TGFbeta-Dependent Mechanism. *PLoS ONE* 8, e53813 (2013).
42. Burr, D. B. Changes in bone matrix properties with aging. *Bone* 120, 85–93 (2019).
43. Zimmermann, E. A. *et al.* Age-related changes in the plasticity and toughness of human cortical bone at multiple length scales. *Proceedings of the National Academy of Sciences* 108, 14416–14421 (2011).
44. Granke, M., Does, M. D. & Nyman, J. S. The Role of Water Compartments in the Material Properties of Cortical Bone. *Calcified Tissue Int* 97, 292–307 (2015).

45. Pfeilschifter, J. *et al.* Concentration of transforming growth factor beta in human bone tissue: relationship to age, menopause, bone turnover, and bone volume. *J. Bone Miner. Res.* 13, 716–730 (1998).
46. Ensrud, K. E. Epidemiology of Fracture Risk With Advancing Age. *The Journals of Gerontology Series A: Biological Sciences and Medical Sciences* 68, 1236–1242 (2013).

# Chapter 2: Materials and Methods

## Murine studies

Male C57BL/6 mice (WT, wild type) aged 2 months (N=3), 1 year, 2 years, and 2 ½ years (N=4), 3 years (N=5) were received from the Buck Institute for Research on Aging. A well characterized line of mice with ablated TGFβ receptor II in osteocytes with deficits to perilacunar/canalicular remodeling was used to interrogate the role of TGFβ driven PLR in age-related bone fragility. In brief, mice possessing *loxP* sites flanking exon 4 of the *Tgfr2* gene on a C57BL/6 background were crossed with hemizygous -10kb-DMP1-Cre<sup>+/-</sup> mice<sup>1,2</sup> in litters with approximately 50% DMP1-Cre<sup>+/-</sup>;TβRII<sup>fl/fl</sup> (TβRII<sup>ocy-/-</sup>) mice with ablated TGFβ receptor II in osteocytes and 50% “control”, DMP1-Cre<sup>-/-</sup>;TβRII<sup>fl/fl</sup> littermate controls (TβRII<sup>ctrl</sup> / Ctrl) . All mice genotypes were confirmed by PCR genotyping. Male and female mice of these lines were allowed to age naturally to 4 months (16 weeks), 6 months (24 weeks), 12 months (48 weeks), and 15 months (60 weeks) before euthanasia and sample collection (N=7/9 per group). Over their lifetime, animals were

housed in groups no greater than 5 in a specific pathogen-free environment with temperature maintained between 68 °F and 74 °F, humidity between 30% and 70%, with a 12-h light/dark cycle and access ad libitum to water and rodent chow (LabDiet 5053). All animal procedures were approved by the Institutional Animal Care and Use Committee of the University of California San Francisco and the Buck Institute for Research on Aging.

### **RNA expression analysis**

Humeri from mice were cleaned of soft tissue, metaphysis and periosteum dissected away, and the marrow removed via centrifugation. Two humeri per animal were snap-frozen in liquid nitrogen and combined in a single tube with 1.5 mL of QIAzol (Invitrogen). Tubes were stored on ice and each bone sample homogenized with a rotor-stator homogenizer (GLH, Omni). Lysate was then stored at -80 °C until RNA extraction<sup>3-5</sup>.

For RNA extraction, QIAzol lysate was thawed, and 220 µL chloroform per mL of lysate was added and mixed well via pipette. After solution began to separate (2-3 mins on benchtop), samples were then centrifuged for 15 minutes at 12,000 g at 4 °C, and the aqueous supernatant was carefully transferred to a clean tube. mRNA was purified using the miRNeasy Mini Kit (Qiagen), following manufacturer's instructions. On-column DNase (Qiagen) was applied for 15 minutes, and the RNA was eluted in 60 µL RNase-free water. RNA concentration was quantified with a NanoDrop spectrophotometer and the product stored at -80 °C until use.

Raw mRNA sequence expression from a pre-selected subset of 813 genes was quantified from purified RNA using the nanoString<sup>6,7</sup> Fibrosis mRNA expression panel and a custom panel of bone specific genes available through the UCSF Skeletal Biology and Biomechanics Core. Quantitative analysis was completed using nanoString nCounter analysis nSolver 4.0 and Advanced Analyses 2.0 available from nanoString<sup>6</sup>. This allowed for robust expression analysis of over 800 genes from 150 ng of RNA<sup>7</sup>.

RNA Sequencing for the aged wildtype mice (Buck Institute) and a group of young (8 week) male  $T\beta RII^{ocy-/-}$  mice and their control (Cre negative) littermates was completed on the Illumina HiSeq 4000 at the UCSF Functional Genomics Core. Single-end 50 bp RNA-seq reads were aligned to the Ensembl mouse GRCm38.87 reference genome using STAR 2.5.2b aligner<sup>8</sup>. Analysis of the aged mice bone resulted in 745 million total reads with an average of 78.7% of these reads aligning uniquely to the mouse genome. Sequencing of the  $T\beta RII^{ocy-/-}$  experiment yielded ~948 million reads with an average read depth of 118 million reads/sample. Average normalized read count for genes of interest was calculated with reference to the young (2 mo.) control group of either experiment. The DESeq2 package in R Statistical Computing Environment<sup>9</sup> was used to find differentially expressed genes with a false discovery rate of 0.1. Normalized read-count comparisons for selected genes were found by normalizing to relevant control group average and statistically compared via Bonferroni corrected student's T-test for multiple comparisons as appropriate.

### **Silver Nitrate Staining**

Femurs were prepared for histological examination as described elsewhere<sup>3,5,10</sup> paraffin-embedded in 7 mm thick blocks, and axially sectioned along the diaphysis at 6-7  $\mu$ m. Dehydrated tissue sections were stained with a Ploton silver nitrate stain<sup>11</sup> for visualization of the osteocyte lacunar/canalicular network in 2D. Images were acquired using a Nikon Eclipse E800 bright-field microscope at 100x with an oil immersion objective. Canalicular length was manually measured with ImageJ<sup>12</sup>.

### **Confocal Fluorescent Imaging of the LCN**

Femurs for fluorescent imaging were cleaned of soft tissue, scraped of the periosteum and fixed in 10% neutral buffered formalin for 48 hrs at 4°C. Bones were demineralized with 0.5M EDTA (pH 7.5) for two weeks. Marrow was gently flushed with warm saline, bones were cryoprotected



in a using a sucrose gradient of 15% and 30% for 30 minutes each before being axially frozen embedded in OCT (Tissue-Tek®). Following protocols as described<sup>5,10,13,14</sup>, 50 µm cryosections of the diaphyseal femur were sectioned on a Microm HM 550 *cryostat* (ThermoFisher) and stained.

Briefly, stains utilized the hydrophobic lipophilic dye, Dil (1,1'-Diocadecyl-3,3,3',3'-Tetramethylindocarbocyanine Perchlorate) (ThermoFisher) at 100 µM in 50% DMSO:50% PBS to visualize the LCN cell membrane surfaces, Alexa Fluor 488-Phalloidin (ThermoFisher) at 165 nM to visualize the cell F-actin cytoskeleton, and DAPI at 4 µM in PBS for identification of cell nuclei. Bone sections were optically cleared using a 2-2-thiodiethonal (TDE, Sigma-Aldrich, St. Louis MO) gradient over 24 hours, mounted in TDE, sealed with a toluene free nail polish, and imaged immediately on a Lecia DMI8 (Leica Microsystems) inverted microscope running on LASX software at 100x with an oil immersion objective. ROIs 75 µm x 75 µm x ≥35 µm were captured for 3 independent regions around the cortex within lamellar bone for each sample at a 500x500 pixel resolution in the XY plane, resulting in a digital pixel resolution of 150 nm/pixel. Given the optical wavelength of the fluorophores used, we were practically diffraction limited to a resolution of ~450 nm, constraining analysis to features greater than ~3 pixels in width. Z step distance was set to 0.3 µm resulting in ≥119 captured planes for each ROI, which were standardized to exactly 119 Z planes (35.7 µm depth) for all 3D analysis. Individual fluorescent channels were background subtracted and merged into composite 8-bit 3D images utilizing FIJI software<sup>12</sup>. The isotropic aspect ratio of 2x1 in the Z direction was corrected for in all 3D reconstructions in Fiji, IMARIS, and Materialise MIMICS for model construction.

Selected areas for network imaging were contained to lamellar and not woven areas of bone containing, by eye, roughly the same numbers of osteocytes to capture as closely as possible similar canalicular regions. This was done to prioritize later network analysis and to limit computational load. Because of region selection, osteocyte volume density is not different in the images between the models, as is an expected and well documented effect of age<sup>13,15</sup> Lower magnitude tile-scans to capture only nuclear signal across the entire bone surface were

completed to investigate osteocyte presence and viability in the models on a larger scale. In this comparison we do find a decrease in osteocyte number in aged compared to young controls, while we found no difference in the  $T\beta RII^{ocyt-/-}$  model compared to its control, in-line with previous results<sup>3,13</sup>. For this reason, osteocyte area density is presented instead of volume density within the models which has been artificially 'selected'. It would be technically unfeasible and computationally prohibitive to attempt canalicular analysis as described in this report on the scale of whole bone cross-sectional area at this time.

## **Image Processing and Structural Analysis**

### *LCN Geometry*

Quantification of canalicular tortuosity, canalicular spacing, and LCN volume fraction in 3D was completed using a combination of FIJI plugins, including BoneJ<sup>16</sup> and the Simple Neurite Tracer. IMARIS (Oxford Instruments), made available by the UCSF Biological Imaging and Development Core, was used to segment and quantify the canalicular sprouting points within the first bifurcation and observe canalicular branching behavior in expanding concentric regions along the canaliculi away from the cell body.

For canalicular spacing and LCN volume fraction, use of BoneJ<sup>16</sup> required additional noise reduction for thresholding to generate binary representations of each data set suitable for use with these protocols. While image processing was uniform across the data sets, results for spacing and volume fraction are displayed as fold-change normalized to the average of the relevant control group to demonstrate the uniformity in distribution and magnitude of difference between the models.

### *Canalicular Dendrite Segmentation and Quantification at the Sprouting Point*

Florescent Confocal image files (.LIF) from Leica DMI8 imaging are imported into Imaris v9.5.1 (Oxford Instruments). The images are background subtracted using the Imaris Image Processing

sub-menu. Using the membrane dye channel as a template, an Imaris 'surface' object is created to identify the osteocyte cell bodies within the imaged region. Small features are removed with a size exclusion filter to prevent canalicular dendrites from being included in the cell body surface object. Cell bodies intersecting the image borders are removed to ensure quantification of only whole cells.

A Distance Transformation operation is completed on the cell surface objects, using MATLAB script XTensions attainable online\*, to create a new channel encoding the radial distances in 3D from the surface of each cell's unique topography.

An ROI surrounding a single cell body is defined and a new surface including canalicular features is created from signal from the full image channel within the defined ROI. This surface is used as a mask to create a channel of canalicular features associated to the enclosed cell body of interest to ease quantitative/computational demand.

Using the Imaris Colocalization tool, the Distance Transform channel and the new canalicular channel are overlaid and regions of canaliculi with a uniform distance in 3D from the surface of the cell are identified.

To identify the canalicular sprouting points, the distance along canalicular regions from the cellular surface is set to the minimum to ensure all identified features are within the region between the cell body surface and where the points where individual canaliculi begin to bifurcate. In order to prevent undercounting from merging of signal from adjacent canaliculi, signal from the areas within the cellular surface object is removed from individual cell signal channels. This allows for the distance at which canalicular signal is captured to be constricted to the immediate location of canalicular sprouting along the cellular surface. The portions of signal are saved into another image channel for reconstructions and quantification.

---

\* <https://imaris.oxinst.com/learning/view/article/distance-transformation>

The new “sprouts” channel is visualized in 3D with the cell body surface model to ensure features have been captured in all dimensions. The signal from the canalicular ‘sprouts’ is rendered as another new surface in 3D, size gated to remove collections of small pixels and larger features not belonging to canalicular sprouts, and the number of independent, non-connected sprouts is recorded as the individual number of canaliculi sprouting from singly analyzed osteocytes.

### **Connectomic Network Analysis**

Connectomic Network Analysis of the LCN was accomplished on skeletonized representative maps of binarized, 8-bit confocal stacks of the LCN (N=5 per group) as described in Kollmannsberger *et al*<sup>17</sup>. Connectomic measurements were completed utilizing the MATLAB (Mathworks) scripts provided from the Kollmannsberger *et al* github\*. Updated scripts with custom MEX files and C+ wrappers were used to run scripts.†

Connectomic analysis via the MATLAB package from Kollmannsberger *et al*<sup>17</sup> is sensitive to noise in the images, thus individual image stacks were prepared manually using ImageJ to assemble a comparable and uniform data set for automated analysis. N=5 image stack ROIs (100 planes at a total Z depth of 30  $\mu$ M) per group were manually selected for analysis to maintain uniform analysis volume and to avoid large aberrations or structures (e.g. blood vessels). MATLAB v2019a, equipped with the Boost Graph Library for MATLAB by Gleich (2008)‡ was used and ran in parallel on an iMac Pro (2017) running macOS Mojave with a 3 GHz Intel Xeon W processor and 128 GB RAM. Automated parallel processing took 3 hours (20 ROIs total) while individual ROIs could run in 15-20 minutes.

---

\* [https://github.com/phi-max/OCY\\_connectomics](https://github.com/phi-max/OCY_connectomics)

† [https://github.com/cschurm/ocy\\_connectomics\\_updated](https://github.com/cschurm/ocy_connectomics_updated)

‡ [https://www.mathworks.com/matlabcentral/fileexchange/10922-matlabbg1?s\\_tid=prof\\_contriblnk](https://www.mathworks.com/matlabcentral/fileexchange/10922-matlabbg1?s_tid=prof_contriblnk)

## **Connectomic Analysis Parameters**

### *Node type*

T-nodes are defined as nodes with  $n=3$  (number of nearest neighbors) and a clustering coefficient (cc), or a measure of the interconnectedness of a node's neighbors to each other. This type of node has the minimal number of connections required to participate in network connections and is a feature of branching, linear networks. C-nodes, or cluster nodes, are defined as nodes with high clustering coefficients ( $cc>0.5$ ) that have high neighbor connectivity and create web-like networks. These nodes are often found in networks with high connectivity and low long-range order. End point nodes have a node degree of 1 and represent the ends of canalicular dendrites that terminate within the matrix without reconnecting to the network. These locations mark discontinuities within the network and non-functional path choices through the network. By definition no node has a degree of 2. Other types of nodes, behaviors, and classifications exist, the most abundant of multiple node types present in the LCN are presented here. A large proportion of nodes on the image borders were removed from analysis because their inclusion would artificially inflate the end-point values.

### *Betweenness Centrality*

Betweenness Centrality (BC) was used to evaluate pathways between cells within the connectomes and is defined as the fraction of shortest paths within a network running through any particular node where high BC scoring nodes align near each other to present commonly used paths within connectomes. For visualization and comparison, we have set an arbitrary cut-off at a BC of 0.01, or nodes that appear in at least 1% of paths within the connectome<sup>17,18</sup>.

### *Diffusion Speed Gain*

A non-dimensional gain in diffusive speed  $G_{net}$ , based on measured network values provided by the connectomics package was calculated and compared across a range of diffusion ratios,  $K$ .

These network values correspond to the average distance from a matrix voxel to the closest portion of the entire LCN (canalicular dendrite or cell body),  $d_{LC}$ , the average distance from a matrix voxel to the nearest cell lacunae,  $d_L$ , and the distance of any point within the canalicular network to nearest cell,  $d_{net}$ . To represent the difference in diffusive speed of a small molecule within the LCN ( $v_{network}$ ) versus the mineralized matrix ( $v_{matrix}$ ), the ratio  $k$  ( $v_{network}/v_{matrix}$ ) was allowed to vary across a range of magnitudes including the regime estimated by Kollmannsberger *et al* and others to be the difference in diffusion coefficients within the two compartments of the bone matrix. The ratio of the combined distances  $d_{LC}$  and  $d_{net}$  over the same combination but with  $d_{net}$  “shortened” by the differences in diffusion speed,  $K$ , resolves as the speed gain term  $G_{net}$  which evaluates the enhancement of diffusion utilizing the network over simple diffusion through the matrix towards the nearest cell.

## **FE Model Generation**

Materialise MIMICS image processing software was employed to generate a three-dimensional model of the osteocytes from fluorescent confocal image stacks. Confocal image stacks of 20 (N=5 per group) osteocytes were imported into MIMICS and thresholded to allow segmentation of the osteocytes. Individual osteocytes were selected from deep within the bone tissue by selecting an approximately 25 x 25 x 25  $\mu\text{m}$  region of interest around a single DAPI nuclear signal. To prevent loss of information during segmentation or inclusion of confounding local features, a minimum distance of 10  $\mu\text{m}$  from the edge of the field of view and from large local landmarks (e.g. blood vessels) was ensured. Models were then meshed using 3-Matic voxel-meshing software (Materialise, Leuven, Belgium) as described previously<sup>19</sup>. Models were dimensionally constrained so that no feature was thinner than the effective optical ‘diffraction limit’ of the used fluorophores (3 pixels / ~450 nm) at any location. At sites where the dendritic dimensions are greater than ~450 nm in diameter, these measured dimensions were used in the mesh. Dimensions of the

pericellular fluid space (PCS), based on previous experimental measurements<sup>20–22</sup>, were used to model the interstitial fluid flow. This uniform 0.08  $\mu\text{m}$  PCS offset was applied to the osteocyte mesh surface followed by a Boolean subtraction to remove the osteocyte volume. This offset was reduced and multiplied by a factor of two to create the constricted (0.04  $\mu\text{m}$ ) and expanded (0.16  $\mu\text{m}$ ) PCS models around the same base cellular geometry. Geometries were meshed using 4-noded tetrahedral elements and exported to COMSOL Multiphysics computational modelling software (Burlington, MA, USA). Similar methods were used to mesh and model three individual canalicular channels at different values of tortuosity across the range found within analyzed networks.

### **Computational Fluid Dynamics**

The properties of the interstitial fluid were assumed to be similar to salt water, with a density of  $997 \text{ kgm}^{-3}$  and a dynamic viscosity of  $0.000855 \text{ kgm}^{-1}\text{s}^{-1}$ <sup>23,24</sup>. Flow within the lacunar-canalicular system was assumed to be laminar in nature. A pressure gradient was applied across the models to represent organ-level mechanical loading that generates regions of compression and tension driving fluid across the LCN<sup>24–26</sup>. An inlet pressure of 300 Pa was assigned to the inlets on one face and the remaining inlets were defined as outlets at a relative pressure of 0 Pa<sup>25,26</sup> similar to the pressure gradient applied by Anderson et al.<sup>24</sup> Models with altered volumes of PCS resulted in altered flow rates under these consistently applied boundary assumptions. Interstitial fluid velocity and shear stress were recorded as the 95<sup>th</sup> percentile values.

### **Skeletal Phenotyping**

In order to maximize outcomes from a single bone, selected bones were utilized for both skeletal phenotyping and mechanical testing. To accommodate this, unfixed femoral midshafts were scanned using a Scanco  $\mu\text{CT}50$  specimen scanner (Scanco Medical, Wangen-Brüttisellen,

Switzerland) with an X-ray potential of 55 kVp, current of 109  $\mu$ A, and voxel size of 10  $\mu$ m. Each scan took 35 minutes to complete during which time samples were submerged in HBSS at room temperature to preserve mechanical integrity. Immediately after scans, samples were placed on ice and within two hours of scanning, midshafts were removed from HBSS, allowed to reach room temperature, and mechanically tested (see following). After 3-point bend mechanical testing, distal femur halves containing femoral condyles were scanned again for trabecular bone. Cortical analysis was conducted in a 1-mm region equidistant from the proximal and distal ends of the bone, using the femoral condyles and the trochanter as major landmarks, while trabecular segmentation and analysis was performed in a 1-mm region below the growth plate. Samples displaying damage near the growth plates from the mechanical tests were excluded from trabecular analysis, this accounted for only about 3% of samples being removed from this outcome. 3D measurements of cortical and trabecular parameters were obtained using Scanco analysis methods as described<sup>27</sup>. Cortical porosity measurements were achieved through manual segmentation of Scanco generated DICOM files utilizing Dragonfly (Object Research Systems, Montreal, Canada.) Briefly, numeric volumes as determined by Dragonfly of hand segmented cortical shells with pores identified were divided by the total volume of the cortical bone from endosteal to periosteal edges including pore volume to achieve “percent cortical porosity” for each sample. Segmentation was aided by Dragonfly’s hole filling tool as part of its bone analysis tool box.

### **Mechanical Testing**

Within two hours of CT scanning, whole hydrated femurs were loaded to failure in three-point bending in the direction of primary physiological bending (posterior compression) using a Bose Electroforce 3200 test frame with an 8-mm span at a fixed displacement rate of 10  $\mu$ m/s. Structural parameters were extracted from load-displacement curves using a custom MATLAB script and material properties were acquired by transforming specific structural properties by their individual



parameters from  $\mu$ CT as described<sup>28</sup>. Following testing, fracture surface cross-sections were imaged by scanning electron microscopy on a Sigma 500 VP FE-SEM (Zeiss) at an excitation voltage of 15 kV and a partial pressure of 35 Pa. Measurements of endosteal and periosteal cross-sectional diameter and thickness were measured with ImageJ and used to calculate moment of inertia assuming an elliptical cross-section and used to verify results from  $\mu$ CT MOI calculations.

### Synchrotron *in situ* Tensile testing

Collagen fibril and hydroxy appetite mineral crystal strains were recorded during uniaxial tension testing of isolated, hydrated ulnae using synchrotron small-angle X-ray scattering (SAXS) and wide-angle X-ray diffraction (WAXD) at beamline 7.3.3 at the Advanced Light Source (LBNL, Berkeley, CA)<sup>29</sup>. This strategy permits simultaneous, real-time measurement of specific strains in the composite materials as compared to bulk tissues as captured by CCD camera and measured with a custom Digital Image Correlation (DIC) MATLAB package. A two-part dental bonding adhesive (OptiBond, Kerr Corporation, Orange, CA) and resin (Aeliteflo, Bisco Dental, Schaumburg, IL) were each cured for 20 seconds on each end of the bone with blue light within a 3D printed “dumbbell” mold (Fig. 2.1) to create regions for clamping without harming the diaphysis exposed to the X-ray beam. In situ tensile tests were performed using a TST350 Tensile Testing Stage (Linkam Scientific Inc.) on hydrated samples at a displacement rate of 2.5  $\mu$ m/s. Small (2x4mm) sandpaper strips were superglued to the surface of the

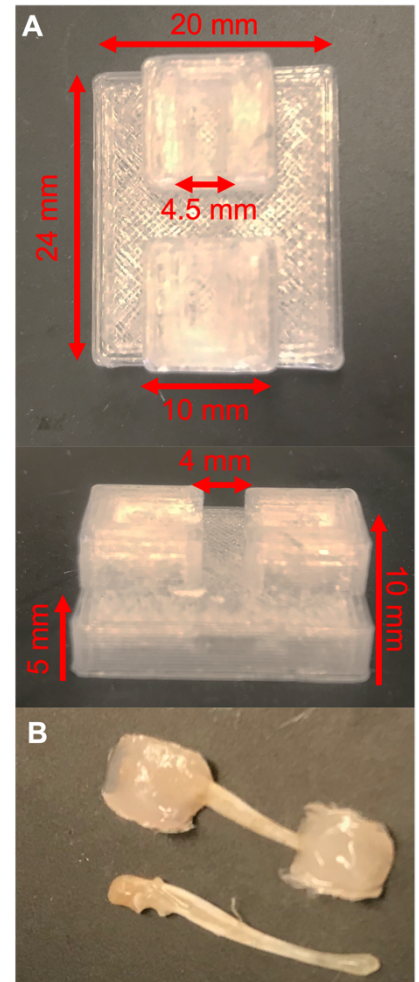


**Figure 2.1: Sample preparation for tensile testing.** A) 3D printed mold for creating “dumbbell” ends for mechanical tensile tests. Inset groove on top is a half cylinder in which mouse ulnae are placed in during embedding. B) Mouse ulna with the fully cured composite caps (above) and with only the cured bonding adhesive (below) showing the 2-step embedding process and how the majority of the diaphysis remains bare for X-ray exposure during testing.

stage clamps to increase friction on the dental composite. During testing, bones were exposed to the synchrotron generated X-ray beam of 10 keV for 0.1 s every 5 s until failure or until total radiation dose reached 30 kGy to mitigate exposure effects on the material performance of the bone<sup>30</sup>. The changes in collagen d-spacing and mineral crystal lattice spacing from the unloaded condition, as seen as a shift in the location of the Bragg scattering peak from SAXS pattern and the Bragg diffraction peak in the WAXD pattern, were used to calculate collagen and mineral associated strains, respectively. Reductions from 2D scattering/diffraction patterns and extraction of parameters from resulting curves were completed via a custom LabVIEW program.

### **Immunohistochemical and Immunofluorescence Imaging**

Proximal femur halves containing the femoral condyle were cleaned of muscle and periosteum and fixed for 48 hours in 10% Neutral Buffered Formalin (NBF) and then incubated for decalcification in 0.5M disodium and tetrasodium EDTA at neutral pH for 2 weeks at 4 degrees C. Following decal, epiphyses are removed, marrow flushed with warm saline, and prepared for cryosectioning as described above and else where<sup>10,13,31</sup>. For imaging of large sections (~35  $\mu\text{m}$ ) of the osteocyte network, femurs were axially sectioned at 50  $\mu\text{m}$  and stained using the lipophilic Dil and actin specific AlexaFluor 488 (Invitrogen) for labeling of osteocyte membranes and cytoskeleton, respectively. Histologic and immunofluorescence assays were completed on 8-10  $\mu\text{m}$  sections. Fluorescent confocal imaging was completed using a Lecia DMI8 (Leica Microsystems) inverted confocal microscope at 100x running LAS X software, while brightfield imaging was completed with a Nikon Eclipse E800 microscope.

### **Biochemical Analysis**

#### *AGEs*

Decalcified, mid-diaphyseal femurs were hydrolyzed in HCl (24 hours, 110°C) and fluorescence of neutralized lysates (excitation 370 nm, emission 440 nm) were referenced to a quinine sulfate

standard and then normalized to the collagen content calculated from the amount of hydroxyproline, as measured by a colorimetric assay with absorbance at 560nm, for quantification of Advanced Glycation End-products (AGEs) within bone as described<sup>31,32</sup>.

### *TGF $\beta$ ELISA*

Protein from bone lysates was harvested as previously described<sup>33</sup>. Briefly, for collection of bone-specific protein lysates, distal tibia halves were centrifuged to remove marrow and stripped of periosteum and connective tissue before being snap frozen in liquid nitrogen. Frozen bones were transferred to chilled pre-filled Bead Mill Tubes (ThermoFischer Scientific, Waltham, MA) containing radioimmunoprecipitation buffer [RIPA - 10mM Tris, pH8, 1mM EDTA, 1mM EGTA, 140 mM sodium chloride, 1% sodium pyrophosphate, 100mM sodium fluoride, 500 $\mu$ M PMSF, 5mg/mL eComplete Mini protease inhibitor tablet (Roche, Basel Switzerland)]. Samples were disrupted using a benchtop bead mill homogenizer (Omni International, Kennesaw, GA) at 4°C. Resulting lysates were briefly centrifuged to collect supernatants that were then sonicated for 8 times (15s/45s rest) in an ice-cold water bath. Serum was collected from blood as described [Dole JBMR 2020]. Raw protein concentration from both bone lysate and serum aliquots was quantified using the Pierce Coomassie (Bradford) Assay Kit (ThermoFischer Scientific, Waltham, MA). Samples were hydrolyzed in 1N HCL at a 1:5 dilution for 10 minutes at room temperature before being neutralized with the same volume of 1.2 N NaOH/0.5M HEPES buffer. Total levels of TGF $\beta$  Ligand were quantified from neutralized samples using the Bio-Plex Pro TGF- $\beta$  Assay Kit (Bio-Rad, Hercules, CA) on a Bio-Plex 200 (Bio-Rad, Hercules, CA) made available by the UCSF Parnassus Flow Cytometry Core. TGF $\beta$  ligand levels were normalized to each samples' original total protein concentration from the Bradford assay.

## Statistical Analysis and Comparison

### *Ch.4 - Disrupted Osteocyte Connectivity and Pericellular Fluid Flow in Bone with Aging and Defective TGF $\beta$ Signaling*

To establish comparable relationships between the control (2 mo. WT, T $\beta$ RII<sup>ctrl</sup>) and degenerated (36 mo. WT, T $\beta$ RII<sup>ocy<sup>-/-</sup></sup>) models, a 2-way ANOVA with multiple post-hoc Tukey-corrected comparisons was completed on canalicular length results from silver nitrate staining. A small interaction term between the effects of background (pure or mixed BL/6) and LCN degeneration (age or TGF $\beta$  signaling disruption) existed accounting for 8.59% of the differences found within the ANOVA on canalicular length; however, evaluation of the effect of background alone (pure or mixed C57BL/6) was found to be non-significant (p=0.6907). In post-hoc comparisons, pairwise comparison between the control groups (2 mo. WT & T $\beta$ RII<sup>ctrl</sup>) were non-significant (p=0.2692) as were comparisons between the degenerated models (36 mo. WT & T $\beta$ RII<sup>ocy<sup>-/-</sup></sup>) (p=0.5083). The four remaining pairwise comparisons between each degenerated model to either control were highly significant (p<0.01), such that young T $\beta$ RII<sup>ocy<sup>-/-</sup></sup> bone was independently statistically different from both sets of control groups from each mouse line, while the aged WT bone was also independently statistically different from both sets of controls. The robust number of independent comparisons that followed the same statistical relationships between controls and the aged WT and young T $\beta$ RII<sup>ocy<sup>-/-</sup></sup> bone imply that, on the 2D canalicular level, these two models of LCN network degeneration are statistically indistinguishable. However, since the effects of age are a combination of multiple processes declining simultaneously, it would be improper to implicate TGF $\beta$  in all further comparisons to such detail. All following statistical comparisons are made between each degenerated model and their proper control (2 mo. WT vs 36 mo. WT, T $\beta$ RII<sup>ctrl</sup> vs T $\beta$ RII<sup>ocy<sup>-/-</sup></sup>) utilizing a two-sided student's t-test with a defined alpha level of 0.05 (indicated by \* on figures). Prism 8.4 (GraphPad Software Inc.) was used for all statistical comparisons. Unless otherwise stated, data is presented as mean  $\pm$  SD.

## *Ch.5 - The Role of TGF $\beta$ -regulated Osteocytic Perilacunar/canalicular Remodeling in Age-related Bone Fragility*

Prism v.9 (Graph-pad, San Diego, CA) was used for all statistical comparisons except for ELISA results. For Prism analyses, a 2-way ANOVA was performed with factors of age and genotype with an alpha level of 0.05. While sex differences are noted throughout, they were not statistically compared due to their difference in biologic mechanism and each sex was run in independent ANOVA comparisons. Within each ANOVA, age had up to three independent levels (4, 12 and 15 months depending on ages included) and genotype had 2 (Ctrl, T $\beta$ RII<sup>ocyt<sup>-/-</sup></sup>). A *priori* planned pairwise post-hoc comparisons were completed with the Fisher's Least Significance Difference Test that does not correct p-value for multiple comparisons, and instead the significant level (alpha = 0.05) was Bonferroni corrected for the number of comparisons being made (alpha = 0.05/7 = 0.007). In a planned manner, not all possible pairwise comparisons are scientifically meaningful and power was not sacrificed for excessive comparisons. In Post-Hoc analysis for factors that violated the Fisher's LSD assumption that all groups are sampled from populations with the same standard deviation, standard Student's T-tests were completed for post-hoc assessment of significance. For ELISA analysis with additional group complexity (factors including age, sex, genotype, tissue source, and ligand sub-type), full ensemble results were first analyzed with univariable and multilevel linear mixed models of the log of concentration to identify which factors (coefficients) most strongly predicted ligand concentration. Afterward, pairwise comparisons were completed with the non-parametric Wilcoxon signed-rank test with significant alpha values Bonferroni-corrected for the specific comparisons being completed in each pairwise comparison. Synchrotron tissue vs material strain regressions were completed with a linear least squares method to generate linear slopes for statistical comparisons via an extra sum-of-squares F test that compares independent fits of a pair of regressions with a global fit. Regressions were considered statistically different if the p-value for the comparison of slopes of independent

regressions to the global fit was below  $\alpha=0.05/8=0.00625$  for an 8-way Bonferroni correction. 8 corrections were determined for the multi-comparisons of the four groups (young control, aged control, young  $T\beta RII^{ocv-/-}$  and aged  $T\beta RII^{ocv-/-}$ ) in two ways: either genotype matched comparisons at the same age or within genotype comparisons across age group.

## References

1. Lu, Y. *et al.* DMP1-targeted Cre expression in odontoblasts and osteocytes. *J. Dent. Res.* **86**, 320–325 (2007).
2. P., L. *et al.* Induced disruption of the transforming growth factor beta type II receptor gene in mice causes a lethal inflammatory disorder that is transplantable. *Blood* **100**, 560–8 (2002).
3. Dole, N. S. *et al.* Osteocyte-Intrinsic TGF- $\beta$  Signaling Regulates Bone Quality through Perilacunar/Canalicular Remodeling. *Cell Rep* **21**, 2585–2596 (2017).
4. Fowler, T. W. *et al.* Glucocorticoid suppression of osteocyte perilacunar remodeling is associated with subchondral bone degeneration in osteonecrosis. *Sci Rep* **7**, 44618 (2017).
5. Yee, C. S., Schurman, C. A., White, C. R. & Alliston, T. Investigating Osteocytic Perilacunar/Canalicular Remodeling. *Curr Osteoporos Rep* **17**, 157–168 (2019).
6. Veldman-Jones, M. H. *et al.* Evaluating Robustness and Sensitivity of the NanoString Technologies nCounter Platform to Enable Multiplexed Gene Expression Analysis of Clinical Samples. *Cancer Res* **75**, 2587–2593 (2015).
7. Geiss, G. K. *et al.* Direct multiplexed measurement of gene expression with color-coded probe pairs. *Nat Biotechnol* **26**, 317–325 (2008).
8. Dobin, A. *et al.* STAR: ultrafast universal RNA-seq aligner. *Bioinformatics* **29**, 15–21 (2012).
9. Love, M. I., Huber, W. & Anders, S. Moderated estimation of fold change and dispersion for RNA-seq data with DESeq2. *Genome Biol.* **15**, 31 (2014).
10. Dole, N. S., Yee, C. S., Schurman, C. A., Dallas, S. L. & Alliston, T. Assessment of Osteocytes: Techniques for Studying Morphological and Molecular Changes Associated with Perilacunar/Canalicular Remodeling of the Bone Matrix. *Methods Mol Biol* **2230**, 303–323 (2021).
11. D., P. *et al.* Improvement in the staining and in the visualization of the argyrophilic proteins of the nucleolar organizer region at the optical level. *Histochem J* **18**, 5–14 (1986).

12. Schindelin, J. *et al.* Fiji: an open-source platform for biological-image analysis. *Nat Methods* **9**, 676–682 (2012).
13. Tiede-Lewis, L. M. *et al.* Degeneration of the osteocyte network in the C57BL/6 mouse model of aging. *Aging* **9**, 2190–2208 (2017).
14. Kamel-ElSayed, S. A., Tiede-Lewis, L. M., Lu, Y., Veno, P. A. & Dallas, S. L. Novel approaches for two and three dimensional multiplexed imaging of osteocytes. *Bone* **76**, 129–140 (2015).
15. Heveran, C. M., Rauff, A., King, K. B., Carpenter, R. D. & Ferguson, V. L. A new open-source tool for measuring 3D osteocyte lacunar geometries from confocal laser scanning microscopy reveals age-related changes to lacunar size and shape in cortical mouse bone. *Bone* **110**, 115–127 (2018).
16. Doube, M. *et al.* BoneJ: Free and extensible bone image analysis in ImageJ. *Bone* **47**, 1076–1079 (2010).
17. Kollmannsberger, P. *et al.* The small world of osteocytes: connectomics of the lacuno-canalicular network in bone. *New J Phys* **19**, 073019 (2017).
18. Weinkamer, R., Kollmannsberger, P. & Fratzl, P. Towards a Connectomic Description of the Osteocyte Lacunocanalicular Network in Bone. *Curr Osteoporos Rep* **17**, 186–194 (2019).
19. Verbruggen, S. W., Vaughan, T. J. & McNamara, L. M. Strain amplification in bone mechanobiology: a computational investigation of the in vivo mechanics of osteocytes. *J Roy Soc Interface* **9**, 2735–2744 (2012).
20. Wang, L. *et al.* In situ measurement of solute transport in the bone lacunar-canalicular system. *P Natl Acad Sci Usa* **102**, 11911–11916 (2005).
21. McNamara, L. M., Majeska, R. J., Weinbaum, S., Friedrich, V. & Schaffler, M. B. Attachment of Osteocyte Cell Processes to the Bone Matrix. *Anatomical Rec* **292**, 355–363 (2009).



22. You, L., Weinbaum, S., Cowin, S. C. & Schaffler, M. B. Ultrastructure of the osteocyte process and its pericellular matrix. *Anatomical Rec Part Discov Mol Cell Evol Biology* **278A**, 505–513 (2004).
23. Verbruggen, S. W., Vaughan, T. J. & McNamara, L. M. Fluid flow in the osteocyte mechanical environment: a fluid–structure interaction approach. *Biomech Model Mechan* **13**, 85–97 (2014).
24. Anderson, E. J., Kaliyamoorthy, S., Alexander, J. I. D. & Tate, M. L. K. Nano–Microscale Models of Periosteocytic Flow Show Differences in Stresses Imparted to Cell Body and Processes. *Ann Biomed Eng* **33**, 52–62 (2005).
25. STECK, R., NIEDERER, P. & TATE, M. L. K. A Finite Element Analysis for the Prediction of Load-induced Fluid Flow and Mechanochemical Transduction in Bone. *J Theor Biol* **220**, 249–259 (2003).
26. P., M., G., C., G., M., A. Montevecchi, R. & M., F. Poroelastic finite element analysis of a bone specimen under cyclic loading. *J Biomech* **32**, 135–144 (1999).
27. Bouxsein, M. L. *et al.* Guidelines for assessment of bone microstructure in rodents using micro–computed tomography. *J Bone Miner Res* **25**, 1468–1486 (2010).
28. Jepsen, K. J., Silva, M. J., Vashishth, D., Guo, X. E. & Meulen, M. C. van der. Establishing Biomechanical Mechanisms in Mouse Models: Practical Guidelines for Systematically Evaluating Phenotypic Changes in the Diaphyses of Long Bones. *J Bone Miner Res* **30**, 951–966 (2015).
29. Hexemer<sup>1</sup>, A. *et al.* A SAXS/WAXS/GISAXS Beamline with Multilayer Monochromator. *J Phys Conf Ser* **247**, 012007 (2010).
30. Barth, H. D. *et al.* Characterization of the effects of x-ray irradiation on the hierarchical structure and mechanical properties of human cortical bone. *Biomaterials* **32**, 8892–8904 (2011).
31. Woessner, J. F. The determination of hydroxyproline in tissue and protein samples containing small proportions of this imino acid. *Arch. Biochem. Biophys.* **93**, 440–447 (1961).

32. Vashishth, D. Advanced glycation end-products and bone fractures. *IBMS BoneKEy* **6**, 268–278 (2009).
33. Nguyen, J., Massoumi, R. & Alliston, T. CYLD, a mechanosensitive deubiquitinase, regulates TGF $\beta$  signaling in load-induced bone formation. *Bone* **131**, 115148 (2019).

# Chapter 3: Considerations for Studying Perilacunar/Canalicular Remodeling & Assorted Protocols

This chapter has been adapted with permission from “Yee, C. S., **Schurman, C. A.**, White, C. R. & Alliston, T . “Investigating Osteocytic Perilacunar/Canalicular Remodeling.” *Curr Osteoporos Rep* (2019) and “Dole, N. S., Yee, **C. S.**, **Schurman, C. A.**, Dallas, S. L. & Alliston, T. “Assessment of Osteocytes: Techniques for Studying Morphological and Molecular Changes Associated with Perilacunar/Canalicular Remodeling of the Bone Matrix.” *Methods Mol Biol* (2021).<sup>1,2</sup>

## I - INTRODUCTION

Osteocytes are one of the most abundant, dynamic, and metabolically active cell types in bone<sup>3,4</sup>. These morphologically distinct cells originate from terminally differentiated osteoblasts that are entrapped within the bone matrix<sup>3,4</sup>. One of the unique characteristics of osteocytes is their formation of a highly organized network within a mineralized matrix<sup>5</sup>. Osteocytes appear as stellate-shaped bodies that extend their long cytoplasmic dendrites into the mineralized bone through narrow canals called canaliculi connecting to other osteocyte dendrites via gap junctions, as well as with bone lining osteoblasts and osteoclasts, and vasculature, to form the

lacunocanalicular network (LCN).<sup>6</sup> The intricate LCN of osteocytes is estimated to span 215m<sup>2</sup> of total bone area, which is much larger than the combined surface areas of the lung, gastrointestinal tract, and skin<sup>5</sup>. Fluid flow through the perilacunar and canalicular spaces, sensed as a mechanical signal by osteocytes, supports osteocyte cellular functions<sup>3,4,7,8</sup>. Osteocytes, in turn, respond to chemical, biological, and physical cues carried by this fluid with changes in cellular behavior. These changes include secretion of osteoclast and osteoblast regulating molecules<sup>9-11</sup>. Thus, an impairment in the integrity of the LCN can affect the metabolic and signaling functions of osteocytes, as well as their mechanosensitivity, which can compromise bone health and increase fracture susceptibility<sup>12,13</sup>.

Until recently, the multifaceted role of osteocytes in bone mechanotransduction, bone remodeling, and mineral homeostasis was largely thought to occur indirectly through osteocyte regulation of osteoclast and osteoblast function. Apart from these indirect mechanisms, osteocytes also maintain mineral homeostasis directly by remodeling the bone matrix surrounding their lacunar and canalicular spaces through the process known as perilacunar/canalicular remodeling (PLR).<sup>14,15</sup> In PLR, osteocytes resorb the organic and mineral components of perilacunar and pericanalicular ECM through a combination of matrix metalloproteases (MMPs), ATPase proton pumps, and other enzymes, such as cathepsin K and carbonic anhydrases<sup>16,17</sup>.

Originally termed as 'osteocyte osteolysis', the concept of PLR emerged from the hypothesis that the surface area of the LCN is much larger than the surface area available for remodeling by osteoblasts and osteoclasts<sup>14,18,19</sup>. Thus, in response to a systemic imbalance in mineral metabolism, engaging osteocytes is far more efficient for removing small amounts of mineral across the enormous LCN area<sup>20</sup>. With this theory, research from the 1900s demonstrated that osteocytic PLR is elicited during metabolic stress to release calcium from the bone surface to increase its bioavailability in order to restore systemic mineral homeostasis<sup>16,18,21</sup>. These early observations of PLR were almost entirely from morphologic analyses. Light and electron microscopy first revealed this phenomenon through enlarged lacunae and rough borders around

osteocytes in bone infection, rickets, or osteomalacia<sup>18,22–24</sup>. Visualization of perilacunar and pericanalicular fluorochrome labels in bone from parathyroid hormone (PTH) treated rats<sup>25</sup> provided early functional evidence for the formation of new mineralized tissue by osteocytes<sup>26</sup>. Morphological evidence in bone from numerous species, including humans, snakes, egg-laying hens, rodents, and hibernating bats and ground squirrels<sup>4,15,21,27</sup>, highlights the extensive conservation of osteocyte PLR, especially in the context of metabolic stress.

The osteocyte resorption machinery is not as clearly defined as it is in osteoclasts. Except for some functional aspects, the structural features of osteocytes that mediate this process remain elusive. Current paradigms in the field suggests that acidifying factors (such as vacuolar H<sup>+</sup> ATPase and carbonic anhydrases) and proteolytic enzymes (such as cathepsin K, tartrate resistant acid phosphatases and matrix metalloproteinases) are secreted within the perilacunar and pericanalicular spaces to resorb both the inorganic (crystalline hydroxyapatite) and the organic (mainly collagen) components of bone matrix<sup>16,28–32</sup>. In healthy bone, the catabolic activity of osteocytes in resorbing LCN bone matrix is balanced by their anabolic activities. Following a phase of resorption, osteocytes replace the bone matrix by upregulating their expression of genes implicated in mineralization, namely Phex, Ank, Dmp1 and Phospho1<sup>33</sup>.

The shift between the catabolic and anabolic phases of PLR appears to be highly dynamic and governed by external stimuli ranging from mechanical to metabolic fluctuations. In lactation, one of the most well-studied examples of PLR in response to metabolic demand, osteocytes exhibit a dramatic increase in lacunar size and canalicular diameter to increase LCN resorptive capacity and meet calcium demand. Upon weaning the osteocyte LCN features return to normal<sup>16,34</sup>. However, in less metabolically demanding situations, PLR appears to be crucial in actively 'rejuvenating' the mineralized collagen bone matrix and in maintaining bone quality. Indeed, suppression of PLR causes bone fragility, even without a loss of bone mass, showing that PLR is a critical cellular mechanism controlling bone quality. In this way, osteoblasts and osteoclasts remodel the external bone surfaces to control bone mass; whereas, osteocytes

remodel the LCN surface to control bone quality to achieve mechanical homeostasis. Thus, it is not surprising that the key regulators of osteoblast and osteoclast function, including vitamin D, parathyroid hormone (PTH) and parathyroid hormone-related peptide (PTHrP), Sclerostin (SOST), and transforming growth factor (TGF $\beta$ ), also regulate PLR<sup>16,30,35-37</sup>. Given the importance of PLR in supporting mineral metabolism and mechanical homeostasis of bone, researchers need more tools to better understand the mechanisms controlling PLR and how it is disrupted in disease.

## **II - Motivation to Investigate PLR**

Several lines of evidence motivate incorporation of PLR outcomes as a standard part of skeletal analyses. First, PLR participates in the crosstalk among osteocytes, osteoblasts, and osteoclasts. Many of the same stimuli already known to regulate osteoclast and osteoblast function also regulate PLR, including glucocorticoids<sup>38-41</sup>, vitamin D<sup>35,42</sup>, ovariectomy<sup>43-47</sup>, PTH<sup>15,30,48</sup> and calcium or phosphate deficiency<sup>16,26,33</sup>, and other mechanisms discussed elsewhere in this work. In addition, PLR may be mechanosensitive. Sclerostin and TGF $\beta$ , both of which are required for the anabolic response of bone to mechanical load, stimulate PLR<sup>36,37,49,50</sup>. Mice exposed to microgravity may remodel the ECM in a mechanosensitive, MMP10-dependent manner<sup>51</sup>. However, in mice with immobilized hind limbs, lacunar properties (size, shape, orientation) are not altered, despite the corresponding decrease in bone volume and load to fracture<sup>16,52,53</sup>. Careful investigation utilizing a range of PLR outcomes may help to unravel these apparently contradictory findings.

Second, the study of PLR will elucidate mechanisms controlling metabolic and mechanical homeostasis in the skeleton. Osteocytes utilize PLR to respond to metabolic stress. The lactation model is currently used as a gold standard model to study PLR, since osteocytes stimulate local mineral resorption to meet the calcium demands of milk production<sup>16,34</sup>. PLR occurs in both male and female mouse bone<sup>9</sup>, though the sex-dependent mechanisms that control baseline PLR

remain to be defined<sup>54</sup>. PLR also plays a critical role in maintaining the material quality of the bone matrix, in part by controlling ECM mineralization and collagen organization<sup>55,56</sup>. Though much is known about the biological control of bone mass, many questions remain about the mechanisms that control this important aspect of bone quality and the ability of bone to resist fracture.

Third, understanding PLR may elucidate new mechanisms of musculoskeletal disease. As with any essential homeostatic process, deregulation of PLR is a product as well as a driver of degenerative disease processes. As for remodeling by osteoblasts and osteoclasts, too much or too little remodeling by osteocytes can be problematic (**Fig. 3.1**). PLR is induced in rickets and osteomalacia<sup>33,35</sup>, but suppressed in aging<sup>57,58</sup>. Relative to young bone, bone from aging humans and mice has many hallmarks of suppressed osteocyte PLR, including decreased lacunar volume, a diminished LCN, hypermineralization, and increased bone fragility<sup>57-59</sup>. This bone fragility is not fully explained by a loss of bone mass and is attributed in part to impaired bone extracellular matrix material properties. Mounting evidence implicates an age-dependent defect in osteocyte PLR, which may in turn further impact the regulation of osteoblast and osteoclast function<sup>57,60-63</sup>.

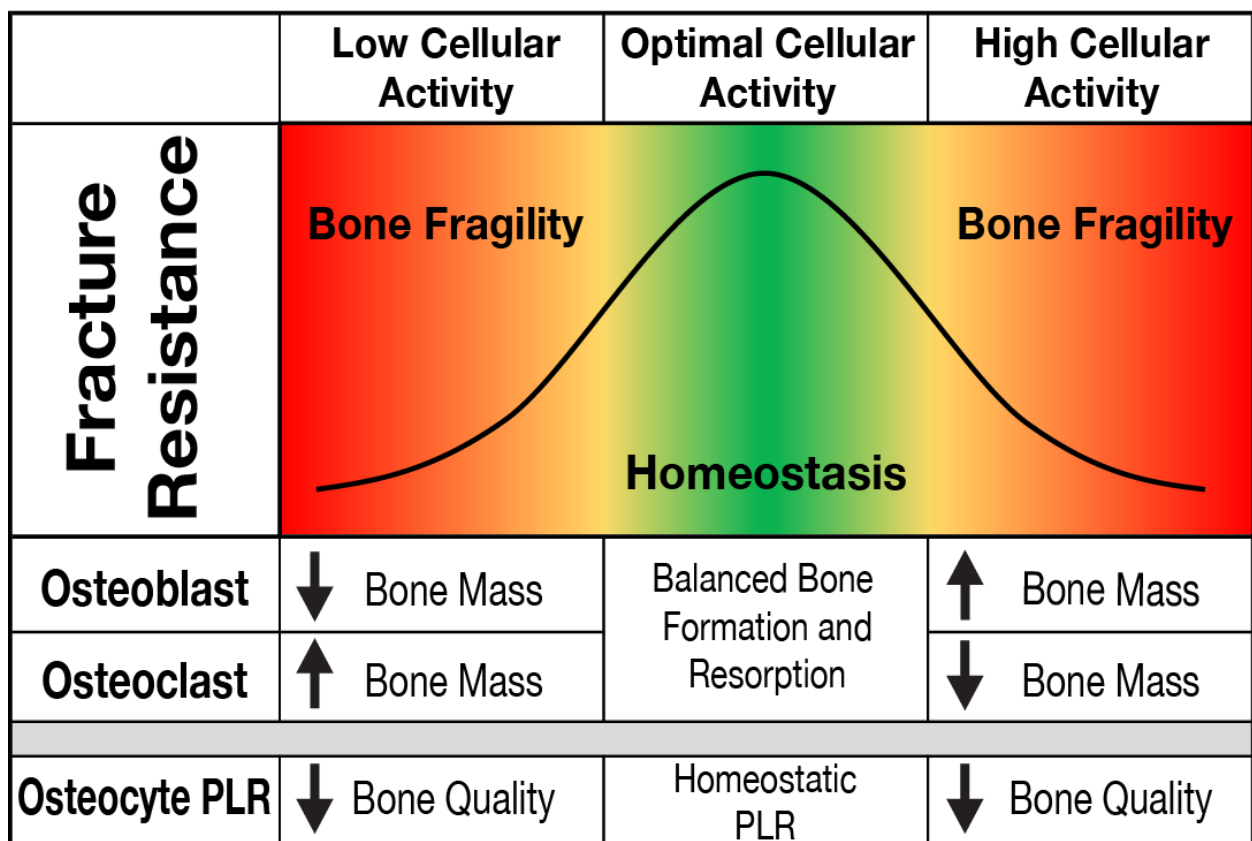


**Figure 3.1: Homeostatic control of bone mass and quality by osteoblasts, osteoclasts, and osteocytes.** During homeostasis (green region), optimal cellular activity of osteoblasts and osteoclasts maintains bone resistance to fracture. Unopposed changes in osteoblast or osteoclast function lead to changes in bone mass that can cause bone fragility (red regions). Osteocyte PLR also contributes to the mechanical homeostasis of bone. As for osteoblasts and osteoclasts, the effect of osteocyte PLR on bone quality is non-linear. Too much or too little osteocytic PLR can compromise bone quality.

While the extent to which PLR is a driver or a side effect of age-related bone fragility is yet unclear, PLR suppression may play a causal role in many diseases of bone and bone quality. For example, in glucocorticoid-induced osteonecrosis, even prior to other symptoms, glucocorticoid treatment suppresses PLR with disruption of the LCN, collagen organization, and matrix mineralization<sup>40</sup>. These changes in mice parallel those in subchondral bone from patients with end stage glucocorticoid-induced osteonecrosis of the femoral head<sup>64</sup>. Given a role for PLR in disease and aging, an improved understanding of PLR may also lead to the identification of new cellular targets for musculoskeletal therapeutics.



Although review of these pioneering studies clearly implicates PLR in skeletal homeostasis and disease, initial interest in PLR was supplanted by the idea that osteoclasts were the primary bone resorbing cell type<sup>15</sup>. Coincidentally, during the time in which PLR was largely overlooked, osteoclast and osteoblast biology advanced tremendously through the use of genetically modified mouse models and other molecular and cellular approaches, leaving our knowledge of osteocyte PLR far behind. As these models are now being employed to investigate the role and regulation of PLR, questions arise about the best PLR outcome measures and techniques used to evaluate them. Traditional morphological approaches alone are insufficient to probe the complex biological mechanisms involved in this process. Several new PLR outcomes have been described, but which of these are most useful to rigorously and efficiently evaluate PLR remains unclear.

### **III - Critical Considerations for the Study of PLR**

Although aspects of PLR are apparent throughout the skeleton, the LCN varies among species, anatomical sites, and bone types. For example, the LCN appears vastly different when comparing the sparse canaliculi in elderly human trabecular bone to the robust network of canaliculi in young mouse cortical bone (**Fig.3.2A, 3.2F**). In addition to age, several other biological factors influence the appearance of the LCN, an important yardstick for generalized osteocyte health and activity. Cortical bones in humans, as well as other large mammals, are composed of Haversian systems, or osteons. Osteocytes within osteons arrange themselves in rings around the central vascular canal, with their canaliculi often perpendicular to the rings. Smaller rodents, in contrast, do not have Haversian systems and their long bones resemble a single large osteon around the marrow cavity<sup>65</sup>, often with internal rings of slightly less organized lamella and osteocyte canaliculi<sup>66</sup>. The effect of structural differences in bone organization on the LCN are likewise apparent in trabecular bone, where the diminished lamellar organization corresponds to less aligned canaliculi (**Fig. 3.2C 3.2F**). Accordingly, the LCN is less aligned in the mouse mandible, which is dominated by

trabecular bone, relative to cortical bone of the mouse femur<sup>38</sup>, where osteocytes are spatially aligned perpendicular to the lamellar plane<sup>38</sup> (**Fig. 3.2E 3.2F**). Even within one bone, proximal to distal and medial to lateral variations in the LCN are apparent. Therefore, care must be taken to consistently analyze LCN parameters at the same region of interest in each bone.

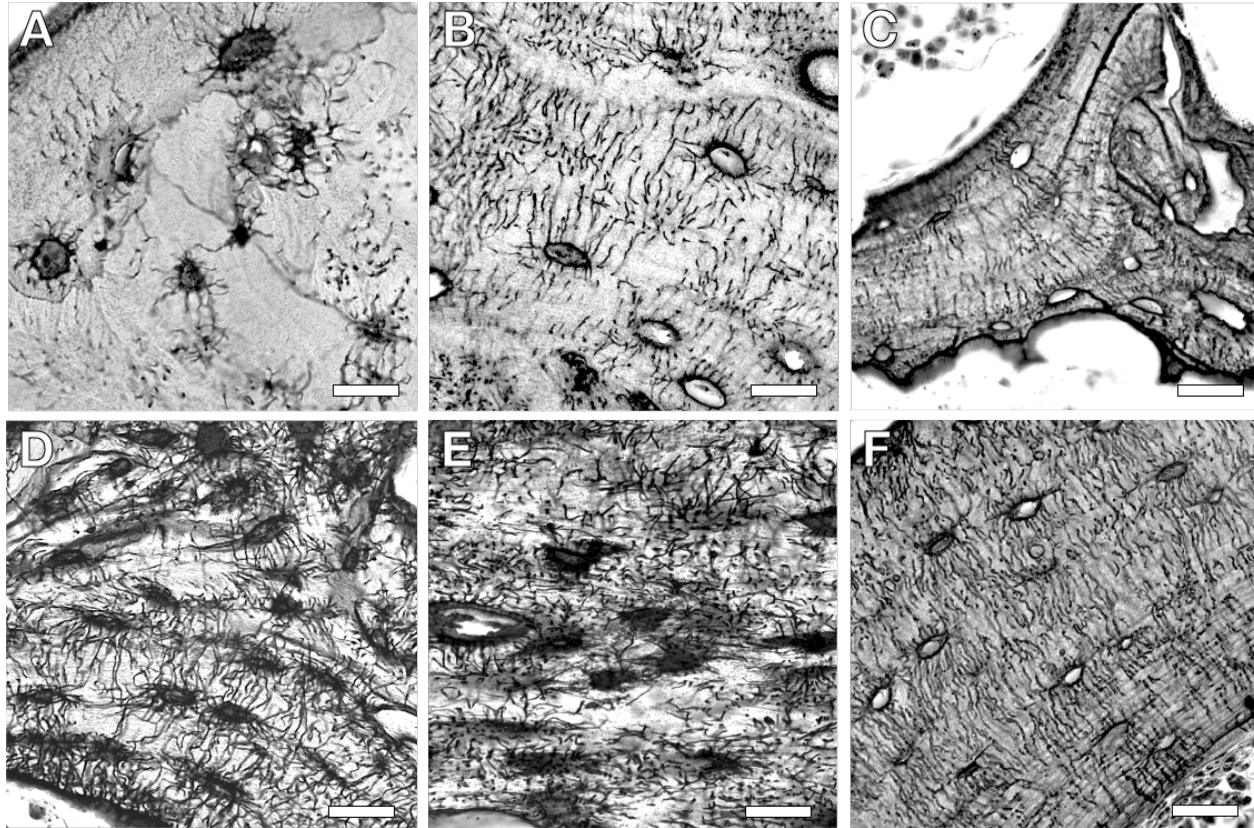


**Figure 3.2: Diversity in the histological appearance of the lacunocanalicular network (LCN) across species and bones.** Differences in the LCN are apparent in silver nitrate stained sections of human (A), rabbit (B), and mouse (C) trabecular bone. LCN variation also appears among bones, as shown from mouse cortical bone of the cochlea (D), mandible (E), and femur (F). Scale bar, 20  $\mu\text{m}$ .

Among the factors that contribute to these anatomic differences in the LCN are site-specific expression and activity of the enzymes required for PLR. For example, MMP2 expression varies across the skeleton, with high levels in the calvaria and low levels in the long bones<sup>29</sup>. This expression pattern likely explains the observation that MMP2-deficient mice have dramatic

alterations of the LCN in calvaria compared to moderate disruption of the LCN in long bones. Likewise, the LCN, collagen organization, and bone matrix mineralization were most affected in mid-cortical bone of MMP13-deficient mice, which was the site of highest MMP13 expression<sup>29</sup>. Similar differences in PLR enzyme expression may contribute to hypermineralization in the endocortical region compared to periosteal region of aging cortical bone<sup>58</sup>. Post-translational control of PLR enzymes may also determine where and how PLR is regulated, since cochlear bone expresses high levels of MMP13 protein, but the hearing and cochlear bone of MMP13-deficient mice was normal<sup>67</sup>. This observation is consistent with the presence of unique mechanisms to control bone remodeling by osteoblasts and osteoclasts in the cochlea. Undoubtedly, a sophisticated network of transcriptional and post-transcriptional mechanisms control bone remodeling by osteocytes, as it does for osteoblasts and osteoclasts.

Variations in the LCN and PLR within and between bones highlight the heterogeneity of the osteocyte population. Though the sources and the reasons for this heterogeneity remain largely unknown, intriguing possibilities include differences in the embryonic origin, exposure to physical stimuli, metabolic supply/demand, innervation, and others. For example, elongated lacunae are observed in cortical bones, such as the tibia, that undergo loading during locomotion<sup>68,69</sup>, compared to calvaria<sup>70</sup>. This suggests that loading and lacunar shape may share a functional relationship, which potentially contributes to the LCN differences along the cortical regions of long bones<sup>66</sup>. Mechanistic studies are needed to establish the causality of these and other observations. Meanwhile, these observations have important practical implications for the study of PLR. Attention to species-specific and anatomically distinct differences in bone must be considered when studying PLR, especially when extrapolating findings from rodent models to understand human clinical conditions.

A number of mechanistic questions about the regulation of PLR further complicate our understanding of this process. Most work focuses on the resorption of perilacunar and pericanalicular bone, while much less is known about the deposition of new ECM. In some cases,

the induction or repression of PLR enzymes corresponds to changes in lacunar size or shape; whereas in others, lacunar size is unchanged, but canalicular networks are altered. The mechanisms that determine when, where, and how proteolysis or acidification exert their effects in the mineral and/or organic phases of the osteocyte microenvironment remain unclear. While these processes initially appeared to be coupled, more recent studies suggest that perilacunar remodeling is distinct from pericanalicular remodeling<sup>16,37</sup>.

Furthermore, the approaches used to study PLR may impact the interpretation of the results. If distinct mechanisms control the resorption of the mineral and organic components of the bone matrix, then the appearance of the LCN may differ depending on whether the outcome is performed on mineralized bone (i.e. quantitative backscatter electron imaging) or demineralized bone (i.e. histological staining of the LCN). Efforts of the scientific community to elucidate the role of PLR in bone homeostasis, and how PLR is regulated normally and pathologically will require attention to the sensitivities of the methods used, as well as to the diverse regulation of PLR throughout the skeleton, across species, and with age. The following discussion considers these issues in light of a number of currently used methods used to observe and study PLR and in some cases protocols used by the Alliston Laboratory are explicitly outlined. It is important to note that combining these approaches with more sophisticated molecular and morphological approaches, such as RNA-Seq or back-scatter SEM, will add rigor and power to the assessment of PLR phenotype in bone tissue<sup>71-74</sup>.

#### IV – Approaches, Considerations, and Techniques for Studying PLR

##### Molecular Assessment of PLR – RT-qPCR and Immunohistochemistry:

Numerous enzymes have been functionally implicated in PLR through *in vivo* studies. Several enzymes, already implicated in bone remodeling by osteoclasts and osteoblasts, are expressed by osteocytes at the time and site of PLR. Studies in genetically modified mouse models have shown a functional role for several of these in PLR, including matrix metalloproteinases (*Mmp2*, *Mmp13*, *Mmp14*), Cathepsin K (*Ctsk*), carbonic anhydrases (*Ca2*), vacuolar H<sup>+</sup> ATPases (*Atp6v1g1*, *Atp6v0d2*, and *Atp6v0b*), and tartrate resistant acid phosphatases (*Acp5*) in PLR<sup>16,31,37,40</sup>. Analysis of gene expression using RT-qPCR and RNA-Seq shows that many of these genes are regulated in a coordinated manner by agents that modulate PLR, such as PTH, PTHrP, TGFβ, and glucocorticoids<sup>16,30,37,40</sup>. Therefore, analysis of changes in mRNA and protein expression of these PLR enzymes provides a good surrogate to quantify dynamic changes in PLR at the molecular level.

An important consideration of osteocyte gene expression analysis is the selection of the proper housekeeping gene. In RT-qPCR, in order to normalize results between conditions to control for differences in RNA isolation or other factors, a housekeeping gene, or a gene with relative stability between the tested conditions, must be used in the delta-delta CT method of quantifying relative gene expression levels<sup>75</sup>. Common housekeeping genes used for other cell types include genes for structural proteins, i.e. beta actin, or genes encoding conserved molecular machinery like ribosomal protein units. Because osteocytes are highly specialized cells, are actively producing diverse amounts of matrix material in their regulation of bone tissue, and have dynamic and situation dependent behaviors, housekeeping genes traditionally used for other cell types, especially genes for structural proteins, may not be suitable as housekeeping genes for evaluation of osteocyte transcriptional behavior. Thus, effort should be taken to evaluate and confirm the appropriate housekeeping gene used in RT-qPCR for osteocytes.

Before investigation into specific gene expression changes, the baselines for osteocyte behavior must be established. Recently, an osteocyte transcriptome has been established<sup>76</sup> defining the generalized landscape of osteocyte expression. From here, housekeeping genes conserved among other cell types can be identified within osteocytes. Instances of important active osteocyte research include areas of age and disease that may impact or alter osteocyte behavior from this baseline behavior. In these conditions, for example in age, expression patterns may change and genes that were once reliable housekeeping genes may be altered, removing them from consideration as housekeeping genes in qPCR experiments. Previous studies in contexts of interest, for example aging<sup>77-79</sup>, can be used to screen for commonly used housekeeping genes. Candidate genes from these studies can be referenced against the osteocyte transcriptome to see if they are utilized by osteocytes or not before testing the stability of these genes in osteocytes. Genes conserved in osteocytes and active in homeostasis as well as in age and disease present themselves as good candidate housekeeping genes because their use tends to not be context dependent or at least may be similar in the contexts being compared.

Before beginning any expression related experiment, the stability of chosen housekeeping genes within osteocytes should first be considered. Several analytical methods exist for gene normalization and stability analysis<sup>80-83</sup> and can be applied to osteocyte expression analysis. In a small experiment, we sought to determine a collection of housekeeping genes for aged osteocytes when traditional housekeeping genes, GAPDH & beta-actin, were found to be unstable with age. Candidate housekeeping genes were selected from a range of previous age-related studies from other tissues. CT expression values for these genes were collected via RT-qPCR from RNA from mice across a range of ages, sexes, and backgrounds. Utilizing RefFinder\*, a free online tool that combines several methods of gene expression normalization<sup>84</sup> candidate gene expression was normalized across samples and then ranked in terms of stability (**Fig. 3.3**). This analysis revealed

---

\* <https://www.heartcure.com.au/reffinder/?type=reference>

novel housekeeping genes and unexpected instability of genes previously used during expression analysis of osteocytes including GAPDH and L19, which ranked last in our analysis. Results from this test emphasize the importance of verifying gene stability in specialized cells such as osteocytes for the investigation of PLR in situations of altered homeostasis.

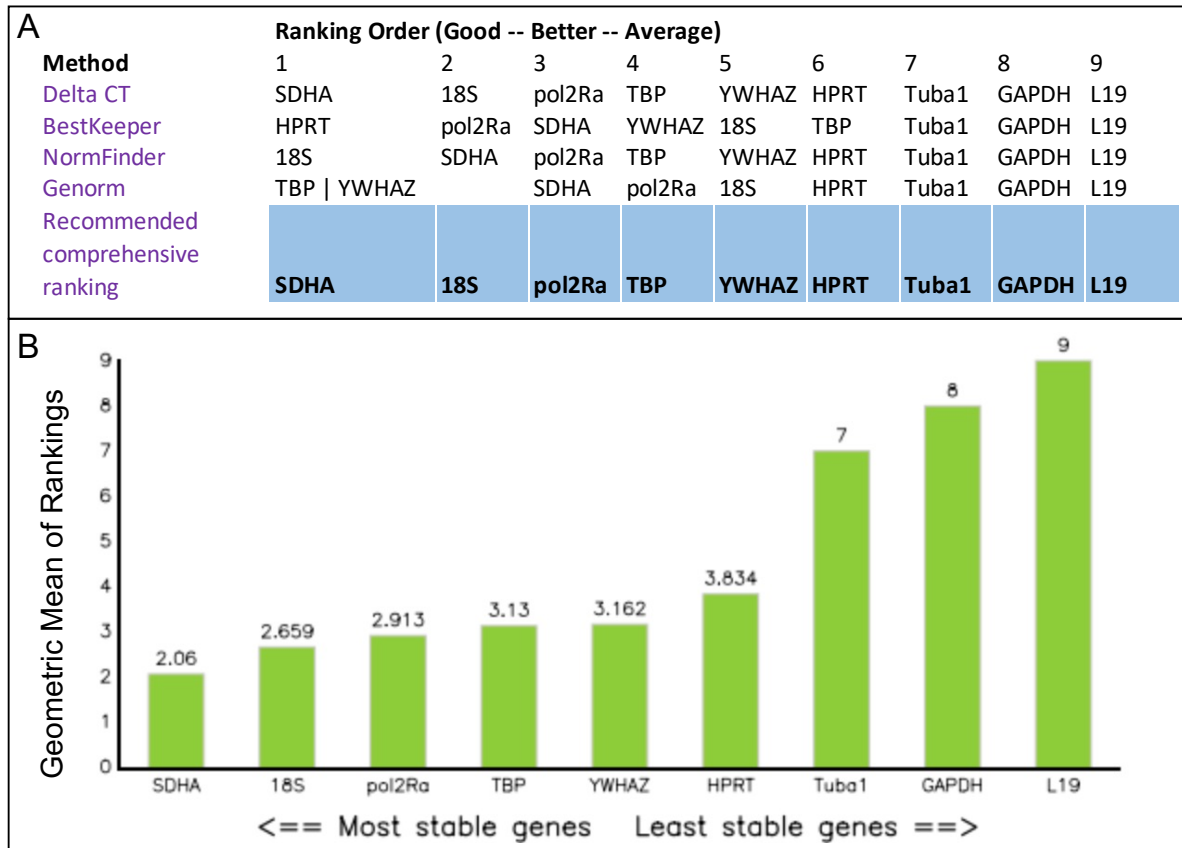


**Figure 3.3: Housekeeping gene selection and stability for aged osteocytes.** qPCR results for osteocyte enriched RNA from 8 aged mice of mixed backgrounds and both sexes were collected for 9 common housekeeping genes, chosen from prior studies of aging in other organ systems. Raw CT values were analyzed via the RefFinder method which combines multiple normalization methods to analyze gene stability and ranked for each methods independently (A) and for the RefFinder combined ranking (B) showing that housekeeping genes SDHA and 18S outperform other commonly used housekeeping genes (GAPDH, L19).

In many cases, ablation of these enzymes in mice causes disruption of the LCN. Specifically, the long bones from lactating mice have increased mRNA expression of cathepsin K, TRAP (ACP5/Acp5), and carbonic anhydrase 1 and 2<sup>16,36,85</sup>. Similar to osteoclasts, osteocytes

simultaneously express acid catalyzed proteases and ATP proton pumps, implying a coordinated effort by the osteocyte to 1) establish extracellular pH gradients within the LCN and 2) activate proteolytic events to resorb the surrounding bone matrix<sup>16,21,37,86,87</sup>. In cortical bone from mice with an osteocyte-specific deletion of the TGF $\beta$  type II receptor, qPCR revealed a coordinated repression of multiple PLR enzymes. The same bones had several features consistent with suppressed PLR, including diminished canalicular networks and bone quality deficits<sup>37</sup>. Other situations that induce or suppress PLR, for example lactation or glucocorticoid treatment, also show coordinated induction or repression of PLR genes respectively<sup>16,40</sup>, suggesting that PLR enzymes may share some common regulatory mechanisms. Since many of these PLR genes are expressed by bone resorbing osteoclasts and other cell types, parallel use of immunohistochemistry (**Fig. 3.4**) is needed to definitively demonstrate that gene expression differences in osteocyte-enriched cortical bone mRNA are primarily due to osteocytes.

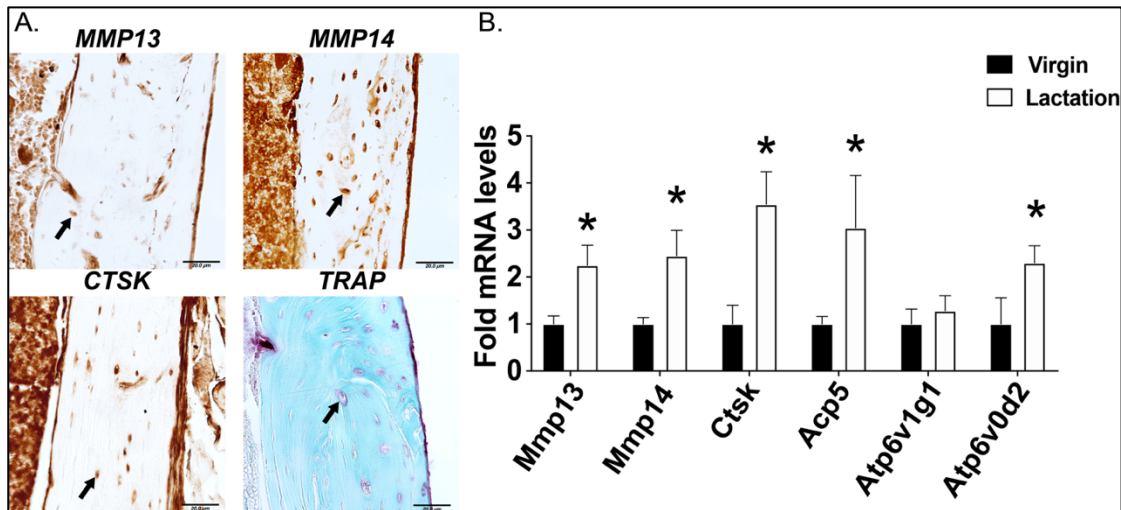


**Figure 3.4: Molecular assessment of PLR.** Immunohistochemistry for PLR-associated proteins MMP13, MMP14, CTSK and TRAP on femurs isolated from 8-week old C57BL6 mice. 7  $\mu$ m thin paraffin embedded bone sections are shown (A). Arrows indicate the osteocytes positive for the respective stain. Scale bar is 20  $\mu$ m. RT-qPCR highlights the lactation mediated induction in PLR-related genes (B). All genes were normalized to 18s RNA as an internal control gene and relative changes in gene expression in the lactating C57/BL6 mice were compared against virgin controls. N=10 mice in each group and \*p>0.05, different from the virgin mice, as calculated from the Student's t-test.



In our laboratory, initial analyses of gene and protein expression typically focus on MMP13 and cathepsin K, followed by MMP2, MMP14, carbonic anhydrase 2, and various ATPases (i.e. ATP6V1G1 and ATP6V0D2) if initial results suggest a role in PLR regulation<sup>16,37</sup>. In some cases, carbonic anhydrase 2 and the ATPases seem to be regulated distinctly from the expression of the proteases, suggesting the possible presence of compensatory mechanisms between the acidification and proteolytic functions of PLR.

## **Protocol - Molecular Assessment of Osteocytic PLR via qRT-PCR**

Expression of genes typically associated with the resorptive activity of osteocytes can be monitored to assess induction of PLR. RNA enriched for osteocytic populations can be isolated and quantified as described below.

### **Materials:**

1. Centrifuge Multifuge 3S-R.
2. Disposable polypropylene round-bottom tubes (15 ml).
3. Polytron Homogenizer (ThermoSavant or equivalent).
4. Bone spinner tubes: Make a small hole at the bottom of a 0.2ml and 0.5ml Eppendorf tubes. Place the 0.2 ml tube nested in the 0.5ml tube and insert this 2-tube assembly nested in a 1.5ml Eppendorf tube to make a bone spinner tube.
5. Polypropylene Eppendorf tubes (1.5 ml).
6. Petri dish (6 and 10 cm diameter).
7. Sectioning materials (scissors, forceps, curved forceps).
8. miRNeasy extraction kit (Qiagen) or equivalent.
9. iScript™ RT kit (BioRad) or equivalent.
10. iQ™ SYBR Green Super Mix (BioRad) or equivalent.
11. Primers for qPCR
12. MyIQ Single-Color-Real-Time detection system (BioRad) or equivalent.

### **Methods**

1. Dissect the bones and remove the periosteal layer and muscle surrounding the bones as quickly as possible.
2. Dissect off the epiphyseal ends of the bones and remove the bone marrow by centrifuging the bones in special bone spinner tubes at 9000 rpm for 15 seconds.

3. Flash freeze the bones *devoid of marrow, periosteum, and epiphyses* in liquid nitrogen for 30 seconds.
4. Following flash freezing, immediately immerse the samples in 15 ml polypropylene tubes containing 1.5 ml QIAzol (analogous to TRIzol) solution for every 20 mg of bone tissue.
5. Dissociate the bone tissue in QIAzol using a Polytron tissue homogenizer at full speed in 10 second bursts 3-4 times, icing the samples between bursts for 5-10 seconds. *Ensure that the samples are on ice during homogenization step.* Homogenized samples can be stored at -80 °C in QIAzol prior to RNA isolation.
6. For total RNA extraction from homogenized lysates, the miRNeasy Mini Kit (Qiagen), which combines a phenol/guanidine-based lysis and a silica-based on-column purification method for efficient and high-quality RNA extraction, may be used<sup>(39)</sup>. This kit allows collection of both mRNA and miRNA. If only the mRNA is useful for your experiments, the RNeasy Kit (Qiagen) can be used with the same protocol.
7. Add 300 µl of chloroform (0.2 times the volume of QIAzol) to the QIAzol cell lysate and mix them thoroughly for 15 seconds.
8. Incubate at room temperature for 2-3 minutes until separation begins to occur.
9. Centrifuge the samples at 12,000 rcf for 15 minutes at 4°C.
10. Transfer the upper aqueous phase to new tube being careful not to disturb or contaminate with the lower phase and follow the standard manufacturer's protocol for isolating RNA. Conduct on-column DNase digestion as recommended in the miRNeasy mini kit protocol.

11. Concentration of the extracted RNA is determined using a NanoDrop™ 1000 spectrophotometer (Nanodrop Technologies). RNA with a 260/280 ratio between 1.8-2.0 and a 260/230 ratio of close to 2.0 is considered of good quality. RNA yields are typically in the range of 7-10 µg from the whole bone (devoid of marrow). From trabecular bone alone, we are able to isolate 5-7 µg of RNA, while cortical bone extraction yields at most 1-2 µg of RNA.
12. Conduct reverse transcription using the iScript cDNA synthesis kit as per the manufacturer's instructions. 1 µg of total RNA is reverse transcribed into cDNA using a final volume of 30 µl reaction mixture.
13. Prepare reaction master mix as per **Table 1** and add RNA samples separately for each reaction.

**Table 3.2: Reverse transcription master mix**

<b>Reagents</b>	<b>1 reaction</b>
<i>5X iScript RT Supermix</i>	<i>4 µl</i>
<i>iScript Reverse Transcriptase</i>	<i>1 µl</i>
<i>RNA template (1 µg)</i>	<i>variable</i>
<i>Nuclease free water</i>	<i>variable</i>
<i>Total volume</i>	<i>20 µl</i>

14. Mix the RNA and iScript master mix and incubate samples in the thermocycler following the temperature gradients described in **Table 2**. Store cDNA at -20°C until use for quantitative RT-qPCR.

**Table 3.3: Thermocycler reverse transcription temperature gradient guide**

<i>Temperature</i>	<i>Time</i>
25 <sup>o</sup> C	5 minutes
46 <sup>o</sup> C	20 minutes
95 <sup>o</sup> C	1 minutes
25 <sup>o</sup> C	Hold

15. Carry out Quantitative RT-qPCR using the iQ-SYBR Green Supermix kit (Bio-Rad) on a MyIQ Single-Color-Real-Time detection system (BioRad). Typically, 50ng of cDNA used in a qPCR reaction mix will obtain Ct readings in the range of 25-30 for the PLR genes in **Table 3**. While the primers are specific for mouse bones, the protocol for RNA extraction and RT-qPCR is applicable to bone specimens from other species.

**Table 4.3: PLR gene primers for RT-qPCR**

<i>Primers for genes</i>	<i>Sequence</i>
18s RNA (FP)	5'-CGAACGTCTGCCCTATCAAC-3'
18s RNA (RP)	5'-GGCCTCGAAAGAGTCCTGTA-3'
Mmp13 (FP)	5'-CGGGAATCCTGAAGAAGTCTACA-3'
Mmp13 (RP)	5'-CTAAGCCAAAGAAAGATTGCATTTTC-3'
Mmp14 (FP)	5'-AGGAGACGGAGGTGATCATCATTG-3'
Mmp14 (RP)	5'-GTCCCATGGCGTCTGAAGA-3'
Mmp2 (FP)	5'-AACGGTCGGAATACAGCAG-3'
Mmp2 (RP)	5'-GTAAACAAGGCTTCATGGGG-3'
Ctsk (FP)	5'-GAGGGCCAACTCAAGAAGAA-3'
Ctsk (RP)	5'-GCCGTGGCGTTATACATACA-3'
Acp5 (FP)	5'-CGTCTCTGCACAGATTGCAT-3'
Acp5 (RP)	5'-AAGCGCAAACGGTAGTAAGG-3'
Atp6v0d2 (FP)	5'-TCTTGAGTTTGAGGCCGACAG-3'
Atp6v0d2 (RP)	5'-GCAACCCCTCTGGATAGAGC-3'
Atp6v1g1 (FP)	5'-CCGTTCTCTCAGCCCAAAGT-3'
Atp6v1g1 (RP)	5'-CTCCGTTCTTTTCGCTTGC-3'

16. Prepare the primer, cDNA and iQ-SYBR green master mix as outlined in

**Table 4.**

**Table 3.4: iQ-SYBR Green mastermix for qPCR**

<b>Reagents</b>	<b>1 reaction</b>	<b>Final Concentration</b>
<i>Nuclease free Water</i>	<i>Variable</i>	-
<i>Forward Primer</i>	<i>Variable</i>	<i>300 nM (100-500 nM) (0.5 μL of 100 μM stock)</i>
<i>Reverse Primer</i>	<i>Variable</i>	<i>300 nM (100-500 nM) (0.5 μL of 100 μM stock)</i>
<i>iQ-SYBR Green Supermix (2x concentration)</i>	<i>10 μL</i>	<i>1x</i>
<i>Template (cDNA)</i>	<i>0.5 μL of 100ng/μL cDNA from RT</i>	<i>Amount of cDNA equivalent to ~1pg to 100 ng of total RNA</i>
<i>Total Reaction Volume</i>	<i>20 μL</i>	

17. Set up the experiment and program the thermocycler to the quantitative RT-qPCR program outlined in **Table 5**.

**Table 3.5: Thermocycler RT-qPCR temperature cycle guide**

<b>Temperature</b>	<b>Time (mins/secs)</b>	<b>No. of cycles</b>
<i>95<sup>o</sup>C</i>	<i>2-3 min.</i>	<i>1</i>
<i>95<sup>o</sup>C</i>	<i>10-15 secs</i>	<i>40</i>
<i>60<sup>o</sup>C</i>	<i>30 secs</i>	
<i>55-95<sup>o</sup>C (in 0.5<sup>o</sup>C increments)</i>	<i>10-30 secs</i>	<i>1</i>

Normalize data to 18s RNA as the internal standard and to the corresponding control group using the  $2^{-\Delta\Delta CT}$  method. For each run, the melting curve and saturation of amplification cycles are controlled by the use of MyIQ software (BioRad).

## **Protocol - Molecular Assessment of Osteocytic PLR via Immunohistochemistry**

### **Materials**

1. Innovex Animal IHC kit
2. Formalin-fixed, paraffin-embedded (FFPE) sections
3. Uni-trieve (Innovex)
4. Primary Antibodies: MMP13 antibody (abcam ab39012); MMP14 antibody (abcam ab38971); Ctsk antibody (abcam ab19027)

### **Methods**

1. Dissect the bones and carefully scrape off the surrounding periosteum and muscle tissue.
2. Fix the cleaned bones immediately in 10% neutral buffered formalin (NBF) for 48 hours.
3. Following fixation, rinse the tissue samples in the 1X PBS solution to remove residual PFA.
4. Decalcify the fixed bones using 0.5 EDTA for 2-4 weeks. Following decalcification, rinse bones in PBS (three times each for 60 minutes at 4° C) and then subjected to paraffin embedding.
5. Utilizing a microtome, generate 6-8 µm thick sections from paraffin blocks according to standard protocols.<sup>88</sup>
6. Deparaffinize and rehydrate tissue sections by immersing the slides in 100% xylene or citrisolv and EtOH gradient as described below.
7. Immerse slides in Citrisolv three times for 5 minutes each.
8. Immerse slides in 100% EtOH for 5minutes
9. Immerse slides in 95% EtOH for 5minutes
10. Immerse slides in 70% EtOH for 5minutes
11. Immerse slides in distilled water for 5minutes.

12. Incubate slides in Uni-trieve for 30 minutes at 60°C.
13. Rinse slides in distilled water two times for 3 minutes each.
14. Incubate slides with Fc-block (329ANK) for 45 minutes at RT.
15. Rinse slides in distilled water two times for 3 minutes each.
16. Incubate slides with Background Buster for 45 minutes at RT.
17. Rinse slides in distilled water two times quickly.
18. Incubate slides with primary antibody in PBS for 1hr at RT or overnight at 4°C. Recommended dilutions of primary antibodies: MMP13- 1:100 diluted in 1X PBS; MMP14- 1:100 diluted in 1X PBS; CTSK- 1:75 diluted in 1X PBS
19. The next day, rinse slides in 1X PBS three times for 3 minutes each.
20. Incubate slides with Secondary Linking Ab (329ANK) for 10 minutes at RT.
21. Rinse slides in PBS three times for 3 minutes each.
22. Incubate slides with Peroxidase (HRP) enzyme for 10 minutes at RT.
23. Rinse slides in 1X PBS three times for 3 minutes each.
24. Incubate slides with DAB working solution for 5 minutes at RT.
25. Rinse slides in 1X PBS thrice for 3 minutes each.
26. Mount slides with an aqueous-based mounting-medium.



## **Protocol - Molecular Assessment of Osteocytic PLR via Tartrate Resistant Acid**

### **Phosphatase Staining**

#### **Materials**

1. Acid phosphatase leukocyte kit (Sigma)
2. Fast Red Violet (Sigma) (CAS# 32348-81-5)
3. Fast Green (Sigma)(CAS# 2353-45-9)
4. 37% formaldehyde
5. Formalin-fixed, paraffin-embedded (FFPE) sections
6. Fast Red Violet Solution: First dissolve 7mg of Fast Red Violet salt in 1ml of 1XPBS.
7. Diazonium salt solution: Gently mix Fast Red Violet solution and with Sodium Nitrite Solution in a 1:1 ratio by tapping or inverting (depending on the volume of the solution). Allow it to stand at RT for 2minutes.
8. 0.02% Fast Green: Dissolve 0.05g of Fast green dye in 250ml of distilled water.
9. Fixative Solution: Mix 25ml citrate solution, 65ml acetone, and 8ml 37% formaldehyde. Store solution at 4<sup>0</sup>C for up to 2 months.

#### **Methods**

1. Deparaffinize and rehydrate tissue samples by immersing the slides in 100% xylene or citrisolv and EtOH gradient as described below.
2. Immerse slides in Citrisolv three times for 5 minutes each.
3. Immerse slides in 100% EtOH for 5 minutes.
4. Immerse slides in 95% EtOH for 5 minutes.
5. Immerse slides in 70% EtOH for 5 minutes.
6. Immerse slides in distilled water for 5 minutes.
7. Incubate slides in Fixative Solution for 30 seconds at RT.

8. Rinse slides in distilled water for 5 minutes.
9. In a coplin jar, make TRAP staining solution by mixing Naphthol AS-BI Phosphate solution (Sigma), Tartrate solution (Sigma), Diazonium salt solution, Acetate solution (Sigma), and deionized water in a ratio of 1:2:2:4:90 respectively.
10. Immediately proceed to incubating slides in TRAP working solution for 1hr at 37°C in the dark.
11. Rinse slides in distilled water for 3 minutes.
12. Counterstain by incubating slides in 0.02% Fast Green for 1 min.
13. Rinse slides in distilled water with 2-3 quick dips.
14. Dry slides before mounting with coverslip and a toluene/xylene-based mounting-medium.

### Visualization of the Lacunocanalicular Network

*Two-dimensional Histological Analysis of the LCN:* Morphological examination of the LCN provided the first evidence of PLR utilizing histological stains to visualize the LCN. Common histological stains include H&E, Alizarin red, or basic fuchsin<sup>89–91</sup>, toluidine blue<sup>39,85</sup> and ploton silver nitrate stains (**Fig. 3.5A, 3.5B**)<sup>25,33,36,38–40,67,85</sup>. For example, H&E and toluidine blue can be used to distinguish empty lacunae from lacunae containing osteocytes in the section plane, while ploton silver nitrate stains can be used for qualitative two-dimensional visualization of both lacuna and canaliculi.

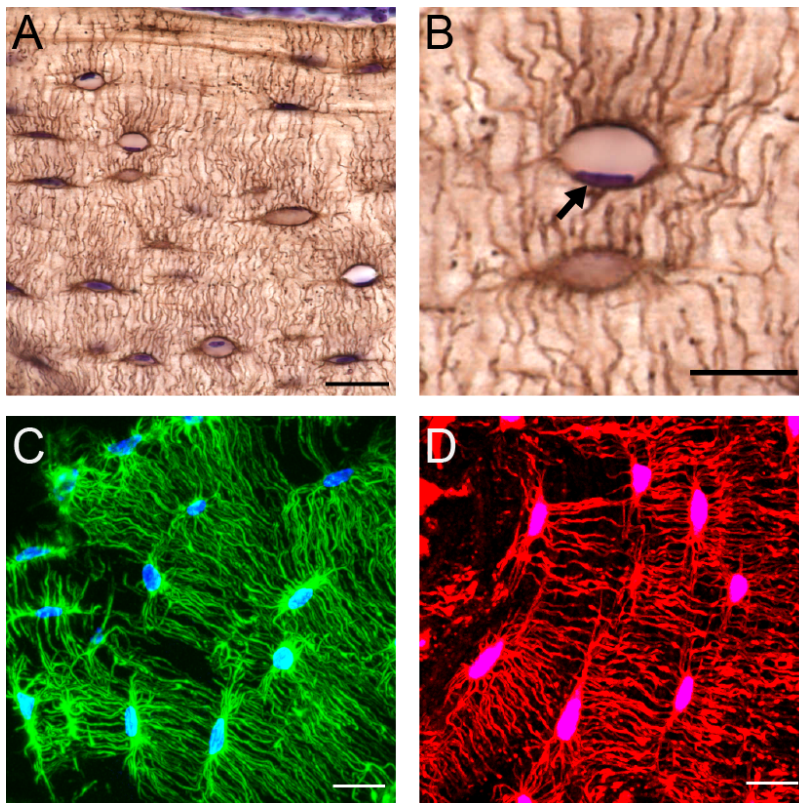


**Figure 3.5: Stains highlighting morphological changes in osteocytes associated with PLR.**

Silver nitrate stain on C57/BL6 mouse bone demonstrates the osteocyte cell network in the paraffin embedded cortical bone (A, scale bar = 20  $\mu$ m) with cresyl violet counter stain for nuclei (purple). Enlarged region of section from A (B, scale bar = 10  $\mu$ m) depicting an osteocyte containing a positively stained cresyl violet nuclei (black arrow) and an osteocyte not presenting a nucleus within the 2D section (white arrow). Fluorescent phalloidin (C, scale bar = 10  $\mu$ m) staining of f-actin (green) and DAPI (blue), can be used to visualize the osteocyte cell network in 3D with frozen, OCT sectioning and confocal microscopy. Dil stain (red) (D, scale bar = 10  $\mu$ m) intercalates into the hydrophobic cell membrane, further illuminating osteocyte cell bodies and dendritic projections in 3D.

Semi-quantitative lacunae and canaliculi measurements have been performed and reported in various ways. For example, lacunae measurements have been reported as percent lacunocanalicular volume<sup>38</sup>, average number of lacunae occupied by osteocytes per bone area<sup>59,92,93</sup>, number of empty lacunae per bone area<sup>57,59,92,94</sup>, lacunar area<sup>5,25,38,92</sup>, and average lacunar area per osteocyte<sup>33</sup>. Canalicular measurements also have been reported as number of canaliculi per osteocyte<sup>33,57,59</sup>, canalicular connectivity<sup>33</sup>, canalicular branching<sup>33</sup> and canalicular length per osteocyte<sup>37,54,94</sup>. Lacunar and canalicular measurements have also been summarized and reported as lacuno-canalicular area<sup>5,67</sup> as well as other parameters<sup>5</sup>. Due to the variety of these measurable LCN outcomes, an established set of lacunar and canalicular parameters is needed. Given the diversity and sheer size of the LCN, the manual nature of most histologic analysis can result in sample size and number of technical replicate images per sample too low or small in scope for adequate observation of the LCN. In addition, the variable nature of histological stains used for LCN visualization has slowed the accurate use of automatic measuring software, which has further limited the field to manual measurements that are time consuming and subjective to the grader – adding to uncontrolled consistency across experiments. These issues are critical to address since PLR changes to the LCN can be subtle and may be localized and can require sufficient expertise to observe reliably and repeatably via histology. These challenges highlight the need for a standardized approach for reproducible staining, consistent selection of regions of interest, adequate biological and technical replicates, and blinded grading to overcome these limitations and significantly increase the rigor of LCN histological outcomes.

*Three-dimensional Visualization of the LCN:* Traditional two-dimensional methods of visualizing morphological features of the LCN are planar and ignore the three-dimensional nature of the osteocyte network. Reconstructing and understanding the complex geometries of the osteocyte LCN are critical for understanding the health, arrangement, and activity of osteocytes involved in PLR. The reliable imaging and reconstruction of the LCN is a challenging endeavor

due to the density of the canalicular network and the nanoscale dimensions of these processes within an optically opaque, three-dimensional material.

Several methods<sup>39,70,95</sup> have focused on capturing the LCN in three dimensions (**Fig. 3.5C,D**). With the advent of confocal microscopy, it has become more feasible to view the LCN in three dimensions<sup>57,96</sup>, while advancements in tissue clearing are pushing the limits of tissue penetration<sup>97,98</sup>. Confocal methods have allowed for the reliable collection of osteocyte lacunar parameters, including lacunar density, lacunar shape<sup>62</sup>, osteocyte surface area and volume<sup>99</sup>, volume fraction of the LCN<sup>100</sup>, canalicular density, canalicular number per osteocyte, canalicular volume, and canalicular length<sup>101</sup>, among many others. Light microscopy, however, is limited by diffraction aberrations that may skew quantitative efforts especially at the nanoscale dimensions of osteocyte canaliculi so care must be taken when observing these features<sup>102</sup>. Multi-photon microscopy has been employed to overcome some of these limitations and has also been successful in further increasing the penetration depth of light microscopy<sup>74,99</sup>. Despite advancements, these techniques are time consuming, data-expensive, and only capture a small window of the LCN. Even with these drawbacks, light-based microscopy remains one of the most common approaches to study of the osteocyte LCN in three dimensions and provides a practical and manageable tool with which to study PLR-related changes in osteocyte function<sup>68,103,104</sup>. Robust protocols used for the visualization of the osteocyte LCN in 2D via ploton silver staining, and in 3D via fluorescent confocal microscopy are supplied below:

## Protocol - Morphological Assessment of Osteocytic PLR via Silver Nitrate Stain (2D)

### Materials

1. 10% Neutral buffered formalin
2. 1X Phosphate Buffered Saline (PBS)
3. 100% Xylene or Citrisolv
4. 100% ethanol (EtOH)
5. 95% ethanol
6. 70% ethanol
7. 0.5 M Ethylenediaminetetraacetic Acid (EDTA)
8. Silver Nitrate
9. Sodium Thiosulfate
10. Acetic Acid
11. Sodium Acetate
12. Cresyl violet
13. Gelatin type B, bloom 100 (bloom is the strength of gelatin)
14. Bone sections
15. Disposable coplin jars. Holds 20-25ml volume and 4 slides.
16. Gelatin-formic acid solution: Dissolve 0.2g gelatin type A, bloom 275 or B, bloom 75 in 10ml of warm water (50-55<sup>0</sup>C). Vortex to dissolve and cool to room temperature (RT). After cooling, add 125 $\mu$ l of 90% formic acid.
17. 50% Silver Nitrate: Dissolve 7.5g of silver nitrate (Spectrum Chemical) in 15ml of water and mix by shaking gently.
18. Silver Nitrate Working Solution: Mix 50% silver nitrate and gelatin-formic acid solution in a 2:1 ratio. **Keep solution in the dark.**
19. 5% Sodium thiosulfate: Dissolve 12.5g sodium thiosulfate in 250ml water.

20. Cresyl violet solution: Dissolve 33.35mg of cresyl violet acetate in 25ml of distilled water.
21. 0.1M Acetic Acid: Dissolve 3ml of glacial acetic acid in 500ml of distilled water.
22. 0.1M Sodium Acetate: Dissolve 200mg of sodium acetate in 15ml of distilled water.
23. Buffer Solution: Mix 235ml of 0.1M acetic acid and 15ml of 0.1M sodium acetate. Adjust pH to 3.5.
24. Cresyl violet Working Solution: Mix 250ml of buffer solution with 25ml of cresyl violet solution. Mix well 30 minutes and keep solution in dark.

## **Methods**

1. Dissect the bones and carefully remove the muscle tissue.
2. Fix the cleaned bones immediately in 10% neutral buffered formalin (NBF) for 48 hours at RT.
3. Following fixation, rinse the tissue samples in 1X phosphate buffered saline (PBS) solution for 10 minutes and at least three times to remove residual NBF.
4. Decalcify the fixed bones by keeping them in 0.5M EDTA solution for 2-4 weeks shaking at 60 revolutions/ min at RT. Change EDTA solution every 3-4 days.
5. Following decalcification, bones will be rinsed in PBS (three 60-minute washes at 4° C) to remove residual EDTA.
6. Proceed with paraffin embedding according to standard protocols.
7. Utilizing a microtome, generate 6-8  $\mu\text{m}$  thick sections according to standard protocols<sup>88</sup>.

8. Deparaffinize and rehydrate tissue samples by immersing the slides in 100% xylene or citrisolv and EtOH gradient as described below.
9. Immerse slides in Citrisolv three times for 5 minutes each.
9. Immerse slides in 100% EtOH for 5minutes.
10. Immerse slides in 95% EtOH for 5minutes.
11. Immerse slides in 70% EtOH for 5minutes.
12. Immerse slides in distilled water for 5minutes.
13. Immerse slides in the freshly made silver nitrate working solution for 60 minutes and store the slides in the dark during this incubation.
14. After silver nitrate incubation, wash the slides three times with distilled water for 5 minutes each.
15. Incubate slides in 5% sodium thiosulfate for 10 minutes and perform three washes with distilled water for 5 minutes each at RT.
16. Following silver nitrate staining, counterstain the slides with cresyl violet working solution for 4-30 minutes.
17. Rinse the slides in distilled water and proceed to dehydrate the sections by incubating the slides in the EtOH gradient (70%, 95%, 100%, 100%) for 5-10 dips each.
18. Immerse slides in 100% Isopropyl alcohol for 5-10 dips.
19. Clear sections by immersing in Citrisolv solution three times each for 5 minutes.
20. Using a toluene/xylene-based permanent mounting-medium add a coverslip onto the slide and prepare it for microscopy.



## Protocol - Morphological Assessment of Osteocytic PLR via Dil/Phalloidin Stain (3D)

### Materials

1. 0.5 M Ethylenediaminetetraacetic Acid (EDTA)
2. Sucrose (10%, 15%, 20% and 30%) solutions prepared in 1X PBS
3. Normal Donkey Serum (NDS)
4. Bovine Serum Albumin (BSA)
5. Dil Stain: 1,1'-Dioctadecyl-3,3',3'-Tetramethylindocarbocyanine Perchlorate (Invitrogen)
6. Dimethyl sulfoxide (DMSO)
7. Alexa Fluor 488 Phalloidin (Invitrogen)
8. 4'-6-Diamidino-2-phenylindole (DAPI)
9. 2,2'-Thiodiethanol (TDE)
10. Frozen optimum cutting temperature (OCT) embedded sections
11. 48-well plate
12. Toluene/ formaldehyde-free nail polish
13. 4% PFA: Add 4g of paraformaldehyde (PFA) to solution containing 50 ml of water and 1ml of 1 M NaOH. Dissolve PFA by continuous stirring on a heating block set to 60°C. Add 10 mL of 10X PBS and allow the mixture to cool to RT. Adjust the pH to 7.4 with 1 M HCl and bring the volume to 100ml. Store 4% PFA aliquots at -20°C for several months and avoid using solution that is repeatedly frozen and thawed.
14. Blocking buffer (PBS/1%NDS/1%BSA): Dissolve 2.5µl Bovine Serum Albumin (BSA) and 2.5µl Normal Donkey Serum (NDS) in 200µl PBS.
15. Dil solution: Dissolve 100µM of Dil stain in 50% DMSO: 50% PBS.

16. Phalloidin solution: Dissolve 5 $\mu$ l of Alexa Fluor 488 Phalloidin stock solution in blocking buffer.
17. DAPI solution: Make 4 $\mu$ g/ml DAPI in 1X PBS.
18. Tissue clearing and mounting media: Prepare 10%, 25%, 50%, 95%, & 97% TDE in 1X PBS using the TDE stock.

## **Methods**

1. Dissect and clean bones of surrounding tissue, remove periosteum from surface of bones.
2. Fix bone samples by incubating in 4% PFA for 48 hours.
3. Rinse the fixed samples in 1X PBS to remove residual PFA and decalcify the bones in 0.5M EDTA for 2-4 weeks on shaker at 60 revolutions/ minute at RT. Change EDTA solution every 3-4 days.
4. Following decalcification, bones will be rinsed in PBS (three 60-minute washes at 4<sup>o</sup> C) to remove residual EDTA.
5. Cut off the ends of the bone and gently remove the bone marrow by flushing with PBS using a syringe and needle.
6. Wash samples in 1XPBS and subject them to a sucrose gradient (10%, 15%, 20%) described in steps 7-9 below.
7. Immerse samples in 15% sucrose solution for 15 minutes at RT.
8. Immerse samples in 20% sucrose solution for 15 minutes at RT.
9. Immerse samples in 30% sucrose solution overnight at 4<sup>o</sup>C
10. Following sucrose gradient, gently dab dry samples with tissue, ensuring no liquid remains in the marrow cavity, and proceed to frozen embedding.
11. Embed samples in OCT media as per standard protocol or as described in the Demineralized Murine Skeletal Histology section of this reference. Cut

40-100  $\mu\text{m}$  thick cryosections of the embedded bones either onto microscope slides or wells of a 48 well plate containing  $\sim 250 \mu\text{l}$  RT 1X PBS.

12. Rinse sections three times with 1X PBS for 5 minutes each until all OCT is removed.
13. Incubate the sections with the blocking buffer overnight at  $4^{\circ}\text{C}$  ( $\sim 50 \mu\text{l}$  per well) in parafilm sealed plate.
14. Rinse the slides in 1X PBS three times each for 5 minutes.
15. Incubate the slides with the Dil solution in the dark at  $4^{\circ}\text{C}$  for 1 week. This dye stains hydrophobic structures including cell membranes, which is why long staining time is required for diffusion throughout the LCN.
16. Rinse the slides in 1X PBS three times each for 5 minutes.
17. Incubate the slides in Phalloidin solution overnight at  $4^{\circ}\text{C}$  in parafilm sealed well plate. This dye stains the actin cytoskeleton.
18. Rinse the slides in 1X PBS three times each for 5 minutes.
19. Incubate the slides in DAPI solution at RT for 30 minutes to stain the osteocyte nuclei.
20. Rinse the slides in 1X PBS five times ( $\sim 250 \mu\text{l}$  per well).
21. For mounting the sections, conduct sequential incubations in TDE gradient solutions namely, 10% TDE, 25% TDE and 50% TDE in PBS. Each of these incubations are 2 hours long and performed at RT. Finally, incubate slides overnight at  $4^{\circ}\text{C}$  in 95% TDE solution in parafilm sealed well plate.
22. Place a drop ( $\sim 10\text{-}20 \mu\text{l}$ ) of 97% TDE onto slide (if slide mounted, wick away previous solution with kim wipe and place 97% TDE directly on tissue) and gently place section directly into drop with forceps, curled sections should

unroll in solution. Place cover slip and seal edges with toluene/formaldehyde free nail polish.

23. Image immediately or store slides in  $-20^{\circ}\text{C}$  for a few weeks.<sup>57</sup>

### Quantitative and Descriptive Parameters of the Osteocyte LCN

Given the broad range of parameters reported about the LCN in both two and three dimensions we suggest a standardization to the reporting of these details. A term representative of the whole LCN should be first supplied, i.e. “LCN area / bone area” in 2D and “LCN volume fraction” in 3D. Terms dissecting the differences of the osteocyte cell bodies or lacunae from the canaliculi are also ideal and include lacunar area (2D) and volume (3D), lacunar number densities (2D/3D), canalicular length (2D\*/3D), canalicular spacing (3D) and tortuosity (3D), and canaliculi per osteocyte or canalicular density. Standardized protocols for the collection for these parameters utilizing publicly available software (ImageJ/Fiji) or other commercially available image processing software (IMARIS) are provided below.

---

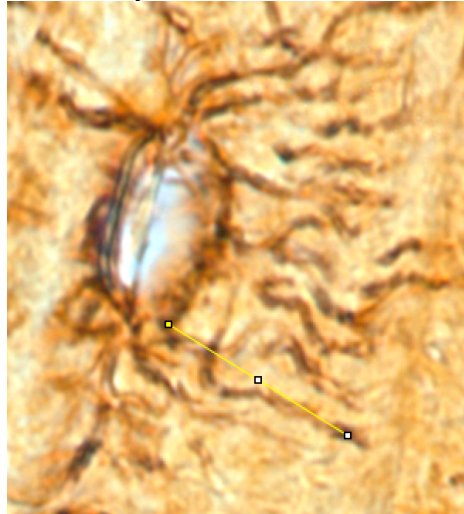
\* Canalicular Length in 2D can be misleading as canaliculi often bend in and out of the focal or cut plane of a traditionally prepared thin paraffin section (6-7  $\mu\text{m}$ ). Use of this term in 2D should be accompanied by the recognition that canaliculi are three dimensional structures and length in 2D does not accurately capture the full length of these features.

## Protocol - Canalicular Length (2D)

### Requires

- RGB image of the Osteocyte LCN via Silver Nitrate Staining
- Fiji (ImageJ)

- 1) Load Image into Fiji (can click and drag)
- 2) Set Scale
  - a. Use the line tool to trace the length of the scale bar
  - b. Analyze > Set Scale
- 3) Duplicate the Image so you can edit /track progress without altering the original image.
  - a. Shift + D or Image > Duplicate
- 4) Using the Line Tracer Tool start from the base of a canaliculi at the edge of the lacuna and extend straight outwards towards the tip/last discernable point of the continuous canaliculi
  - a. Hit "M" key to measure



- 5) Hit "Delete" key to delete the pixels underneath the line tracer
  - b. This helps keep track of which canaliculi you have already measured
  - c. Ensure you are working on the Duplicated copy, do NOT alter original image
- 6) Repeat steps 4-5 for
  - d. 10 canaliculi / cell
  - e. 3-5 cells per image
  - f. 3-4 images per mouse
- 7) Average ALL observations from above for a single (1) averaged biologic replicate
  - g. Collect 6-8 biologic replicates per group

## Protocol - LCN Area / Bone Area (2D)

### Requires


- RGB image of the Osteocyte LCN via Silver Nitrate Staining
  - Fiji (ImageJ)
- 1) Load image into FIJI (can click and drag)
  - 2) Convert from RGB image type to 8-Bit by splitting color channels
    - a. Image → Colors → Split Channels
    - b. Select which channel gives best nature contrast and detail in 8-Bit (usually Red)
    - c. Close unwanted color channels
  - 3) Background Subtraction
    - a. Process → Subtract Background
      - i. You can mess around with the “rolling ball radius”, depending on your feature size it will need to change. The default value is 50, 20 does a good job but can get too busy.
  - 4) Enhance Local Contrast
    - a. Process → Enhance Local Contrast (CLAHE)
  - 5) Convert to Binary Image
    - a. Process → Binary → Make Binary
      - i. **IFF** this inverts the expected B&W areas (i.e. lacuna are not white with black borders) you will need to invert the Look Up Table to create a negative image
      - ii. Image → Lookup Tables → Invert LUT\
  - 6) Set Scale Bar
    - a. Analyze → Set Scale
  - 7) Manually Section out and fill in Lacuna
    - a. When selecting Black or White, only use color selector from toolbar, don't try to select a black or white from a color palate.
    - b. Use paint brush tool to circle around lacuna in white to separate them from rest of network
    - c. Ensure that Lacuna borders are solid black (no pixel gaps) and fill in Black with paint can.
  - 8) Measure Lacunar Area
    - a. Analyze → Analyze Particles
      - i. Set a lower bound around 5-10 um to exclude small features
      - ii. Can set a larger bound to exclude obviously large features. Lacuna are usually within 20-60 um in area.
      - iii. Select Show “Outlines” in the drop down menu
      - iv. Check “Display Results”, “Summarize”, and “Exclude on Edges”
  - 9) Repeat steps 6-7 until you are satisfied with the results
    - a. Save results by copy-paste into excel or saving results as a .CSV file

## Protocol - Lacunar Number Density from 2D Fluorescent Tile Scans or Large Bone

### Sections

#### Requires:

- ImageJ
- Florescent Image of (large) bone cross section with osteocytes labeled. DAPI or other nuclear stain is appropriate.
  - Ensure that a scale bar is part of the image or know the pixel dimensions

- 1) Load color (RGB) image/file into ImageJ
  - 2) Set Scale
    - a. Use the line tool to trace the length of the scale bar
    - b. Analyze > Set Scale
  - 3) Remove Background
    - a. Process > Subtract Background
    - b. Rolling Ball Radius begin at 50 pixels, adjust smaller if needed
    - c. No other options should be selected in menu window
  - 4) Increase contrast
    - a. Shift + C or Image>Adjust>Brightness and Contrast
    - b. Adjust to bring cells out and remove tail end of background that's left
  - 5) Convert to 8-bit
    - a. Image > Type > 8-bit
  - 6) Invert image to for white background with grey bone/cells
    - a. Shift + I or Edit > Invert
  - 7) Clean Edges to remove soft tissue
    - a. Polygon Selection tool on tool bar
    - b. Click to Loop around soft tissue pieces and delete
- 
- 8) Despeckle Background
    - a. Process > Noise > Despeckle
  - 9) Save your Grey Scale Image
    - a. File > Save as... > Tiff...
  - 10) Measure Inner and Outer Area
    - a. Using the Polygon Selection tool, outline the endosteal circumference
    - b. Analyze > Measure or "M"
    - c. If "area" isn't recorded, go to "Analyze > set measurements" and select area as a portion
    - d. Repeat with periosteal circumference
    - e. Subtract inner area from outer area for full bone area
  - 11) Convert to Binary
    - a. Process > Binary > Make Binary
  - 12) Remove additional background if necessary
    - a. Process > Noise > Despeckle
    - b. Process > Binary > Erode
    - c. Use whatever methods you'd like to continue to clean up background
  - 13) Check size of cells
    - a. Zoom in until can loop a single cell with the polygon tool (Shift + "+")
    - b. Measure area of a few cells to get an idea of the range of sizes of cells
  - 14) Count Cells
    - a. Analyze > Measure Particles



- b. Set Upper and Lower Bounds from sizes from Step 13
  - c. Select Show Ellipses to view results
  - d. Select "Display Results", "Exclude on Edges", and "Summarize"
- 15) View the Ellipses Map results to validate if identifying cells correctly
- a. Adjust Upper and Lower Bounds and re-run Step 14 if necessary
- 16) Calculate Osteocyte Density
- a. Number of cells from Step 14 divided by Area from Step 10

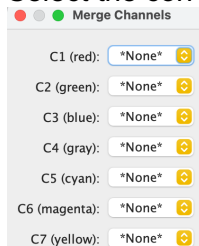
## Protocol - Whole Mount Image Processing to generate RGBs, 8-Bit, and Binary Images

(3D)

### Requires

- Independent color image stacks of LCN from Fluorescent Confocal Microscopy
  - If following the included whole mount protocol, this should be 3 separate image channels
    - Blue – Dapi
    - Green – Phalloidin
    - Red – Dil
- Fiji (ImageJ)


- 1) Click and drag each folder to open in Fiji as 1 color channel per image stack
  - a. If used the “Confocal Image File Sorter”<sup>\*</sup> python script to sort images from the Leica, the folders should correspond as:
    - ch00 – Dapi (Blue)
    - ch01 – Phalloidin (Green)
    - ch02 – Dil (Red)
  - b. Do NOT open as a “Virtual Stack” ensure this option is not selected during import
- 2) Remove Background
  - a. Process > Subtract Background
  - b. Rolling Ball Radius begin at 50 pixels, adjust smaller if needed
  - c. No other options should be selected in menu window
- 3) Increase contrast
  - a. Shift + C or Image>Adjust>Brightness and Contrast
  - b. Adjust to bring cells out and remove tail end of background that’s left
  - c. Complete this for each color channel, each color will have its own amount of adjusting that can be done
    - i. DAPI can be boosted the most since we are only using this to identify nuclei, Dil will only be able to be boosted some without saturating the image
- 4) Despeckle the DAPI channel **only**
  - a. Process > Noise > Despeckle
- 5) Merge the 3 channels into 1 overlaid image
  - a. Image > Color > Merge Channels...
  - b. Select the corresponding image stacks for their color i.e. C1 (red) – ch02 (Dil)

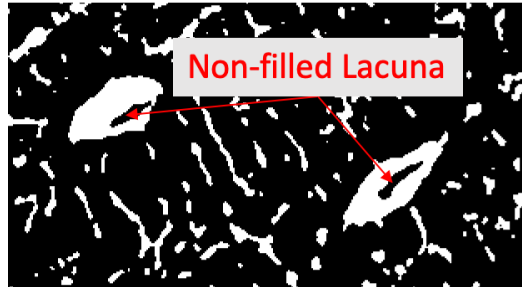


- c. Channels c4-C7 are not used to generate an RGB

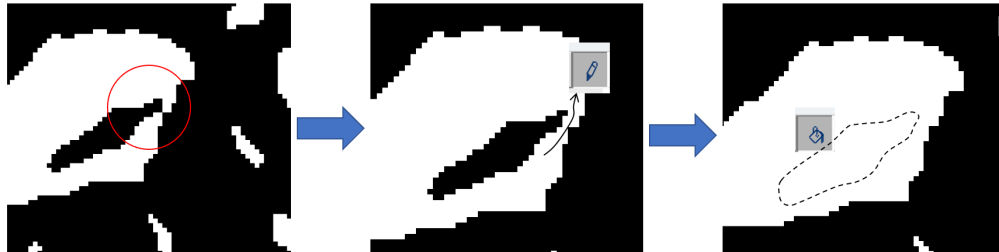
---

\* The python automated file sorter code can be found within the “Protocols” directory within the Alliston Lab Server

- d. Select “Make composite” and “Keep Sources Images”
- e. Images are not technically “merged” at this point, they are simply overlaid which allows us to still adjust each channel independently
- 6) View composite image and adjust color balance here if necessary
  - a. Image > Adjust > Color Balance
- 7) Convert to an RGB Color Image
  - a. Image > Type > RGB Color
  - b. Select “slices” to merge the entire stack
  - c. Select “Keep Source” to not lose the independent channels if desired
  - d. This step fuses all three of the overlaid “Merged” channels into one true RGB colored image
- 8) Remove excess background from merging
  - a. Process > Subtract Background
  - b. Process > Noise > Depseckle
- 9) Save this image as your composite RGB within the directory the original image channels came from
  - a. File > Save as... > Image Sequence
  - b. Feel free to close any excess windows you still have open (channels, merged, etc..) before moving on ONCE you have saved the RGB
- 10) Convert the RGB into a grey scale 8-bit image
  - a. Image > Type > 8 bit
- 11) Adjust Brightness and Contrast if Desired
  - a. Shift + C or Image > Adjust > Brightness/Contrast
  - b. If adjusting be careful to not increase the brightness and boost background noise
  - c. If removing background at this step by moving lower bound, only do so by 2-3 steps, many smaller features of the LCN at this level are close to “noise”
- 12) Save this version as your 8-bit/Grey Scale Image
  - a. File > Save as... > Image Sequence
- 13) Convert to Binary
  - a. Image > Adjust > Auto Local Threshold
    - i. Use the “Otsu” thresholding method
    - ii. Try a radius of 15 to start, adjust from here as necessary
    - iii. Select “White objects on a black background”
    - iv. Select “Stack”
    - v. Hit “Ok” to start the run, this may take several seconds or minutes as each stack will be thresholded individually
- 14) Reduce noise if necessary
  - a. Process > Noise > Despeckle
- 15) Manually ‘fill’ any lacuna that are not fully white
  - a. Use the paint brush or paint can tools , fill in any black portions of obvious lacuna with white (you will need to step through adjacent layers 1 at a time, you can do this with the sideways arrow keys on your keyboard



- b. Use care when using the paint can tool, if ANY internal pixels are touching **even a single pixel diagonally** to the outer black edge Fiji considers them continuous features and the entire image will become white. Use the paintbrush, pen, or pencil tools in white to sever this connection before using the paint can



- i. You can undo errors with Edit > Undo or Ctrl+Z

16) Save image as Binary version

- a. File > Save as... > Image Sequence

## Protocol - LCN Volume Fraction (3D)

### Requires

- Binary 3D stack image of LCN
  - BoneJ Plug-in for Fiji
- 1) Open Binary Image Stack of the LCN
    - a. Click and drag folder containing your binary image into Fiji bar
  - 2) Set Scale
    - a. Use the line tool to trace the length of the scale bar
    - b. Analyze > Set Scale
      - i. If you have collected your images from the Leica at 100x, the pixel scale is **6.8 pixels/micron**
  - 3) Use BoneJ to calculate Volume Fraction
    - a. Plugins > BoneJ > Fraction > Area/Volume Fraction
    - b. Results should appear in the BoneJ table pop-up, can copy and paste into Excel from here or other record
    - c. BV and TV results may be given in inches<sup>3</sup>, ignore and record "BV/TV"

BoneJ assumes you are analyzing trabecula and thus gives BV/TV results, simply ignore and record as the LCN volume fraction

## Protocol - Canalicular Spacing (3D)

### Requires

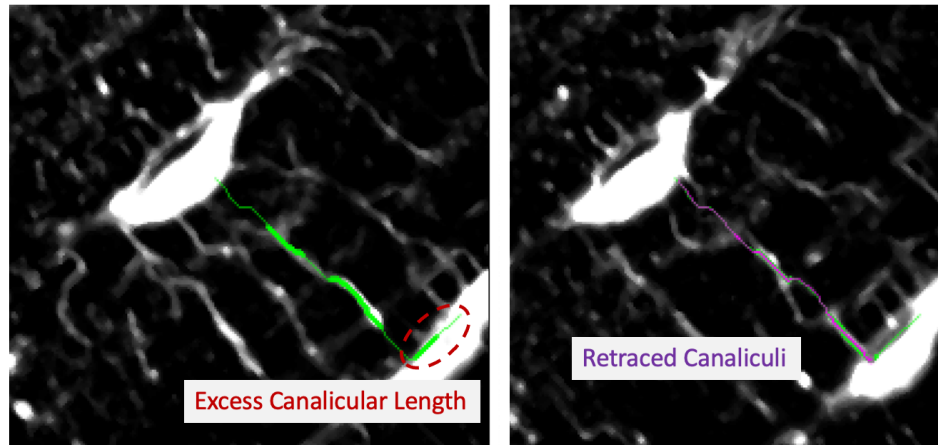
- Binary 3D stack image of LCN
  - BoneJ Plug-in for Fiji
- 1) Open Binary Image Stack of the LCN
    - a. Click and drag folder containing your binary image into Fiji bar
  - 2) Set Scale
    - a. Use the line tool to trace the length of the scale bar
    - b. Analyze > Set Scale
      - i. If you have collected your images from the Leica at 100x, the pixel scale is **6.8 pixels/micron**
  - 3) Use BoneJ to calculate average canalicular spacing
    - a. Plugins > BoneJ > Thickness
    - b. If asked about anisotropy, ignore and continue
    - c. Select “Both” to analyse both thickness and spacing (sometimes the plugin will confuse which is which so just run both)
    - d. Select “show thickness map” and “mask thickness map” to identify which parameter you want to keep later
      - i. The “mask thickness” should be the image for the spacings and should be name Tb\_Sp when generated
      - ii. Bonej assumes we are working with uCT of trabecula so just rename to Canalicular Spacing
    - e. To clear the BoneJ table if it becomes too crowded
      - i. Pluginns > Bonej > Table > Clear Bonej results

## Protocol - Canalicular Tortuosity (3D)

### Requires

- 8bit 3D stack image of LCN
- Neuroanatomy Plugin for Fiji

- 1) Open 8-bit Image Stack of the LCN
  - a. Click and drag folder containing your 8-bit image into Fiji bar
- 2) Launch the Simple Nuerite Tracer (SNT)
  - a. Plugins > Neuroanatomy > SNT...
- 3) Set defaults
  - a. 3D tab, Viewer > New with Image > Apply
    - i. 2 for resampling factor is fine for observation, 1 does not resample so higher canalicular resolution but more noise
  - b. Main tab, filters for visibility of paths (2) Only nodes within 2 nearby Z-slices
- 4) Begin tracing single canaliculi
  - a. Start by clicking on one lacuna and then a neighboring one to begin tracing
  - b. When finished, click "Finish" to save trace
- 5) Trim excess length
  - a. Once a trace has been made and accepted, start another trace on top of the original at the point where it begins to **EXIT** the cell of origin and terminate it once it **ENTERS** the lacunar boarder of the terminal cell



- b. Delete the old trace from the 'Path Manager' (right click menu, delete)
- 6) Trace and measure single connections from every osteocyte within the image to its nearest neighbor (if possible).
    - a. Generally aiming for ~20 connections per image, can do more
    - b. If not enough cells, you can manually measure multiple connections between the same cells
      - i. Since the SNT will always search for the shortest path you may likely retrace a connection you have already made. To manually create new paths between previously connected cells, you can build unique paths step-wise. Start down a new canaliculi identified by eye a short distance,. After a segment of a path is created you can continue to build off of it if you do not select "Finish" and instead click "Yes" after asked for "Keep new segment?". Continue to build the new path in small manageable

lengths until you have completed the new path, then select "Finish" to save

- 7) Periodically save your traced connections as traces files
  - a. File > Export as > TRACES
  - b. Save into the directory with your processed image folders
  - c. The tracing process can take some time, this lets you pause and save your progress, it can also bug and crash since its Fiji so ALWAYS save your progress
- 8) When you are done, export your data
  - a. Analysis > Path Properties: Export CSV
  - b. Save these spreadsheets, they are the raw numeric data
- 9) Calculate Average Tortuosity
  - a. Open .CSV in excel
  - b. Calculate end-to-end Euclidian Distance for each path/row in spread sheet
$$d = \sqrt{(x_1 - x_2)^2 + (y_1 - y_2)^2 + (z_1 - z_2)^2}$$
  - c. Tortuosity ( $\tau$ ) = total path length / Euclidian Distance
  - d. The average of paths from 3 (or more) ROI's (stacks) per mouse (50-60 paths) is 1 biologic replicate
  - e. Collect 5-6 biologic replicates / group



## Protocol - Canalliculi per Osteocyte (3D)

### Requires

- Independent color image stack of LCN from Fluorescent Confocal Microscopy
    - Use best quality channel of the canalliculi that you have usually:
      - Green – Phalloidin
      - Red – Dil
  - IMARIS (v9.5.1)
- 1) Convert file stack into IMARIS file with IMARIS Image Converter software
  - 2) In IMARIS 9.5.1 change to scene mode and 'Add Image' from File > Open (Fig.6A)
  - 3) Background subtract the image using the Imaris Image Processing sub-menu.
  - 4) Using the membrane dye (Dil, red, **Fig.3.6A**) channel as a template, create an Imaris 'surface' object of the osteocyte cell bodies within the imaged region (**Fig. 3.6B**).
    - a. Use the "Slice" sub menu to measure how large the long axis of one osteocyte cell body is, use this value as the pixel dimension for background subtracting within the surface creation wizard
    - b. Remove small features with the size exclusion filter to prevent canalicular dendrites from being included in the cell body surface object
    - c. Add an additional filter "distance from axis XYZ" to remove objects touching the boundaries of the volume (**Fig. 3.6C**).
  - 5) Complete a distance transformation around the new osteocyte surface objects (**Fig. 3.6D**)
    - a. This requires an installed Matlab XTensions attainable online\*
    - b. When installed will be found in the "Tools" submenu when a surface is selected/highlighted (Gear Wheel)
    - c. Complete it "outside" the surface object to create a channel encoding the radial distances in 3D from the surface of each cell's unique topography
  - 6) Generate a new surface object encompassing only a single cell (**Fig. 3.6E**)
    - a. Set the background subtraction size close to the width of the canalliculi as measured from the "slice" menu
    - b. This creates a new surface of the cell along with canalliculi (**Fig. 3.6F**)
  - 7) Use this new surface as a mask to generate a second new channel of only the signal from the original image belong to the segmented cell (**Fig. 3.6G**)
    - a. Click the 'pencil' submenu when the surface is selected as select "Mask"
    - b. Set source at the original image
    - c. Set pixels outside to zero
  - 8) Open the Imaris Colocalization sub-menu to identify canalicular portions at set distances from the cell body
    - a. Set channel 1 as the newly segmented channel of a single cell and its associated canalliculi
    - b. Set channel 2 as the distance transform channel
    - c. In the upper right, change the selection mode to "Polygon"

---

\* <https://imaris.oxinst.com/learning/view/article/distance-transformation>

- d. Click and drag selected polygon to capture the portion of signal you would like to keep. Portions within the polygon region will appear as highlighted in white on the screen (**Fig. 3.6H**)
  - i. It can be easier to select specific portions of signal along the edges of the selection window by changing the polygon shape into a triangle with a thin point, and then sliding the point up and down the edge of the region where there is signal to position your segmented area directly at the edge of the cell (**Fig. 3.6I**)
- 9) Set the distance to the canalicular surface as close to the cell membrane as possible and then select “Generate Colocalization Channel” to create a new channel containing signal from only the canalicular sprouting regions
  - a. In order to prevent undercounting from merging of signal from adjacent canaliculi, signal from the cell membrane may be removed prior to attempting colocalization (**Fig. 3.6J**).
    - i. Use the initial “Cells” surface from step 4 to create a mask on top of the segmented cellular channel. Set voxels **inside** to zero. This creates a channel of only canalicular signal. Use this within the colocalization tool instead of the version containing the cell membrane. This will allow you to set your colocalization point to the exact edge of the sprouting region without merging adjacent canaliculi (**Fig. 3.6K**)
- 10) Return to the 3D viewing menu to visualize sprouting regions in 3D with the cell body surface model to ensure features have been captured in all dimensions (**Fig. 3.6L**).
- 11) Create a final new surface object this time using the new colocalization channel as the source image. (**Fig. 3.6M**)
  - a. Use the size exclusion step of the surface creation wizard to remove small features less than 3-4 pixels.
  - b. When the new surface is finalized, highlight it and navigate to its statistics sub - menu (bottom left, graph icon) and record the number of individual objects. This is the number of canalicular sprouts for that single analyzed cell
- 12) Repeat this process, steps 6-11, for 3-5 cells within your image.
- 13) Analyze as much as 10 individual cells from across 2-3 volumes from a single animal. This number averaged is considered 1 biologic replicate.
- 14) Collect data from 5-8 N / group

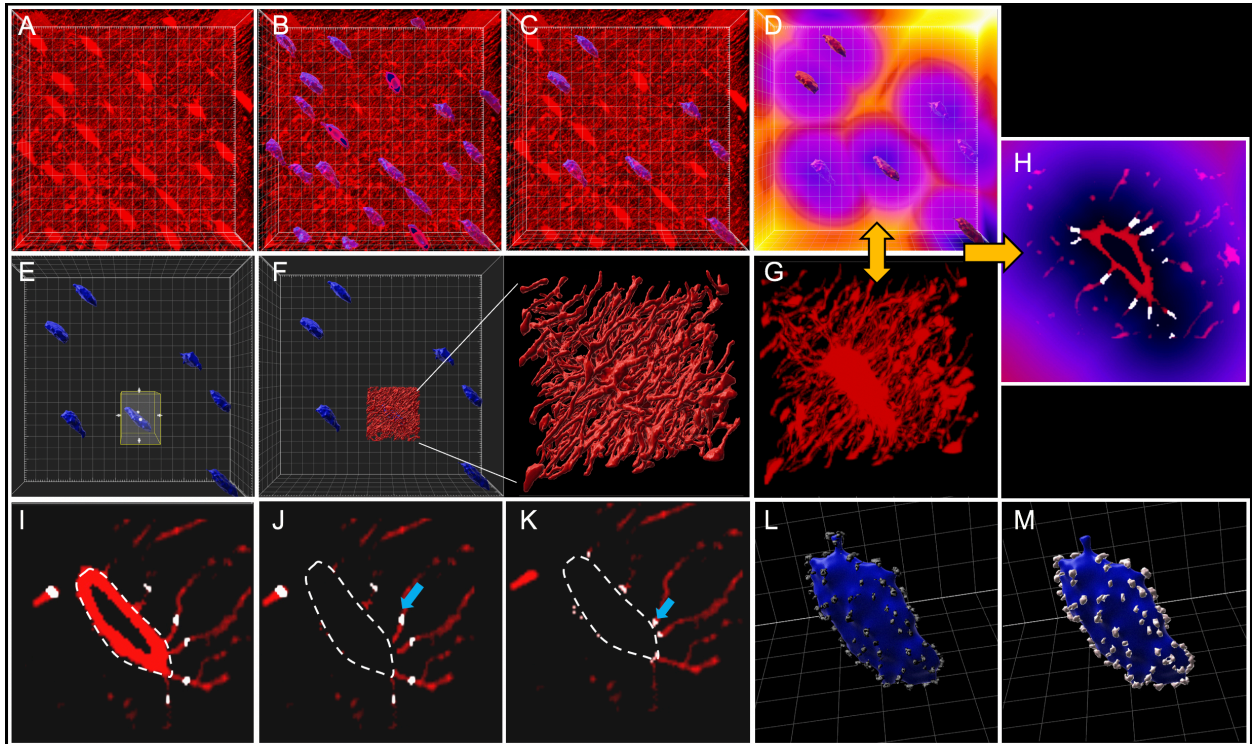


**Figure 3.6: Canalicular Dendrite Segmentation and Quantification at the Sprouting Point via IMARIS** A) Background subtracted 3D construction of Dil (red) florescent staining of the osteocyte network in Imaris. B) Identification and surface renderings of osteocyte cell bodies (blue) by size filtering smaller volume canalicular features. C) Cells intersecting the image boundaries are removed from the cellular surface models. D) Distance Transformation generates a map defining regular distances from the cellular surface models. E) An ROI around a single osteocyte is defined to create a surface model of an osteocyte and its associated dendrites in 3D (F). G) Raw fluorescent signal segmented from the larger image using the single cell surface model as a mask. H) Overlap of single cell fluorescent signal and the Distance Transformation map within the Imaris Colocalization Tool identifies canalicular signal (white) at uniform distances from the cellular surface. Identification (I) and removal (J) of the cell body (white dashed line) florescent signal from the canalicular signal channel (G) prevents merging of signal from adjacent canaliculi within the Colocalization tool when the distance along the canalicular regions is constricted from an arbitrary distance away from the cell surface (J, blue arrow) to the direct location of canalicular sprouting at the cell surface (K, blue arrow). (L) Segmented canalicular signal (grey) from sprouting points is visualized in 3D along the cell surface (blue), size filtered to remove small and large aberrations, and rendered as 3D surfaces (M) for quantification of canalicular dendrite sprouts per single osteocytes.

## V - Evaluation of the Bone Extracellular Matrix

PLR plays a critical role in maintaining bone quality, at least in part through its effects on the organic and mineral components of the bone extracellular matrix<sup>105</sup>. The unique physical features of collagen and mineral afford opportunities to monitor their composition and organization in bone and how they are affected by PLR induction or suppression.

*Organic Extracellular Matrix:* Observation of collagen organization provides clues to osteocytic action. Collagen birefringence is a property that can be assessed using polarized light microscopy because of collagen's naturally ordered structure. Staining with picosirius red, an anionic dye that binds to cationic collagen fibers, enhances this birefringence under polarized light<sup>106,107</sup>. Using this technique, we and others find that PLR suppression due to MMP-deficiency, glucocorticoid treatment, or aging<sup>29,40</sup> disrupts the normally aligned lamellar arrangement of collagen. In some but not all cases, PLR suppression in mouse models or in human disease correlates with reduced collagen alignment and reduced bone quality<sup>37</sup>. Indeed, these changes in collagen organization with PLR suppression are apparent even in situations where remodeling by osteoclasts and osteoblast is sufficiently intact to retain normal bone mass. The causal relationship between PLR and collagen organization remains an area of active investigation.

*Mineralized Extracellular Matrix:* Osteocytes also actively engage in the management of mineral. Mineral resorption by osteocytes has been confirmed in studies of lactation, PTH treatment or regulation, and in disease models such as chronic kidney disease, Vitamin D deficiency, and hypophosphatemia<sup>16,33,35,108</sup>. While several enzymes are thought to be active in the process of mineral regulation, most evidence of lacunar resorption focuses on the idea that osteocytes dynamically regulate the pH within the perilacunar fluid between the cell membrane and the bone mineral surface to exert control over the mineral environment<sup>30</sup>. In addition, multiple imaging techniques reveal enlarged osteocyte lacunar size during resorption events (i.e. lactation) and lower bone mineral density. These effects are rapidly reversed once resorption pressure is lifted (i.e. weaning), implying osteocyte-specific deposition of mineral<sup>30</sup>.

*In vivo* administration of small fluorescent molecules that associate into depositing bone has long been used for spatiotemporal visualization of bone mineralization at periosteal and endosteal surfaces. Fluorescent labels also confirm osteocytes' ability to participate in bone formation<sup>26</sup>. Double fluorochrome labeling has been a useful approach to assess the dynamics of bone formation by osteoblasts and the calculation of the bone formation rate<sup>16,57,66</sup>. However, the timing of fluorochrome administration has yet to be optimized for the reproducible visualization of osteocyte-specific mineral deposition in homeostatic PLR. For example, fluorescent labeling in post-lactating mice show osteocyte-specific deposition of mineral<sup>16</sup>; however, virgin and non-lactating controls did not show double labelling. These findings imply that lactation represents a significant change to osteocyte remodeling behavior and not homeostatic PLR, and that this technique may not yet be optimized to observe homeostatic changes in matrix deposition and resorption, which may be more rapid or subtle.

Other methods that have been used to observe the mineralization state around lacuna and osteocyte canaliculi<sup>16,35</sup> include X-ray computed tomography imaging, X-ray diffraction and absorption, and several forms of electron microscopy. These methods rely on differing attenuation of signal from radiation sources by the different elemental constituents within the bone. Changes in the mineralization of the perilacunar and pericanalicular bone matrix indirectly give important insight into osteocyte function. Nonetheless, these methods are insensitive to changes in cells or matrix that occur only in the organic phase. Care must be taken to integrate information derived from radiographic approaches with that derived from cellular and histological outcomes.

X-ray based imaging is the most common method used to observe changes in the mineralized portions of bone due to its high energy and very low wavelengths. Micro-computed tomography ( $\mu$ CT) scanners with voxel sizes of a few microns can identify osteocyte lacunae. More advanced  $\mu$ CT imaging is beginning to push the resolution of these techniques from the microscale (500 nm) into the nanoscale (50 nm)<sup>12,109</sup>, which is needed to resolve individual

canaliculi (200-350 nm). These nanoscale approaches are for small specimens (16  $\mu\text{m}^2$  field of view). Synchrotron radiation Micro-Tomography (SR $\mu$ T) techniques can reliably capture larger segments of the LCN (40  $\text{mm}^2$ ) and provide qualitative and quantitative outcomes of matrix mineralization and lacunar size and shape<sup>37,67</sup>. The best SR $\mu$ T beamlines can resolve detail down to the canalicular level (30-40 nm with a field of view of as much as 75-80  $\mu\text{m}^2$ )<sup>110</sup>. However, these SR $\mu$ T approaches are time consuming, computationally intensive, and require specialized use of synchrotron light sources not accessible to all researchers<sup>39,103,104</sup>. Especially since access to these resources is limited, we advocate adoption of online digital data-sharing practices to make these valuable and large SR $\mu$ T datasets publicly available through established repositories including the Materials Data Repository hosted by National Institute of Standards and Technology (NIST), or other third-party repositories i.e. TomoBank<sup>111</sup>. This approach would expand access to any investigator to develop and apply new analytical tools to answer the many remaining questions about PLR.

Several other specialized Electron Microscopy and X-Ray techniques have also been used to study the osteocyte LCN. Some of these include ptychographic X-ray CT, transmission X-ray microscopy CT, serial-focused ion beam SEM (serial FIB SEM), serial block-face SEM (SBF SEM), back scatter SEM, surface relief (acid etching) SEM, and others as extensively reviewed elsewhere<sup>34,39,70,112,113</sup>. Even as the field advances through application of these approaches, additional investigation is needed to understand how changes in these imaging parameters relate to changes in the cellular function of osteocytes at homeostasis, in metabolic stress, and in disease.

## VI - Future Directions

Answering the many questions about osteocytic perilacunar/pericanalicular bone remodeling will require the systematic and integrated application of approaches described here, as well as new and more sophisticated *in vivo* and *in vitro* outcomes. In particular, additional research is needed to elucidate the cellular mechanisms responsible for morphological changes that are apparent using histologic and radiographic approaches. Such studies may reveal distinct functional roles for perilacunar vs pericanalicular remodeling, peri-osteocytic acidification vs proteolysis, or remodeling of the mineral vs organic phases of the peri-osteocytic bone matrix.

Improvements to current methods that could be particularly helpful include robust algorithms to facilitate efficient and quantitative analysis of the LCN in 2D and in 3D. Though many groups have worked intensively to achieve automated detection and quantification of the LCN, this goal remains elusive at this time. Standardized use of common LCN parameters would facilitate comparison across studies.

Continued advances in imaging will provide a critical foundation for asking more mechanistic questions. This includes more widespread availability of  $\mu$ CT with nanometer length scale resolution, so that lacunar and canalicular networks can be visualized and quantified across larger fields of view. Utilization of fluorescent stains, reporter proteins<sup>114</sup>, and immunofluorescence, along with specimen clearing and advanced microscopy, would improve our ability to relate structural features to important biological outcomes. Approaches to monitor pH at high spatiotemporal resolution *in vivo* and *in vitro* would complement current outcomes. These approaches could be applied to discern cellular or molecular changes *in vivo* upon PLR induction and suppression, particularly in the presence of gain and loss of function perturbations, or disease-inducing or resolving interventions.

Finally, application of unbiased approaches such as RNAseq and mass spectrometry may be helpful in the identification of specific new RNA or serum markers of PLR. An ideal marker

would be osteocyte-specific, have a functional role in matrix remodeling, and be dynamically regulated with PLR. Not only would these markers improve the precision of research efforts to understand PLR, but they could also support the identification of new diagnostics of skeletal disease or therapeutic interventions to prevent it. Given the role of PLR in skeletal metabolism, bone fragility, joint disease, and aging, our collective efforts to better understand osteocytic remodeling could have significant clinical impact.

\* Protocols discussed and outlined herein may be found at the Alliston Laboratory website:  
<https://allistonlab.ucsf.edu>



## References:

1. Yee, C. S., Schurman, C. A., White, C. R. & Alliston, T. Investigating Osteocytic Perilacunar/Canalicular Remodeling. *Curr Osteoporos Rep* 17, 157–168 (2019).
2. Dole, N. S., Yee, C. S., Schurman, C. A., Dallas, S. L. & Alliston, T. Assessment of Osteocytes: Techniques for Studying Morphological and Molecular Changes Associated with Perilacunar/Canalicular Remodeling of the Bone Matrix. *Methods Mol Biol* 2230, 303–323 (2021).
3. Bonewald, L. F. The amazing osteocyte. *Journal of Bone and Mineral Research* 26, 229–238 (2011).
4. Dallas, S. L., Prideaux, M. & Bonewald, L. F. The Osteocyte: An Endocrine Cell ... and More. *Endocr Rev* 34, 658–690 (2013).
5. Buenzli, P. R. & Sims, N. A. Quantifying the osteocyte network in the human skeleton. *Bone* 75, 144–150 (2015).
6. Anna, T. & Alberta, Z. Do osteocytes contribute to bone mineral homeostasis? Osteocytic osteolysis revisited. *Bone* 44, 11–16 (2009).
7. Wang, L. *et al.* In situ measurement of solute transport in the bone lacunar-canalicular system. *P Natl Acad Sci Usa* 102, 11911–11916 (2005).
8. Klein-Nulend, J., Bakker, A. D., Bacabac, R. G., Vatsa, A. & Weinbaum, S. Mechanosensation and transduction in osteocytes. *Bone* 54, 182–190 (2013).
9. Asagiri, M. & Takayanagi, H. The molecular understanding of osteoclast differentiation. *Bone* 40, 251–264 (2007).
10. TAKAYANAGI, H. The Role of NFAT in Osteoclast Formation. *Ann Ny Acad Sci* 1116, 227–237 (2007).
11. Baron, R. & Kneissel, M. WNT signaling in bone homeostasis and disease: from human mutations to treatments. *Nat Med* 19, 179–192 (2013).

12. Hove, R. P. van *et al.* Osteocyte morphology in human tibiae of different bone pathologies with different bone mineral density — Is there a role for mechanosensing? *Bone* 45, 321–329 (2009).
13. Tsourdi, E., Jähn, K., Rauner, M., Busse, B. & Bonewald, L. F. Physiological and pathological osteocytic osteolysis. *J Musculoskel Neuron* 18, 292–303 (2018).
14. Qing, H. & Bonewald, L. F. Osteocyte remodeling of the perilacunar and pericanalicular matrix. *International Journal of Oral Science* 1, 59–65 (2009).
15. Wysolmerski, J. J. Osteocytic osteolysis: time for a second look? *Bonekey Reports* 1, 229 (2012).
16. Qing, H. *et al.* Demonstration of osteocytic perilacunar/canalicular remodeling in mice during lactation. *J. Bone Miner. Res.* 27, 1018–1029 (2012).
17. Komori, T. Functions of the osteocyte network in the regulation of bone mass. *Cell Tissue Res* 352, 191–198 (2013).
18. Belanger, L. F. Osteocytic osteolysis. *Calcified tissue research* 4, 1–12 (1969).
19. Jande, S. S. & Bélanger, L. F. Electron microscopy of osteocytes and the pericellular matrix in rat trabecular bone. *Calc Tiss Res* 6, 280–289 (1970).
20. Bonewald, L. F. Osteocytes as Dynamic Multifunctional Cells. *Ann Ny Acad Sci* 1116, 281–290 (2007).
21. McGee-Lawrence, M. E., Carey, H. V. & Donahue, S. W. Mammalian hibernation as a model of disuse osteoporosis: the effects of physical inactivity on bone metabolism, structure, and strength. *Am J Physiology-regulatory Integr Comp Physiology* 295, R1999–R2014 (2008).
22. A., R. & W., V. Recherches experimentales sur la formation ducal et sur les modifications des tissus dans les pseudarthroses. *Archives of Physiology* 1881;Ser. II:419–58 (1881).
23. CA., B. Morphology and inframicroscopic structure of osteocytes. *Acta anatomica* 51:209–25 (1962).

24. Recklinghausen, F. von. *Untersuchungen über Rachitis und Osteomalacie*. (Jena, Fischer, 1910).
25. Tazawa, K. *et al.* Osteocytic osteolysis observed in rats to which parathyroid hormone was continuously administered. *J Bone Miner Metab* 22, 524–529 (2004).
26. Baylink, D. & Wergedal, J. Bone formation by osteocytes. *Am J Physiology-legacy Content* 221, 669–678 (1971).
27. Steinberg, B., Singh, I. J. & Mitchell, O. G. The effects of cold-stress, hibernation, and prolonged inactivity on bone dynamics in the golden hamster, *Mesocricetus auratus*. *J Morphol* 167, 43–51 (1981).
28. Inoue, K. *et al.* A crucial role for matrix metalloproteinase 2 in osteocytic canalicular formation and bone metabolism. *J. Biol. Chem.* 281, 33814–33824 (2006).
29. Tang, S., Herber, R. P., Ho, S. & Alliston, T. Matrix metalloproteinase-13 is required for osteocytic perilacunar remodeling and maintains bone fracture resistance. *Journal of Bone and Mineral Research* 27, 1936–1950 (2012).
30. Jahn, K. *et al.* Osteocytes Acidify Their Microenvironment in Response to PTHrP In Vitro and in Lactating Mice In Vivo. *Journal of Bone and Mineral Research* 32, 1761–1772 (2017).
31. Lotinun, S. *et al.* Cathepsin K-deficient osteocytes prevent lactation-induced bone loss and parathyroid hormone suppression. *J Clin Investigation* 130, 3058–3071 (2019).
32. Holmbeck, K. *et al.* The metalloproteinase MT1-MMP is required for normal development and maintenance of osteocyte processes in bone. *Journal of cell science* 118, 147–156 (2005).
33. Tokarz, D. *et al.* Hormonal Regulation of Osteocyte Perilacunar and Canalicular Remodeling in the Hyp Mouse Model of X-Linked Hypophosphatemia. *Journal of Bone and Mineral Research* 33, 499–509 (2017).

34. Kaya, S. *et al.* Lactation-Induced Changes in the Volume of Osteocyte Lacunar-Canalicular Space Alter Mechanical Properties in Cortical Bone Tissue. *Journal of Bone and Mineral Research* 32, 688–697 (2017).
35. Rolvien, T. *et al.* Vitamin D regulates osteocyte survival and perilacunar remodeling in human and murine bone. *Bone* 103, 78–87 (2017).
36. M., K. *et al.* Sclerostin regulates release of bone mineral by osteocytes by induction of carbonic anhydrase 2. *J Bone Miner Res* 28, 2436–48 (2013).
37. Dole, N. S. *et al.* Osteocyte-Intrinsic TGF- $\beta$  Signaling Regulates Bone Quality through Perilacunar/Canalicular Remodeling. *Cell Rep* 21, 2585–2596 (2017).
38. Alemi, A. S. *et al.* Glucocorticoids cause mandibular bone fragility and suppress osteocyte perilacunar-canalicular remodeling. *Bone Reports* 9, 145–153 (2018).
39. Ciani, A. *et al.* Ptychographic X-ray CT characterization of the osteocyte lacuno-canalicular network in a male rat's glucocorticoid induced osteoporosis model. *Bone Reports* 9, 122–131 (2018).
40. Fowler, T. W. *et al.* Glucocorticoid suppression of osteocyte perilacunar remodeling is associated with subchondral bone degeneration in osteonecrosis. *Sci Rep* 7, 44618 (2017).
41. E, L., Nancy *et al.* Glucocorticoid-treated mice have localized changes in trabecular bone material properties and osteocyte lacunar size that are not observed in placebo-treated or estrogen-deficient mice. *J. Bone Miner. Res.* 21, 466–476 (2006).
42. Busse, B. *et al.* Vitamin D Deficiency Induces Early Signs of Aging in Human Bone, Increasing the Risk of Fracture. *Sci Transl Med* 5, 193ra88-193ra88 (2013).
43. Sharma, D. *et al.* Alterations in the osteocyte lacunar–canalicular microenvironment due to estrogen deficiency. *Bone* 51, 488–497 (2012).
44. Kafantari, H., Kounadi, E., Fatouros, M., Milonakis, M. & Tzaphlidou, M. Structural alterations in rat skin and bone collagen fibrils induced by ovariectomy. *Bone* 26, 349–353 (2000).

45. Ciani, C., Sharma, D., Doty, S. B. & Fritton, S. P. Ovariectomy enhances mechanical load-induced solute transport around osteocytes in rat cancellous bone. *Bone* 59, 229–234 (2014).
46. Sharma, D. *et al.* The effects of estrogen deficiency on cortical bone microporosity and mineralization. *Bone* 110, 1–10 (2018).
47. Gatti, V., Azoulay, E. M. & Fritton, S. P. Microstructural changes associated with osteoporosis negatively affect loading-induced fluid flow around osteocytes in cortical bone. *J Biomech* 66, 127–136 (2018).
48. Divieti, P. *et al.* Receptors for the Carboxyl-Terminal Region of PTH(1–84) Are Highly Expressed in Osteocytic Cells\*\*This work was supported by the NIH Grant DK-11794. *Endocrinology* 142, 916–925 (2001).
49. Nguyen, J., Tang, S. Y., Nguyen, D. & Alliston, T. Load Regulates Bone Formation and Sclerostin Expression through a TGFbeta-Dependent Mechanism. *PLoS ONE* 8, e53813 (2013).
50. Robling, A. G. *et al.* Mechanical stimulation of bone in vivo reduces osteocyte expression of Sost/sclerostin. *J. Biol. Chem.* 283, 5866–5875 (2008).
51. Blaber, E. A. *et al.* Microgravity Induces Pelvic Bone Loss through Osteoclastic Activity, Osteocytic Osteolysis, and Osteoblastic Cell Cycle Inhibition by CDKN1a/p21. *Plos One* 8, e61372 (2013).
52. Bach-Gansmo, F. L., Wittig, N. K., Brüel, A., Thomsen, J. S. & Birkedal, H. Immobilization and long-term recovery results in large changes in bone structure and strength but no corresponding alterations of osteocyte lacunar properties. *Bone* 91, 139–147 (2016).
53. Zhang, D. *et al.* Retention of osteocytic micromorphology by sclerostin antibody in a concurrent ovariectomy and functional disuse model. *Ann Ny Acad Sci* 1442, 91–103 (2019).
54. Dole, N. S., Yee, C. S., Mazur, C. M., Acevedo, C. & Alliston, T. TGFβ regulation of perilacunar/canalicular remodeling is sexually dimorphic. *J Bone Mineral Res Official J Am Soc Bone Mineral Res* (2020) doi:10.1002/jbmr.4023.

55. Vijayan, V. & Gupta, S. Role of osteocytes in mediating bone mineralization during hyperhomocysteinemia. *J Endocrinol* 233, 243–255 (2017).
56. Kerschnitzki, M. *et al.* The organization of the osteocyte network mirrors the extracellular matrix orientation in bone. *J Struct Biol* 173, 303–311 (2011).
57. Tiede-Lewis, L. M. *et al.* Degeneration of the osteocyte network in the C57BL/6 mouse model of aging. *Aging* 9, 2190–2208 (2017).
58. Busse, B. *et al.* Decrease in the osteocyte lacunar density accompanied by hypermineralized lacunar occlusion reveals failure and delay of remodeling in aged human bone. *Aging Cell* 9, 1065–1075 (2010).
59. Kobayashi, K. *et al.* Mitochondrial superoxide in osteocytes perturbs canalicular networks in the setting of age-related osteoporosis. *Sci Rep* 5, 576 (2015).
60. Jilka, R. L. & O'Brien, C. A. The Role of Osteocytes in Age-Related Bone Loss. *Curr Osteoporos Rep* 14, 16–25 (2016).
61. Farr, J. N. *et al.* Targeting cellular senescence prevents age-related bone loss in mice. *Nat Med* 23, 1072–1079 (2017).
62. Heveran, C. M., Rauff, A., King, K. B., Carpenter, R. D. & Ferguson, V. L. A new open-source tool for measuring 3D osteocyte lacunar geometries from confocal laser scanning microscopy reveals age-related changes to lacunar size and shape in cortical mouse bone. *Bone* 110, 115–127 (2018).
63. Carter, Y., Thomas, C. D. L., Clement, J. G. & Cooper, D. M. L. Femoral osteocyte lacunar density, volume and morphology in women across the lifespan. *J Struct Biol* 183, 519–526 (2013).
64. Weinstein, R. S. Glucocorticoid-Induced Osteoporosis and Osteonecrosis. *Endocrin Metab Clin* 41, 595–611 (2012).
65. Bach-Gansmo, F. L., Irvine, S. C., Brüel, A., Thomsen, J. S. & Birkedal, H. Calcified Cartilage Islands in Rat Cortical Bone. *Calcified Tissue Int* 92, 330–338 (2013).

66. Ip, V., Toth, Z., Chibnall, J. & McBride-Gagy, S. Remnant Woven Bone and Calcified Cartilage in Mouse Bone: Differences between Ages/Sex and Effects on Bone Strength. *PLoS ONE* 11, e0166476 (2016).
67. Jáuregui, E. J. *et al.* Parallel mechanisms suppress cochlear bone remodeling to protect hearing. *Bone* 89, 7–15 (2016).
68. Lai, X. *et al.* The dependences of osteocyte network on bone compartment, age and disease. *Bone Research* 3, E318 (2015).
69. Canè, V. *et al.* Size and density of osteocyte lacunae in different regions of long bones. *Calcified Tissue Int* 34, 558–563 (1982).
70. Hemmatian, H., Bakker, A. D., Klein-Nulend, J. & Lenthe, G. H. van. Aging, Osteocytes, and Mechanotransduction. *Curr Osteoporos Rep* 15, 401–411 (2017).
71. Schneider, P., Meier, M., Wepf, R. & Müller, R. Towards quantitative 3D imaging of the osteocyte lacuno-canalicular network. *Bone* 47, 848–858 (2010).
72. Dong, P. *et al.* QUANTIFICATION OF THE 3D MORPHOLOGY OF THE BONE CELL NETWORK FROM SYNCHROTRON MICRO-CT IMAGES | Dong | Image Analysis & Stereology. *Image Analysis & Stereology* (2014) doi:10.5566/ias.v33.p157-166.
73. Schneider, P., Meier, M., Wepf, R. & Müller, R. Serial FIB/SEM imaging for quantitative 3D assessment of the osteocyte lacuno-canalicular network. *Bone* 49, 304–311 (2011).
74. Sano, H. *et al.* Intravital bone imaging by two-photon excitation microscopy to identify osteocytic osteolysis in vivo. *Bone* 74, 134–139 (2015).
75. Livak, K. J. & Schmittgen, T. D. Analysis of Relative Gene Expression Data Using Real-Time Quantitative PCR and the  $2^{-\Delta\Delta C_T}$  Method. *Methods* 25, 402–408 (2001).
76. Youlten, S. E. *et al.* Osteocyte transcriptome mapping identifies a molecular landscape controlling skeletal homeostasis and susceptibility to skeletal disease. *Nat Commun* 12, 2444 (2021).

77. McLoughlin, K. J., Pedrini, E., MacMahon, M., Guduric-Fuchs, J. & Medina, R. J. Selection of a Real-Time PCR Housekeeping Gene Panel in Human Endothelial Colony Forming Cells for Cellular Senescence Studies. *Frontiers Medicine* 6, 33 (2019).
78. González-Bermúdez, L., Anglada, T., Genescà, A., Martín, M. & Terradas, M. Identification of reference genes for RT-qPCR data normalisation in aging studies. *Sci Rep-uk* 9, 13970 (2019).
79. Touchberry, C. D., Wacker, M. J., Richmond, S. R., Whitman, S. A. & Godard, M. P. Age-related changes in relative expression of real-time PCR housekeeping genes in human skeletal muscle. *J Biomol Techniques Jbt* 17, 157–62 (2006).
80. Pfaffl, M. W., Tichopad, A., Prgomet, C. & Neuvians, T. P. Determination of stable housekeeping genes, differentially regulated target genes and sample integrity: BestKeeper – Excel-based tool using pair-wise correlations. *Biotechnol Lett* 26, 509–515 (2004).
81. Andersen, C. L., Jensen, J. L. & Ørntoft, T. F. Normalization of Real-Time Quantitative Reverse Transcription-PCR Data: A Model-Based Variance Estimation Approach to Identify Genes Suited for Normalization, Applied to Bladder and Colon Cancer Data Sets. *Cancer Res* 64, 5245–5250 (2004).
82. Vandesompele, J. *et al.* Accurate normalization of real-time quantitative RT-PCR data by geometric averaging of multiple internal control genes. *Genome Biol* 3, research0034.1 (2002).
83. Silver, N., Best, S., Jiang, J. & Thein, S. L. Selection of housekeeping genes for gene expression studies in human reticulocytes using real-time PCR. *Bmc Mol Biol* 7, 33 (2006).
84. Xie, F., Xiao, P., Chen, D., Xu, L. & Zhang, B. miRDeepFinder: a miRNA analysis tool for deep sequencing of plant small RNAs. *Plant Mol Biol* 80, 75–84 (2012).
85. Clarke, M. V. *et al.* A Role for the Calcitonin Receptor to Limit Bone Loss During Lactation in Female Mice by Inhibiting Osteocytic Osteolysis. *Endocrinology* 156, 3203–3214 (2015).
86. Lloyd, S. A., Loisel, A. E., Zhang, Y. & Donahue, H. J. Evidence for the role of connexin 43-mediated intercellular communication in the process of intracortical bone resorption via osteocytic osteolysis. *Bmc Musculoskelet Di* 15, 122–122 (2014).



87. Xiong, J. & O'Brien, C. A. Osteocyte RANKL: New insights into the control of bone remodeling. *J Bone Miner Res* 27, 499–505 (2012).
88. Skinner, R. A. Handbook of Histology Methods for Bone and Cartilage. 167–184 (2003) doi:10.1007/978-1-59259-417-7\_10.
89. FROST, H. M. In vivo osteocyte death. *J Bone Jt Surg Am Volume* 42-A, 138–43 (1960).
90. Ghazali, Mohd. bin, Isa, Mohd. & Hoo, P. C. A Technique for the Simultaneous Staining of Osteocytes and Osteons in Frozen Sections of Decalcified Bone. *Stain Technol* 55, 47–48 (2009).
91. Webster, D. J., Schneider, P., Dallas, S. L. & Müller, R. Studying osteocytes within their environment. *Bone* 54, 285–295 (2013).
92. Mullender, M. G., Meer, D. D. van der, Huiskes, R. & Lips, P. Osteocyte density changes in aging and osteoporosis. *Bone* 18, 109–113 (1996).
93. Piemontese, M. *et al.* Low bone mass and changes in the osteocyte network in mice lacking autophagy in the osteoblast lineage. *Sci Rep-uk* 6, 24262 (2016).
94. Chandra, A. *et al.* Suppression of Sclerostin Alleviates Radiation-Induced Bone Loss by Protecting Bone-Forming Cells and Their Progenitors Through Distinct Mechanisms. *J Bone Miner Res* 32, 360–372 (2017).
95. Cardoso, L., Fritton, S. P., Gailani, G., Benalla, M. & Cowin, S. C. Advances in assessment of bone porosity, permeability and interstitial fluid flow. *Journal of Biomechanics* 46, 253–265 (2013).
96. Kamel-ElSayed, S. A., Tiede-Lewis, L. M., Lu, Y., Veno, P. A. & Dallas, S. L. Novel approaches for two and three dimensional multiplexed imaging of osteocytes. *Bone* 76, 129–140 (2015).
97. Greenbaum, A. *et al.* Bone CLARITY: Clearing, imaging, and computational analysis of osteoprogenitors within intact bone marrow. *Sci Transl Med* 9, eaah6518 (2017).

98. Berke, I. M., Miola, J. P., David, M. A., Smith, M. K. & Price, C. Seeing through Musculoskeletal Tissues: Improving In Situ Imaging of Bone and the Lacunar Canalicular System through Optical Clearing. *PLoS ONE* 11, e0150268 (2016).
99. Tokarz, D. *et al.* Intravital imaging of osteocytes in mouse calvaria using third harmonic generation microscopy. *PLoS ONE* 12, e0186846 (2017).
100. Repp, F. *et al.* Spatial heterogeneity in the canalicular density of the osteocyte network in human osteons. *Bone Reports* 6, 101–108 (2017).
101. Staines, K. A. *et al.* Hypomorphic conditional deletion of E11/Podoplanin reveals a role in osteocyte dendrite elongation. *J Cell Physiol* 232, 3006–3019 (2017).
102. Huang, B., Babcock, H. & Zhuang, X. Breaking the Diffraction Barrier: Super-Resolution Imaging of Cells. *Cell* 143, 1047–1058 (2010).
103. Tanaka, T. *et al.* Analysis of Ca<sup>2+</sup> response of osteocyte network by three-dimensional time-lapse imaging in living bone. *J Bone Miner Metab* 36, 519–528 (2018).
104. Cao, R., Xiao, W., Wu, X., Sun, L. & Pan, F. Quantitative observations on cytoskeleton changes of osteocytes at different cell parts using digital holographic microscopy. *Biomed Opt Express* 9, 72 (2017).
105. Feng, X. Chemical and Biochemical Basis of Cell-Bone Matrix Interaction in Health and Disease. *Curr Chem Biology* 3, 189–196 (2009).
106. Lattouf, R. *et al.* Picrosirius Red Staining. *J Histochem Cytochem* 62, 751–758 (2014).
107. Junqueira, L. C. U., Bignolas, G. & Brentani, R. R. Picrosirius staining plus polarization microscopy, a specific method for collagen detection in tissue sections. *Histochem J* 11, 447–455 (1979).
108. Moysés, R. M. A. & Schiavi, S. C. Sclerostin, Osteocytes, and Chronic Kidney Disease – Mineral Bone Disorder. *Semin Dialysis* 28, 578–586 (2015).
109. Khoury, B. M. *et al.* The use of nano-computed tomography to enhance musculoskeletal research. *Connect Tissue Res* 56, 106–119 (2015).

110. Müller, B. R., Lange, A., Harwardt, M. & Hentschel, M. P. Synchrotron-Based Micro-CT and Refraction-Enhanced Micro-CT for Non-Destructive Materials Characterisation. *Adv Eng Mater* 11, 435–440 (2009).
111. Carlo, F. D. *et al.* TomoBank: a tomographic data repository for computational x-ray science. *Meas Sci Technol* 29, 034004 (2018).
112. Müller, R. Hierarchical microimaging of bone structure and function. *Nature reviews. Rheumatology* 5, 373–381 (2009).
113. Peyrin, F., Dong, P., Pacureanu, A. & Langer, M. Micro- and Nano-CT for the Study of Bone Ultrastructure. *Curr Osteoporos Rep* 12, 465–474 (2014).
114. Kalajzic, I. *et al.* Dentin matrix protein 1 expression during osteoblastic differentiation, generation of an osteocyte GFP-transgene. *Bone* 35, 74–82 (2004).

# Chapter 4: Disrupted Osteocyte Connectivity and Pericellular Fluid Flow in Bone with Aging and Defective TGF $\beta$ Signaling

## Introduction

Age-related bone fragility results from the concomitant decline of bone mass and bone quality over a lifetime. Deregulation of osteoclast and osteoblast function with age contributes directly to this bone fragility, especially the loss of bone mass<sup>1,2</sup>. Although osteocytes comprise 90-95% of all bone cells, relatively little is known about their role in the age-related decline in bone health. Osteocytes reside within the bone matrix in a series of cavities and channels, known as the lacunocanalicular network (LCN)<sup>3,4</sup>. Within the LCN, osteocytes act as master regulators of bone health by supplying nutrients to other osteocytes distal to the vasculature, by coordinating the activity of osteoblasts, osteoclasts, and other cell types to balance bone deposition and resorption<sup>5,6</sup>, by sensing and responding to mechanical forces<sup>7</sup>, and by actively remodeling their surrounding bone matrix via perilacunar/canalicular remodeling (PLR)<sup>8-10</sup>. Recent advancements

in optical imaging have provided morphologic evidence for the degeneration of the LCN and the osteocyte network with age<sup>11-13</sup>, but how these architectural changes to the osteocyte network impact aged bone health remains unclear.

Aged bone demonstrates several defects including losses in mechanostimulation<sup>14</sup>, uncoupling of bone deposition and resorption<sup>1,2</sup>, alterations to bone material properties<sup>15,16</sup>, and degeneration of the LCN<sup>17</sup>. Mechanical load applied at the organ scale compresses the mineralized bone tissue, driving interstitial fluid flow through the organic pericellular matrix that lines the mineralized walls of the LCN<sup>18-21</sup>, with the resulting fluid-induced stresses and strains in osteocytes transduced into biochemical cues. Osteocytes respond to fluid flow with increased expression of bone anabolic genes and a corresponding increase in bone formation in young, murine tibial loading studies<sup>22</sup>. However, bones from middle-aged mice experience tempered responses to load that progressively worsen with age<sup>1,14,23,24</sup>. Additionally, osteocytic PLR maintains bone matrix material properties, one of several aspects of bone quality that decline with age, leading to the increased risk of fragility fractures in elderly individuals, even those with clinically normal bone mass<sup>8,9,25-28</sup>. Age also takes a toll on the osteocyte LCN, with a loss of canaliculi and changes in lacunar geometries in old bone<sup>11,13,29</sup>. Similarly, microcracks caused by fatigue loading can cause severe localized damaged to the LCN, with a loss of connectivity and nutrient supply leaving local osteocytes vulnerable, and preventing local adaptive remodeling<sup>30</sup>. Because osteocytes rely on the LCN for mechanosensation and for coordinating bone remodeling to maintain bone mass and quality, we hypothesized that the age-related degeneration of the LCN plays a causal role in the decline in bone health and increased skeletal fragility in aging.

Several hallmarks of aged bone also appear in bone from mice with limited transforming growth factor beta (TGF $\beta$ ) signaling, including impaired mechanical adaptation, poor bone quality, and LCN degeneration. First, in mice that express a dominant negative version of TGF $\beta$  receptor type II (T $\beta$ RII), bone apposition in response to loading was significantly impaired compared to wild

type controls, implicating intact TGF $\beta$  signaling in the anabolic response of bone to mechanical stimulation<sup>31</sup>. Second, osteocyte-intrinsic ablation of T $\beta$ RII (T $\beta$ RII<sup>ocy-/-</sup>) causes severe bone quality defects without meaningful changes to cortical bone mass, including reduced fracture toughness<sup>9</sup>. Third, silver nitrate staining of the LCN shows that bones from T $\beta$ RII<sup>ocy-/-</sup> mice have a shortened canalicular phenotype, which is attributed to the coordinated repression of genes required for PLR, such as MMP13, MMP14, and Cathepsin K<sup>9,32</sup>. Thus a similar set of bone phenotypes arise from the systemic effects of aging and from the osteocyte-intrinsic effects of T $\beta$ RII ablation. However, the extent to which these similarities are mechanistically related remains unclear. Either way, given the importance of TGF $\beta$  in fracture repair, osteogenesis imperfecta<sup>33</sup>, Camurati Engelman disease<sup>34</sup> (CED), and other human skeletal syndromes<sup>35</sup>, understanding the role of TGF $\beta$  in maintaining the LCN and bone strength may give new insight to clinical bone fragility.

Functional analysis of the osteocyte LCN faces challenges in isolating and manipulating specific LCN features, especially within the complex, mineralized ECM. Here we apply quantitative in silico approaches to probe the function of osteocyte networks, visualized deep within cortical bone using confocal laser scanning microscopy<sup>11-13</sup>. We test the hypothesis that LCN degeneration, whether due to systemic aging or osteocyte-intrinsic TGF $\beta$  deficiency, compromises osteocyte mass transport and mechanosensation. Unraveling the functional consequences of LCN degeneration could advance the search for therapeutically tractable mechanisms to improve bone mass or bone quality with age.

## Results

### ***Suppressed T $\beta$ RII levels and canalicular architecture in aged and T $\beta$ RII<sup>ocy-/-</sup> bone.***

The reported degeneration of the LCN with aging<sup>11,17</sup> led us to examine the effect of aging on skeletal gene expression in osteocyte-enriched cortical bone. We used Nanostring arrays, including a custom array of over 800 genes associated with skeletal cell differentiation,

extracellular matrix (ECM) remodeling, and relevant signaling pathways such as Wnt, PTH, and TGF $\beta$ . Relative to young mouse cortical bone (2 mo), genes implicated in ECM remodeling and TGF $\beta$  signaling were among the most strongly repressed in aging (36 mo) (**Fig. 4.1A**). The age-dependent LCN degeneration corresponded with the repression of MMP13, MMP14, and other ECM remodeling enzymes implicated in osteocyte perilacunar/canalicular remodeling (PLR), a process that supports the maintenance of the LCN<sup>8-10,32</sup>. Investigation of all genes within the TGF $\beta$  signaling KEGG pathway included in the Nanostring arrays showed systematic deregulation of TGF $\beta$  signaling with aging (**Fig. 4.1A, 4.1B, black bars**). The most significantly repressed genes are those encoding the canonical TGF $\beta$  R-Smad (Smad3) and TGF $\beta$  target genes Smad6 and Ski. Systemic aging also leads to the repression of the TGF $\beta$  type II receptor in bone, with a magnitude comparable to that observed in mice with genetical ablation of a floxed *Tgfr2* allele in osteocytes under control of 10 kb DMP1-Cre, relative to Cre-negative controls (**Fig. 4.1B, grey bars**). Also like aging bone, bone from these T $\beta$ RII<sup>ocy-/-</sup> mice also expresses low levels of MMP13 and MMP14<sup>9</sup>.

Whether due to aging or to osteocytic *Tgfr2* deficiency, the deterioration of the osteocyte LCN is evident. Staining of the LCN in paraffin sections shows the sparse canaliculi in old or T $\beta$ RII<sup>ocy-/-</sup> bone relative to young or T $\beta$ RII<sup>ctrl</sup> bone (**Fig. 4.1C-F**). Quantitative analysis shows that, relative to their controls, the average canalicular length is reduced in both old and T $\beta$ RII<sup>ocy-/-</sup> bone, and statistically indistinguishable between each other (**Fig. 4.1G**). Therefore, to understand the functional impact of LCN degeneration, resulting either from systemic aging or from osteocyte-intrinsic defects in TGF $\beta$  signaling, we evaluated LCN structure and function in each of these two mouse models.

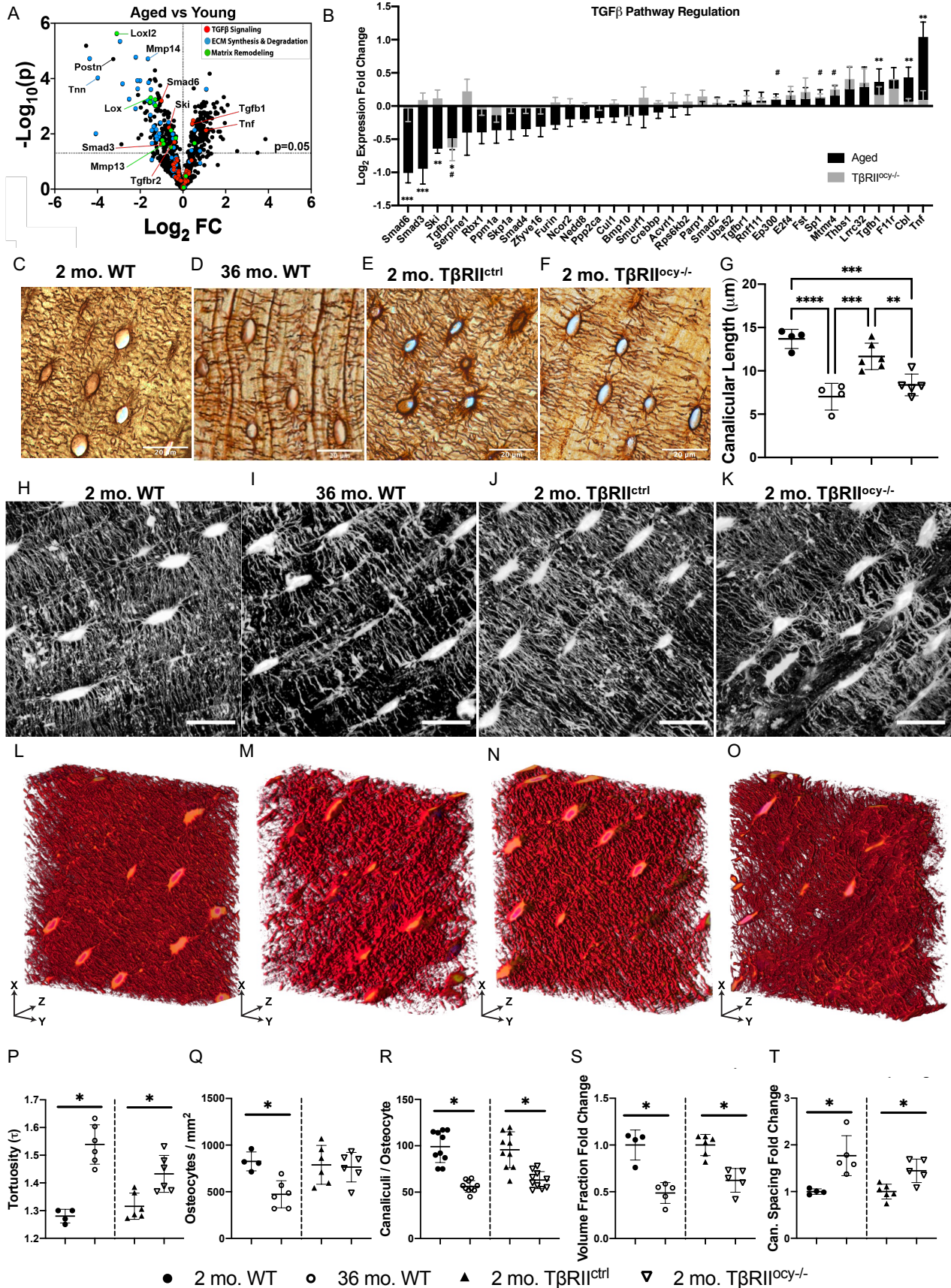




**Figure 4.1: Aged and  $T\beta RII^{ocy-/-}$  bone share molecular and canalicular morphologic changes.** A) Volcano plot of 800+ genes from nanoString panels shows downregulation of genes involved in matrix interaction and remodeling in aged bones. B) Log<sub>2</sub> expression fold change of TGFβ signaling pathway genes from nanoString showing systemic regulation with age (36 mo. N=4 vs 2 mo. N=3, black bars). RNA from  $T\beta RII^{ocy-/-}$  bone shows significant repression of only Tgfr2 ( $T\beta RII^{ocy-/-}$  vs  $T\beta RII^{ctrl}$  N= 4 ea. grey bars). \* significant effect wrt. age, # significant effect wrt.  $T\beta RII^{ocy-/-}$ , \* p< 0.05, \*\* p<0.01, \*\*\* p< 0.001 by student's t-test. Silver nitrate staining (C-F) of the osteocyte lacunocanalicular networks showing shortened canalicular lengths in 2D at 36 mo. (N=4) or with disrupted TGFβ signaling (N=5). Young C57BL/6 mice (n=4) showed no significant differences in canalicular length to  $T\beta RII^{ctrl}$  mice (n=6), additionally mice with ablated TGFβ signaling showed no significant differences from aged mice \*, + indicates Tukey corrected p value to 2 mo. C57BL/6 mice or 2 mo.  $T\beta RII^{ctrl}$  mice respectively (G) \*\* p<0.01, \*\*\* p< 0.001, \*\*\*\* p< 0.0001. Maximum z-projections (H-K) of a single plane of osteocytes (~12 μm). Scale bar = 20 μm. (L-O) 3D reconstructions of 75 x 75 x ~35 μm sections of LCN captured by confocal imaging showing loss of canaliculi and canalicular organization in aged (I,M) (N=6) and  $T\beta RII^{ocy-/-}$  (K,O) (n=6) mice compared to 2 mo. WT controls (H,L) (N=4) and 2 mo.  $T\beta RII^{ctrl}$  mice (J,N) (n=6) respectively. Quantification of LCN parameters completed in 3D within a 30 μm thick selection (P-T) shows similar changes in aged and  $T\beta RII^{ocy-/-}$  bone, with the exception of osteocyte area density (Q) showing loss of cell bodies in only aged bone. \* p<0.05 by students t-test to proper control.

Limitations of visualizing this elaborate three-dimensional network in thin paraffin sections led us to examine the LCN using fluorescent confocal microscopy of thick cleared cortical bone sections (**Fig. 4.1H-O**). These detailed three-dimensional images strikingly reveal the loss of canalicular density and organization in aged or  $T\beta RII^{ocy-/-}$  bone.\* Quantitative analysis of these images shows that the shortened canalicular phenotype of old or  $T\beta RII^{ocy-/-}$  bone, apparent in paraffin sections (**Fig. 4.1G**), in part results from canaliculi bending in and out of the focal plane due to increased canalicular tortuosity,  $\tau$ , (**Fig. 4.1P**).

Consistent with previous findings, canalicular architecture is altered by defective TGFβ signaling without changes to lacunar number as previously noted by Synchrotron radiation Micro-Tomography (SRμT)<sup>9</sup>, but both lacunar and canalicular features deteriorate with age<sup>11,13</sup> (**Fig. 4.1Q,R**). Analyses of canalicular features revealed similar patterns of canalicular alterations in aged and  $T\beta RII^{ocy-/-}$  bone relative to controls, with reduced canalicular dendrite numbers (**Fig. 4.1R**) observed through Imaris-aided quantification of the direct canalicular sprouting point before

---

\* <https://movie-usa.glencoesoftware.com/video/10.1073/pnas.2023999118/video-1>

the first bifurcation as well as reduced LCN volume fraction and increased canalicular spacing (**Fig. 4.1S-T**). How these changes to osteocyte canalicular architecture precisely impact cellular performance is unknown.

### ***Maintenance of network architecture but loss of nodal interactions with age and TGF $\beta$ signaling disruption***

Given the challenges in manipulating and observing osteocyte networks in vivo and in vitro, we applied in silico approaches to probe the functional implications of LCN degeneration on osteocyte connectivity, mass transport, and mechanosensitivity. First, using network scale connectomic analysis, a non-dimensional collection of nodes and edges is constructed on top of 3D osteocyte networks derived from bone of young and old, or T $\beta$ RII<sup>ctrl</sup> and T $\beta$ RII<sup>ocy-/-</sup> mice (**Fig. 4.2A**)<sup>36,37</sup>. Nodal analysis provides important insight into the prevalence and type of canalicular junctions, which can impact solute transport and fluid mechanics<sup>38</sup>.

Although the average number of nodes was decreased in both the aged and T $\beta$ RII<sup>ocy-/-</sup> models compared to young or Cre-negative controls (**Fig. 4.2B**), underlying aspects of network architecture are unaffected by LCN degeneration. For example, mean node degree ( $n$ ), a measure of network architecture that reflects the number of connected nearest neighbors, is equal across all groups, when excluding end-point nodes (**Fig. 4.2C, left**), emphasizing high level maintenance of network organization. Furthermore, while the osteocyte density within the connectomes was kept constant to prioritize canalicular path behavior (**Fig. 4.2D**) the primary node types (t and c nodes) remain proportionally constant with age or with TGF $\beta$ -deficiency (**Fig. 4.2E-F**). However, increases in the number of end-point nodes in the LCN of aged and T $\beta$ RII<sup>ocy-/-</sup> bone stratified them from their controls (**Fig. 4.2G**). The increase in end-point nodes ( $n=1$ ) in aged and T $\beta$ RII<sup>ocy-/-</sup> networks significantly affects LCN architecture by lowering the mean node degree (**Fig. 4.2C, right**) by identifying an increase in non-functional path choices where canaliculi

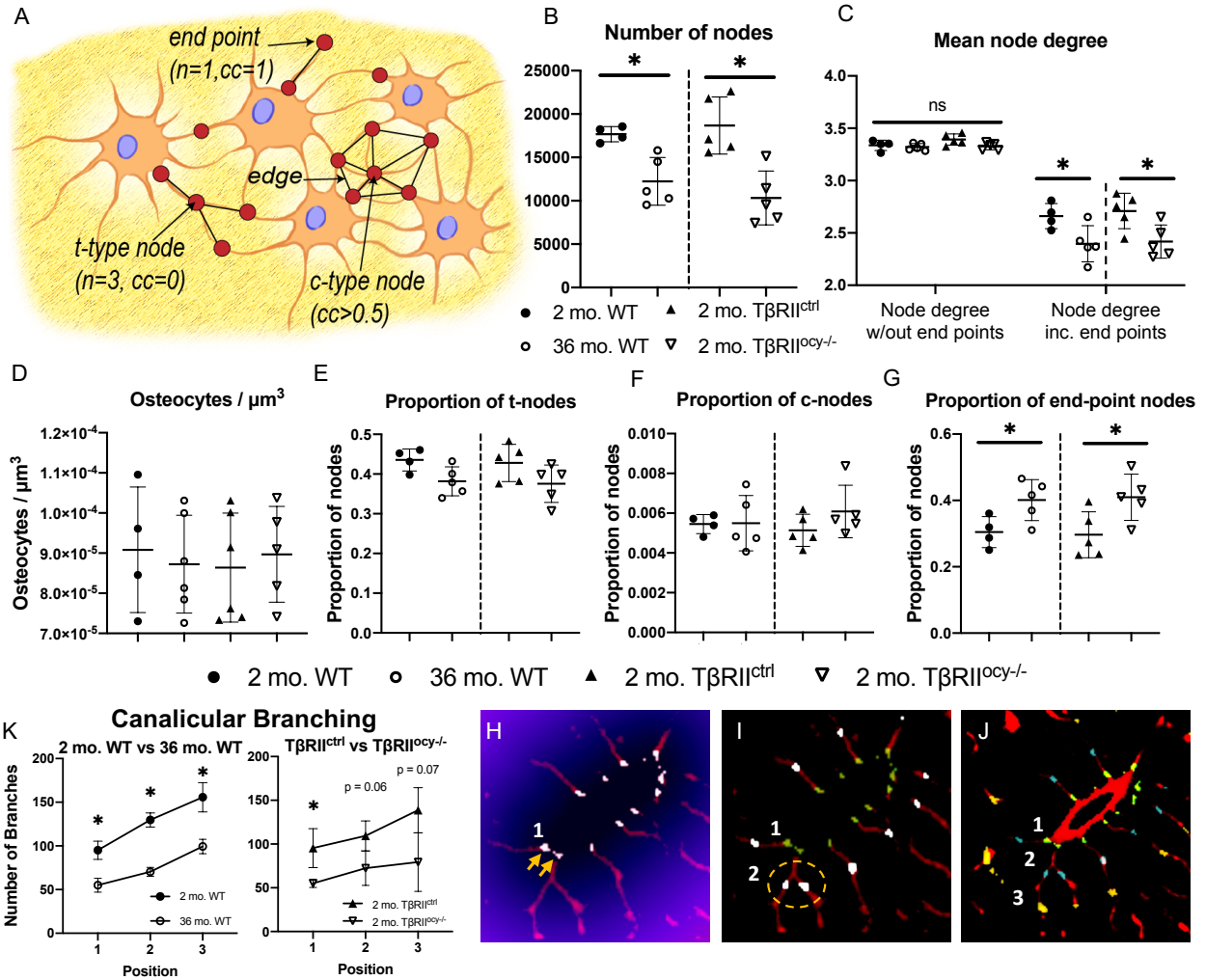


**Figure 4.2: Nodal analysis shows maintenance of network architecture but loss of total network interactions with age and  $TGF\beta$  signaling disruption in osteocytes.** Individual node classification (A) from connectomic analysis of the LCN from skeltonized confocal images shows a dramatic loss of total identified nodes (B) in aged and  $T\beta RI I^{ocyt-/-}$  bone compared to controls. Mean node degree (connections per node) without considering end-point nodes (C, left) shows maintenance of the underlying network architecture even with degeneration. In contrast, inclusion of end-point nodes (C, right) demonstrates the detrimental effect of disjointed paths in the network. While maintaining equal osteocyte number within volumes studied (D), the relative proportion of branch-like t nodes (E) and cluster-like c nodes (F) persisted across all models, while there was an increase in the proportion of end-point nodes (G) in degenerated models. Canalicular branching identified through segmentation in expanding concentric positions away from the cell body (K) reveals degenerated models showed specific loss of canaliculi number at the sprouting point (H, yellow arrows) but continued to branch normally at the first region of bifurcation (I, dashed yellow) and again further into the network (J, yellow). \*  $p < 0.05$  to young, WT controls.  $N=5$  for all groups.

terminate within the matrix without reconnecting to the network, revealing higher numbers of discontinuities at the termini of canaliculi in degenerated models. Investigation of branching through segmentation of canalicular features at regular concentric distances away from the cell body (**Fig. 4.2K**) shows that, although degenerated models lose canalicular number at the root (**Fig. 4.2H**), remaining canaliculi in the aged and  $T\beta RII^{ocy-/-}$  models expand at similar rates to controls within the first region of canalicular bifurcation (**Fig. 4.2I, white**) and again at further into the network (**Fig. 4.2J, yellow**). Therefore, as the LCN ages in cortical bone, rather than changing canalicular organization and adopting a more web-like state as found in woven bone<sup>36,37,39</sup>, it undergoes pruning by which dendrites retract or degenerate, but branching near cell bodies is unaffected.

#### **Aged and $T\beta RII^{ocy-/-}$ osteocyte networks have impaired transport capabilities**

While higher-order LCN structure is preserved with age and  $TGF\beta$  disruption, the loss of canaliculi and *canalicular junctions* may limit fluid and solute movement. If mass transport through the LCN is compromised, it could influence osteocyte nutrient exchange and the ability of osteocytes to signal with one another and with other cell types. Therefore, to determine the effect of LCN degeneration on mass transport, we applied Betweenness Centrality (BC) analysis to the LCN connectomes of young and old,  $T\beta RII^{ctrl}$  and  $T\beta RII^{ocy-/-}$  bones. BC is defined as the fraction of shortest paths within a network running through any particular node (**Fig. 4.3E**) where high BC scoring nodes represent heavily used paths (**Fig. 4.3A-D**). Nodes that appear in at least 1% of paths within the connectome are shown in color, with red nodes being the most heavily utilized.

Using BC analysis, we find that with age or osteocytic  $TGF\beta$ -deficiency, the number of available paths is reduced, with the obvious consequence that remaining paths are much more heavily utilized. Specifically, the proportion of nodes scoring above the 1% threshold is increased in the LCN of aged and  $T\beta RII^{ocy-/-}$  bones compared to their young and  $T\beta RII^{ctrl}$  controls (**Fig. 4.3F**).

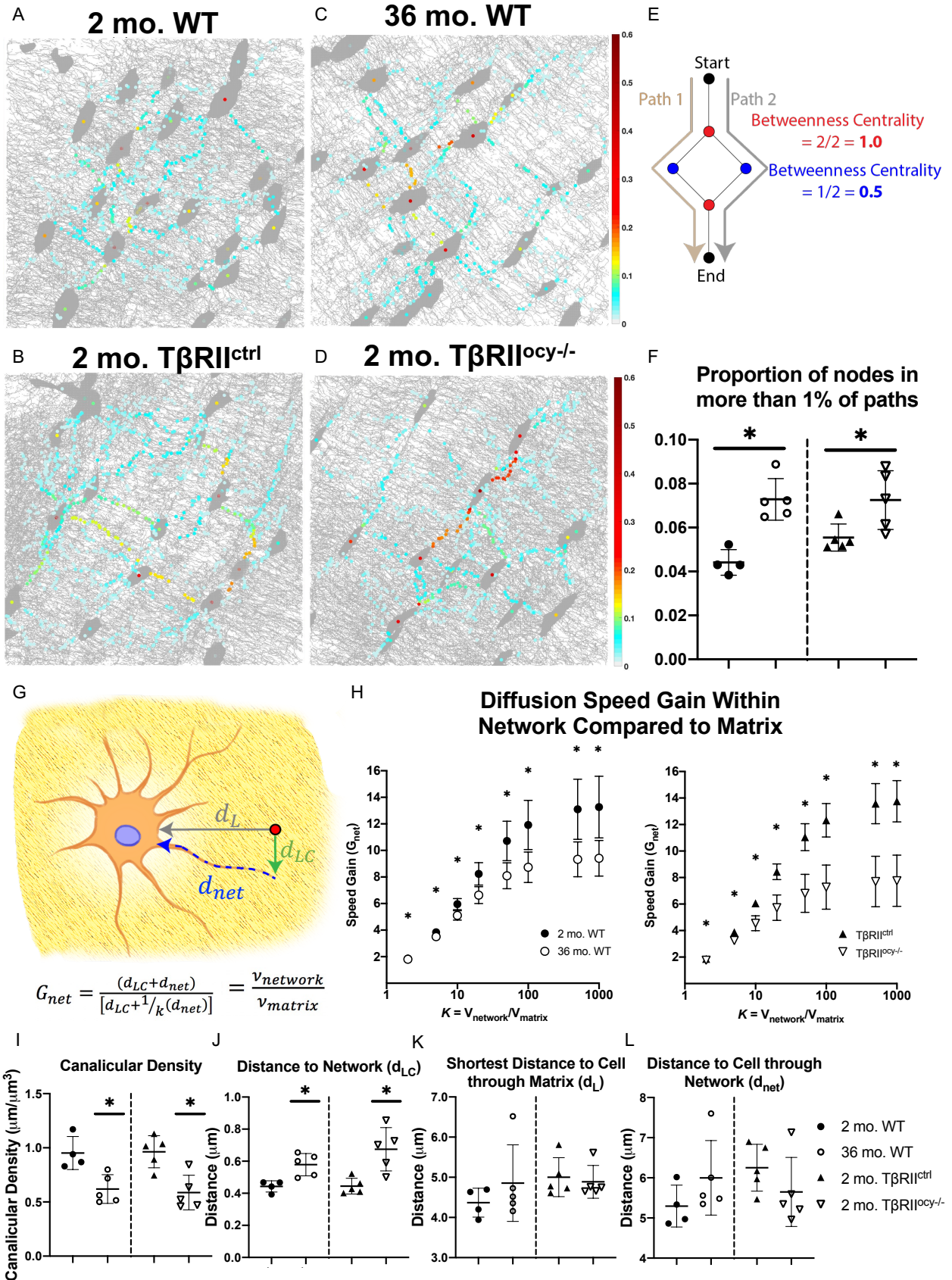


**Figure 4.3: Aged and  $T\beta RII^{ocy-/-}$  osteocyte networks have limited pathway availability and lower transport capabilities in in silico connectomic models.** Projection of 3D skeletonized maps of the LCN with nodes color-mapped to their individual betweenness centrality (BC) values (A-D). Colorbar indicates BC score for individually plotted nodes. Higher BC scoring nodes align to show heavily used pathways within the network ( $BC > 0.01$ ), with a higher fraction in degenerated models (F) indicating more limited pathway choice. See Supplemental Videos 2 & 3 for 3D representation. Comparison of transport capacity within bone from the skeletonized-connectomic network models show an increase in non-dimensional diffusive speed gain (G) in networks of young, control bones compared to respective degenerated models (H). This is primarily driven by a decrease to canalicular length density (I) in degenerated models increasing distance to the LCN from the matrix ( $d_{LC}$ , J) rather than an increase in distance to the nearest cell directly through the matrix ( $d_L$ , K) or from points within the LCN to the nearest lacuna through the network ( $d_{net}$ , L). \*  $p < 0.05$ . N=5 for all groups.

Low scoring nodes (blue,  $BC = 0.01-0.1$ ) abundant in healthy, young bone, dissipate in the degenerated models indicating fewer available paths for mass transport within the networks. In contrast, fewer paths exist in old or  $T\beta RII^{ocy-/-}$  bone and are much more heavily utilized (yellow-red,  $BC > 0.1$ ), features that are readily apparent in videos showing BC values within the 3D connectomes.\* Therefore, the greater reliance on fewer pathways with age is a feature of these compromised networks.

We next modeled the effect of LCN degeneration on its ability to complete a diffusive task using measured network distances and physical diffusion constants (**Fig. 4.3G**). With a smaller diffusive speed gain than controls, the aged LCN has diminished ability to shuttle material through the network (**Fig. 4.3H**). The effect of aging on the diffusivity of the LCN was almost identical to that resulting from osteocyte-intrinsic loss of TGF $\beta$  signaling (**Fig. 4.3H**). In both cases, the diminished diffusivity is largely due to the decreased canalicular density (**Fig. 4.3I**). With ~40% lower canalicular length-density, the distance a molecule must travel to get from the ECM to the LCN ( $d_{LC}$ , **Fig. 4.3J**) is significantly increased in degenerated networks compared to their respective controls. Other variables that affect diffusive speed gain ( $d_L$  and  $d_{net}$  **Fig. 4.3K-L**) remain unchanged by LCN degeneration in these models. Intuitively, this analysis shows that, of

---

\* <https://movie-usa.glencoesoftware.com/video/10.1073/pnas.2023999118/video-2>  
<https://movie-usa.glencoesoftware.com/video/10.1073/pnas.2023999118/video-3>

the many LCN features disrupted by aging or osteocytic TGF $\beta$ -deficiency, including canalicular number and tortuosity, the loss of canalicular number or density is the most important driver of the reduced diffusivity in this model.

### **Fluid dynamics modeling demonstrates lower fluid velocity and shear stress as a function of pericellular space volume and not canalicular tortuosity**

Given the importance of the LCN for osteocyte mechanosensation, we sought to determine how LCN fluid flow shear stress changes following LCN degeneration, due to either systemic aging or osteocyte-intrinsic suppression of TGF $\beta$  signaling. To that end, we used computational fluid dynamics to model load-induced interstitial fluid flow within the pericellular space (PCS) surrounding single osteocytes (**Fig. 4.4A**). Standard PCS volumes were modeled from the same set of confocal fluorescence images of osteocyte networks from young and old, and T $\beta$ RII<sup>ctrl</sup> and T $\beta$ RII<sup>ocy<sup>-/-</sup></sup> bone (**Fig. 4.4B**). Computational complexity limited our analysis to individual osteocytes, which were segmented consistently to eliminate confounding local features, such as blood vessels. Using these models, we can easily modify the dimensions of the PCS parametrically to mimic volume changes caused by the suppression (**0.5x, Fig. 4.4C**) or induction (**2x, Fig. 4.4D**) of perilacunar/canalicular remodeling. Even at the single cell scale, the loss of osteocyte surface area surface in aged and T $\beta$ RII<sup>ocy<sup>-/-</sup></sup> bone is still evident (**Fig. 4.4E**). The 2-fold in silico changes in PCS thickness roughly double or half the total calculated volume of the modeled LCNs within each group, whereas differences between young and old, or T $\beta$ RII<sup>ctrl</sup> and T $\beta$ RII<sup>ocy<sup>-/-</sup></sup> bone account for no more than a 60% change in PCS volume (**Fig. 4.4F**).

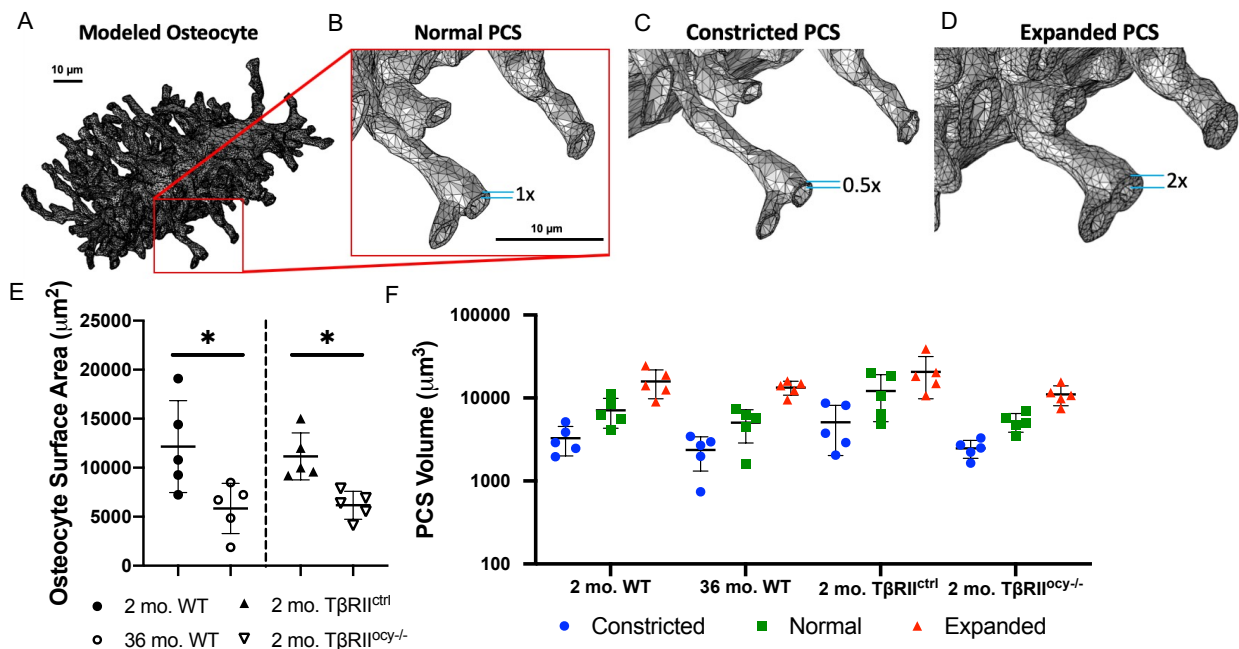


**Figure 4.4: Finite Element models of individual osteocytes.** A) Meshing of individual osteocytes and (B) modeling of surrounding pericellular space at standard width ( $0.08 \mu\text{m}$ ) and constricted or expanded width by a factor of 2 (C,D,  $0.04$ ,  $0.16 \mu\text{m}$  respectively). Osteocyte surface area (E) varied between controls and degenerated models. Manipulation of PCS thickness caused commensurate changes in PCS volume (F) with greater changes within groups (age/genotype) at different PCS thicknesses than between groups at the same PCS thickness.

Modeling of interstitial fluid flow at constant volume and pressure revealed profound differences in the shear stress magnitude and distribution in the PCS of old and  $T\beta\text{RII}^{\text{ocy-/-}}$  osteocytes, relative to their young or  $T\beta\text{RII}^{\text{ctrl}}$  controls (**Fig. 4.5A**). Maximum fluid velocities of  $686.95 \mu\text{m/s}$  around young osteocytes, and similarly  $525.70 \mu\text{m/s}$  for  $T\beta\text{RII}^{\text{ctrl}}$  osteocytes, were approximately double those predicted for osteocytes from aged and  $T\beta\text{RII}^{\text{ocy-/-}}$  bones, at  $242.82 \mu\text{m/s}$  and  $321.86 \mu\text{m/s}$ , respectively (**Fig. 4.5B**). Likewise, maximum shear stresses are significantly higher for young and  $T\beta\text{RII}^{\text{ctrl}}$  osteocytes than for aged and  $T\beta\text{RII}^{\text{ocy-/-}}$  cells (**Fig. 4.5C**).

These reductions in fluid velocity and shear stress with LCN degeneration could arise from several factors, such as changes in canalicular length (**Fig. 4.1G**), LCN or PCS volume (**Fig. 4.1T**, **Fig. 4.4G**), or tortuosity (**Fig. 4.1Q**). Using fluid dynamics modeling we tested the contribution of PCS volume and tortuosity to fluid flow shear stress. We were surprised to find, by modelling



fluid flow in individual canaliculi across a range of tortuosity, that increasing tortuosity had no significant effect on either fluid velocity or shear stress (**Fig. 4.5D**). This suggests that osteocytes in degenerated networks do not gain any mechanosensitive advantage by generating canalicular tortuosity.

On the other hand, the expanded PCS volume, and the resulting increased flow rates, generated significantly greater maximum fluid velocities than in baseline conditions, while constriction of this space had the opposite effect (**Fig. 4.5E**). Remarkably, PCS expansion increased the fluid flow velocity and shear stress predicted for aged or  $T\beta RII^{ocv-/-}$  osteocytes such that these values were statistically indistinguishable from young or  $T\beta RII^{ctrl}$  controls at baseline PCS volumes (**Fig. 4.5F,G**). These findings emphasize the importance of PCS volume on osteocyte pericellular fluid movement and highlight the potential to rescue impaired osteocyte mechanosensation due to LCN degeneration in aging by increasing PCS volume.

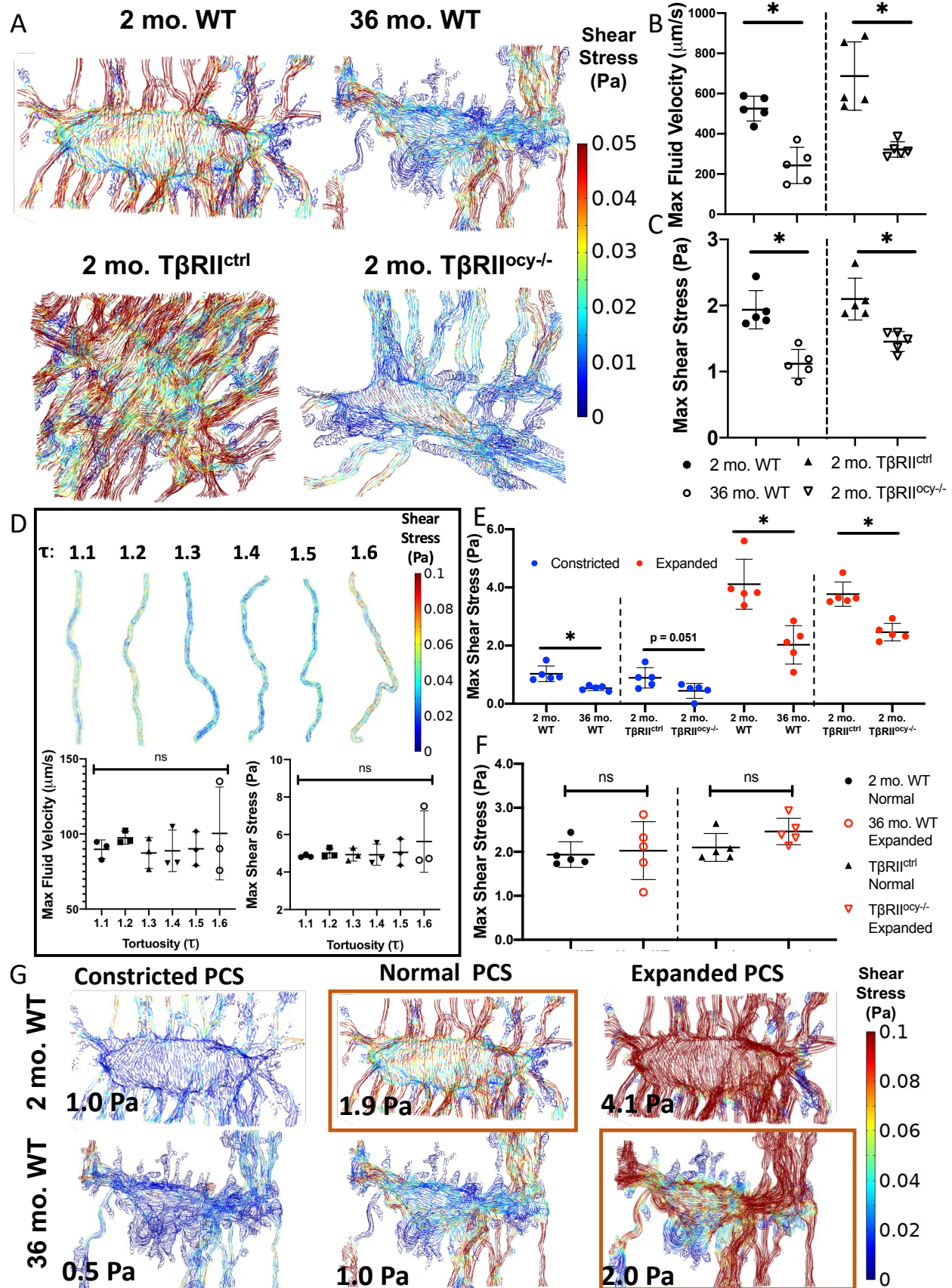


**Figure 4.5: Fluid dynamics modeling demonstrates lower fluid velocity and shear stress as a function of pericellular space volume and not canalicular morphology.** Visualization of streamlines (A) and quantification of fluid flow within the pericellular space (PCS) around single osteocytes from both aged and  $T\beta RII^{ocy-/-}$  show significant reductions to fluid velocity and shear stress compared to controls (B,C N=5, 3 individual cells per N). In contrast, no appreciable change in flow within single canaliculi (D) of varying tortuosities was observed. Parametric modulation of PCS volume around the same osteocyte geometries maintains trends between models as seen in the base condition, but overall magnitude changes when the PCS is constricted or expanded (E). Expansion of the PCS in degenerated models recovers shear stress values to levels comparable to young controls at standard PCS volume (F). Streamline visualization of the effect of volume modulation (G) shows recovery of shear magnitude for aged osteocytes with an expanded PCS volume to that observed for young osteocytes (outlined in orange). \*  $p < 0.05$ .

## Discussion

This study provides the first evidence that the decline of bone health with age is mechanobiologically linked to the age-related degeneration of osteocyte lacunocanalicular network structure and function. By examining the functional implications of LCN degeneration on osteocyte mass transport and pericellular fluid flow, this work informs the biological and physical decline of bone during aging and suggests strategies to defend against this loss. Specifically, by utilizing a combination of in silico analyses we identified that reductions in canalicular number and connections reduce diffusion within the LCN and pericellular fluid velocity, a driver of osteocyte mechanosensation. Connectomics analysis revealed the LCN architectural changes that occur with age in cortical bone and how LCN pruning limited pathway availability and mass transport in old bone. FE modeling identified that loss of osteocyte canaliculi alone is sufficient to reduce the LCN surface area and limit shear mechanostimulation along this surface. Finally, FE modeling showed that deficits to fluid velocity and associated shear of aged osteocytes are recoverable by increasing PCS volume, even without changing the remaining architecture of the LCN. These observations apply whether LCN degeneration results from systemic aging or from a targeted defect in osteocytic  $TGF\beta$  signaling. Thus, this work identifies lost fluid dynamics and mechanostimulation as consequences of LCN pruning in response to osteocyte  $TGF\beta$  deficiency

or aging, and provides evidence that restoration of osteocyte stimulation through pericellular fluid flow is physically possible without the need to regrow lost canaliculi.

A key strength of this study is the ability to distinguish the functional effects of lacunar and canalicular changes by comparing LCN degeneration in aging and  $T\beta RII^{ocy-/-}$  mice. Previous studies of the LCN of aged bone note canalicular losses as well as diminished osteocyte number and lacunar size<sup>11,13,29</sup>, confounding the ability to dissect lacunar and canalicular contributions to LCN function. On the other hand,  $T\beta RII^{ocy-/-}$  bone lost canaliculi to the same extent as aged bone with no change in lacunar number. This finding using optical imaging is similar to previous findings in this model using Synchrotron radiation Micro-Tomography (SR $\mu$ T) documenting no loss to lacunar number with TGF $\beta$  signaling disruption<sup>9</sup>, highlighting the ability to assess the contribution of the canalicular network to osteocyte function and health using this model. Therefore, canalicular loss, in either model, is sufficient to compromise key aspects of osteocyte function, including mass transport and mechanosensation.

As in  $T\beta RII^{ocy-/-}$  bone<sup>9</sup>, aged bone showed suppression of genes encoding T $\beta$ RII and PLR enzymes. Since PLR supports the maintenance of the osteocyte LCN<sup>10,40</sup> reduced TGF $\beta$  signaling may play a causal role in the age-related degeneration of the LCN. While the molecular mechanism responsible for declining TGF $\beta$  signaling and PLR with age in bone has yet to be explored, this work establishes that both aged and  $T\beta RII^{ocy-/-}$  bone share canalicular defects that impair the LCN in both form and function. Although the effects of DMP1-Cre/T $\beta RII^{fl/fl}$  on osteocyte morphology and health have previously been recapitulated through pharmaceutical inhibition of TGF $\beta$  signaling in skeletally mature mice, it is important to note that the constitutive nature of the removal of T $\beta$ RII through DMP1 may also occur in “late-stage” osteoblasts as they begin their transition into osteocytes. While this may result in some lingering developmental defects impacting the osteoblast-osteocyte transition, and thus unrelated biologically to the aged-related loss of canaliculi, the  $T\beta RII^{ocy-/-}$  phenotype is still canalicular-specific and also subtle compared

to other models of altered TGF $\beta$  signaling within the skeleton where phenotypes are much more severe<sup>33,34</sup>. Additionally, disruptions to TGF $\beta$  signaling are independently observed in our nanoString analysis of aged osteocytes, including specifically T $\beta$ RII, supporting the rationale to utilize this mouse model in parallel with aged mice. To definitively address the role of TGF $\beta$  signaling in mature osteocytes within the LCN, the use of an inducible Cre mouse without additional skeletal effects is desired, while our model is sufficient in understanding the canalicular contributions to LCN degeneration.

These imaging and computational analyses point to the role of canalicular loss and pruning in LCN degeneration in both aged and T $\beta$ RII<sup>ocy-/-</sup> bone. LCN pruning can occur prior to, or independently of, osteocyte death, since canalicular density is low in T $\beta$ RII<sup>ocy-/-</sup> bone even when osteocyte density is preserved. Concentric canalicular feature identification showed a primary defect of whole canalicular loss in degenerated models while remaining dendrites branch and expand normally, while end-point nodal classification identifies pruning at the distal end of processes as they withdraw from the network, severing connectivity. Both these alterations to the network compromise the size and pervasiveness of the network throughout the bone matrix and, along with previous work estimating the size limit for particle diffusion through the LCN of 40kD<sup>41,42</sup>, compromise osteocyte function. This is supported by our findings that predict a 30-45% reduction in the speed of particle movement through degenerated networks. These limitations to mass transport within bone impact all three major bone cell types since osteocytes rely on the LCN for nutrient supply<sup>25</sup> as well as for signaling to osteoclasts and osteoblasts. Thus canalicular morphology is altered in multiple ways, raising further questions about the different biologic processes that control different aspects of canalicular morphology and how this may impact cellular crosstalk, bone remodeling, and the decline in bone mass and bone quality with age<sup>43</sup>.

Fluid flow within the LCN is a primary mechanism by which mechanical stimulation drives bone anabolism, a response that is diminished in aged bone<sup>44</sup> that additionally depends on

canalicular path availability. While fluid shear stress has previously been postulated to stimulate osteocytes, as is presented here as a functional outcome/defect, it is likely that the fluid stimulation occurs via fluid drag-induced strain at molecular attachments and focal adhesions along canalicular dendrites and the canalicular wall<sup>42,45</sup>. Therefore the changes in velocities reported here likely have commensurate effects on the strain stimulation of the osteocytes, as has been shown in previous modelling studies<sup>19,46–48</sup>. While losses of osteocyte cell bodies and changes to lacunar geometry towards smaller and rounder lacunae with age<sup>13,49</sup> have already been implicated in reduced fluid flow in the LCN<sup>50</sup>, here we report complementary canalicular changes with age. Given that the osteocyte canaliculi is predicted to be the primary mechanosensing portion of the LCN<sup>50,51</sup> knowledge of which of these geometric changes most diminishes fluid flow remains a significant knowledge gap.

Our prior work, using idealized canalicular models, predicted that tortuosity would slightly increase localized mechanical stimulation<sup>19</sup>. Thus, we hypothesized that the increased canalicular tortuosity may allow aged or  $T\beta RII^{ocy-/-}$  osteocytes to increase local mechanical stimulation. Stream line plots qualitatively identified local regions of enhanced fluid shear around canalicular bends, but these hotspots were insufficient to overcome the greater loss of fluid velocity and shear stimulation caused by canalicular loss. Because these models applied a uniform baseline PCS thickness of 0.08  $\mu\text{m}$ , derived from prior studies, the effects of other known local changes in canaliculi are undetectable in this model, such as canalicular hillocks near tethering elements<sup>42,52,53</sup>. Nonetheless, these models demonstrate the importance of LCN surface area and canalicular loss on fluid stimulation.

Despite localized increases in canalicular shear, we were surprised to find that the severe bending of canaliculi in aged and  $T\beta RII^{ocy-/-}$  bone is insufficient to overcome the losses in physical stimulation in the models caused by the broader degeneration of the LCN. Inclusion of proteoglycan tethering elements may reduce the magnitude of lost stimulation in these models<sup>52</sup>.

However, since mechanostimulation at either the surface of the canalicular dendrite or on perpendicular tethering elements will increase or decrease with flow velocity, this finding refutes the idea that control of canalicular geometry alone is a meaningful way to restore lost mechanical stimulation with age driven by the broader loss of LCN volume that is the result of pruning.

On the other hand, osteocytes have the capacity to modulate the size and quality of their pericellular space through PLR<sup>10,54</sup>. For example, relative to bone from virgin control mice, canalicular diameter increases by 20-30% with lactation, and returns to baseline after weaning<sup>54</sup>, demonstrating expansion and constriction of the local PCS. Our fluid dynamics modeling demonstrates the important functional implications of changing PCS diameter through a process like PLR. First, a 50% constriction of the young wild type osteocyte PCS renders a shear stress that matches aged and  $T\beta RII^{ocy-/-}$  osteocytes at baseline PCS thickness. Second, doubling the PCS of aged and  $T\beta RII^{ocy-/-}$  osteocytes returned shear stress to levels that were indistinguishable from young or wild type controls. How these changes to the PCS impact the proteoglycan-rich PCM and its modulation of local fluid drag or tensional homeostasis<sup>55</sup> remains to be determined. Nonetheless, control of the pericellular space, possibly through PLR, presents a mechanism by which osteocytes can homeostatically adapt their mechanical microenvironment to reclaim meaningful amounts of lost physical stimulation in age and disease, although further resorption of bone would need to be carefully considered in osteoporotic cases.

This *in silico* work highlights the opportunity to overcome experimental complexities inherent in studying the relationship between osteocyte LCN structure and function. Of the many LCN features sensitive to age<sup>11,17</sup> or  $TGF\beta$ -deficiency<sup>9</sup>, these computational models allowed us to identify those that are most important for the impaired mechanosensitivity of bone in each model<sup>14,38,48</sup>. Given the important role of PCS volume, agents that regulate PLR emerge as potential therapeutic candidates to restore function lost in aged bone and motivate further study.

## **Acknowledgements**

This research was supported by NIH-NIDCR grant R01 DE019284 (T.A.), NIH-NIA grant F31 AG063402 (C.S.) This project also received funding from the European Union's Horizon 2020 research and innovation programme under the Marie Skłodowska-Curie grant agreement No 748305 (S.V.). UCSF cores used to complete this work include the Skeletal Biology and Biomechanics Core of the Core Center for Musculoskeletal Biology and Medicine (NIH P30 AR066262) and the Biological Imaging and Development Core and staff for support using IMARIS. The authors thank Dr. X.E. Guo for helpful discussions, the Guo Laboratory at Columbia University for computational resources (MIMICS), Dr. R. Orendorff for software expertise and support with the MATLAB scripts, and Drs. S. Melov and J. Garrison at the Buck Institute for Research on Aging for donation of young and aged murine tissues.



## References

1. Razi, H. *et al.* Aging Leads to a Dysregulation in Mechanically Driven Bone Formation and Resorption. *J Bone Miner Res* 30, 1864–1873 (2015).
2. Almeida, M. Aging mechanisms in bone. *Bonekey Reports* 1, (2012).
3. Buenzli, P. R. & Sims, N. A. Quantifying the osteocyte network in the human skeleton. *Bone* 75, 144–150 (2015).
4. Bonewald, L. F. The amazing osteocyte. *Journal of Bone and Mineral Research* 26, 229–238 (2011).
5. Schaffler, M. B. & Kennedy, O. D. Osteocyte Signaling in Bone. *Curr Osteoporos Rep* 10, 118–125 (2012).
6. Schaffler, M. B., Cheung, W.-Y., Majeska, R. & Kennedy, O. Osteocytes: Master Orchestrators of Bone. *Calcified Tissue Int* 94, 5–24 (2014).
7. Uda, Y., Azab, E., Sun, N., Shi, C. & Pajevic, P. D. Osteocyte Mechanobiology. *Curr Osteoporos Rep* 15, 318–325 (2017).
8. Osteocyte-directed bone demineralization along canaliculi. *Bone* 84, 279–288 (2016).
9. Dole, N. S. *et al.* Osteocyte-Intrinsic TGF- $\beta$  Signaling Regulates Bone Quality through Perilacunar/Canalicular Remodeling. *Cell Rep* 21, 2585–2596 (2017).
10. Qing, H. *et al.* Demonstration of osteocytic perilacunar/canalicular remodeling in mice during lactation. *J. Bone Miner. Res.* 27, 1018–1029 (2012).
11. Tiede-Lewis, L. M. *et al.* Degeneration of the osteocyte network in the C57BL/6 mouse model of aging. *Aging* 9, 2190–2208 (2017).
12. Kamel-ElSayed, S. A., Tiede-Lewis, L. M., Lu, Y., Veno, P. A. & Dallas, S. L. Novel approaches for two and three dimensional multiplexed imaging of osteocytes. *Bone* 76, 129–140 (2015).

13. Heveran, C. M., Rauff, A., King, K. B., Carpenter, R. D. & Ferguson, V. L. A new open-source tool for measuring 3D osteocyte lacunar geometries from confocal laser scanning microscopy reveals age-related changes to lacunar size and shape in cortical mouse bone. *Bone* 110, 115–127 (2018).
14. Meakin, L. B., Galea, G. L., Sugiyama, T., Lanyon, L. E. & Price, J. S. Age-Related Impairment of Bones' Adaptive Response to Loading in Mice Is Associated With Sex-Related Deficiencies in Osteoblasts but No Change in Osteocytes. *J Bone Miner Res* 29, 1859–1871 (2014).
15. Nalla, R. K., Kruzic, J. J., Kinney, J. H. & RITCHIE, R. O. Effect of aging on the toughness of human cortical bone: evaluation by R-curves. *Bone* 35, 1240–1246 (2004).
16. Zimmermann, E. A. *et al.* Age-related changes in the plasticity and toughness of human cortical bone at multiple length scales. *Proceedings of the National Academy of Sciences* 108, 14416–14421 (2011).
17. Tiede-Lewis, L. M. & Dallas, S. L. Changes in the osteocyte lacunocanalicular network with aging. *Bone* 122, 101–113 (2019).
18. Weinbaum, S., Cowin, S. C. & Zeng, Y. A model for the excitation of osteocytes by mechanical loading-induced bone fluid shear stresses. *J Biomech* 27, 339–360 (1994).
19. Verbruggen, S. W., Vaughan, T. J. & McNamara, L. M. Mechanisms of osteocyte stimulation in osteoporosis. *J Mech Behav Biomed* 62, 158–168 (2016).
20. STECK, R., NIEDERER, P. & TATE, M. L. K. A Finite Element Analysis for the Prediction of Load-induced Fluid Flow and Mechanochemical Transduction in Bone. *J Theor Biol* 220, 249–259 (2003).
21. Ganesh, T., Laughrey, L. E., Niroobakhsh, M. & Lara-Castillo, N. Multiscale finite element modeling of mechanical strains and fluid flow in osteocyte lacunocanalicular system. *Bone* 137, 115328 (2020).

22. Silva, M. J. *et al.* Tibial Loading Increases Osteogenic Gene Expression and Cortical Bone Volume in Mature and Middle-Aged Mice. *Plos One* 7, e34980 (2012).
23. Chermiside-Scabbo, C. J. *et al.* Old Mice Have Less Transcriptional Activation But Similar Periosteal Cell Proliferation Compared to Young-Adult Mice in Response to in vivo Mechanical Loading. *J Bone Miner Res* 35, 1751–1764 (2020).
24. Holguin, N., Brodt, M. D., Sanchez, M. E. & Silva, M. J. Aging diminishes lamellar and woven bone formation induced by tibial compression in adult C57BL/6. *Bone* 65, 83–91 (2014).
25. Kerschnitzki, M. *et al.* Architecture of the osteocyte network correlates with bone material quality. *Journal of Bone and Mineral Research* 28, 1837–1845 (2013).
26. George, W. T. & Vashishth, D. Susceptibility of aging human bone to mixed-mode fracture increases bone fragility. *Bone* 38, 105–111 (2006).
27. Burr, D. B. Changes in bone matrix properties with aging. *Bone* 120, 85–93 (2019).
28. Wainwright, S. A. *et al.* Hip Fracture in Women without Osteoporosis. *J Clin Endocrinol Metab* 90, 2787–2793 (2005).
29. Heveran, C. M. *et al.* Chronic kidney disease and aging differentially diminish bone material and microarchitecture in C57Bl/6 mice. *Bone* 127, 91–103 (2019).
30. Colopy, S. A. *et al.* Response of the osteocyte syncytium adjacent to and distant from linear microcracks during adaptation to cyclic fatigue loading. *Bone* 35, 881–891 (2004).
31. Nguyen, J., Tang, S. Y., Nguyen, D. & Alliston, T. Load Regulates Bone Formation and Sclerostin Expression through a TGFbeta-Dependent Mechanism. *PLoS ONE* 8, e53813 (2013).
32. Tang, S., Herber, R. P., Ho, S. & Alliston, T. Matrix metalloproteinase-13 is required for osteocytic perilacunar remodeling and maintains bone fracture resistance. *Journal of Bone and Mineral Research* 27, 1936–1950 (2012).
33. Grafe, I. *et al.* Excessive transforming growth factor- $\beta$  signaling is a common mechanism in osteogenesis imperfecta. *Nature Medicine* 20, 670–675 (2014).

34. Janssens, K., Dijke, P. ten, Ralston, S. H., Bergmann, C. & Hul, W. V. Transforming growth factor-beta 1 mutations in Camurati-Engelmann disease lead to increased signaling by altering either activation or secretion of the mutant protein. *J. Biol. Chem.* 278, 7718–7724 (2003).
35. Dallas, S. L., Alliston, T. & Bonewald, L. F. Transforming Growth Factor- $\beta$ . in *Principles of Bone Biology* 1145–1166 (Principles of Bone Biology, 2008).
36. Kollmannsberger, P. *et al.* The small world of osteocytes: connectomics of the lacuno-canalicular network in bone. *New J Phys* 19, 073019 (2017).
37. Weinkamer, R., Kollmannsberger, P. & Fratzl, P. Towards a Connectomic Description of the Osteocyte Lacunocanalicular Network in Bone. *Curr Osteoporos Rep* 17, 186–194 (2019).
38. Wittig, N. K. *et al.* Canalicular Junctions in the Osteocyte Lacuno-Canalicular Network of Cortical Bone. *Acs Nano* 13, 6421–6430 (2019).
39. Lai, X. *et al.* The dependences of osteocyte network on bone compartment, age and disease. *Bone Research* 3, E318 (2015).
40. Hesse, B. *et al.* Canalicular Network Morphology Is the Major Determinant of the Spatial Distribution of Mass Density in Human Bone Tissue: Evidence by Means of Synchrotron Radiation Phase-Contrast nano-CT. *Journal of Bone and Mineral Research* 30, 346–356 (2015).
41. Wang, L., Ciani, C., Doty, S. B. & Fritton, S. P. Delineating bone's interstitial fluid pathway in vivo. *Bone* 34, 499–509 (2004).
42. Wang, L. *et al.* In situ measurement of solute transport in the bone lacunar-canalicular system. *P Natl Acad Sci Usa* 102, 11911–11916 (2005).
43. Wijenayaka, A. R. *et al.* Sclerostin stimulates osteocyte support of osteoclast activity by a RANKL-dependent pathway. *PLoS ONE* 6, e25900 (2011).
44. Gatti, V., Azoulay, E. M. & Fritton, S. P. Microstructural changes associated with osteoporosis negatively affect loading-induced fluid flow around osteocytes in cortical bone. *J Biomech* 66, 127–136 (2018).

45. Han, Y., Cowin, S. C., Schaffler, M. B. & Weinbaum, S. Mechanotransduction and strain amplification in osteocyte cell processes. *P Natl Acad Sci Usa* 101, 16689–16694 (2004).
46. Anderson, E. J. & Tate, M. L. K. Idealization of pericellular fluid space geometry and dimension results in a profound underprediction of nano-microscale stresses imparted by fluid drag on osteocytes. *J Biomech* 41, 1736–1746 (2008).
47. Kamioka, H. *et al.* Microscale fluid flow analysis in a human osteocyte canaliculus using a realistic high-resolution image-based three-dimensional model. *Integr Biol* 4, 1198–1206 (2012).
48. Verbruggen, S. W., Vaughan, T. J. & McNamara, L. M. Fluid flow in the osteocyte mechanical environment: a fluid–structure interaction approach. *Biomech Model Mechan* 13, 85–97 (2014).
49. Yee, C. S., Schurman, C. A., White, C. R. & Alliston, T. Investigating Osteocytic Perilacunar/Canalicular Remodeling. *Curr Osteoporos Rep* 17, 157–168 (2019).
50. Verbruggen, S. W., Garrigle, M. J. M., Haugh, M. G., Voisin, M. C. & McNamara, L. M. Altered Mechanical Environment of Bone Cells in an Animal Model of Short- and Long-Term Osteoporosis. *Biophys J* 108, 1587–1598 (2015).
51. Burra, S. *et al.* Dendritic processes of osteocytes are mechanotransducers that induce the opening of hemichannels. *Proc National Acad Sci* 107, 13648–13653 (2010).
52. McNamara, L. M., Majeska, R. J., Weinbaum, S., Friedrich, V. & Schaffler, M. B. Attachment of Osteocyte Cell Processes to the Bone Matrix. *Anatomical Rec* 292, 355–363 (2009).
53. You, L., Weinbaum, S., Cowin, S. C. & Schaffler, M. B. Ultrastructure of the osteocyte process and its pericellular matrix. *Anatomical Rec Part Discov Mol Cell Evol Biology* 278A, 505–513 (2004).
54. Kaya, S. *et al.* Lactation-Induced Changes in the Volume of Osteocyte Lacunar-Canalicular Space Alter Mechanical Properties in Cortical Bone Tissue. *Journal of Bone and Mineral Research* 32, 688–697 (2017).
55. Tang, Y. *et al.* MT1-MMP-Dependent Control of Skeletal Stem Cell Commitment via a  $\beta$ 1-Integrin/YAP/TAZ Signaling Axis. *Dev Cell* 25, 402–416 (2013).

# Chapter 5: The Role of TGF $\beta$ -regulated Osteocytic Perilacunar/canalicular Remodeling in Age-related Bone Fragility

## Introduction

Age-related bone fragility is the consequence of changes to material, cellular, and molecular mechanisms controlling both bone mass and bone quality over a lifetime. While age-related imbalances to the behaviors of osteoblast and osteoclasts, the bone lining cells responsible for depositing and resorbing bone respectively, are direct causes to age-related bone loss and osteoporosis, mechanisms controlling bone quality with age are less well understood. Consideration of bone quality is key in understanding age-related bone fragility and preventing fracture because losses to bone mass alone are not entirely predictive of fragility fracture in aged-

populations and even individuals receiving treatment for bone loss can still exhibit fragility fracture despite meaningful increases to bone mass<sup>1,2</sup>.

Bone quality consists of a collection of several interconnecting parameters including bone microarchitecture, bone tissue material properties, alterations to the chemical composition of bone, microdamage, and others<sup>3,4</sup>. Thus, bone quality and the age-related changes to it spring from the fundamental changes to bone organization, matrix material properties, and nanoscale mechanics. Targeting and understanding bone quality at the molecular scale offers potential new avenues to advance fracture prevention in the absence of bone mass deficits and will help close the gap of understanding behind the cellular and material mechanisms that lead to molecular bone aging and its resultant fragility.

Transforming growth factor beta (TGF $\beta$ ) is one of the few known molecular regulators of both bone mass and bone quality, exerting its effects through its action on all members of the bone remodeling unit<sup>3,5-8</sup>. Alterations to TGF $\beta$  signaling within the skeleton can lead to dysplasia and increased fragility in diseases including osteogenesis imperfecta and Camurati-Englemann disease<sup>9,10</sup>. TGF $\beta$  is deposited within the bone matrix by osteoblasts and osteocytes and released upon osteoclastic resorption. Liberated and activated from the bone matrix, TGF $\beta$  has multiple cellular targets within the skeleton impacting osteoclast differentiation, recruitment, and function and survival<sup>6</sup> and osteoblast proliferation and migration<sup>8,11</sup> helping balance both bone resorption and formation<sup>12,13</sup>. The role for TGF $\beta$  in osteocytes regulates homeostatic perilacunar/canalicular remodeling (PLR), by which osteocytes both resorb and replace their surrounding bone matrix in a dynamic process that supports bone quality and fracture resistance<sup>14-16</sup>. While hypothesized changes to TGF $\beta$  signaling with age are thought to be linked to imbalanced osteoclast and osteoblast action and thus bone loss with age<sup>17</sup>, the role of TGF $\beta$ -directed osteocyte perilacunar/canalicular remodeling in maintaining aspects of bone quality with age are unclear.

Previously, in a model of disrupted TGF $\beta$  signaling in osteocytes through removal of the TGF $\beta$  receptor type II (T $\beta$ RII) by Cre recombinase expressed under control of the DMP1 promoter, young male mice demonstrated several alterations to bone quality that resemble hallmarks of age-related bone fragility. Osteocyte-intrinsic ablation of T $\beta$ RII (T $\beta$ RII<sup>ocy-/-</sup>) resulted in severe bone quality defects without meaningful changes to cortical bone mass, including reduced fracture toughness similar to age-related bone fragility<sup>16</sup>. 3D visualization of the osteocyte lacunar/canalicular network (LCN) revealed that bones from T $\beta$ RII<sup>ocy-/-</sup> mice have increased canalicular tortuosity and lower canalicular number, cellular defects similarly found in aged bone<sup>18,19</sup>. The degeneration of the osteocyte LCN within T $\beta$ RII<sup>ocy-/-</sup> males occurred alongside coordinated repression of genes required for PLR, such as MMP13, MMP14, and Cathepsin K. Transcriptional arrays performed on osteocyte-enriched cortical bone RNA from wild-type aged mice showed lower expression of matrix modifying enzymes such as MMP13, MMP14 and Loxl2, among many others<sup>19</sup>. Results from this experiment also demonstrated systematic repression of the TGF $\beta$  signaling pathway in the bones of aged male mice. Thus, osteocyte-intrinsic repression of TGF $\beta$  signaling and the repression of PLR generates an “aged” brittle bone phenotype while aged bone displays lost activity within this same pathway hinting at a shared molecular mechanism.

Age-related fracture incidence and risk displays a large gender disparity with some estimates of increased fracture incidence in females as much as three times higher than men<sup>20-22</sup>. While much of this difference can be accounted for by differences in bone mass through differences in peak bone mass accrual, mature bone size, and an earlier decline in bone mass with age in females than males<sup>23,24</sup>, approximately half of age-related hip fractures in women do not occur in individuals with low bone mass<sup>2</sup>. This highlights the importance of understanding the contribution of bone quality towards fracture resistance specifically in females, especially in the light of evidence that the osteocyte LCN, whose integrity is linked to bone quality and cellular



function and is maintained by PLR<sup>19,25</sup>, degenerates more rapidly with age in females than in males<sup>18,26,27</sup> emphasizing sexually dimorphic aging in osteocytes. Interestingly, female T $\beta$ RII<sup>ocy-/-</sup> mice do not exhibit the same bone quality defects at young ages as their male counterparts. However, females did fail to induce further PLR during lactation, a metabolic challenge during which PLR is used to liberate calcium from the bone mineral for milk production<sup>14,28</sup>. The lack of this homeostatic mechanism in mutant reproductive age females raises additional concerns about PLR's contributions to declines in bone strength later in life, suggesting that the loss of TGF $\beta$ -directed PLR may be critical in the material decline of bone in aging females.

Age-related bone fragility in both sexes has been independently associated to stiffening of collagen within the bone matrix through increased crosslinking in the form of advanced glycation end products<sup>29,30</sup> (AGEs). These direct changes to the bone collagen matrix, among other chemical alterations, contribute to the reduced ability for collagen within aged bone to strain, as seen in synchrotron generated X-ray exposure during mechanical tests. Mechanical tensile tests on aged bone link a specific molecular culprit of increased collagen crosslinking with age to reduced mechanical performance on the molecular scale, but the cellular mechanisms responsible for their accumulation are currently unknown. Given the importance of osteocyte PLR in remodeling the internal bone compartments and the documented loss of expression of specific genes utilized by osteocytes to remodel their matrix, including several MMPs and other proteolytic enzymes, in aged bone, here we test the hypothesis that age-related degeneration of bone strength and quality via alterations to the bone material matrix are caused, at least in part, by a loss of TGF $\beta$  signaling and osteocyte activity.

## Results

### Aged and $T\beta RII^{ocy-/-}$ Bone Show Related Expression Changes to Bone Remodeling Genes and Regulatory Pathways

To determine similar molecular mechanisms of osteocyte function, RNA sequencing was performed on osteocyte enriched cortical bone from two independent sets of mice, 1) a series of progressively aged male mice from the C57BL/6 line (Buck Institute) and 2) a set of mice with osteocyte-specific ablation of TGF $\beta$  receptor II ( $T\beta RII^{ocy-/-}$ ) with bone quality defects and losses to perilacunar/canalicular Remodeling (PLR) activity. Aged mice were compared to young (2 months) mice from the same colony while  $T\beta RII^{ocy-/-}$  mice were compared to their littermate Wild-type controls (Ctrl).

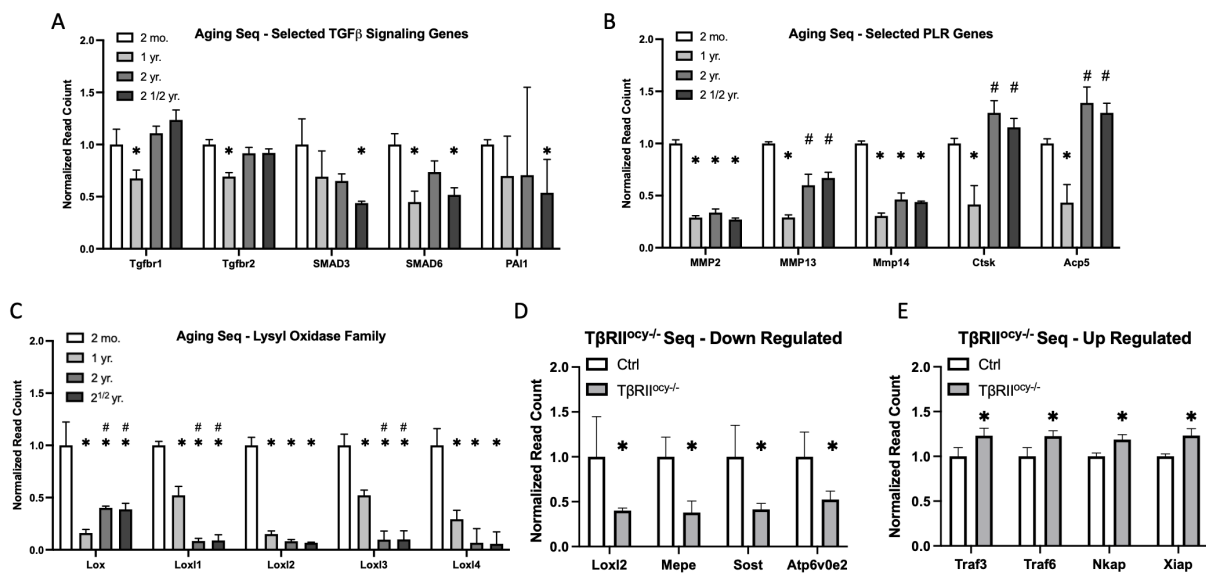


**Figure 5.1: Similar transcriptional regulation in aged bone and bone with osteocytic interruptions to TGF $\beta$  signaling.** RNA from progressively aged mice displayed reductions to expression by RNA sequencing for genes within the TGF $\beta$  signaling pathway (A) and genes utilized in osteocyte perilacunar canalicular remodeling (B). The Lysyl Oxidase family of enzymes responsible for enzymatic collagen maturation was also significantly repressed in aged bone (C). RNA sequencing for mice with osteocytic interruptions to TGF $\beta$  signaling, with known inhibition of PLR, displayed reductions to other markers of osteocyte behavior (D) including Lox12, and increased markers of inflammation frequently found in aged tissues such as markers of TNF and NF-kB signaling (E) and the senescence associated gene linked to osteoarthritis X-link Inhibitor of Apoptosis (*Xiap*). \*  $p < 0.008$  wrt. 4 months or wild type Ctrl. #  $p < 0.008$  wrt. 1 yr.

Aged C57BL/6 (WT) mice showed age-related changes to genes involved in PLR including matrix metalloproteinases 2, 13, and 14, while genes encoding acid-catalyzed enzymes Cathepsin K and ACP5 showed reductions at one year of age but rebounding activity at two (24 months) and two and a half years (30 months) of age (**Fig. 5.1A**). These mice also show commensurate changes to genes involved in TGF $\beta$  signaling including on the receptor level (*Tgfb1*, *Tgfb2*), the intracellular transducer level (*Smad3*, *Smad6*), as well as reductions to downstream target genes (*Pai1*) (**Fig. 5.1B**). In line with reductions to TGF $\beta$  signaling, aged bone demonstrated losses to expression of the TGF $\beta$ -regulated Lysyl Oxidase family of enzymes responsible for maturation of collagen type 1 in the bone extracellular matrix<sup>41</sup> (**Fig. 5.1C**).

In addition to reduced expression of genes important for bone remodeling through perilacunar canalicular remodeling, T $\beta$ RII<sup>ocy-/-</sup> bone showed differential regulation of genes in other important cellular functions. For example, T $\beta$ RII<sup>ocy-/-</sup> bone exhibited a loss in expression in Lysyl Oxidase-like 2 (*Loxl2*), one of the major isoforms of Lysyl Oxidase, indicating losses to osteocyte regulation of bone matrix crosslinking in these mice similar to what was found in aged-bone sequencing. Along the same lines, T $\beta$ RII<sup>ocy-/-</sup> mice showed losses to both *Mepe* and *Sost* as well as several membrane-bound ATP-driven ion channels, e.g. *ATP6v0e2*, genes important for osteocyte function, bone mineralization, and coordination of bone homeostasis. (**Fig. 5.1D**). Selected genes up-regulated in T $\beta$ RII<sup>ocy-/-</sup> bone, relative to Cre-negative controls (**Fig. 5.1E**) suggest increases to activity in both the TNF and NF- $\kappa$ B pathways through increased expression of *Traf3* and *Traf6*, members of the TNF receptor superfamily, and *Nkap*, an effector of NF- $\kappa$ B signaling. Interestingly, the senescent marker *Xiap*, X-linked Inhibitor of Apoptosis, linked to senescent-induced osteoarthritis<sup>42</sup>, was also found to a significantly differentially regulated and induced gene in these mice.

## **Aging and Losses to TGF $\beta$ Signaling affect Male and Female LCNs Differently**

The osteocyte lacunar/canalicular network is one of the largest cellular networks within the body whose functions range from cell-cell communications, maintenance of mineral homeostasis, and nutrient transport to the sensation of mechanical cues and the regulation of distal bone cell behavior in response to mechanical loading<sup>43,44</sup>. All osteocyte functions within the skeleton rely on the integrity and organization of the LCN, which degenerates or becomes disorganized in age and disease<sup>19</sup>. Alterations to the LCN in these situations have functional consequences and thus are a good marker to assess osteocyte health and function. To assay cellular health and the integrity of the osteocyte LCN, fluorescent confocal microscopy was used to capture and reconstruct large sections of the cellular network within the bone of young and aged T $\beta$ RII<sup>ocy-/-</sup> mice and their age-matched controls in 3D (**Fig. 5.2A, 5.2D**). Structural measurements of each network were made. Canaliculi per osteocyte is the most direct measure of osteocyte health and network integrity. In males, young T $\beta$ RII<sup>ocy-/-</sup> bone showed a genotype-dependent loss of canaliculi per osteocyte compared to controls. While the wild-type control bones displayed an expected age-related loss of canalicular connections, T $\beta$ RII<sup>ocy-/-</sup> males did not show further significant losses to cellular connections up to 15 months (**Fig. 5.2B**). An additional parameter that captures changes within the LCN is canalicular tortuosity, or the excess winding of individual channels between two adjacent osteocytes. Canalicular tortuosity in young lamellar bone increased with age in wild type mice, but young male T $\beta$ RII<sup>ocy-/-</sup> bone displayed early degeneration of the LCN as marked by increased canalicular tortuosity that was maintained with aging, (**Fig. 5.2C**). Female T $\beta$ RII<sup>ocy-/-</sup> bone, on the other hand, again displayed a resistance to the effect of diminished osteocytic TGF $\beta$  signaling at young ages, showing no differences in canalicular number and osteocyte canalicular tortuosity at young ages compared to controls (**Fig. 5.2E, 5.2F**). With age, both T $\beta$ RII<sup>ocy-/-</sup> and control females showed losses to canalicular number and increases to

canalicular tortuosity compared to their young counterparts but never differed between the genotypes at the same ages.

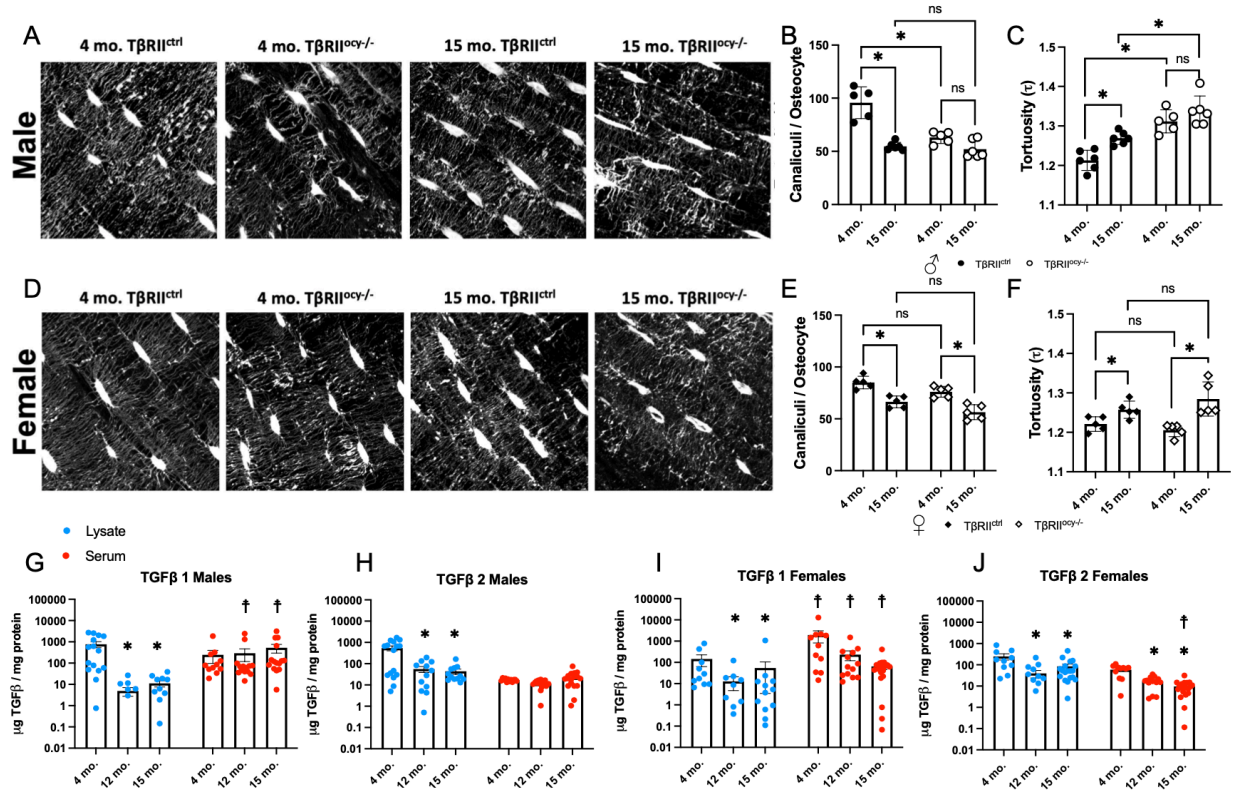


**Figure 5.2: Age-related degeneration of the osteocyte network in males occurs in a  $TGF\beta$ -dependent method but may occur through other mechanisms in females.** Visualization of the osteocyte lacunar/canalicular network via fluorescent confocal microscopy (A,D) shows a genotype specific degeneration of the network in males with losses to canaliculi/osteocyte (B) and increased canalicular tortuosity (C) in  $T\beta RII^{ocy-/-}$  bone that does not worsen with age. Females showed only age-related changes to these parameters that with mirrored changes in both genotypes (E,F).  $TGF\beta$  ligand levels from multiplexed ELISA of homogenized bone lysate showed age-related reductions to ligand abundance in the bone of both males and females (G-J). Circulating ligand levels remained stable over time in males but showed decreases in females, possibly influencing cellular changes. (B-f) \* $p < 0.0125$  in post-hoc pairwise Fischer's LSD test after two-way ANOVA (G-J) \* $p < 0.008$  wrt. 4 mo. within genotype control, † $p < 0.008$  wrt. age matched genotype control in post-hoc pairwise Fischer's LSD test after two-way ANOVA.

### Depletion of $TGF\beta$ Ligand Levels in Bone, but not in Circulation, with Age

$TGF\beta$  ligand, produced by both osteoblasts and osteocytes, is embedded in an inactive, latent state within the forming mineralized bone matrix. Upon bone resorption, either through osteoclastic action or locally by osteocyte perilacunar/canalicular resorption, this growth factor is

released, and activated either through acid catalyzation or mechanical force, from the bone matrix and is able to interact locally or systemically. In bone, TGF $\beta$  has many roles, including balancing bone deposition and resorption by controlling osteoblast and osteoclast numbers and activity and for regulating osteocyte PLR. Given the importance of TGF $\beta$  in regulating the behavior of cells that manage bone mass and quality, and the deregulation of bone cell activity with age, we sought to quantify the amount of ligand, and thus one measure of signaling potential, of TGF $\beta$  in bone over time. Though TGF $\beta$  ligand was quantified in both T $\beta$ RII<sup>ocy-/-</sup> bone and controls, very few genotype dependent differences were observed and genotype overall was not a significant predictor of ligand abundance in both uni- and multivariable linear mixed models (**Table 5.1**). Removal of genotype as a fit variable from this analysis did not alter the resultant fit coefficients (not shown), emphasizing its lack of influence on ligand abundance. The most significant predictor of ligand abundance overall from either tissue source was age, with coefficient weight increasing with time. In pairwise comparisons of ligand amount via age (i.e. vs 4 mo.), both TGF $\beta$ 1 and TGF $\beta$ 2 concentrations decreased with age in lysate analysis in both males and females (**Fig. 5.2G-J**). TGF $\beta$ 3 was too dilute or under the limit of detection of this assay for statistical analysis from either tissue source. The only significant trend with age in serum was a decrease over time in TGF $\beta$ 2 in females (**Fig. 5.2J**). Pairwise comparisons between tissue source (bone lysate vs serum), showed that, in both males and females, the levels of TGF $\beta$ 1 were higher in serum than in bone lysate, while TGF $\beta$ 2 levels were equivalent, except in 15-month-old females where TGF $\beta$ 2 levels in serum were lower than lysate concentrations. Investigation of interactions between variables in the multivariate analysis revealed a small interaction between gender and tissue source, showing that while there are no differences in the amount of TGF $\beta$  within bone, females overall had 25% more circulating ligand levels than males. Interaction of time and gender however, showed that although both sexes experienced losses of total ligand amount with time, females showed a greater loss than males.

**Table 5.1: Univariable and Multilevel linear mixed models describe age as the primary driver of lost TGF $\beta$  ligand abundance.** Prediction of ligand abundance from TGF $\beta$  ELISA shows the strongest predictor of concentration is age, followed by what tissue type (bone or serum) samples were taken from with serum usually having higher amounts of concentration. There is a small but significant association for females to exhibit higher ligand concentration than males. Genotype (T $\beta$ RII<sup>ocy-/-</sup> vs Ctrl) was not a significant predictor of ligand abundance.

Variables		Mean (SD)	Coefficient (univariable)	Coefficient (multilevel)
Age	4 mo.	-1.1 (1.0)	-	-
	12 mo.	-2.4 (1.7)	-1.32 (-1.76 to -0.87, p<0.001)	-1.36 (-1.83 to -0.89, p<0.001)
	15 mo.	-2.7 (1.8)	-1.58 (-2.01 to -1.15, p<0.001)	-1.56 (-2.01 to -1.11, p<0.001)
Tissue Source	Bone (lysate)	-2.8 (2.0)	-	-
	Serum	-1.5 (1.0)	1.32 (1.03 to 1.61, p<0.001)	1.44 (1.18 to 1.70, p<0.001)
Sex	Male	-1.9 (1.5)	-	-
	Female	-2.4 (1.9)	-0.49 (-0.81 to -0.18, p=0.002)	-0.34 (-0.66 to -0.01, p=0.020)
Genotype	T $\beta$ RII <sup>ctrl</sup>	-2.1 (1.7)	-	-
	T $\beta$ RII <sup>ocy-/-</sup>	-2.2 (1.8)	-0.04 (-0.35 to 0.28, p=0.819)	0.00 (-0.32 to 0.32, p=0.499)

### T $\beta$ RII<sup>ocy-/-</sup> Males Exhibits Accelerated Aging in Tissue Scale Mechanics

To determine tissue scale bone quality changes in the T $\beta$ RII<sup>ocy-/-</sup> bone and the contributions of PLR to age-related bone fragility, the T $\beta$ RII<sup>ocy-/-</sup> model of poor bone quality was allowed to age alongside its littermate controls and whole tissue scale bone strength was assayed via three point bending mechanical tests. Mice ages were grouped as young, but skeletally mature, (4 months) and aged with separate cohorts at 1 year (12 months) and at a later time point of 15 months in both male and female mice. Genotype-dependent alterations in tissue-scale skeletal mechanics - stiffness, force at fracture, and post-yield displacement - were found to be limited primarily to male T $\beta$ RII<sup>ocy-/-</sup> mice and these differences became more pronounced with age. Control males displayed normal growth and aging patterns<sup>45</sup> including the expected age-related losses in post-yield displacement from 4 to 12 months that remained stable thereafter from 12 to 15 months. The changes in WT mice with age were mirrored in young T $\beta$ RII<sup>ocy-/-</sup> bones. Specifically, young male T $\beta$ RII<sup>ocy-/-</sup> bones exhibited increased bending stiffness and ultimate fracture load compared

to age-matched controls (**Fig.5.3A, 5.3B**) that matched values seen in the aged controls.  $T\beta RII^{ocy-/-}$  bones, however, continued to display aging effects as seen in continued increases in stiffness and strength over time, remaining greater than controls at each time point. Post-yield displacement also demonstrated similar, if inverse, changes demonstrating an aged-like phenotype in young  $T\beta RII^{ocy-/-}$  bone with limited flexibility (**Fig. 5.3C**). This remained low with no further age-related significant changes in knockouts with time. Compared to age-matched controls,  $T\beta RII^{ocy-/-}$  post-yield displacement remained significantly lower, emphasizing an additional deficit in tissue level structural properties caused by the disruption in osteocytic TGF $\beta$  signaling.

While the resolution of three-point bending can be insensitive to material property changes, especially in the presence of macrostructural differences, aspects of these tests can be utilized for material insight. Unfortunately, observation of bending modulus (stiffness normalized by bone shape) in males (**Fig.5.3D**) as well as Work to Fracture as defined by the area under the Load-Displacement curve (**Sup. Fig. 5.1**) did not show significant differences between genotypes at any age. Work to Fracture, another material scale property gleanable from these tests, calculated as the area under the Load-Displacement curve, is a combination of a materials stiffness and post-yield behavior. Investigation into the Load-Displacement curves showed that although  $T\beta RII^{ocy-/-}$  bones were stiffer than controls and load values rose more rapidly than controls during testing, they tended to fracture sooner and terminate the length of the curve where control bones were more ductile displaying longer post-yield behavior before fracture. Thus, the two portions of this parameter independently showed differences in opposite directions in the genotypes, mathematical confounding the material assessment of these bones via Work to Fracture. However, observation of the fracture surfaces of the bones post-testing via SEM (**Fig. 5.3I, Supp. 5.1 E,F**) revealed striking differences between male controls and  $T\beta RII^{ocy-/-}$  bones. While control bones frequently displayed jagged or oblique fracture surfaces, evidence of cracking



and crack deflection mechanisms utilized by brittle materials during fracture to dissipate stress and increase toughness<sup>46</sup>,  $T\beta RII^{ocy-/-}$  bones did not display these behaviors and had flat fracture surfaces almost directly perpendicular to the direction of loading, indicative of a material weakness in male  $T\beta RII^{ocy-/-}$  bones not identified by this specific test.

Mechanical testing of female bones matched previous results of in young bone and revealed possible divergence from normal aging patterns with age in knockout females. Female controls and  $T\beta RII^{ocy-/-}$  bones did not significantly differ in terms of whole bone stiffness at any age but did show some trends towards increased stiffness over time as expected of aging (**Fig. 5.3E**). Similar relationships were found for other parameters including post yield displacement, fracture force, and bending modulus (**Fig. 5.3F-H**). Within their genotype, female  $T\beta RII^{ocy-/-}$  bones from 4 to 12 months displayed a significant increase to fracture load, likely the result of changes to bone structure and increases to their average bone size at this age. The only other significant change with age in females was a loss of post yield displacement in control females from 4 to 15 months, traditional of normal aging in bone. Female bones of each genotype did exhibit some other marginal age-related changes over time but not to a significant level over the time studied. Interestingly, female  $T\beta RII^{ocy-/-}$  bones at higher ages trended to exhibit some increases over controls to fracture load resembling the activity of male  $T\beta RII^{ocy-/-}$  bone but these changes were not significant

While sex differences are generally not compared in this study, females overall showed lower mechanical outcomes in structural and material parameters than males. Males did show greater percentage changes with age than females in both genotypes from 4 to 15 months.

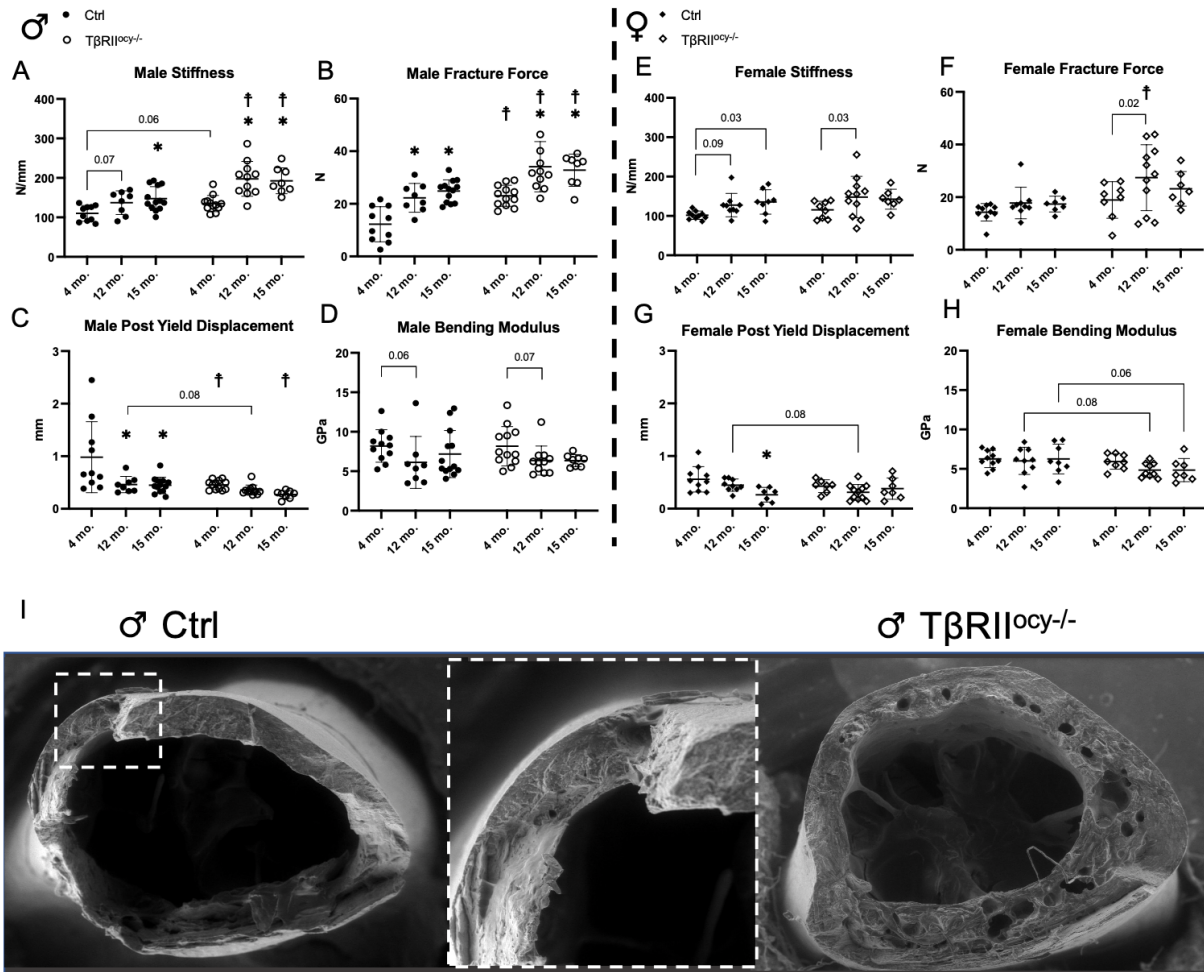


**Figure 5.3: *TβRII<sup>ocy-/-</sup>* bone demonstrates tissue level fragility similar to aged bone stiffening.** Three-point bend mechanical testing of femurs from *TβRII<sup>ocy-/-</sup>* bone and aged matched controls at 4, 12, and 15 months show an increase in stiffness (A) and fracture load (B) along with a decrease in post yield displacement (C) in male *TβRII<sup>ocy-/-</sup>* mice. Age-related trends in *TβRII<sup>ocy-/-</sup>* bone over time resembled accelerated patterns of aging in their wild type controls. Bending modulus was not any different by genotype for males but saw some age-related trending decreases (D). Females (E-H) do not show significant changes to their genotype controls except for elevated fracture load at 12 months. Fracture surfaces from male controls by SEM showed jagged and oblique fracture surfaces indicative of cracking that was absent from *TβRII<sup>ocy-/-</sup>* bone with flat fracture surfaces (I). \*p<0.008 wrt. 4 mo. within genotype control, †p<0.008 wrt. age matched genotype control in post-hoc pairwise Fischer's LSD test after two-way ANOVA.

### Accelerated Growth and Aging in $T\beta RII^{ocy-/-}$ Skeletal Morphology

To understand the changes to bone structural properties from 3-point bending, skeletal phenotyping via  $\mu$ CT of the cortical midshaft was completed to assay changes in bone shape and growth in  $T\beta RII^{ocy-/-}$  bone compared to controls. The most visually obvious (**Fig.5.4A**) difference in male  $T\beta RII^{ocy-/-}$  bone shafts compared to controls was the presence of large intracortical pores at young ages (**Fig. 5.4B**) that persisted or increased throughout their lifetimes. By 15 months, control bone began to display some porosity that decreased the difference between themselves and knockout mice at this age. Cortical porosity is a hallmark of normal aging in bone and is seen in other age-related human skeletal morbidities such as osteoporosis and diabetes<sup>47</sup>. These porosities result in a “trabecularization” of the cortex which resulted in thinner cortical thickness measurements by traditional Scanco algorithmic methods (**Fig. 5.4C**) despite a visual increase in “apparent” cortical thicknesses visually (**Fig. 5.4A**).

In addition to these porosities, there is a genotype-specific alteration in young male  $T\beta RII^{ocy-/-}$  bone shape towards larger, more circular bone compared to age-matched controls. Overall, increased size in the  $TGF\beta$  deficient males is noted by the increased area moment of inertia and total volume (**Fig.5.4D, 5.4E**) in the  $T\beta RII^{ocy-/-}$  bones. In mechanics, the area moment of inertia describes the resistance to bending or rotation of an object around a particular axis. For a hollow cylinder, such as diaphyseal cortical bone, this can be loosely described as  $MOI_n = \pi(d_o^4 - d_i^4)/64$  for rotation about any given ‘n’ axis and is influenced by the inner and outer diameters of the hollow cylinder. As such, it is a more precise description of bone shape illustrating the expansion of the cortical shell than the more granular total volume measurement that emphasizes bone mass rather than shape. Loss of genotype significance ( $P < 0.007$ ) at 12 or 15 months in either parameter is likely due to growth, such that control bones catch up with the accelerated growth within the  $T\beta RII^{ocy-/-}$  mice. Both controls and  $TGF\beta$ -deficient bone showed

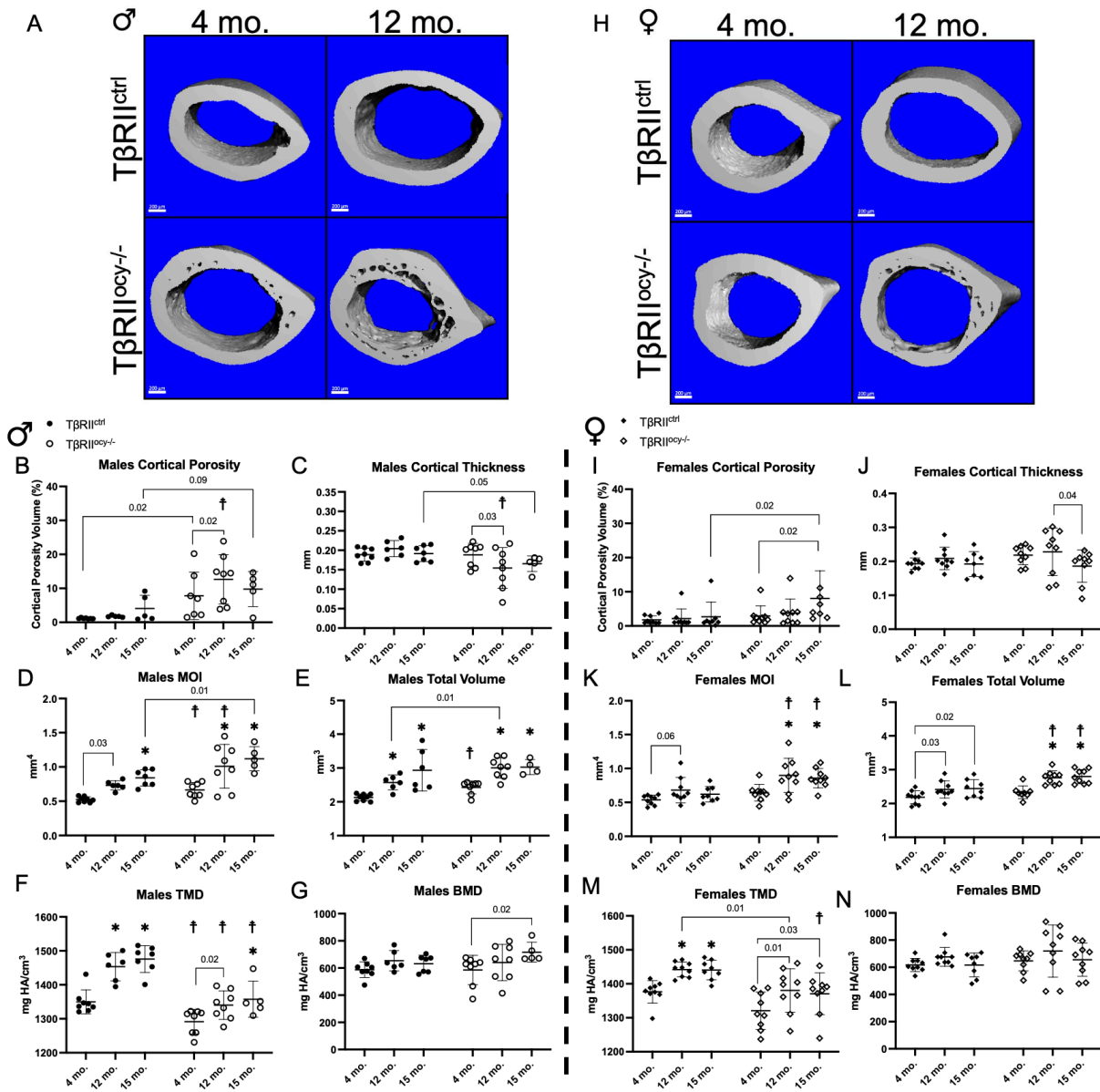


**Figure 5.4: Accelerated bone growth and aging in  $T\beta RII^{ocy-/-}$  cortical bone.** Male  $T\beta RII^{ocy-/-}$  bone exhibits several signs of an accelerated age-like phenotype including the development of intracortical porosities (A,G) that results in a trabecularization of the cortex and thus thinner cortical thickness measurements (B) the progressively worsen with age. Accelerated growth was also seen in male  $T\beta RII^{ocy-/-}$  bone through increased moment of inertia (C) and total volume (D) measurements. Though  $T\beta RII^{ocy-/-}$  males demonstrated a lower bone mineral density (E) the tissue mineral content as measured by TMD (F) within the analyzed volumes were no different across genotypes. Females do not show any genotype specific differences up until 1 year where they begin to display small increases to porosity and cortical trabecularization (H,I,N) increased bone size similar to males (J,K). Females also displayed lower bone mineral density and a slower age-related accrual bone (L) with no difference in total mineral density (M). \* $p < 0.008$  wrt. 4 mo. within genotype control, † $p < 0.008$  wrt. age matched genotype control in post-hoc pairwise Fischer's LSD test after two-way ANOVA.

significant expansion of bone with age compared to their young (4 mo.) counterparts, as expected of normal growth.

Tissue mineral density, describing the mass per volume of mineralized bone tissue (TMD), showed an age-related accrual of bone mineral in each genotype consistent with traditional growth and bone aging<sup>45,48</sup>. However,  $T\beta RII^{ocy-/-}$  males compared to controls displayed a lower TMD and mineral density within the bone at all ages studied (**Fig. 5.4F**)<sup>45,48</sup>. In addition,  $T\beta RII^{ocy-/-}$  males demonstrated a slower rate of accrual not showing significantly elevated TMD in comparison to their 4-month-old counterparts until 15 months. This contrasts with the assessment of mineral density inclusive of soft tissue and marrow across the whole bone, as seen in bone mineral density (BMD) (**Fig. 5.4G**) values where  $T\beta RII^{ocy-/-}$  males are not significantly different from controls despite their lower TMD. This is likely due to the increased size and amount of bone physically present in knockouts.

Female cortical bone morphology was largely resistant to the effects of disrupting TGF $\beta$  signaling in osteocytes at young ages (**Fig. 5.4H**), as was noted previously<sup>15</sup>. In addition, up to one year of age, bone growth in the  $T\beta RII^{ocy-/-}$  females is normal with no significant differences in the cortical compartment with respect to age matched controls (**Fig. 5.4I-N**), although at 12- and 15-months  $T\beta RII^{ocy-/-}$  females exhibited elevated MOI and total volumes compared to their age-matched controls, similar to the enlargement seen in the males. Other genotype-specific differences in the females include the beginnings of the formation of intracortical pores in the 15-month old female  $T\beta RII^{ocy-/-}$  bone (**Fig. 5.4I**) leading to the beginnings of cortical trabecularization (**Fig. 5.4H, 5.4J**), and lightly decreased tissue mineral density (**Fig. 5.4M**) in knock-out females compared to controls which reach significant levels by 15 months. Similar to males in this parameter,  $T\beta RII^{ocy-/-}$  females were slower to accumulate bone mineral with age their wild type controls.

**Table 5.2: Male  $T\beta RII^{ocy-/-}$  trabecular bone displays resistance to aging in  $\mu CT$  parameters.**

Trabecular bone parameters measured by  $\mu CT$  showed mainly genotype specific differences in males where male  $T\beta RII^{ocy-/-}$  resisted traditional age-related bone loss as seen in sustained BV//TV and TB.BMD and a tempered loss in connective density (CD) impacted by maintained Trabecular number and spacing with age. while control males and females of both genotypes experienced age-related bone loss. \* $p < 0.008$  wrt. 4 mo. within genotype control,  $^{\dagger}p < 0.008$  wrt. age matched genotype control in post-hoc pairwise Fischer's LSD test after two-way ANOVA.

Sex	Genotype	Age (mo)	BV/TV	TB. TMD (mg HA/cm <sup>3</sup> )	CD (1/mm <sup>3</sup> )	TB.N (1/mm)	TB.Sp (mm)	TB.Th (mm)	
M	T $\beta$ RII ctrl	4	0.16±0.04	1044.81±46.54	235.35±48.24	5.23±0.37	0.19±0.02	0.045±0.005	
		12	0.07±0.07 <sup>*</sup>	1112.88±31.58 <sup>*</sup>	71.38±118.28 <sup>*</sup>	3.11±1.12 <sup>*</sup>	0.35±0.10 <sup>*</sup>	0.049±0.006	
		15	0.05±0.05 <sup>*</sup>	1143.29±41.13 <sup>*</sup>	40.78±44.10 <sup>*</sup>	2.65±0.71 <sup>*</sup>	0.40±0.10 <sup>*</sup>	0.053±0.008	
	T $\beta$ RII ocy <sup>-/-</sup>	4	0.22±0.09	1110.76± 8.43 <sup>†</sup>	204.19±61.45	5.29±0.86	0.18±0.04	0.050±0.008	
		12	0.18±0.05 <sup>†</sup>	1160.49±30.16	146.04±89.69 <sup>*,†</sup>	4.24±0.60 <sup>†</sup>	0.23±0.03 <sup>†</sup>	0.052±0.009	
		15	0.17±0.06	1125.68±64.34	100.11±67.18 <sup>*</sup>	3.33±0.52 <sup>*</sup>	0.31±0.05 <sup>*</sup>	0.063±0.020	
	F	T $\beta$ RII ctrl	4	0.11±0.03	1125.09±16.84	115.69±38.85	3.76±0.32	0.27±0.03	0.050±0.002
			12	0.08±0.09	1205.10±57.69 <sup>*</sup>	12.83±11.95 <sup>*</sup>	2.07±0.45 <sup>*</sup>	0.51±0.10 <sup>*</sup>	0.069±0.033
			15	0.06±0.05	1195.93±53.49 <sup>*</sup>	16.73±21.98 <sup>*</sup>	1.77±0.27 <sup>*</sup>	0.59±0.09 <sup>*</sup>	0.063±0.023
T $\beta$ RII ocy <sup>-/-</sup>		4	0.18±0.10	1161.28±28.78	97.51±55.42	3.65±1.03	0.30±0.13	0.072±0.023	
		12	0.09±0.09	1192.31±35.88	25.91±19.64 <sup>*</sup>	2.20±0.51 <sup>*</sup>	0.49±0.10 <sup>*</sup>	0.064±0.022	
		15	0.09±0.09	1190.79±46.77	22.01±30.24 <sup>*</sup>	1.86±0.37 <sup>*</sup>	0.60±0.11 <sup>*</sup>	0.071±0.025	

Within the trabecular compartment (**Table 5.2**), control males saw rapid decreases to trabecular number and spacing with age as early as 6 months (not shown), resulting in lower connectivity density but saw no changes to trabecular thickness over time. Controls saw typical age-related losses to trabecular BV/TV, indicative of increases to age-related bone resorption and osteopenia<sup>45</sup>. Young male  $T\beta RII^{ocy-/-}$  bone showed increased BV/TV in comparison to control mice as well as higher mineral density (TB. TMD) but no differences to parameters such as trabecular number, thickness, or spacing. In contrast, BV/TV remained elevated over time in  $T\beta RII^{ocy-/-}$  males compared to controls, although it experienced marginal age-related losses, showing tempered age-related bone losses in knockout males. Trabecular thickness remained stable overtime in both controls and  $T\beta RII^{ocy-/-}$  bone and never differed from each other during the time observed.

Female trabecular values also were largely similar between genotypes, while age-related trends were more obvious than in male bones. In contrast to the male  $T\beta RII^{ocy-/-}$  bone that resisted aging, female mice of both genotypes experienced age-related losses to trabecular connectivity and trabecular number and increases to trabecular spacing without significant changes to

trabecular thickness (Table 5.2). Interestingly, similar to male  $T\beta RII^{ocy-/-}$  bone, female  $T\beta RII^{ocy-/-}$  trabecula showed significantly increased mineral density (TMD) and BV/TV at younger ages. These genotype differences were small however and disappeared with age.

## **Epistatic Relationship of Aging and Osteocytic-TGF $\beta$ Signaling Extends to Nanoscale Material Mechanisms**

In order to investigate the epistatic relationship between the changes in material properties with age and disruption to osteocytic TGF $\beta$  signaling as evidenced by the lack of cracking in male  $T\beta RII^{ocy-/-}$  bones during whole bone mechanical tests, synchrotron generated X-ray scattering and diffraction was utilized to investigate the composite materials of bone, collagen and hydroxyapatite mineral during mechanical stress<sup>30,49,50</sup>. Synchrotron X-ray exposure allows for the discrimination between collagen and mineral status through the difference in interaction of the X-ray beam with the periodic structures on different length scales of the bone composite materials. As described by Bragg's law,  $2d\sin\theta=n\lambda$ , where n is the number or order of peak observed, theta ( $\theta$ ), the angle at which incident X-rays on a material are returned (scattered, diffracted, reflected, etc..) to a detector depends on the wavelength of the X-ray ( $\lambda$ ) and the periodic distance between the material interacting with the beam (d). Leveraging the capability of synchrotron X-ray light sources to generate high intensity monochromatic X-rays (single, constant X-ray wavelength  $\lambda$ ), Bragg's Law mandates that the only remaining factor that can impact the angle of return from synchrotron X-ray-exposed material is the d-spacing. The hierarchical and ordered structure of bone is well suited for use with X-rays in this method because both collagen and hydroxyapatite display ordered, periodic structures that exist on length scales of different magnitudes. Collagen's ordered structure results in a d-spacing between consecutive collagen fibrils of approximately 67 nanometers, where the mineral c-lattice periodicity (the mineral crystal dimension parallel to the orientation of collagen periodicity) exists on a length scale approximately

100 times smaller than collagen's at 6-7 angstroms. This difference in periodic structure length in collagen and mineral generates separate signals from collagen and mineral components of bone from a monochromatic X-ray source. Collagen weakly scatters (shallow theta angle) X-rays while bone mineral diffracts (high theta) incident X-rays. This aspect of bone's hierarchical structure allows for Small Angle X-ray Scattering (SAXS) and Wide Angle X-ray Diffraction (WAXD) to be used to dissect the behaviors of collagen from mineral in bone. During exposure, when bone material is strained during mechanical testing, the periodic distances in each composite material stretch changing the relative d-spacing and altering the scattered or diffracted angle of the X-ray. This changes the position of the X-ray signal on the detector that can be traced over time throughout the mechanical test revealing the stretching, or straining, of the composite material from the separate SAXS and WAXD signals (**Fig. 5.5A**). Changes in the d-spacings over time are compared to the original unstrained d-spacing to generate composite material specific strains and that are then related to tissue level to determine the performance of bone's nanoscale components with respect to whole tissue deformation.

Within these *in-situ* synchrotron tensile tests, the amount of strain carried by the composite material (collagen or mineral) can be determined by plotting the composite material's X-ray captured strains against the tissue scale strain as calculated from whole tissue images captured on camera. Fitting this relationship can give an indication how much of tissue strain is captured by the specific composite material strain on the nanoscale, where a slope of 1 in this plot would indicate 100% of tissue strain is captured by whatever material is represented. For example, the slope of this line from the SAXS scans for the young, control males is around 0.75, indicating collagen is carrying the majority of strain on the nanoscale. With age, the best-fit slope of collagen specific strain to tissue strain increased from  $m=0.75$  at 4 months to  $m=0.84$  by 12 months, indicating that collagen is bearing a larger amount of tissue strain at 1 year of age than it was at 4 months implying an increased ability for aged collagen to carry strain, or a stiffening of the



collagen matrix with age. Compared to age and sex matched controls, collagen from the young  $T\beta RII^{ocy-/-}$  males displayed an inability to strain when uniaxially stretched with a best-fit slope of

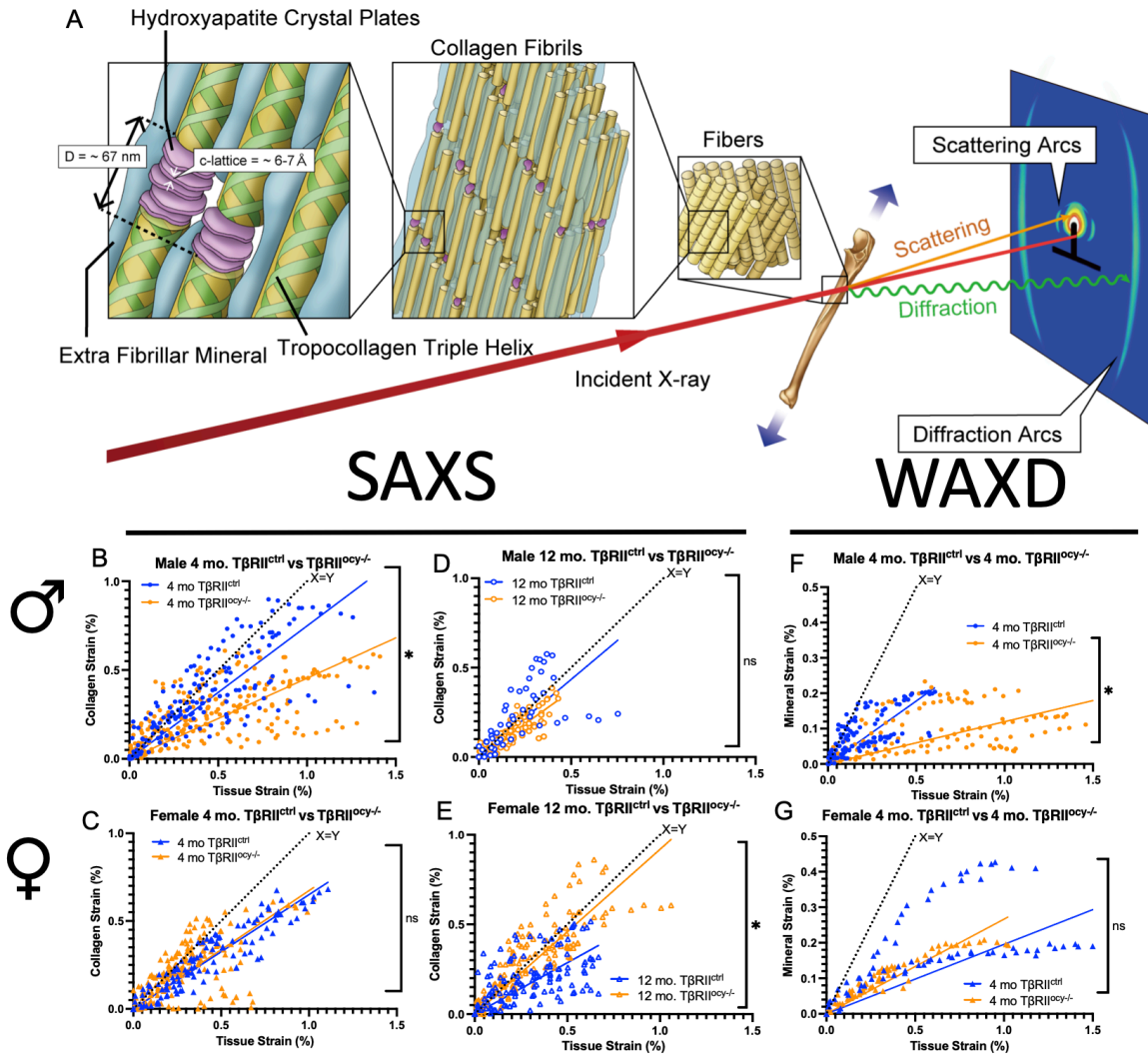


**Figure 5.5: Synchrotron SAXS/WAXD shows altered collagen behavior in  $T\beta RII^{ocy-/-}$  bone during in situ tensile testing.** Synchrotron generated X-ray exposure during tensile testing of forearm bones of  $T\beta RII^{ocy-/-}$  and controls at multiple ages generates signals unique to organic collagen (SAXS) and inorganic mineral components (WAXD) of bone based on their hierarchical size, order, and structure (A). Young  $T\beta RII^{ocy-/-}$  males showed a deficiency in collagen strain capacity compared to controls (B) that was not seen in female knockouts (C). With age, collagen in all genotypes tightened increasing strain capacity (slopes of best fits). Male and female  $T\beta RII^{ocy-/-}$  increased in strain capacity faster than their age-matched controls such that  $T\beta RII^{ocy-/-}$  males caught up with their controls (D) and females outpaced their age-matched controls in terms of strain capacity (E). Young mineral performance mirrored collagen behavior with young male  $T\beta RII^{ocy-/-}$  bones demonstrating an inability for mineral to carry strain (F) while females remained unaffected (G). \* indicates  $p < 0.006$  in comparisons of individual slopes to global fit in an extra sum-of-squares F test.

its collagen to tissue strain  $m=0.45$ , where the control bones rise with a slope of  $m=0.75$ , a value significantly lower than controls (**Fig. 5.5B**).  $T\beta RII^{ocy-/-}$  females do not display this collagen associated weakness at young ages as the males do, where fits of control bones result in a slope of  $m=0.65$  and female  $T\beta RII^{ocy-/-}$  at  $m=0.67$ . Both sets of scatter plots were able to be fit using the same regression and were determined to be non-statistically different from one another (**Fig. 5.5C**). Like its controls, 12 months,  $T\beta RII^{ocy-/-}$  bone also demonstrated an increase in its material to tissue strain slope from  $m=0.45$  to  $m=.74$ . This is a greater relative increase in slope from 4 months to 12 months, of 64%, than male controls, who only increased by 12%. With age, collagen carries increased amounts of tissue strain in both  $T\beta RII^{ocy-/-}$  males and controls, a process that is accelerated in  $T\beta RII^{ocy-/-}$  bone such that by 12 months  $T\beta RII^{ocy-/-}$  has overcome its initial inability to engage in straining and is no longer statistically distinguishable from its age-matched controls (**Fig.5.5D**). For females, control bones did not display any significant age-related changes to collagen strain slope values from  $m=0.65$  at 4 months to  $m=0.57$  at 12 months, fits were statistically insignificant between each other (**Supp. Fig. 5.2B**). However, Female  $T\beta RII^{ocy-/-}$  bones saw a dramatic increase in collagen-tissue strain from  $m=.67$  to a slope of  $m=0.92$ , resulting in a fit slope significantly different from control females at the same age (**Fig. 5.5E**).

In within-genotype comparisons between age groups, (i.e. male 4 mo. control vs 12 mo. control), to observe the effect of aging alone within each mouse line, slopes from fits for male control mice at 4 and 12 months do not differ from one another ( $P=0.1382$ ) (**Supp. Fig. 5.2A**) and neither do fits from female controls at the same ages ( $P=0.023$ ) (**Supp. Fig. 5.2B**), although this trended to see a small amount of slackening in female collagen with age. However, in the aged comparisons within the  $T\beta RII^{ocy-/-}$  line, there was significant amounts of tightening over time in both the males and females ( $P<0.0001$  for each) (**Supp. Fig. 5.2C-D**).

Comparison of mineral behavior from WAXD in the young bones showed similar results as SAXS.  $T\beta RII^{ocy-/-}$  males displayed a deficiency for the mineral to be strained or stretched when comparing best fit slopes of  $m=0.38$  for controls and  $m=0.24$   $T\beta RII^{ocy-/-}$ , fits statistically different from one another ( $p<0.0001$ ) (**Fig.5.5F**). Fits from mineral-tissue strains from WAXD for females resulted in slopes of  $m=0.2$  for controls and  $0.25$  for  $T\beta RII^{ocy-/-}$ . Likely because of high variability in individual tests and low sample number (N) from this test, comparisons of these fits are currently statistically insignificant (**Fig.5.5G**).

### **Collagen Modification and Arrangement is altered in $T\beta RII^{ocy-/-}$ mice**

Post-translational modification of type I collagen in the form of inter-fibril crosslinks has been shown to alter mechanical properties of bone in situations of normal aging and diseases such as diabetes<sup>29</sup>. While there are multiple types of chemical crosslinks present in the collagen fiber super structure, they predominantly fall under two categories: either enzymatically or non-enzymatically generated<sup>51</sup>. Enzymatic crosslinks form as part of the normal maturation of collagen during its self-assembly and are regulated by the family of Lysyl Oxidase enzymes and are site limited to specific amino acids residues along the collagen fiber. The normal maturation process transforms weaker divalent crosslinks to more stable trivalent crosslinks imparting stability to the collagen superstructure<sup>52</sup>. With time these types of crosslinking events stabilize and reach a homeostatic level in fully mature collagen. Non-enzymatic crosslinks, on the other hand, occur spontaneously on any open lysine or arginine residue along or between collagen fibrils and can accumulate to up to 5-10 times greater than their enzymatic counterparts with aging<sup>52</sup>. This spontaneous crosslinking is often a result of glycosylation or glycooxidation events that can form permanent excessive intra- and interfibrillar chemical connections among collagen fibers. These types of crosslinks are known as Advanced Glycosylation End-products (AGEs) and negatively impact collagen's ductility and ability to engage in specific deformation mechanisms such as

sacrificial bonding and inter-fibril sliding during deformation<sup>53</sup>. Additional AGEs that do not form crosslinks but instead interact with the surface receptor of AGEs, RAGE, can also form as part of this process and these have many different impacts on bone metabolism and remodeling<sup>54</sup>. One of the most common species of crosslinking AGEs that form within bone is pentosidine, a cyclic 5-member carbon structure that naturally fluoresces allowing for it to be relatively easily quantified using a standard plate reader. Pentosidine represents only a fraction of crosslinking AGEs in bone as other non-fluorescent AGEs do accumulate in bone, including Carboxymethyl lysine (CML), and these are associated with increased risk of osteoporosis and fracture.<sup>55-57</sup> Given the importance of collagen ductility in bone quality and strength, and the abundance to which AGEs naturally accumulate in bone over time, fluorescent AGEs were quantified in the bones of  $T\beta RII^{ocy-/-}$  and control mice.

Quantification of fluorescent AGEs from  $T\beta RII^{ocy-/-}$  bones from both sexes showed no genotype-dependent differences at young ages compared to control mice (**Fig.5.6A, 5.6B**). By 12 months, both control and  $T\beta RII^{ocy-/-}$  bones showed an increase in AGE content compared to their young within-genotype counterparts, as is expected of aging bone. Interestingly, both male and female  $T\beta RII^{ocy-/-}$  bone saw an additional amount of AGE accumulation compared to their age-matched wild-type controls at 12 months, resulting in the aged  $T\beta RII^{ocy-/-}$  bones to have the highest concentration of AGEs normalized to total collagen content. There were no differences in AGE concentration between male and female mice within genotypes at both ages studied.

An additional marker of collagen health and a marker of bone remodeling and proper upkeep is collagen orientation. Collagen within lamellar bone is normally aligned in regular parallel sheets, or lamella. Disorganization of this arrangement has been noted in the bones of mice with disrupted osteocyte perilacunar remodeling through losses of MMP13, a proteolytic enzyme responsible for mediating collagen degradation<sup>58</sup>, and in glucocorticoid induced osteocyte death and osteonecrosis<sup>33</sup>. To evaluate ensemble collagen order, a feature of the SAXS pattern

describing collagen orientation was quantified. During exposure, scattering of X-rays from bone generates smeared ‘arcs’ of signal whose width describes how well collagen is aligned, thus analyzing the intensity distribution of these arcs yields information about collagen lamellar orientation. The numeric representation of this ‘smearing’ feature of the scattering arcs is known

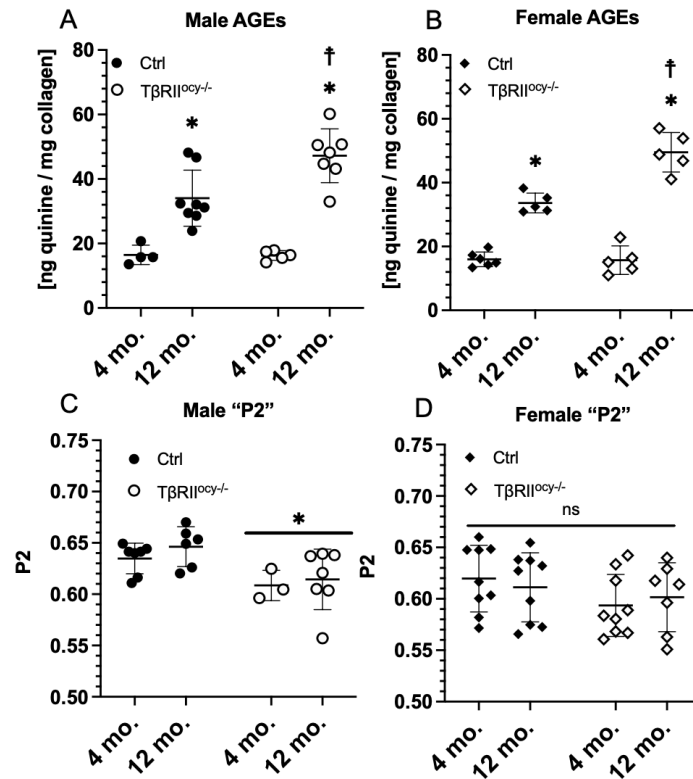


**Figure 5.6: Collagen quality is impacted by both age and osteocytic TGFβ signaling.** Quantification of nonenzymatic collagen crosslinking in the form of advanced glycation end products (AGEs) shows an accelerated rate of accumulation in male and female TβRII<sup>ocy-/-</sup> bone (A,B), while collagen structural order as assayed by synchrotron generated SAXS showed a marginal but statistically significant loss of order in male (C), but not female (D), TβRII<sup>ocy-/-</sup> bone independent of age.

as the “Hermans Orientation Factor” or the Second Legendre Coefficient (P2)<sup>59,60</sup>, and ranges from 1, perfectly linearly aligned collagen fibers, to 0, representing complete randomness and disorder in the fiber arrangement.

Comparison of this parameter from the unstrained condition from male and female control and TβRII<sup>ocy-/-</sup> bone at both 4 months and 12 months showed a minor loss of orientation in male TβRII<sup>ocy-/-</sup> bones as a main effect of genotype in two-way ANOVA analysis, with no change with

respect to age, and no alterations to female bones in either genotype at either age (**Fig. 5.6C, 5.6D**).

### **Discussion**

Age-related bone fragility arises as a consequences of lost bone mass and quality, but while mechanisms controlling bone mass with age are well understood, the cellular and molecular culprits behind lost bone quality are not clear and there is a lack of treatments specifically targeting this root cause of age-related fracture. TGF $\beta$  is one of few known master regulators of cellular activity across all main bone cell types with many congenital skeletal dysplasias attributed to either under or over activation, further signifying its importance as a keystone in skeletal homoeostasis during growth and aging<sup>5,9,11,17,61</sup>. Aged bone shares many tissue and cellular level characteristics to bone with limited TGF $\beta$  signaling in osteocytes including reduced fracture resistance, a degenerated osteocyte LCN, and lower levels of gene expression for enzymes involved in osteocyte PLR. Additionally, naturally aged bone shows decreases to gene expression within the TGF $\beta$  signaling pathway on the receptor, transducer, and effector levels. Given the conspicuous similarities in these models of bone fragility and the implication of lost TGF $\beta$  signaling as a potential mechanism behind the development of bone fragility, we hypothesized that specific molecular defects common with age may arise due to a loss in TGF $\beta$ -directed osteocyte perilacunar canalicular remodeling, or a loss of bone material matrix upkeep on the cellular and molecular levels.

The role of TGF $\beta$  in systematic aging is complex but has been linked to processes such as cellular senescence, inflammation, neurodegenerative disorders, cancer, and obesity among others<sup>62</sup>. In many of these cases, increases to the level of TGF $\beta$  signaling have been implicated as a potential root molecular cause<sup>32</sup>. While TGF $\beta$  is generated by a wide variety of cell types, it is actively stored in the mineralized matrix of the skeleton in an inactive state by bone forming osteoblasts and osteocytes<sup>17</sup>. Upon bone resorption, TGF $\beta$  ligand is released from storage within

the bone matrix and converted into its active form allowing it to act both locally and systemically. With age, there is a natural uptick in bone resorption as osteoclast action and number increases<sup>17,63</sup>, potentially releasing elevated levels of TGF $\beta$  into circulation while simultaneously depriving internal bone osteocytes of a needed stimulus for proper bone upkeep. This hypothesis could help explain the seemingly contradictory nature of age-related TGF $\beta$  effects where systemic aging is associated with heightened activity in this pathway while reductions to it in bone lead to disruptions in normal cellular activity and subsequent bone fragility. While there are many factors of this theory left to be interrogated, deprivation of the signaling events caused by TGF $\beta$  ligand within osteocytes through a removal of Tgfr2 at the cellular level results in the generation of a bone phenotype eerily reminiscent of aged bone complete with degenerated osteocyte networks and increased bone fragility. Given these deficits appear at young ages in T $\beta$ RII<sup>ocy-/-</sup> bone, interrogation of what other processes of bone growth or aging arise over time within this TGF $\beta$  deprived context can help elucidate specifically what aspects of bone aging and its mechanical consequences are solely or partially dependent on functioning TGF $\beta$  signaling within osteocytes.

The tracking of several aspects of bone quality across the lifetime of mice with osteocytic interruptions to TGF $\beta$  signaling confirmed several aspects of our initial hypothesis. While aged bone does resemble young bones with disrupted TGF $\beta$  signaling in osteocytes<sup>19</sup>, it was unclear what portions of the aged phenotype were TGF $\beta$  specific and osteocytic in origin. Visualization of the osteocyte network from young and aged T $\beta$ RII<sup>ocy-/-</sup> mice offered the most direct assessment of the effects of age and TGF $\beta$  deprivation. Young male knockouts showed the greatest initial changes with losses to LCN integrity through lost osteocyte canalicular number and increases to individual canalicular tortuosity, changes we have demonstrated to be hallmarks of larger degeneration within the network with negative functional impact. Again, similar to previous results<sup>15</sup>, young females of this line were resistant to the effects of lost Tgfr2 in homeostatic conditions as measured by these parameters. With age, control males displayed the same defects

that young  $T\beta RII^{ocy-/-}$  mice showed while aged  $T\beta RII^{ocy-/-}$  mice did not display any further degeneration of their network. This is potentially because at the cellular level, the inability of osteocytes to engage in TGF $\beta$  signaling is sufficient to generate an aged cellular phenotype, signifying that aging in the male bones occurs through a TGF $\beta$ -dependent mechanism. Over time, females of both genotypes demonstrated canalicular loss and increased network tortuosity, showing that although the mechanism by which they degrade may be TGF $\beta$  independent, the phenotypic and functional consequences of age are the same for both males and females.

The TGF $\beta$  superfamily is highly diversified and has the ability to engage in signaling not only through its own receptors, but also through various other related receptors including those for activin and BMPs<sup>62</sup>, and many of these receptors are relevant to osteocyte responses to relevant stimuli including fluid flow shear stress<sup>64</sup>. Thus, despite the ability for young mutant females to compensate for the loss of *Tgfr2* in some measures of bone quality as seen here and in previous studies<sup>15</sup>, the age-related degeneration of the LCN in female bone may not be entirely TGF $\beta$  independent. ELISA results document the loss of ligand from both the bone compartment and from circulation. While the direct levels of crosstalk among receptors in the TGF $\beta$  family are not known in this context, the decreased capability for these events to occur with age would be directly related to decreasing amounts of ligand and signaling capability. Thus, as ligand levels within bone drop with age, specific defects related to the loss of TGF $\beta$  may arise from the loss of signaling either on the receptor or the ligand level, even if female systems have a mechanism to compensate for loss of *Tgfr2*.

On the tissue scale, the loss of TGF $\beta$  signaling in young bone seems to result in an accelerated aging or growth of bone. From three-point bend tests young male  $T\beta RII^{ocy-/-}$  mice demonstrated lost ductility as exhibited by the loss in post-yield displacement and a compensatory increase to stiffness and failure load compared to controls. Overtime, control bone also increased in stiffness and ultimate load while also losing ductility, as expected of age in bone. By 15 months



control bone quantitatively resembled the 4-month-old  $T\beta RII^{ocy-/-}$  bone in these measurements, signifying that young  $T\beta RII^{ocy-/-}$  males did display an aged macromechanical phenotype early in life. Interestingly,  $T\beta RII^{ocy-/-}$  bone progressively followed typical age-related trends continuing to increase stiffness and strength overtime, implying that while these bones were predisposed to obtain age-related defects early, they can accrue more severe changes over time. This is significant because it emphasizes the difference in mechanism on the biologic scale from cells to whole tissue where the cellular defect, if established early, may continue to impact progressive change on the tissue scale.

Female  $T\beta RII^{ocy-/-}$  bone primarily displayed aging effects rather than genotype differences to bone mechanics through time-dependent trends towards increases in stiffness and fracture load. Interestingly though,  $T\beta RII^{ocy-/-}$  females did begin to display some possible accelerated aging past 12 months with increased fracture force and a small loss in post yield displacement. This pattern is similar to what occurred in male mice, and their emergences later in life in females suggests that the resistance or compensation for lost  $TGF\beta$  signaling capability in females may dissipate over time raising additional questions about the molecular mechanisms supporting osteocyte behavior in females. Overall, however, changes to bone mechanics in the aged  $T\beta RII^{ocy-/-}$  females hints that in aged contexts, lost osteocyte function contributes to changes to bone mechanics in females.

The changes to bone mechanics seen on the tissue scale are primarily alterations to parameters stemming from bone structure, but the reason for the alterations to structure are unclear.  $T\beta RII^{ocy-/-}$  male alterations to bone shape, seen through  $\mu$ CT of the femoral shafts, included increases to bone volume, MOI, and cortical thickness. Following simple application of beam theory, it is logical that increases to bone thickness and size would result in a less pliable structure that is able to withstand higher loads prior to fracture. Interestingly,  $T\beta RII^{ocy-/-}$  males were hypomineralized, likely resulting in a bone with lower modulus, as seen in nanoindentation of

these bones previously . This loss of bone mineral density would directly impact the unit for unit ability for bone to resist deformation and support load implicating a loss in material properties as well as changes to structural ones. Three-point bending tests can obscure differences in material properties as it is sensitive to structural changes within the material tested. In the  $T\beta RII^{ocy-/-}$  males with elevated stiffness, this was noticed in the lack of an expected material difference between the genotypes seen through bending modulus. This is due to the normalization of stiffness by bone size that is required in this method for obtaining moduli. Because  $T\beta RII^{ocy-/-}$  males on average displayed the larger overall bone size, these changes in tissue level stiffness did not translate to a detectable material level difference by this method.

Several observations from this study suggest that  $T\beta RII^{ocy-/-}$  bone does have material scale differences. Primarily, the mechanisms of failure during three-point bending raised concerns about the integrity of the bone material.  $T\beta RII^{ocy-/-}$  males fractured at lower strain and failed to engage in traditional toughening mechanisms such as crack deflection, signifying a material deficit that may predispose them to fragility fracture. This is evidenced by the flat fracture surfaces of  $T\beta RII^{ocy-/-}$  bone in contrast to the jagged and often oblique fracture surfaces of controls. Observation of the load-displacement curves generated during three-point bending (**Supp. Fig. 5.1A,B**) shows dips (red asterix) of load values during testing of controls corresponding to cracking events where built up stress within the material may have been dissipated before continued deformation of material increased applied load. These behaviors were absent from male  $T\beta RII^{ocy-/-}$  who's behavior during testing was to rapidly increase load at lower strain and more often catastrophically fail without engaging in much post yield deflection. The inability to engage in cracking signifies a more fundamental change to the bone material and supports the role of osteocytic  $TGF\beta$  signaling in a critical toughening mechanism.

An additional marker of lower material scale properties in the  $T\beta RII^{ocy-/-}$  bone is the significant absence of bone mineral density as seen in  $\mu$ CT assessment of TMD. Male mutants

at all ages displayed a lower mineral density than controls at all ages, implying a less mineralized bone matrix with possibly inferior material properties. This signal of lower material properties in the male  $T\beta RII^{ocy-/-}$  mice was demonstrated by females around the same time that changes to bone mechanics begin to emerge in female knockouts. By 12 months, female  $T\beta RII^{ocy-/-}$  bone compared to their age matched controls, begin to demonstrate lost TMD, showing significant differences by 15 months. Following the idea that lost material property would feedback and result in compensatory change in size tracks in females  $T\beta RII^{ocy-/-}$  bone post 12 months, implying that females lose their ability to regulate bone homeostasis after a certain point and become to resemble their male counterparts on the tissue scale.

One important aspect of the  $T\beta RII^{ocy-/-}$  phenotype is the generation of intracortical pores. While the precise mechanism for the appearance is currently unclear, these pores represent a significant change to bone architecture underlying cellular behavior. Additionally, their accelerated emergence in females of this line post reproductive age points again to females succumbing to lost osteocyte  $TGF\beta$  signaling capacity. Importantly, the development of intracortical pores is a feature of other diseases in bone related to aging including obesity and diabetes. Aged bone naturally forms these additional pore structures<sup>18,47</sup> and has obvious impacts to bone health, increasing bone surface area and availability for osteoclastic bone resorption. While how and why pores like these form in bone with age and disease is unknown, their presence in bone without functioning  $TGF\beta$  signaling in osteocytes further points to the importance of this cellular process in maintaining bone health and how its loss may predispose or be casual in bone aging.

Changes to bone mechanics, losses to mineral density, and the inability to engage in cracking during failure prompted the investigation of bone material properties. Given that limiting  $TGF\beta$  signaling in osteocytes directly impacts osteocyte's ability to manipulate their surrounding bone through PLR by loss of matrix remodeling enzymes, we sought to determine how this impacts bone mechanics on the same relevant scale. Results from *in-situ* synchrotron tensile

tests showed that collagen from male  $T\beta RII^{ocy-/-}$  bone had an inability to engage in fibril straining as seen by a lack of increasing collagen D periodicity during bone stretching. This confirmed a material scale defect in the young  $T\beta RII^{ocy-/-}$  males, where bone that is more pliable would result in lower bending resistance and explain the corresponding need for altered bone structure to compensate. However, quantification of excess collagen crosslinking via AGE fluorescence did not show differences between young controls and knockout bones, eliminating non-enzymatic crosslinking as a molecular defect responsible for this specific weakness.

Although non-enzymatic crosslinking is not sufficient to explain the initial weakness present in young  $T\beta RII^{ocy-/-}$  bone, AGEs are not often present in high enough concentrations in young bone to be of consequence. With age, AGE concentration can increase as much as ten times initial concentrations increasing their relevance to bone mechanics with age. Given that osteocytes normally recycle their surrounding matrix, halting or diminishing this behavior may increase the rate at which AGEs accumulate in bone. Quantification of AGEs in aged  $T\beta RII^{ocy-/-}$  bone revealed this with AGE concentrations in aged knockouts significantly elevated compared to wildtype controls. While wild type mice did show about twice their initial value of AGE crosslinking from 4 to 12 months, as expected of age-related increases to AGEs,  $T\beta RII^{ocy-/-}$  bones contained triple the amount of their 4-month values, demonstrating an accelerated accumulation of non-enzymatic crosslinking in the bone without osteocytic bone remodeling. This resulted in 12-month  $T\beta RII^{ocy-/-}$  bones, in both males and females, to contain approximately 30% higher AGEs than normally aged controls. This occurred alongside dramatic increases to  $T\beta RII^{ocy-/-}$  collagen strain in both aged conditions, where controls with lower amounts of non-enzymatic crosslinking did not display significantly increased collagen strain. This is perhaps because in wild type mice this amount of accumulation does not yet have a mechanical consequence or that there are other regulatory mechanisms at play promoting proper collagen function absent in knockout bones. The data from these experiments suggest that loss of osteocytic TGF $\beta$  signaling compromises

material properties of the bone collagen matrix in two ways: 1) unknown deficits that result in collagen with insufficient tensile properties as seen in the young male  $T\beta RII^{ocy-/-}$  bone and 2) an accelerated accumulation of non-enzymatic crosslinks with age, including fluorescent AGEs (pentosidine) and likely others (CML), that can increase crosslinking within the matrix resulting in a stiffer bone. While the young females did not display this first deficit, perhaps due to some compensatory mechanism, it is important to note that collagen tightening and accelerated AGE accumulation did occur in knockout females at 12 months, again suggesting that females begin to display the effects of lost  $TGF\beta$  signaling in osteocytes over time. Whatever the case for normal aging, proper  $TGF\beta$  signaling in osteocytes limits the accumulation of AGE chemical alterations to the bone matrix that have mechanical consequences towards bone stiffening.

Synchrotron analysis of mineral behavior from WAXD revealed similar patterns of material regulation in young bone. In the  $T\beta RII^{ocy-/-}$  males, mineral crystal lattice spacing did not increase in knockouts during bone straining to the same rate as controls. This may be because the bone itself is hypomineralized and the mineral crystals less able to transfer strain among themselves. The absence of this behavior in mutant females, and non-significant differences in TMD at this time in female  $T\beta RII^{ocy-/-}$  and control bones supports this claim, although WAXD results from females requires clarification at this time.

The loss of  $TGF\beta$  signaling in osteocytes generates an accelerated aging phenotype in bone by altering cellular performance that compromises fundamental material properties and leads to altered bone structure. In the absence of  $TGF\beta$ , the osteocyte network degenerates, an early sign of cellular dysfunction. Osteocytes normally regulate their surrounding bone material with a wide range of secreted factors that require  $TGF\beta$  for expression including matrix modeling and remodeling enzymes such as *Loxl2* and *Mmp13*. Loss of this cellular action results in a collagen matrix with insufficient tensile properties. In addition, the removal of osteocytic  $TGF\beta$  signaling results in a hypomineralized bone matrix, possibly leading to a softer, more pliable

mineral. The inability to regulate both the organic and mineralized inorganic components of bone on the cellular scale results in bone with poor material quality that cannot properly engage in molecular deformation and toughening mechanisms, as seen through the lack of collagen strain from SAXS and an absence of crack deflection on the tissue scale during failure. Through unknown mechanisms,  $T\beta RII^{ocy-/-}$  bone seems to compensate for their poor material quality by increasing the amount of bone present and by altering their bone shape. With time  $TGF\beta$  mutant bone demonstrates an accelerated accumulation of nonenzymatic collagen crosslinking compared to age-matched genotype controls, likely influencing the rate at which collagen strains during mechanical stress, perhaps as another compensatory mechanism or more straightforwardly a consequence of lost cellular bone remodeling. In any case, this results in less pliable bone potentially more prone to fragility fracture. The changes that occur in younger  $T\beta RII^{ocy-/-}$  bone foretell the changes that occur in wildtype bone over time. Wildtype bone demonstrates similar changes to bone shape with age as well as increases to nonenzymatic collagen crosslinking. Several markers of  $TGF\beta$  signaling and PLR are decreased in aged bone, suggesting that lost osteocyte mediated bone remodeling is behind changes to bone material with age, namely the increase in nonspecific collagen crosslinking and the consequent tightening of the bone matrix. While these changes can occur along-side changes declines bone mass with age, the identification of the accelerated accumulation of AGEs in a  $TGF\beta$  deficient context reveals a bone-mass independent, osteocyte-specific mechanism that negatively impacts bone quality.

Synthesis of these findings reveal a role for  $TGF\beta$  mediated osteocyte PLR in age-related bone quality. As PLR acts as a homeostatic mechanism that maintains bone quality, losses to its behavior would consequently result in lack of regulation of chemical and material changes to the bone matrix with age. Wildtype aged bone demonstrated losses to  $TGF\beta$  signaling gene expression while levels of  $TGF\beta$  ligand decline in bone with age suggesting that cellular behaviors

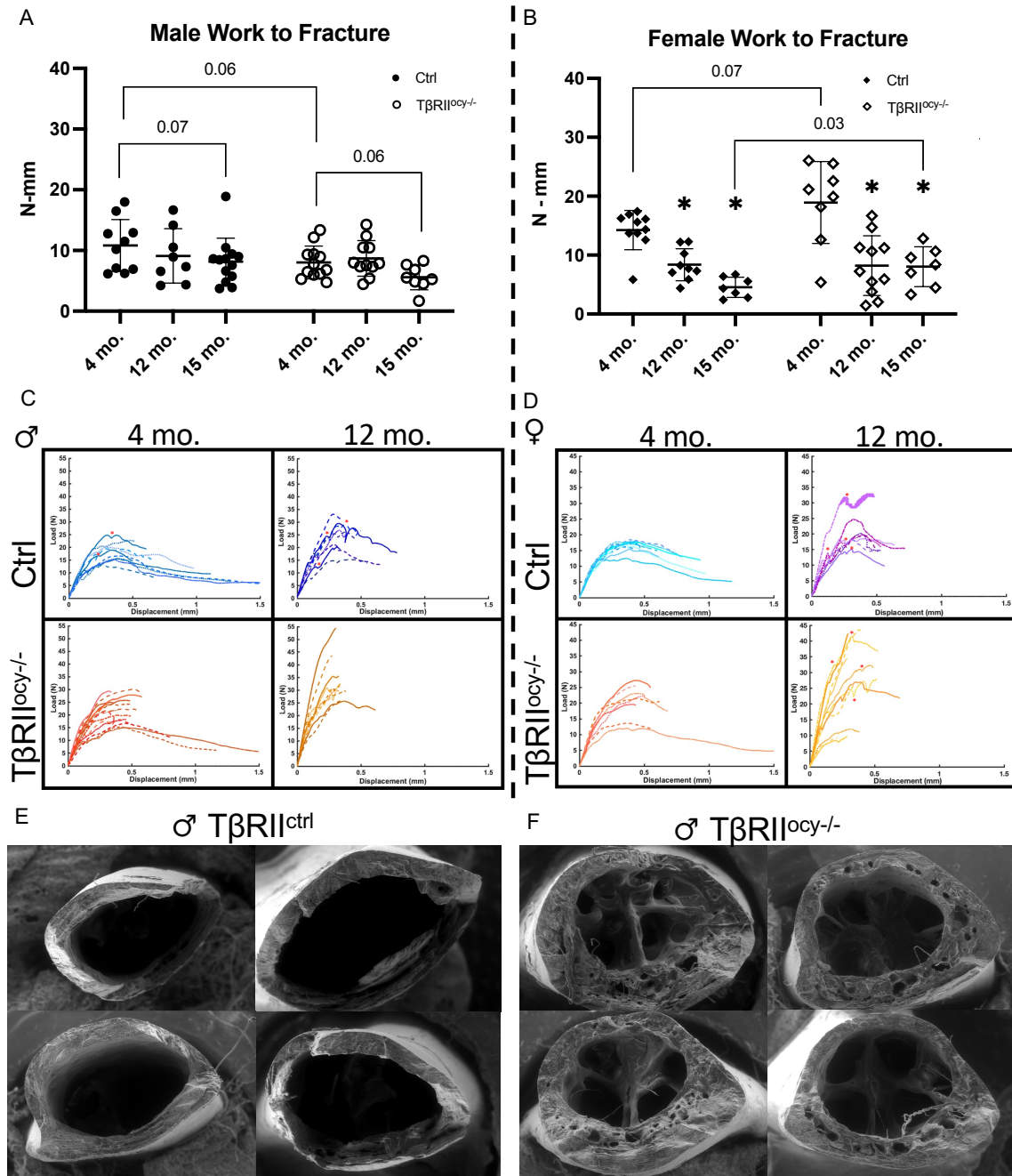
regulated by this pathway would decrease with age as well, as was seen in losses to PLR gene expression with age. Age-related alterations to the osteocyte LCN, which mirrored changes seen in young  $T\beta RII^{ocy-/-}$  bone, confirm a cellular defect with age that is related to the documented loss of  $TGF\beta$  signaling. Suppression of osteocyte regulatory behaviors result in changes to the bone material, namely chemical alterations to the collagen matrix, which on the nanomechanical scale was seen in increases to collagen strain and was mirrored by changes on the tissue scale through increased bone stiffness and lost bone ductility with age. Thus, maintaining osteocytic PLR over a lifetime may be a tractable way to prevent the alterations to bone material properties with age, protect bone toughness, and reduce fragility fracture in elderly populations.

While the role for osteocytic PLR in maintaining bone quality with age has been elucidated, several questions remain about the root of bone quality deficits in the young, male  $T\beta RII^{ocy-/-}$  bone and the role for osteocytic  $TGF\beta$  signaling in early bone growth and maturation. Young  $T\beta RII^{ocy-/-}$  males demonstrated deficits to bone density, collagen orientation, collagen strain, all while demonstrating tissue level increases to stiffness. Specifically, the lack of both collagen and mineral components of  $T\beta RII^{ocy-/-}$  bone to carry strain on the nanoscale, as seen through *in situ* synchrotron tensile tests, raise concern about the integrity and chemical composition of the bone matrix on the molecular scale. Compositional analysis that could confirm a molecular root for changes to material properties would require techniques such as FTIR or Raman Spectroscopy analysis. This future work would be critical for understanding the role of osteocytes in bone development and maturation as osteocytes may also be the cellular agent responsible for the maturation of enzymatic collagen crosslinks. The turnover from divalent to trivalent crosslinks in collagen are part of the normal maturation process in collagen and increases to crosslinking would increase the ability for collagen to carry strain. The enzymes responsible for these specific transformations include the Lysyl Oxidase family of enzymes, and RNAseq from young male  $T\beta RII^{ocy-/-}$  revealed that *Loxl2*, one of the main *Lox* isoforms, is significantly decreased in the bones

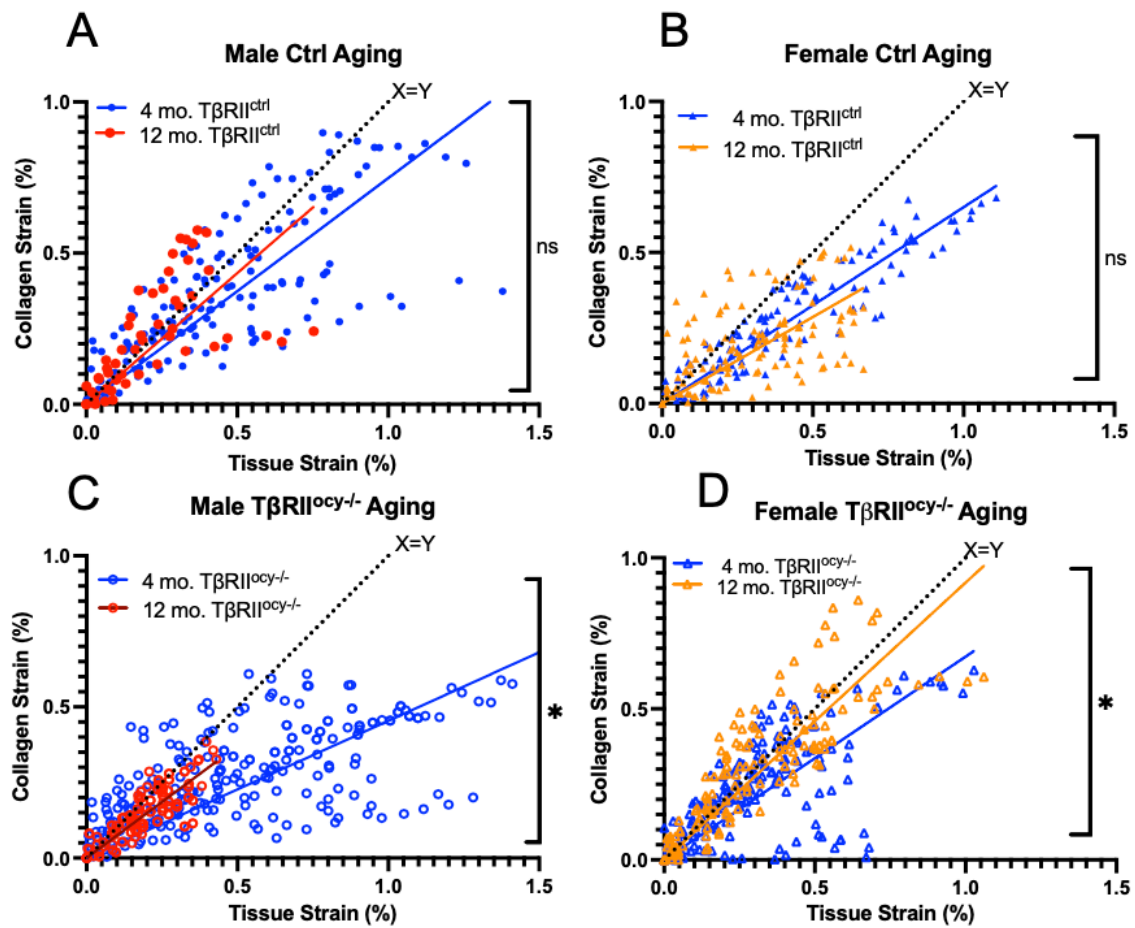
of these mice. Lox and its isoforms are tightly regulated by TGF $\beta$  signaling in many contexts<sup>41</sup>, thus lack of appropriate TGF $\beta$  signaling in osteocytes may be behind the loss of Lox-induced collagen crosslinking leading to the inability of young T $\beta$ RII<sup>ocy-/-</sup> collagen to carry strain. Changes to bone matrix material properties could result in the compensatory changes to bone size that are demonstrated in young T $\beta$ RII<sup>ocy-/-</sup> bone. Investigation of the molecular regulatory systems responsible for these tissue level architectural changes in this context may also reveal mechanisms by which aged and disease bone also acquire these changes, namely intracortical porosities, that may negatively impact bone strength. Thus, continued investigation into the specific ways in which TGF $\beta$  signaling in bone helps shape material and tissue scale properties during growth and development are warranted.



Supplemental Figures



**Supplemental Figure 5.1: Evaluation of load-displacement curves revealed changes to mechanical behavior during bending tests despite no change to energy dissipated during fracture.**



**Supplemental Figure 5.2: Within genotype comparison of collagen strain with age shows increased collagen strain in male and female  $T\beta RII^{ocy-/-}$  bone.**

## References

1. Hillier, T. A., Cauley, J. A., Rizzo, J. H., Pedula, K. L., Ensrud, K. E., Bauer, D. C., Lui, L., Vesco, K. K., Black, D. M., Donaldson, M. G., LeBlanc, E. S. & Cummings, S. R. WHO absolute fracture risk models (FRAX): Do clinical risk factors improve fracture prediction in older women without osteoporosis? *J Bone Miner Res* **26**, 1774–1782 (2011).
2. Wainwright, S. A., Marshall, L. M., Ensrud, K. E., Cauley, J. A., Black, D. M., Hillier, T. A., Hochberg, M. C., Vogt, M. T. & Orwoll, E. S. Hip Fracture in Women without Osteoporosis. *J Clin Endocrinol Metab* **90**, 2787–2793 (2005).
3. Alliston, T. Biological regulation of bone quality. *Curr Osteoporos Rep* **12**, 366–375 (2014).
4. Seeman, E. & Delmas, P. D. Bone Quality — The Material and Structural Basis of Bone Strength and Fragility. *New England Journal of Medicine* **354**, 2250–2261 (2006).
5. Guive, B., Mehdi, B., K, N., Ravi, Stephen, S., H, F., Ellen, W, M., Grayson, J, M., Sally, O, R., Robert, Rik, D. & Tamara, A. TGF-beta regulates the mechanical properties and composition of bone matrix. *Proc. Natl. Acad. Sci. U.S.A.* **102**, 18813–18818 (2005).
6. S, M., Khalid, G, C., Carol, Guive, B., Elizabeth, S., Ryan, M., C., Holly, D., Maria, N., Hong, P., Xiang, N, N., Daniel H., S, I.-M., Sophi, W, B., John, R, H., William, H, W., Darren, O, R., Robert, J, S., Larry, Rik, D., A, G., Theresa & Tamara, A. Pharmacologic inhibition of the TGF-beta type I receptor kinase has anabolic and anti-catabolic effects on bone. *PLoS ONE* **4**, e5275
7. Chang, J. L., Brauer, D. S., Johnson, J., Chen, C. G., Akil, O., Balooch, G., Humphrey, M. B., Chin, E. N., Porter, A. E., Butcher, K., RITCHIE, R. O., Schneider, R. A., Lalwani, A., Derynck, R., Marshall, G. W., Marshall, S. J., Lustig, L. & Alliston, T. Tissue-specific calibration of extracellular matrix material properties by transforming growth factor-beta and Runx2 in bone is required for hearing. *EMBO Rep.* **11**, 765–771 (2010).
8. Filvaroff, E., Erlebacher, A., Ye, J., Gitelman, S. E., Lotz, J., Heillman, M. & Derynck, R. Inhibition of TGF-beta receptor signaling in osteoblasts leads to decreased bone remodeling and increased trabecular bone mass. *Development* **126**, 4267–4279 (1999).

9. Kinoshita, A., Saito, T., Tomita, H., Makita, Y., Yoshida, K., Ghadami, M., Yamada, K., Kondo, S., Ikegawa, S., Nishimura, G., Fukushima, Y., Nakagomi, T., Saito, H., Sugimoto, T., Kamegaya, M., Hisa, K., Murray, J. C., Taniguchi, N., Niikawa, N. & Yoshiura, K. Domain-specific mutations in TGF $\beta$ 1 result in Camurati-Engelmann disease. *Nat Genet* **26**, 19–20 (2000).
10. Grafe, I., Yang, T., Alexander, S., Homan, E. P., Lietman, C., Jiang, M. M., Bertin, T., Munivez, E., Chen, Y., Dawson, B., Ishikawa, Y., Weis, M. A., Sampath, T. K., Ambrose, C., Eyre, D., Bächinger, H. P. & Lee, B. Excessive transforming growth factor- $\beta$  signaling is a common mechanism in osteogenesis imperfecta. *Nature Medicine* **20**, 670–675 (2014).
11. Wu, M., Chen, G. & Li, Y.-P. TGF- $\beta$  and BMP signaling in osteoblast, skeletal development, and bone formation, homeostasis and disease. *Bone Res* **4**, 16009 (2016).
12. Tang, S. Y. & Alliston, T. Regulation of postnatal bone homeostasis by TGF $\beta$ . *BoneKEY Reports* **2**, 255 (2013).
13. L, D., Sarah, Tamara, A. & F, B., Lynda. in *Principles of Bone Biology* 1145–1166 (Principles of Bone Biology, 2008).
14. Kaya, S., Pljakic, J. B., Ferlenguez, Z. S., Majeska, R. J., Cardoso, L., Bromage, T. G., Zhang, Q., Flach, C. R., Mendelsohn, R., Yakar, S., Fritton, S. P. & Schaffler, M. B. Lactation-Induced Changes in the Volume of Osteocyte Lacunar-Canalicular Space Alter Mechanical Properties in Cortical Bone Tissue. *Journal of Bone and Mineral Research* **32**, 688–697 (2017).
15. Dole, N. S., Yee, C. S., Mazur, C. M., Acevedo, C. & Alliston, T. TGF $\beta$  regulation of perilacunar/canalicular remodeling is sexually dimorphic. *J Bone Mineral Res Official J Am Soc Bone Mineral Res* (2020). doi:10.1002/jbmr.4023
16. Dole, N. S., Mazur, C. M., Acevedo, C., Lopez, J. P., Monteiro, D. A., Fowler, T. W., Gludovatz, B., Walsh, F., Regan, J. N., Messina, S., Evans, D. S., Lang, T. F., Zhang, B., Ritchie, R. O., Mohammad, K. S. & Alliston, T. Osteocyte-Intrinsic TGF- $\beta$  Signaling Regulates Bone Quality through Perilacunar/Canalicular Remodeling. *Cell Rep* **21**, 2585–2596 (2017).

17. Weivoda, M. M., Ruan, M., Pederson, L., Hachfeld, C., Davey, R. A., Zajac, J. D., Westendorf, J. J., Khosla, S. & Oursler, M. J. Osteoclast TGF- $\beta$  Receptor Signaling Induces Wnt1 Secretion and Couples Bone Resorption to Bone Formation. *J Bone Miner Res* **31**, 76–85 (2016).
18. Tiede-Lewis, L. M., Xie, Y., Hulbert, M. A., Campos, R., Dallas, M. R., Dusevich, V., Bonewald, L. F. & Dallas, S. L. Degeneration of the osteocyte network in the C57BL/6 mouse model of aging. *Aging* **9**, 2190–2208 (2017).
19. Schurman, C. A., Verbruggen, S. W. & Alliston, T. Disrupted osteocyte connectivity and pericellular fluid flow in bone with aging and defective TGF- $\beta$  signaling. *Proc. Natl. Acad. Sci. U.S.A.* **118**, e2023999118 (2021).
20. Staa, T. P. van, Dennison, E. M., Leufkens, H. G. M. & Cooper, C. Epidemiology of fractures in England and Wales. *Bone* **29**, 517–522 (2001).
21. Lobo, E., Marcos, G., Santabárbara, J., Salvador-Rosés, H., Lobo-Escolar, L., Cámara, C. D. la, Aso, A., Lobo-Escolar, A. & Workgroup, Z. Gender differences in the incidence of and risk factors for hip fracture: A 16-year longitudinal study in a southern European population. *Maturitas* **97**, 38–43 (2017).
22. Group, E. P. O. S. (EPOS), Felsenberg, D., Silman, A. J., Lunt, M., Armbrecht, G., Ismail, A. A., Finn, J. D., Cockerill, W. C., Banzer, D., Benevolenskaya, L. I., Bhalla, A., Armas, J. B., Cannata, J. B., Cooper, C., Dequeker, J., Eastell, R., Felsch, B., Gowin, W., Havelka, S., Hozzowski, K., Jajic, I., Janott, J., Johnell, O., Kanis, J. A., Kragl, G., Vaz, A. L., Lorenc, R., Lyritis, G., Masaryk, P., Matthis, C., Miazgowski, T., Parisi, G., Pols, H. A. P., Poor, G., Raspe, H. H., Reid, D. M., Reisinger, W., Schedit-Nave, C., Stepan, J. J., Todd, C. J., Weber, K., Woolf, A. D., Yershova, O. B., Reeve, J. & O'Neill, T. W. Incidence of Vertebral Fracture in Europe: Results From the European Prospective Osteoporosis Study (EPOS). *J Bone Miner Res* **17**, 716–724 (2002).
23. Alswat, K. A. Gender Disparities in Osteoporosis. *J Clin Medicine Res* **9**, 382–387 (2017).

24. Seeman, E. The structural basis of bone fragility in men. *Bone* **25**, 143–147 (1999).
25. Kerschnitzki, M., Kollmannsberger, P., Burghammer, M., Duda, G. N., Weinkamer, R., Wagermaier, W. & Fratzl, P. Architecture of the osteocyte network correlates with bone material quality. *Journal of Bone and Mineral Research* **28**, 1837–1845 (2013).
26. D., V., J., G., G. & P., F., D. Sexual dimorphism and age dependence of osteocyte lacunar density for human vertebral cancellous bone. *Anatomical Rec Part Discov Mol Cell Evol Biology* **282**, 157–62 (2005).
27. Ashique, A. M., Hart, L. S., Thomas, C. D. L., Clement, J. G., Pivonka, P., Carter, Y., Mousseau, D. D. & Cooper, D. M. L. Lacunar-canalicular network in femoral cortical bone is reduced in aged women and is predominantly due to a loss of canalicular porosity. *Bone Reports* **7**, 9–16 (2017).
28. Qing, H., Ardeshirpour, L., Pajevic, P. D., Dusevich, V., Jahn, K., Kato, S., Wysolmerski, J. & Bonewald, L. F. Demonstration of osteocytic perilacunar/canalicular remodeling in mice during lactation. *J. Bone Miner. Res.* **27**, 1018–1029 (2012).
29. Acevedo, C., Sylvia, M., Schaible, E., Graham, J. L., Stanhope, K. L., Metz, L. N., Gludovatz, B., Schwartz, A. V., Ritchie, R. O., Alliston, T. N., Havel, P. J. & Fields, A. J. Contributions of Material Properties and Structure to Increased Bone Fragility for a Given Bone Mass in the UCD-T2DM Rat Model of Type 2 Diabetes. *J. Bone Miner. Res.* **27**, 219–1075 (2018).
30. Zimmermann, E. A., Schaible, E., Bale, H., Barth, H. D., Tang, S. Y., Reichert, P., Busse, B., Alliston, T., Ager, J. W. & RITCHIE, R. O. Age-related changes in the plasticity and toughness of human cortical bone at multiple length scales. *Proceedings of the National Academy of Sciences* **108**, 14416–14421 (2011).
31. Lu, Y., Xie, Y., Zhang, S., Dusevich, V., Bonewald, L. F. & Feng, J. Q. DMP1-targeted Cre expression in odontoblasts and osteocytes. *J. Dent. Res.* **86**, 320–325 (2007).

32. P., L., J., L., M., E., M., C., C., M., S., J., S., L., R., H. & S., K. Induced disruption of the transforming growth factor beta type II receptor gene in mice causes a lethal inflammatory disorder that is transplantable. *Blood* **100**, 560–8 (2002).
33. Fowler, T. W., Acevedo, C., Mazur, C. M., Hall-Glenn, F., Fields, A. J., Bale, H. A., RITCHIE, R. O., Lotz, J. C., Vail, T. P. & Alliston, T. Glucocorticoid suppression of osteocyte perilacunar remodeling is associated with subchondral bone degeneration in osteonecrosis. *Sci Rep* **7**, 44618 (2017).
34. Bouxsein, M. L., Boyd, S. K., Christiansen, B. A., Guldberg, R. E., Jepsen, K. J. & Müller, R. Guidelines for assessment of bone microstructure in rodents using micro-computed tomography. *J Bone Miner Res* **25**, 1468–1486 (2010).
35. Jepsen, K. J., Silva, M. J., Vashishth, D., Guo, X. E. & Meulen, M. C. van der. Establishing Biomechanical Mechanisms in Mouse Models: Practical Guidelines for Systematically Evaluating Phenotypic Changes in the Diaphyses of Long Bones. *J Bone Miner Res* **30**, 951–966 (2015).
36. Hexemer<sup>1</sup>, A., Bras<sup>2</sup>, W., Glossinger<sup>1</sup>, J., Schaible<sup>1</sup>, E., Gann<sup>1</sup>, E., Kirian<sup>1</sup>, R., MacDowell<sup>1</sup>, A., Church<sup>1</sup>, M., Padmore, B. R. and H. & Padmore, H. A SAXS/WAXS/GISAXS Beamline with Multilayer Monochromator. *J Phys Conf Ser* **247**, 012007 (2010).
37. Barth, H. D., Zimmermann, E. A., Schaible, E., Tang, S. Y., Alliston, T. & Ritchie, R. O. Characterization of the effects of x-ray irradiation on the hierarchical structure and mechanical properties of human cortical bone. *Biomaterials* **32**, 8892–8904 (2011).
38. Dole, N. S., Yee, C. S., Schurman, C. A., Dallas, S. L. & Alliston, T. Assessment of Osteocytes: Techniques for Studying Morphological and Molecular Changes Associated with Perilacunar/Canalicular Remodeling of the Bone Matrix. *Methods Mol Biol* **2230**, 303–323 (2021).
39. Schindelin, J., Arganda-Carreras, I., Frise, E., Kaynig, V., Longair, M., Pietzsch, T., Preibisch, S., Rueden, C., Saalfeld, S., Schmid, B., Tinevez, J.-Y., White, D. J., Hartenstein, V., Eliceiri, K., Tomancak, P. & Cardona, A. Fiji: an open-source platform for biological-image analysis. *Nat Methods* **9**, 676–682 (2012).

40. Nguyen, J., Massoumi, R. & Alliston, T. CYLD, a mechanosensitive deubiquitinase, regulates TGF $\beta$  signaling in load-induced bone formation. *Bone* **131**, 115148 (2019).
41. Sethi, A., Mao, W., Wordinger, R. J. & Clark, A. F. Transforming Growth Factor- $\beta$  Induces Extracellular Matrix Protein Cross-Linking Lysyl Oxidase ( LOX) Genes in Human Trabecular Meshwork Cells. *Investigative Ophthalmology & Visual Science* **52**, 5240–5250 (2011).
42. Peilin, W., Songsong, T., Chengyu, Z., Zhi, C., Chunhui, M., Yinxian, Y., Lei, Z., Min, M., Zongyi, W., Mengkai, Y., Jing, X., Tao, Z., Zhuoying, W., Fei, Y. & Chengqing, Y. Directed elimination of senescent cells attenuates development of osteoarthritis by inhibition of c-IAP and XIAP. *Biochimica Et Biophysica Acta Bba - Mol Basis Dis* **1865**, 2618–2632 (2019).
43. Dallas, S. L., Prideaux, M. & Bonewald, L. F. The Osteocyte: An Endocrine Cell ... and More. *Endocr Rev* **34**, 658–690 (2013).
44. Bonewald, L. F. The amazing osteocyte. *Journal of Bone and Mineral Research* **26**, 229–238 (2011).
45. Chen, H., Zhou, X., Fujita, H., Onozuka, M. & Kubo, K.-Y. Age-Related Changes in Trabecular and Cortical Bone Microstructure. *Int J Endocrinol* **2013**, 213234 (2013).
46. Ritchie, R. O., Buehler, M. J. & Hansma, P. Plasticity and toughness in bone. *Physics Today* **62**, 41–47 (2009).
47. Patsch, J. M., Burghardt, A. J., Yap, S. P., Baum, T., Schwartz, A. V., Joseph, G. B. & Link, T. M. Increased cortical porosity in type 2 diabetic postmenopausal women with fragility fractures. *J Bone Miner Res* **28**, 313–324 (2013).
48. Seeman, E. Structural basis of growth-related gain and age-related loss of bone strength. *Rheumatology Oxf Engl* **47**, iv2–iv8 (2008).
49. Reznikov, N., Shahar, R. & Weiner, S. Bone hierarchical structure in three dimensions. *Acta Biomaterialia* **10**, 3815–3826 (2014).



50. Gupta, H. S., Seto, J., Wagermaier, W., Zaslansky, P., Boesecke, P. & Fratzl, P. Cooperative deformation of mineral and collagen in bone at the nanoscale. *Proceedings of the National Academy of Sciences* **103**, 17741–17746 (2006).
51. Karim, L., Tang, S. Y., Sroga, G. E. & Vashishth, D. Differences in non-enzymatic glycation and collagen cross-links between human cortical and cancellous bone. *Osteoporosis Int* **24**, 2441–2447 (2013).
52. Garnero, P. The contribution of collagen crosslinks to bone strength. *BoneKEy Reports* **1**, 182 (2012).
53. Buehler, M. J. Nature designs tough collagen: Explaining the nanostructure of collagen fibrils. *Proc National Acad Sci* **103**, 12285–12290 (2006).
54. Plotkin, L. I., Essex, A. L. & Davis, H. M. RAGE Signaling in Skeletal Biology. *Curr Osteoporos Rep* **17**, 16–25 (2019).
55. Barzilay, J. I., Bůžková, P., Zieman, S. J., Kizer, J. R., Djoussé, L., Ix, J. H., Tracy, R. P., Siscovick, D. S., Cauley, J. A. & Mukamal, K. J. Circulating Levels of Carboxy-Methyl-Lysine (CML) Are Associated With Hip Fracture Risk: The Cardiovascular Health Study. *J Bone Miner Res* **29**, 1061–1066 (2014).
56. Thomas, C. J., Cleland, T. P., Sroga, G. E. & Vashishth, D. Accumulation of carboxymethyl-lysine (CML) in human cortical bone. *Bone* **110**, 128–133 (2018).
57. Hein, G., Wiegand, R., Lehmann, G., Stein, G. & Franke, S. Advanced glycation end-products pentosidine and Nε-carboxymethyllysine are elevated in serum of patients with osteoporosis. *Rheumatology* **42**, 1242–1246 (2003).
58. M., M., C., J., W., J., S., Y., C., J., F., A., C., A., N., B., K., S., K., W., F., T., C., L., J., A., D., C., K., A., P., V., T. & T., A. Osteocyte dysfunction promotes osteoarthritis through MMP13-dependent suppression of subchondral bone homeostasis. *Bone Res* **7**, 34 (2019).
59. Meek, K. M. & Boote, C. The use of X-ray scattering techniques to quantify the orientation and distribution of collagen in the corneal stroma. *Prog Retin Eye Res* **28**, 369–392 (2009).

60. White, J. L. & Spruiell, J. E. The specification of orientation and its development in polymer processing. *Polym Eng Sci* **23**, 247–256 (1983).
61. Pfeilschifter, J., Diel, I., Scheppach, B., Bretz, A., Krempien, R., Erdmann, J., Schmid, G., Reske, N., Bismar, H., Seck, T., Krempien, B. & Ziegler, R. Concentration of transforming growth factor beta in human bone tissue: relationship to age, menopause, bone turnover, and bone volume. *J. Bone Miner. Res.* **13**, 716–730 (1998).
62. Tominaga, K. & Suzuki, H. I. TGF- $\beta$  Signaling in Cellular Senescence and Aging-Related Pathology. *Int J Mol Sci* **20**, 5002 (2019).
63. Chung, P., Zhou, S., Eslami, B., Shen, L., LeBoff, M. S. & Glowacki, J. Effect of Age on Regulation of Human Osteoclast Differentiation. *J Cell Biochem* **115**, 1412–1419 (2014).
64. Aykul, S. & Martinez-Hackert, E. Transforming Growth Factor- $\beta$  Family Ligands Can Function as Antagonists by Competing for Type II Receptor Binding\*. *J Biol Chem* **291**, 10792–10804 (2016).
65. Monteiro, D. A., Dole, N. S., Campos, J. L., Kaya, S., Schurman, C. A., Belair, C. D. & Alliston, T. Fluid shear stress generates a unique signaling response by activating multiple TGF $\beta$  family type I receptors in osteocytes. *FASEB journal : official publication of the Federation of American Societies for Experimental Biology* **35**, e21263 (2021).

# Chapter 6: Summary, Conclusions, and Future Directions

## Summary and Conclusions

Osteocyte perilacunar/canalicular remodeling (PLR) is a dynamic process by which bone embedded osteocytes resorb, replace, and renew their surrounding bone matrix. Given the dramatic size and surface area of the osteocyte cellular network, second in the body only to the nervous system, this cellular process has immense potential as a mechanism of material upkeep and supporter of bone quality within the skeleton. The role of the skeleton in supplying mechanical support and motion to the body places it under great mechanical stress and strain leading to wear and damage over time that may lower its structural integrity. Fragility fracture, fractures that occur at subcritical energies, are most common in aged individuals or in those with congenital dysplasia - conditions that worsen the material strength of the bone. In these situations, the physical material of the skeleton suffers from a lack of quality on the molecular scale resulting in an uncoupling of

bone mass from bone strength leading to bone fragility. Aging throughout the body is marked by a broad decline in cellular function, so it stands to reason that the skeleton and skeletal cells would not be uniquely immune to deleterious aging. If age-related bone fragility is related specifically to bone quality and bone material properties, then the cellular mechanisms, namely osteocyte perilacunar/canalicular remodeling (PLR), responsible for its upkeep are implicated in bone fragility. Thus, PLR's nature as a cellularly derived mechanism portends its susceptibility to aging and declines to bone quality with time. In broad strokes, this supports the idea that healthy osteocytes provide a homeostatic mechanism for renewal of bone material maintaining its mechanical strength, and with age this process declines leading to an accumulation of damage/alterations to the skeleton that lower both bone quality and fracture resistance. Much is still unknown about the molecular regulators of osteocyte PLR, much less its regulation over time, or how these molecular pathways interact with other mechanisms of aging. What age-related defects arise within bone as specific consequences of arrested osteocyte bone remodeling, and strategies to prevent or restore these weaknesses, remain a large knowledge gap in the effort to protect skeletal health with age.

Herein, I explore the role for one specific regulatory mechanism, the Transforming Growth Factor Beta (TGF $\beta$ ) pathway, and its role in the age-related changes to osteocyte function and thus the development of bone fragility interrogated. Previously, TGF $\beta$  was shown to be a main molecular regulator of osteocyte PLR in young homeostatic conditions where loss of TGF $\beta$  signaling in the osteocytes of young males resulted in the development of severe bone quality defects<sup>1</sup>. Interestingly, the defects within bone resulting from osteocytic TGF $\beta$  deprivation eerily resembled aged bone, including poor fracture resistance and a degenerated osteocyte lacunar/canalicular network. Results provided here document decreases to TGF $\beta$  signaling within aged bone for the first time, including a loss of TGF $\beta$  receptor II, the specific defect experimentally induced within osteocytes to create young bone without functional TGF $\beta$  signaling. These cellular, molecular, and mechanical similarities lead to the hypothesis that age-related bone fragility

stemming from a loss in osteocyte-controlled bone quality is the result of decreases to TGF $\beta$  signaling over time in osteocytes.

Systemically, TGF $\beta$  exerts potent growth inhibitory activities in various cell types, and increased TGF $\beta$  signaling with age has been linked to the phenotypes of cellular senescence, stem cell aging, inflammation, and tissue fibrosis<sup>2-4</sup>. In addition, accumulated evidence has indicated a multifaceted association between TGF $\beta$  signaling and other aging-associated disorders, including Alzheimer's disease, muscle atrophy, and obesity<sup>5-8</sup>. Within bone, TGF $\beta$  balances the cellular activities of the three main bone cell types, regulating osteocyte PLR, promoting osteoblast differentiation and migration, and promoting bone resorbing osteoclast survival. With age, TGF $\beta$  may be partially responsible for the uncoupling of bone resorption and bone deposition by increasing surface osteoclast numbers, but its role in osteocyte aging and its decreased activity within aged bone remains unexplained. TGF $\beta$  itself is stored in a latent form within the bone matrix and is activated upon bone resorption. Over time as osteoclastic bone resorption increases, increasing amounts of local TGF $\beta$  ligand may be liberated from the bone matrix allowing it to act systemically to drive distal responses to TGF $\beta$  while depleting local bone cells of this important homeostatic stimuli. This change in ligand balance may help to partially explain the seemingly contradictory nature of TGF $\beta$  signaling increasing and driving aging systemically and the loss of it locally in bone leading to the declines of bone-regulatory mechanisms. Thus, activity within the TGF $\beta$  signaling pathway with age may be reduced at multiple stages including both at the ligand and receptor levels and beyond.

Within the landscape of altered local and systemic changes to TGF $\beta$  signaling with age, the loss of osteocyte intrinsic TGF $\beta$  signaling with age within the bone is an important potential mechanism by which age-related bone fragility may arise through lost osteocyte bone remodeling. Results from this work explore the functional consequences of age on the osteocyte network, the importance of osteocyte PLR in maintaining bone quality over time, and propose a role for the decline in osteocyte TGF $\beta$  signaling as a driving factor behind these changes in bone.

Osteocytes reside within bone in cavities termed “lacuna” and extend their long cytoplasmic dendrites into the mineralized bone through narrow canals called “canaliculi” connecting to other osteocyte dendrites via gap junctions, as well as with bone lining osteoblasts and osteoclasts, and vasculature, to form the lacunocanalicular network (LCN). Entombed within the mineralized matrix of bone, osteocytes rely on the integrity of the LCN and their cellular connections for both function and survival. Thus, the osteocyte LCN is a hallmark and marker of generalized osteocyte health. While the greater architecture of LCN can change based on location and bone type, a healthy LCN is characterized by its many, mostly linear, canalicular connections, as this aides in fluid motion within the LCN that drives nutrient exchange and mechanosensation. Degeneration of this architecture either by a loss of canalicular connections or a change in pathway geometry may compromise these important functions of the LCN that are the backbone behind osteocyte behavior. Independent, side-by-side, observations of LCN architectural change in both aged osteocytes and osteocytes without functional TGF $\beta$  signaling showed increases to osteocyte canalicular tortuosity and lost canalicular numbers per osteocyte, raising questions of precise functional consequences of degeneration in both these models. Interestingly, TGF $\beta$  deficient bone did not demonstrate the losses of entire osteocyte cell bodies that the aged cohort did, signifying that TGF $\beta$  may have a role in specifically maintaining osteocyte canaliculi. The shared canalicular defects in both models also resulted in similar outcomes for functional tests of these networks. In both simulated diffusion and fluid flow dynamics, the degenerated networks performed worse than controls identifying osteocyte-specific functional losses that are tied to connectivity of the LCN within bone. These experiments showed that the functional losses experienced by aged osteocytes can be recapitulated in young bone through removal of TGF $\beta$  signaling, implicating TGF $\beta$  signaling in functional aging of the osteocyte LCN.

Although TGF $\beta$  is implicated in the functional losses, leveraging of behaviors controlled by TGF $\beta$ , namely PLR and osteocyte resorption of local pericellular space, provides a way to

restore some amounts of LCN function lost with age. For example, relative to bone from virgin control mice, canalicular diameter can increase by 20-30% during lactation and returns to baseline after weaning, demonstrating expansion and constriction of the local PCS<sup>9</sup>. Thus, PLR could be a mechanism that can influence remaining LCN architecture even in a diseased or aged bone. In computer models, doubling of the pericellular space around both of aged and T $\beta$ RII<sup>ocy-/-</sup> osteocytes returned modeled fluid shear stress to levels that were indistinguishable from young or wild type controls. This demonstrated that control of the pericellular space, possibly through TGF $\beta$  mediated PLR, presents a mechanism by which osteocytes can adapt their mechanical microenvironment to reclaim meaningful amounts of lost physical stimulation in age and disease.

While the degeneration of the LCN in both aged bone and bone with TGF $\beta$  signaling disruption matched each other and were both correlated to the same functional consequences, the casual role of TGF $\beta$  in aging was not clear. Analysis of gene expression within the TGF $\beta$  pathway from aged bone confirmed a negative regulation of TGF $\beta$  signaling in these bones at all levels within the pathway including losses to expression on the receptor, transducer, and target gene level as well as increased expression of antagonists of the pathway including markers of TNF and NF- $\kappa$ B<sup>10-12</sup>. In a separate analysis, TGF $\beta$  ligand levels in bone measured through ELISA showed decreases in total ligand abundance, and thus signaling capability, within bone over time. These findings confirmed for the first time a generalized loss of overall TGF $\beta$  signaling within aged bone. Previous studies have described the role of TGF $\beta$  in mediating osteocytic bone remodeling to maintain bone quality while these results support the idea that age-related bone fragility may arise due to lost TGF $\beta$  mediated cellular bone remodeling.

While disrupting TGF $\beta$  signaling in young osteocytes was sufficient to generate a phenotype resembling aged bone at the level of specific cellular changes and increases to bone fragility, and aged bone does display reductions to TGF $\beta$  signaling and share mechanical and functional loss with T $\beta$ RII<sup>ocy-/-</sup> bone, it was unclear what portions of the aged phenotype were

TGF $\beta$  specific and osteocytic in origin. In order to interrogate the role of TGF $\beta$  in generating an age-related phenotype, mice with eliminated TGF $\beta$  signaling in osteocytes were aged alongside control littermates to observe differences in the development of bone quality defects with age within the two lines. Observation of the LCN from these mice over time showed lost osteocyte canalicular number and increases to individual canalicular tortuosity in the young male knockouts compared to their young control counterparts, and no further significant changes to the LCN with age up to 15 months in males. By 15 months, wild type males displayed the same defects that young T $\beta$ RII<sup>ocy-/-</sup> mice showed. This is potentially because at the cellular level, the inability to engage in TGF $\beta$  signaling is sufficient to generate an aged cellular phenotype, signifying that cellular aging in the male bones may occur primarily through a TGF $\beta$ -dependent mechanism. Over time, females of both genotypes demonstrated canalicular loss and increased network tortuosity, showing that although the mechanism by which they degrade may be TGF $\beta$  independent, the phenotypic and functional consequences of age are the same for both males and females.

Changes to the cellular network in these bones hinted at altered cellular performance and maintenance of bone quality and material properties. Osteocytes normally regulate their surrounding bone material with a wide range of secreted factors that are regulated in a TGF $\beta$  dependent manner<sup>1</sup>. Expression data from young T $\beta$ RII<sup>ocy-/-</sup> males showed loss of the matrix remodeling enzyme Loxl2, which aids in the enzymatic maturation of collagen crosslinking, and other previous results documented the loss of other remodeling enzymes such as MMP13 in these mice<sup>1</sup>. Changes to the matrix modifying enzymes resulted in important functional changes within the bone matrix to insufficient tensile properties. In addition, the removal of osteocytic TGF $\beta$  signaling resulted in a hypomineralized bone matrix, possibly leading to a softer, more pliable mineral phase. The inability to regulate both the organic and mineralized inorganic components of bone on the cellular scale resulted in bone with poor material quality.



Interestingly,  $T\beta RII^{ocy-/-}$  bone seemed to compensate for their poor bone material quality by increasing the amount of bone present and by altering bone shape. These changes in bone shape in the knock-out bones foretold the eventual changes that the wild-type bone would eventually experience including periosteal expansion and the development of internal porosities often seen in age and in diseases such as diabetes. This provides evidence that bone growth is influenced by  $TGF\beta$  but is also managed through  $TGF\beta$ -independent mechanisms.

With time, the lack of osteocytic PLR in  $T\beta RII^{ocy-/-}$  bone resulted in increased accumulation of nonenzymatic collagen crosslinking, increasing collagen strain perhaps as another compensatory mechanism for initial poor bone quality or more straightforwardly a consequence of lost osteocytic PLR. In any case, this resulted in stiffer bone that is potentially more prone to fragility fracture. Control bones demonstrated similar changes, increases to non-enzymatic collagen crosslinking and tissue level bone stiffening, but to a lesser extent. This is perhaps because our ending time-point of 15 months for this study is not sufficiently aged into see dramatic changes in bone with initially intact  $TGF\beta$  signaling. However, age mice have been shown to display these specific chemical changes to their bone matrix and consequently demonstrate poor bone quality and mechanics<sup>13</sup>. Results from our own highly aged mice at 30 months old revealed expression-related repression of several markers of  $TGF\beta$  signaling and PLR, suggesting that lost osteocyte mediated bone remodeling is behind changes to bone material with age, namely the increase in nonspecific collagen crosslinking and the consequent tightening of the bone matrix. While these changes to the collagen matrix can occur along-side declines to bone mass with age, the identification of the accelerated accumulation of AGEs in a  $TGF\beta$  deficient context reveals a bone-mass independent, osteocyte-specific mechanism that negatively impacts bone quality with age.

## Considerations and Future Directions

While the major findings from this work are significant in that they reveal the cellular process behind a specific material level alteration within bone that occurs with age, several considerations and future work will further solidify these claims as well as reveal other mechanisms behind bone aging.

The noticed increase to collagen strain capability with age is likely a combination of changes in several types of collagen crosslinking with age and not solely the effect of the single fluorescent AGE, pentosidine, that we have evaluated, but we have not fully assessed other cross-linking types in our aged conditions. One important consideration about the claims made is that currently we can only make correlative comments on the mechanical influence of nonspecific crosslinking on collagen mechanics within bone. There exist other forms of crosslinking - namely enzymatically generated trivalent mature crosslinks pyridinoline (PYD), deoxypyridinoline (DPD), and other forms of nonenzymatic crosslinks such as carboxymethyl lysine (CML) - but we have not evaluated the condition of these in our samples at this time and thus cannot attribute all the change in collagen behavior to fluorescent AGEs alone. However, previous work has demonstrated no statistical correlation with DYD or PYD concentration and bone mechanical properties in aged contexts, and instead note a high correlation between AGEs and mechanical stiffness. Of course, these observations are all correlative as it is hard to demonstrate causality at the moment in vivo without a way to directly enact AGE clearance. Agents that may modulate large amounts of bone turnover, i.e. PLR, may be a future method of demonstrating the direct control of collagen crosslinking from the cellular level via bone turnover.

Currently, young male  $T\beta RII^{ocv-/-}$  mice demonstrate a lack in collagen strain capability compared to their wildtype controls. Analysis of AGE crosslinking in these samples showed no difference in the amount of fluorescent crosslinks between these two groups at this time. This implies that the AGE crosslinking does not greatly impact the collagen mechanics at young ages, in line with other previous studies. In addition, the great difference in collagen behavior must be

attributed to other kinds of chemical modifications in the organic matrix of bone besides fluorescent AGEs. The other major species of crosslinking in young bone that does have mechanical influence is the transition from immature divalent crosslinks (dihydroxylysinonorleucine (DHLNL) and hydroxylysinonorleucine (HLNL)) to their stronger trivalent forms (PYD and DPD). This conversion is enzymatically enacted by Lysyl Oxidase (Lox) and its numerous isoforms (Loxl2-4). There exist many positive regulators of these enzymes, TGF $\beta$  among them. RNAseq from young T $\beta$ RII males showed a significant loss of Loxl2 in the bones of these mice, suggesting that these mice may have a deficiency in the normal maturation of collagen crosslinking. This would result in bones with immature collagen and poor tensile properties, as we have seen by SAXS. In order to confirm that this initial defect stems from a lack of TGF $\beta$  driven Lox enacted conversion of divalent to trivalent crosslinks, direct measurements of the different species of enzymatic crosslinks in these bones would reveal whether or not the deficiency stems from the lack of normal bone maturation. Compositional techniques such as FTIR, Raman Spectroscopy, or HPLC are all possible methods that could interrogate these changes. At the time of writing, a set of bones from young T $\beta$ RII mice have been set aside for analysis by FTIR but are not included in this current write up. This specific role for TGF $\beta$  in bone growth and maturation is most important at young ages before nonenzymatic crosslinking dominates in mechanical influence on bone, and the rapid increase in collagen strain with age in the T $\beta$ RII<sup>ocy-/-</sup> males at 12 months overcoming their initial mechanical deficiency demonstrates this effect. Given that the lack of collagen strain in the young T $\beta$ RII<sup>ocy-/-</sup> males represents a developmental defect, this initial collagen deficiency does not seem to be associated with “aging” post normal skeletal maturation as much as other processes like the spontaneous generation of AGE crosslinks in bone.

In addition to a more complete understanding of the condition of collagen, the mineral components of bone should be looked at with greater detail as well. Currently, we have only a

small number of samples that we have analyzed via WAXD to observe mineral specific deformations during mechanical testing. From these we can see that the mineral within the  $T\beta RII^{ocy-/-}$  males also demonstrates an inability to carry strain. While currently the  $T\beta RII^{ocy-/-}$  males show statistically different behavior within the mineral compared to their age-matched genotype controls, the females do not. These behaviors match observations in the young bones during SAXS assessment of collagen behavior, but these tests are low in N and very well could be skewed by the small number of replicates. Increasing replicate numbers for the WAXD is an important next step in confirming the nanomechanical behavior of the mineral crystals during testing. In addition, there is currently no WAXD data for the aged cohorts, so knowledge of the effect of age on the mineral is unknown, which may be critical in understanding the development of bone fragility and attributing the fault to either the organic or inorganic portions of bone or to both. In the synthesis of information about bone quality in these animals, it will be important to understand the status of the mineral, especially given that young male  $T\beta RII^{ocy-/-}$  bone is hypomineralized and previous results via nanoindentation have shown a small, but statistically significant, loss in indentation modulus. These findings suggest that the bone mineral is more susceptible to mechanical stress and confirmation of this via WAXD will help us understand where fragility arises in this model and its dynamic behavior with age will elucidate the effects of aging on the mineral crystals of bone.

A current exciting and ongoing area of investigation in our system is interrogation of the molecular landscape at play in the samples observed here. At the time of writing, there are efforts to complete analysis for RNA sequencing on aged bones with osteocytic specific losses to  $TGF\beta$  signaling. These results will give us a greater knowledge of the molecular tools active within the osteocytes responsible for bone upkeep, their regulation and relation to  $TGF\beta$  signaling, and their behavior with age. Given our knowledge of the role of osteocytes in bone remodeling via PLR and the nano-mechanical data from SAXS, we suspect there to be a lack of expression for genes

involved in PLR, e.g. MMP13, CatK, Acp5, etc..., but we will not know this for sure until expression results can be confirmed. In addition, while the RNAseq should give us a detailed knowledge of gene expression, these RNA samples analyzed are not entirely osteocytic in nature. In order to more precisely attribute these changes to osteocytes, immunofluorescence and immunohistologic methods are additionally being advanced on tissues sections to visualize changes in expression within osteocytes and not neighboring cells.

In addition to the outstanding data to be collected as discussed above, there are new avenues of research that are prompted by the findings from this work. First, the mechanism by which the  $T\beta RII^{ocy-/-}$  bone compensates for its lost material behavior to change its structural properties and increase its stiffness and ultimate load capacity is unknown. Physically, we observe an increase in bone stiffness and overall strength in the  $T\beta RII^{ocy-/-}$  mice that can be attributed to the change in bone shape and size. What remains unexplained is how regulatory cells in these mice “know” that their bone material suffers from insufficient strength on the molecular scale and then enact this accelerated growth in turn to compensate. This question is of particular interest in that it opens up questions surrounding the role of  $TGF\beta$  in osteocyte mechanosensation. The relationship with bone loading and bone formation with  $TGF\beta$ , especially in the context of the regulation of SOST, is complex and results from our own lab demonstrate multifaceted responses<sup>14–17</sup>. In conditions of a dominant negative  $TGF\beta$  receptor II, mice do not respond to the anabolic effects of load in that loss of  $TGF\beta$  responsiveness prevents the inhibition of SOST. Constitutively active SOST expression would prevent osteoblast differentiation and thus inhibit bone formation. However, in the  $T\beta RII^{ocy-/-}$  mice, others from the lab have shown increased SOST expression in osteocytes in the knees and the jaws of these animals, two particularly mechanically active regions. Increased levels of SOST in these regions raises questions about the homeostatic regulation of SOST versus the mechanically induced expression after large amount of bone loading required for anabolic responses. In addition, we observe in this work that

bone formation is likely increased overall in these mice since the bones are larger and grow more quickly than their control counterparts. These intriguing findings suggest that the role of TGF $\beta$  and mechanotransduction in osteocytes is a complex regulatory mechanism likely context and time dependent and is thus a fertile area of future research.

Another area of future research that may have clinical benefit stems from the findings within the female T $\beta$ RII<sup>ocy-/-</sup> bone. The females of this line demonstrate either protection or a compensatory mechanism that prevents the loss of function within osteocytes in a TGF $\beta$  deprived context. These mice demonstrate intact homeostatic PLR and do not develop the same developmental defects that the young males of this line do, including a maintenance of collagen order and mechanical behavior. With age however, characteristics of lost osteocyte behavior begin to emerge at an accelerated rate and the bones of females begin to behave more similarly to the aged males. This would imply the females lose their protective or compensatory mechanism with age. One initial thought is quite obviously that this mechanism is regulated through an endocrine or hormonal mechanism. Estrogen has many positive effects on bone including the preservation of bone mass by promoting the apoptosis of osteoclasts through a TGF $\beta$  dependent mechanism.<sup>18</sup> Estrogen also promotes synthesis and activation of TGF $\beta$  ligand in bone, which in a balanced context, also promotes and regulates bone quality.<sup>19</sup> Post-reproductive age, estrogen levels fall in mammals leading to a host of changes, including potential dramatic changes in bone mass and strength, and potentially specifically to bone quality related parameters as well. Given that TGF $\beta$  directed PLR declines with age, it is possible that the concurrent losses to both TGF $\beta$  and estrogen effects in females may play compounding effects towards the losses to bone quality. An interesting proposal though would be to 1) know what the mechanism is that circumvents TGF $\beta$  susceptibility in females 2) prevent its loss with age in females and 3) utilize it as a method to defend bone quality with age as TGF $\beta$  itself declines. Thus, exploration of the hormonal

landscape and sex-hormone dependent regulation of the bone remodeling machinery is an important field of basic biology with high levels of clinical relevancy and significance.

A final area of future work concerns the utilization and leveraging of existent osteocyte machinery to defend or improve bone health. PLR is an important homeostatic mechanism that maintains bone health. Given that this process slows in aged bone, it seems reasonable that reactivation of this cellular behavior may reinvigorate lost bone quality. Unfortunately, one of the only well-known direct regulators of osteocyte PLR is TGF $\beta$  and there are several difficulties with utilizing TGF $\beta$  alone to treat bone quality deficits. As previously discussed, TGF $\beta$  is involved in a host of other age-related pathologies, most of which are related to over expression within this pathway leading to tissue fibrosis or other debilitating conditions. These concerns exclude systemic TGF $\beta$  supplementation as a choice for treatment. Thus, a study screening novel agents that can selectively modulate osteocyte behavior and PLR while avoiding the detrimental effects of elevated TGF $\beta$  signaling elsewhere in the body is highly desirable.

## References

1. Dole, N. S., Mazur, C. M., Acevedo, C., Lopez, J. P., Monteiro, D. A., Fowler, T. W., Gludovatz, B., Walsh, F., Regan, J. N., Messina, S., Evans, D. S., Lang, T. F., Zhang, B., Ritchie, R. O., Mohammad, K. S. & Alliston, T. Osteocyte-Intrinsic TGF- $\beta$  Signaling Regulates Bone Quality through Perilacunar/Canalicular Remodeling. *Cell Rep* 21, 2585–2596 (2017).
2. Minagawa, S., Araya, J., Numata, T., Nojiri, S., Hara, H., Yumino, Y., Kawaishi, M., Odaka, M., Morikawa, T., Nishimura, S. L., Nakayama, K. & Kuwano, K. Accelerated epithelial cell senescence in IPF and the inhibitory role of SIRT6 in TGF- $\beta$ -induced senescence of human bronchial epithelial cells. *Am J Physiol-lung C* 300, L391–L401 (2011).
3. Debacq-Chainiaux, F., Borlon, C., Pascal, T., Royer, V., Eliaers, F., Ninane, N., Carrard, G., Friguet, B., Longueville, F. de, Boffe, S., Remacle, J. & Toussaint, O. Repeated exposure of human skin fibroblasts to UVB at subcytotoxic level triggers premature senescence through the TGF- $\beta$ 1 signaling pathway. *J Cell Sci* 118, 743–758 (2005).
4. Saito, A., Horie, M. & Nagase, T. TGF- $\beta$  Signaling in Lung Health and Disease. *Int J Mol Sci* 19, 2460 (2018).
5. Tominaga, K. & Suzuki, H. I. TGF- $\beta$  Signaling in Cellular Senescence and Aging-Related Pathology. *Int J Mol Sci* 20, 5002 (2019).
6. Vincent, H. K., Raiser, S. N. & Vincent, K. R. The aging musculoskeletal system and obesity-related considerations with exercise. *Ageing Res Rev* 11, 361–373 (2012).
7. Fain, J. N., Tichansky, D. S. & Madan, A. K. Transforming Growth Factor  $\beta$ 1 release by human adipose tissue is enhanced in obesity. *Metabolis* 54, 1546–1551 (2005).
8. Caraci, F., Spampinato, S., Sortino, M. A., Bosco, P., Battaglia, G., Bruno, V., Drago, F., Nicoletti, F. & Copani, A. Dysfunction of TGF- $\beta$ 1 signaling in Alzheimer's disease: perspectives for neuroprotection. *Cell Tissue Res* 347, 291–301 (2012).
9. Kaya, S., Pljakic, J. B., Ferlenguez, Z. S., Majeska, R. J., Cardoso, L., Bromage, T. G., Zhang, Q., Flach, C. R., Mendelsohn, R., Yakar, S., Fritton, S. P. & Schaffler, M. B. Lactation-Induced



Changes in the Volume of Osteocyte Lacunar-Canalicular Space Alter Mechanical Properties in Cortical Bone Tissue. *Journal of Bone and Mineral Research* 32, 688–697 (2017).

10. Schurman, C. A., Verbruggen, S. W. & Alliston, T. Disrupted osteocyte connectivity and pericellular fluid flow in bone with aging and defective TGF- $\beta$  signaling. *Proc. Natl. Acad. Sci. U.S.A.* 118, e2023999118 (2021)

11. Bitzer, M., Gersdorff, G. von, Liang, D., Dominguez-Rosales, A., Beg, A. A., Rojkind, M. & Böttinger, E. P. A mechanism of suppression of TGF-beta/SMAD signaling by NF-kappa B/RelA. *Gene Dev* 14, 187–97 (2000).

12. Yamane, K., Ihn, H., Asano, Y., Jinnin, M. & Tamaki, K. Antagonistic Effects of TNF- $\alpha$  on TGF- $\beta$  Signaling Through Down-Regulation of TGF- $\beta$  Receptor Type II in Human Dermal Fibroblasts. *J Immunol* 171, 3855–3862 (2003).

13. Zimmermann, E. A., Schaible, E., Bale, H., Barth, H. D., Tang, S. Y., Reichert, P., Busse, B., Alliston, T., Ager, J. W. & RITCHIE, R. O. Age-related changes in the plasticity and toughness of human cortical bone at multiple length scales. *Proceedings of the National Academy of Sciences* 108, 14416–14421 (2011).

14. Bailey, K. N., Nguyen, J., Yee, C. S., Dole, N. S., Dang, A. & Alliston, T. Mechanosensitive Control of Articular Cartilage and Subchondral Bone Homeostasis in Mice Requires Osteocytic Transforming Growth Factor  $\beta$  Signaling. *Arthritis Rheumatol* 73, 414–425 (2021).

15. Nguyen, J., Tang, S. Y., Nguyen, D. & Alliston, T. Load Regulates Bone Formation and Sclerostin Expression through a TGFbeta-Dependent Mechanism. *PLoS ONE* 8, e53813 (2013).

16. Nguyen, J., Massoumi, R. & Alliston, T. CYLD, a mechanosensitive deubiquitinase, regulates TGF $\beta$  signaling in load-induced bone formation. *Bone* 131, 115148 (2019).

17. Monteiro, D. A., Dole, N. S., Campos, J. L., Kaya, S., Schurman, C. A., Belair, C. D. & Alliston, T. Fluid shear stress generates a unique signaling response by activating multiple TGF $\beta$  family type I receptors in osteocytes. *FASEB journal : official publication of the Federation of American Societies for Experimental Biology* 35, e21263 (2021).

18. Hughes, D. E., Dai, A., Tiffée, J. C., Li, H. H., Mundy, G. R. & Boyce, B. F. Estrogen promotes apoptosis of murine osteoclasts mediated by TGF- $\beta$ . *Nat Med* 2, 1132–1136 (1996).
19. Gao, Y., Qian, W.-P., Dark, K., Toraldo, G., Lin, A. S. P., Guldberg, R. E., Flavell, R. A., Weitzmann, M. N. & Pacifici, R. Estrogen prevents bone loss through transforming growth factor  $\beta$  signaling in T cells. *P Natl Acad Sci Usa* 101, 16618–16623 (2004).

## Publishing Agreement

It is the policy of the University to encourage open access and broad distribution of all theses, dissertations, and manuscripts. The Graduate Division will facilitate the distribution of UCSF theses, dissertations, and manuscripts to the UCSF Library for open access and distribution. UCSF will make such theses, dissertations, and manuscripts accessible to the public and will take reasonable steps to preserve these works in perpetuity.

I hereby grant the non-exclusive, perpetual right to The Regents of the University of California to reproduce, publicly display, distribute, preserve, and publish copies of my thesis, dissertation, or manuscript in any form or media, now existing or later derived, including access online for teaching, research, and public service purposes.

DocuSigned by:

*Charles Schurman*

0AB7D87220D845B...

Author Signature

2/28/2022

Date